10 September 2004

Science

Vol. 305 No. 5690
Pages 1513–1660 $10

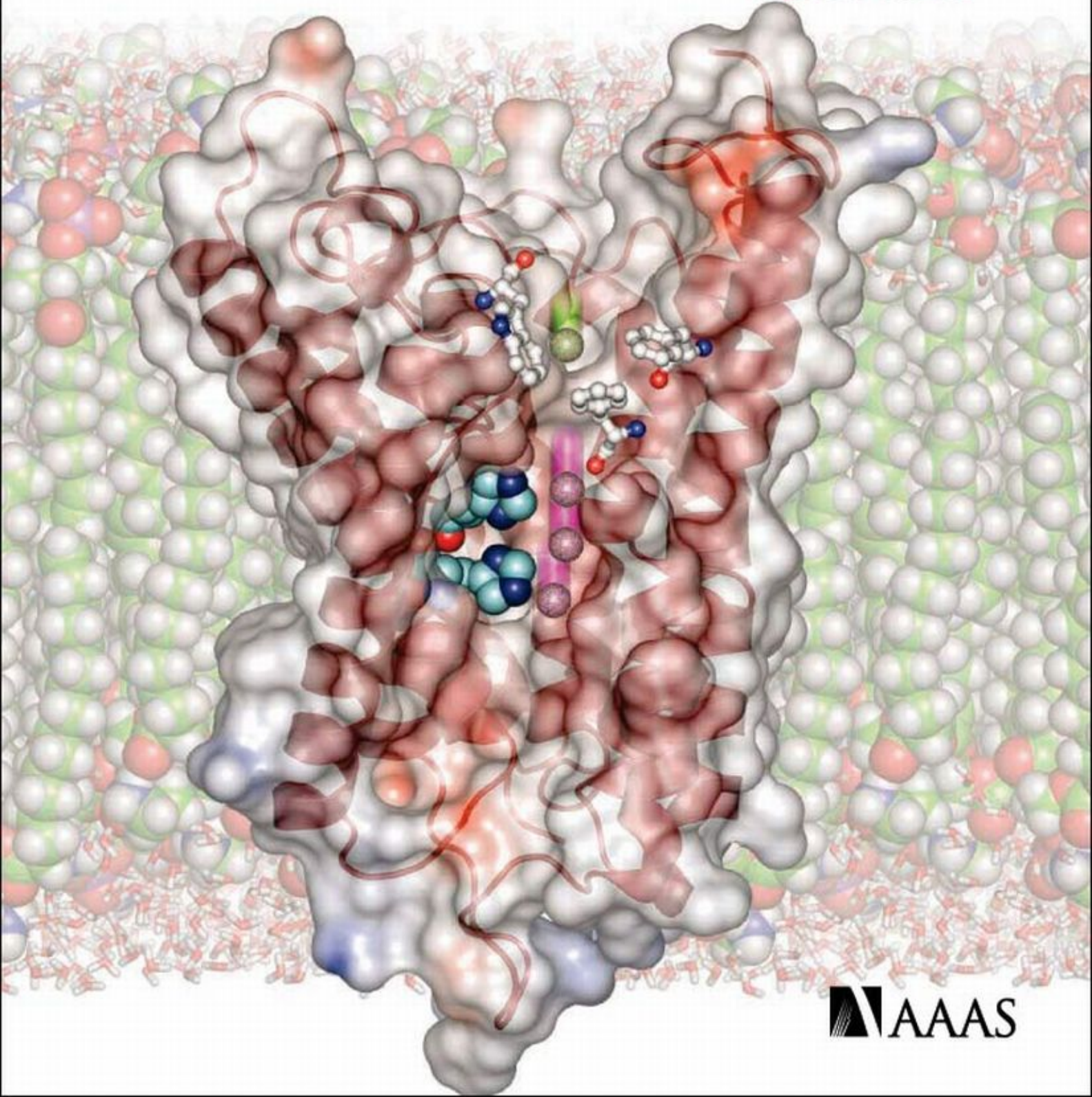

AAAS

Science

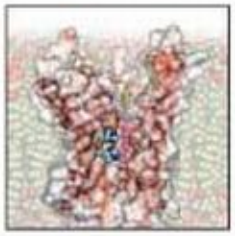

COVER Crystallographic structure of AmtB, a bacterial channel that transports the gas ammonia. During transport, ammonium ions (NH_4^+, the green sphere) are recruited and π-cation stabilized; then only uncharged ammonia (NH_3) enters the hydrophobic channel itself (three purple spheres). This mechanism prevents leakage of other ions or transmembrane potential. See page 1587. [Image: S. Khademi]

Volume 305
10 September 2004
Number 5690

DEPARTMENTS

1554

NEWS OF THE WEEK

1568

NEWS FOCUS

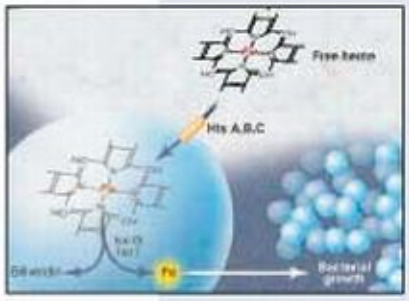

1577 & 1626

LETTERS

BOOKS *ET AL.*

POLICY FORUM

PERSPECTIVES

Contents continued

Science

SCIENCE EXPRESS www.sciencexpress.org

APPLIED PHYSICS

Controlling the Dynamics of a Single Atom in Lateral Atom Manipulation

J. A. Stroscio and R. J. Celotta

In a scheme for a possible atomic switch, the tip of a scanning tunneling microscope can be used to move a cobalt atom among almost equivalent adsorption sites and change the favored binding site.

PHYSICS

Single-Atom Spin-Flip Spectroscopy

A. J. Heinrich, J. A. Gupta, C. P. Lutz, D. M. Eigler

Low-temperature scanning tunneling microscopy reveals the magnetic excitations of a single manganese atom adsorbed on different surfaces, including the energy required to flip its spin.

CELL SIGNALING

Jun Turnover Is Controlled Through JNK-Dependent Phosphorylation of the E3 Ligase Itch

M. Gao, T. Labuda, Y. Xia, E. Gallagher, D. Fang, Y.-C. Liu, M. Karin

A single protein kinase activates both an enzyme that tags proteins for degradation and one of the proteins that it tags, a key transcription factor.

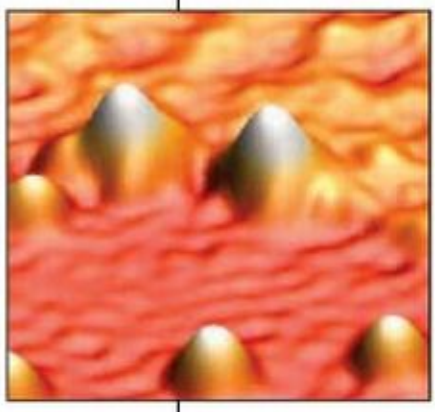

TECHNICAL COMMENT ABSTRACTS

BREVIA

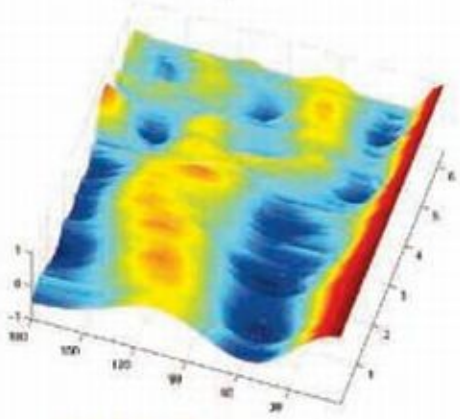

1574 & 1594

RESEARCH ARTICLES

REPORTS

Contents continued

REPORTS CONTINUED

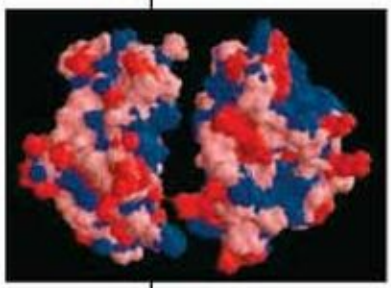

1605

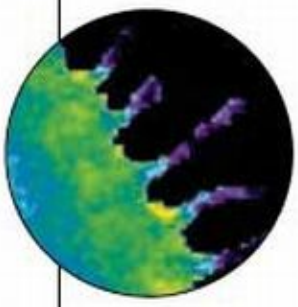

1615

1632

AAAS
ADVANCING SCIENCE, SERVING SOCIETY

SCIENCE (ISSN 0036-8075) is published weekly on Friday, except the last week in December, by the American Association for the Advancement of Science, 1200 New York Avenue, NW, Washington, DC 20005. Periodicals Mail postage (publication No. 484660) paid at Washington, DC, and additional mailing offices. Copyright © 2004 by the American Association for the Advancement of Science. The title SCIENCE is a registered trademark of the AAAS. Domestic individual membership and subscription (51 issues): $130 ($74 allocated to subscription). Domestic institutional subscription (51 issues): $500. Foreign postage extra: Mexico, Caribbean (surface mail) $55; other countries (air assist delivery) $85. First class, airmail, student, and emeritus rates on request. Canadian rates with GST available upon request; GST #125488122. Publications Mail Agreement Number 1069624. Printed in the U.S.A.

Change of address: allow 4 weeks, giving old and new addresses and 8-digit account number. Postmaster: Send change of address to Science, P.O. Box 1811, Danbury, CT 06813–1811. Single copy sales: $10.00 per issue prepaid includes surface postage; bulk rates on request. Authorization to photocopy material for internal or personal use under circumstances not falling within the fair use provisions of the Copyright Act is granted by AAAS to libraries and other users registered with the Copyright Clearance Center (CCC) Transactional Reporting Service, provided that $13.00 per article is paid directly to CCC, 222 Rosewood Drive, Danvers, MA 01923. The identification code for Science is 0036-8075/05 $15.00. Science is indexed in the *Reader's Guide to Periodical Literature* and in several specialized indexes.

Contents continued

sciencenow www.sciencenow.org Daily News Coverage

Fur-Replacement Therapy
Stem cells from hair follicles regenerate skin and hair in mice.

Earthquake Theory Shaken
A long period of calm doesn't necessarily mean the "big one" is coming.

Hidden Cost to Treated Water?
Toxic byproducts of chloramine suggest an unexpected hazard.

MiSciNet looks to its ancestors.

science's next wave www.nextwave.org Career Resources for Young Scientists

Global/US: Blending Biology and Bioinformatics *M. Yandell*
A scientist navigates between the worlds of bench research and computer programming.

Global/US: Navigating the 21st Century IT Marketplace *C. Parks*
Three professors at Auburn University discuss preparing for a career in information technology.

MiSciNet: Ancestors of the Sciences *Next Wave Staff*
A new Web page highlights the achievements of scientists and engineers of Native American, African, and Hispanic descent.

UK: Your Ph.D. in the Starting Blocks *The CareerDoctor*
Get tips on managing your project and your supervisor, and learn what to expect of new Ph.D. students.

Europe: More Personal Journeys *Edited by A. Forde*
Our ongoing series on the experiences of Marie Curie Fellows explores life outside the lab in Italy.

GrantsNet: Funding News for September 2004 *Edited by S. Martin*
Read about new opportunities from the National Institutes of Health, Cancer Research Institute, and more.

science's sage ke www.sageke.org Science of Aging Knowledge Environment

Perspective: TOR Pathway—Linking Nutrient Sensing to Life Span *P. Kapahi and B. Zid*
Pathway provides clues to the mechanism of life-span extension by dietary restriction.

News Focus: Will a Filet a Day Keep the Neurologist Away? *M. Leslie*
Fish oil molecule forestalls neuron damage in Alzheimer's mice.

News Focus: Leashing *Leishmania* *R. J. Davenport*
Some old mice fight parasitic infection better than young mice do.

Angling to prevent dementia.

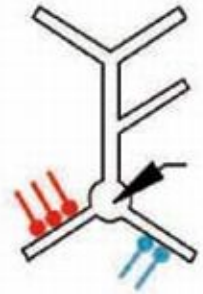

Dendrites integrate multiple signals.

science's stke www.stke.org Signal Transduction Knowledge Environment

Perspective: On the Fight Between Excitation and Inhibition—Location Is Everything *B. W. Mel and J. Schiller*
Meaningful interactions between excitatory and inhibitory synapses are highly spatially restricted.

Review: Human RAS Superfamily Proteins and Related GTPases *J. Colicelli*
Members of this large protein family regulate oncogenesis, nuclear transport, translation, and more.

Separate individual or institutional subscriptions to these products may be required for full-text access.

Composition of Jupiter's Atmosphere

When the Cassini spacecraft flew by Jupiter on its way to Saturn, the Composite Infrared Spectrometer (CIRS) took measurements of the jovian upper atmosphere. **Kunde *et al.*** (p. 1582, published online 19 August 2004) found enhancements of some hydrocarbons in the aurorae associated with temperature and magnetic field effects. Carbon dioxide and hydrogen cyanide added to the stratosphere by the impact of comet Shoemaker-Levy 9 have not been transported or diffused very much, possibly because polar vortices are inhibiting the diffusion of these species to higher latitudes.

Macrocyclic Libraries via DNA

DNA recognition has been exploited in several ways to synthesize libraries of macrocycles. **Gartner *et al.*** (p. 1601, published online 19 August 2004) linked single-stranded DNA to the peptide-like building blocks of macrocycles. DNA recognition of complementary strands brought the ring components into proximity so that ring-closure reactions could be performed. Specific macrocycles can then be selected for their protein affinity or enzymatic inhibition, and then identified by amplifying their DNA tags. A library of 65 such compounds was constructed.

Suddenly Turbulent

Despite having been studied for more than 100 years, the transition from laminar to turbulent flow in pipes is not understood. For other flow geometries, the source of the initial instabilities can be identified, but theory predicts that pipe flow should remain laminar for all flow rates. Recent numerical calculations suggested that traveling waves may be the reason the flow becomes turbulent. **Hof *et al.***'s (p. 1594; see the Perspective by **Busse**) hypothesis is now confirmed through experimental observations.

Slippery But Still Wet

The hydrophobic effect (the poor solvation of nonpolar parts of molecules) is thought to play a key role in protein folding. Large nonpolar side chains would create a layer largely depleted of water when hydrophobic domains are brought together. However, this situation is based mainly on a consideration of van der Waals interactions between solutes and water. **Zhou *et al.*** (p. 1605) have performed molecular dynamics simulations of the BphC enzyme, a two-domain protein that collapses into a globular structure in which complementary hydrophobic faces align. Only a weak water depletion, with a water density about 10 to 15% lower than the bulk, was formed between the hydrophobic domains. The authors find that when electrostatic effects are artificially removed in their simulations, the dewetting transition reappears and the collapse transition occurs at a much faster rate.

Dendrimeric Diblock Copolymers

Diblock copolymers can phase-separate into a rich array of morphologies, and dendrimer polymers allow many different functionalities to be placed onto highly branched compact molecules. **Cho *et al.*** (p. 1598) combined these two architectures into a single molecule and examined the phase behavior of a dendron grafted onto a long linear chain segment. The molecules show the same spherical, cylindrical, and lamellar structures seen in normal diblock copolymers, but also an unusual continuous cubic structure. The mechanical and charge transport properties of the polymers could be correlated with the observed phases.

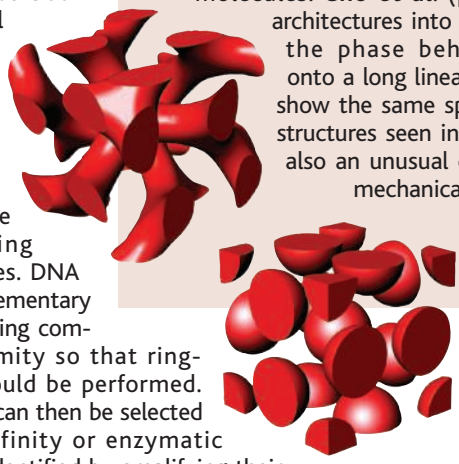

Phytoplankton Feel the Heat

The marine pelagic ecosystem is the largest one on Earth, yet little is known how global warming might affect it. Phytoplankton make up the base of the marine food web and support the rest of the larger organisms in the oceans. **Richardson and Schoeman** (p. 1609; see the news story by **Stokstad**) studied the impact of climate change on the abundance of marine planktonic food web over large space and time scales in the Northeast Atlantic. Their analysis of more than 100,000 samples over 45 years shows that climate warming has increased in the abundance of phytoplankton in cooler regions and a decrease in warmer ones.

Ensuring Adequate Gas Supplies

In an uncertain world, survival may depend on leaving nothing to chance. In biochemical terms, the way to place a spontaneously occurring process under control is to make an enzyme that catalyzes the reaction. Biological membranes are inherently permeable to gases, such as oxygen, yet **Khademi *et al.*** (p. 1587; see the cover and the Perspective by **Knepper and Agre**) now describe a bacterial protein that functions as an ammonia channel. The crystal structure of AmtB reveals a vestibule where the water-soluble species NH_4^+ is deprotonated and a hydrophobic conduit enables NH_3 to cross the membrane. The human analog of AmtB is the well-known rhesus or Rh factor.

Take That Copper

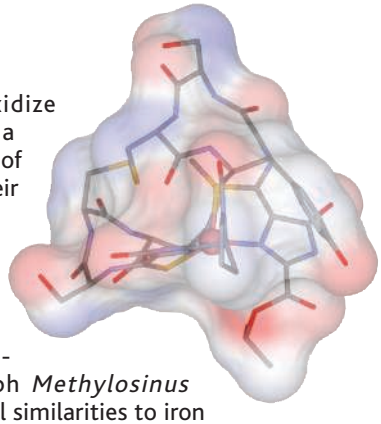

Methanotrophic bacteria oxidize methane, and copper plays a central role in the metabolism of these organisms. However, their copper trafficking mechanism is not well defined. **Kim *et al.*** (p. 1612) have identified and determined the structure of methanobactin, a copper-sequestering small molecule from the methanotroph *Methylosinus trichosporium* OB3b. Structural similarities to iron

CONTINUED ON PAGE 1529

CREDITS: (TOP TO BOTTOM) CHO *ET AL.*; KIM *ET AL.*

Published by AAAS

siderophores suggest that this molecule may function as a copper-siderophore by binding copper extracellularly and mediating its transport into cells.

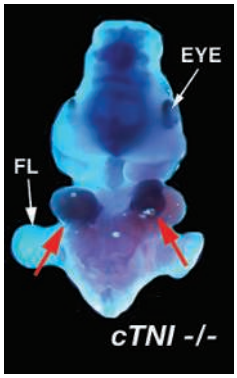

Forming Hearts sans Fusion

In the early developing vertebrate heart, bilateral cardiac mesoderm migrates to the ventral midline and then fuses to form the primitive heart tube. Subsequently, looping morphogenesis and chamber specification are observed. It has been generally thought that the fusion event must occur in order for these latter events to take place. However, **Li *et al.*** (p. 1619) now show that looping and septation can occur in the absence of heart fusion as seen with *Foxp4* mutant embryos, which display two complete hearts without fusion. The early bilateral precardiac mesoderm is preprogrammed to differentiate multiple cell types and to complete the complex morphological steps required for formation of the mature four-chambered heart.

Bacterial Persistence and Antibiotic Resistance

The inherent persistence of bacterial populations after exposure to antibiotics or other stress is well known but little understood. Such persistence is distinct from acquired antibiotic resistance and, on regrowth, such bacteria are still antibiotic sensitive (see the Perspective by **Levin**). **Balaban *et al.*** (p. 1622, published online 12 August 2004;) investigated the growth dynamics of various mutant and wild-type *Escherichia coli* using a microfluidic device to track individual organisms. At least three different phenotypes were revealed. Those with a normal growth rate were killed. Type I persisters exited stationary phase very slowly—hours rather than minutes after nutrients were restored. Type II persisters arose by a spontaneous switch from the normal growth rate to grow consistently more slowly, regardless of growth conditions, and, rarely, could switch back to the normal growth rate. Many pathogens have become resistant to the β-lactam antibiotics, like penicillin, by a variety of mechanisms, including mutation of penicillin-binding protein genes, destruction of the antibiotic by β-lactamases, or by inhibition of uptake by the bacterial cells. **Miller *et al.*** (p. 1629, published online 12 August 2004; see the Perspective by **Levin**) describe another mechanism for avoiding the lethal effects of antibiotics. Damage to penicillin binding protein 3 activates the DpiBA two-component signal transduction cascade and eventually triggers the SOS DNA repair response. When SOS kicks in, cell division pauses, and the bacteria escape lethal damage, at least from short-term antibiotic exposure, because synthesis of new cell walls shuts down.

Tracking Iron Sources of Pathogenic Bacteria

In geochemistry, different isotopes are classically used to track the source of an element. **Skaar *et al.*** (p. 1626; see the Perspective by **Rouault**) have devised a technique for use in living systems that combines stable isotope labeling with computational genome analysis. They could distinguish whether iron was taken from heme or from transferrin by the pathogenic bacterium *Staphylococcus aureus*, and discovered a previously unrecognized heme uptake system. Mutations in this system attenuate pathogenicity in model infections in the worm, *Caenorhabditis elegans,* and in the mouse. Drugs that target this system could prove useful in treating human infections.

Falling Together

Although coevolution has led to the tight interdependence of many species, little is known of the frequency with which the demise of one species causes the demise of another. **Koh *et al.*** (p. 1632) present a probabilistic model, scaled with empirical data, to estimate the number of such coextinction events across a wide range of coevolved systems. From this analysis, they derive a quantitative estimation of the possible cascading effects of species loss of endangered taxa. This work has implications for the understanding of historical extinctions and coevolution, as well as the conservation of biodiversity.

CREDIT: LI *ET AL.*

Published by AAAS

International Science Meetings

Progress in science depends heavily on the worldwide exchange of ideas, information, data, materials, and people. Although the Internet has accelerated information exchange and created virtual scientific communities, personal interactions at international scientific meetings are vital for the development and communication of scientific knowledge. In a world of increasing military, political, and religious conflict, how should scientists and international scientific organizations decide where to hold their meetings and whom to invite? Should scientists and their representative bodies boycott certain countries?

Personal conscience will direct the decisions of individual scientists about which meetings to attend. But independent scientific organizations and meeting organizers are in a different situation: They should ground their decisions on principles accepted by the scientific community. The Principle of the Universality of Science, articulated in the International Council for Science's Statute 5 (see www.icsu.org), provides relevant guidance. The essential elements of the principle are nondiscrimination and equity: All scientists should have the possibility of participating without discrimination and on an equitable basis in legitimate scientific activities, including attendance at international meetings.

In practice, the Principle of Universality means that any country is a legitimate host if it is willing to host scientific meetings at which scientists from all other countries are considered without discrimination as possible attendees. Conversely, a country that denies access (normally by refusing to grant entry visas) to scientists from other countries should be considered an unsuitable host. Naturally, other factors such as legitimate concerns for personal security might affect the selection of a meeting venue. What is essential is that those making the choice do so without discriminating on the basis of such factors as politics, ethnicity, or religion.

All scientists should have the possibility of participating without discrimination.

One topic has caused particular angst both for individual scientists and for scientific organizations in selecting meeting venues. It is the record of the proposed host country with respect to human rights. If freedom of expression is suppressed, or if universally accepted rights are denied to some on grounds such as gender, should scientists attend such a meeting? For the individual attendee, that's a challenge to personal conscience. But the Principle of Universality would argue that a government's disrespect for human rights alone is not a valid reason for refusing to consider that country as a meeting venue. If such a nation were willing to hold an international scientific meeting equitably, scientific organizations and scientists should be willing to consider attending. Indeed, such meetings may provide occasions to demonstrate solidarity with otherwise isolated national scientific communities. It would be naïve to ignore the possibility that a political regime might use the hosting of an international scientific meeting to confer legitimacy on its other policies, including restrictions on human rights. Even under those circumstances, however, scientists are often able to communicate in ways that help refute such attempts at distortion.

It is worth noting that this principle is consistent with other rules we apply in science. Two years ago, a group of investigators refused to send special materials used in a published paper to scientists from another nation, on the grounds that they had strong objections to the policies of the nation from which the requesting scientists came. Because the refusal violated standard journal policies governing the sharing of data and materials, the journal required that the materials be sent.

In an increasingly complex world, adherence to the Principle of Universality is critical if the international scientific community wants to continue to meet and exchange freely. To start picking and choosing countries as meeting hosts on the basis of politically dictated factors, including the important issue of human rights, is to step onto a slippery slope. In truly exceptional circumstances, such a step could be justified. If so, however, the decision-makers would need to be confident that they themselves were not being discriminatory or inequitable, and that the potential benefit to society clearly outweighed the costs imposed by the restrictions. By actively supporting universality, the international scientific community could by its own example help ameliorate the discriminatory policies and practices that regrettably do exist in many countries.

Jane Lubchenco
Goverdhan Mehta

Jane Lubchenco is president of the International Council for Science (ICSU) and Distinguished Professor at Oregon State University in Corvallis, Oregon. Goverdhan Mehta is president-elect of ICSU and a professor at the Indian Institute of Science in Bangalore, India.

Published by AAAS

EDITORS' CHOICE

edited by Gilbert Chin

***Dascyllus marginatus* swimming among *Stylophora pistillata*.**

ECOLOGY/EVOLUTION

Rapid Fin Movement Sleep

Coral and fish species often live in mutualistic associations, in which both partners benefit from the other's presence. For the fish, the association is usually obligatory, as they depend on the coral for both shelter and foraging (for zooplankton). The corals can survive on their own, but nevertheless show faster growth and greater reproductive output when fish are present; fish enhance nutrient input to corals via excretion and can protect them from predators and clear them of sediment.

Goldshmid *et al.* have documented another mechanism by which fish can benefit coral. In a reef of branching coral near the Red Sea port of Eilat, sleeping zooplanktivorous fish aerate their coral hosts at night. The fish, which were filmed by infrared video camera in their resting positions among the coral branches, spend the night sleep-swimming with their fins in vigorous motion. In the absence of fish, measurements showed that oxygen availability to the corals was severely reduced, to less than 30% of ambient levels. These observations may explain how dominant branching corals (whose morphologies hinder the free flow of water) can inhabit zones of relatively calm water. — AMS

Limnol. Oceanogr. **49**, 1832 (2004).

IMMUNOLOGY

Inciting Local Reactions

Most immune responses kick off within the lymph nodes and spleen, which are distal to sites of infection. In these secondary lymphoid organs, naïve B and T lymphocytes are introduced to antigens that have been delivered from the infected tissue and, once activated, they then disperse to deal with the pathogen.

Moyron-Quiroz *et al.* show that a distinct lymphoid tissue that forms locally at the site of infection contributes to clearing a respiratory virus. In mice engineered to lack lymph nodes and spleen (SLP mice), the appearance of activated B and T lymphocytes in response to influenza virus infection was found to be delayed but not otherwise impaired. Histological examination of lungs from these infected mice revealed sites with induced bronchus-associated lymphoid tissue (iBALT). Although the pathways leading to iBALT formation appeared distinct from those involved in the development of conventional lymphoid tissue, these sites possessed organized regions of proliferating T and B cells equivalent to those normally found in lymph nodes and spleen. Furthermore, SLP mice cleared virus efficiently and with reduced immune pathology, suggesting that iBALT may support locally efficient pathogen clearance while minimizing the global cost of a systemic immune reaction. — SJS

Nature Med. 10.1038/nm1091 (2004).

GEOLOGY

Mass Wasting

Taiwan consists of an active mountain belt, produced by the collision of the Eurasian and Philippine Sea plates, which forms the spine of the island. The mountains are being eroded by the many landslides caused by earthquakes and typhoons. Taiwan averages about four typhoons per year, and on 25 August 2004, Typhoon Aere produced wind damage, landslides, and flooding on the northeastern coast.

Dadson *et al.* have measured the changes in sediment concentrations in rivers (normalized to the water discharge rate) for a typhoon (Herb, August 1996), earthquake (moment magnitude 7.6 Chi-Chi, September 1999), typhoon (Toraji, July 2001) sequence. They found that at any given water discharge rate, the sediment load carried by a flood increased by a factor of 4 in the epicentral area: The earthquake, which produced 20,000 landslides, increased the rate of erosion, the amount of sediment delivered to the watershed, and the amount of sediment that is ultimately deposited in marine basins around the coast. Not only do these destructive events provide a natural laboratory to measure rates of erosion directly, but this particular sequence suggests that prehistoric large earthquakes and their rate of recurrence might be decipherable from the offshore sedimentary record. — LR

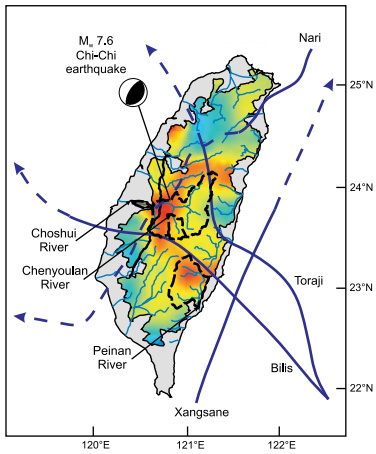

Map showing the paths (blue) of four recent typhoons, the Chi Chi event, and the normalized change in suspended sediment load (color scale).

Geology **32**, 733 (2004).

CHEMISTRY

A Mercury Bridge

Environmental contamination by mercury and other heavy metal ions is a growing problem, and detection requires sensors that are both highly selective and sensitive. Ono and Togashi have developed a DNA-based sensor that meets these requirements. Their 22-nt oligo contains two 9-nt mercury-binding sequences and a 4-nt linker, and is capped by a fluorophore at one end and a fluorescence quencher at the other. When Hg^{2+} ions bridge apposing thymines, the fluorophore and quencher are brought together in a hairpin configuration, and fluorescence drops. The sensor is more sensitive (40 nM) than previously reported small-molecule sensors and can detect Hg^{2+} ions even in the presence of a 10-fold excess of other heavy metals. — JFU

Angew. Chem. Int. Ed. **43**, 4300 (2004).

CONTINUED ON PAGE 1535

CREDITS: (TOP) RUTH MOTRO-REEF; (BOTTOM) DADSON *ET AL.*, *GEOLOGY* **32**, 733 (2004)

Published by AAAS

CELL BIOLOGY

Putting Supplies to Use

The fragile X mental retardation protein (FMRP) is an RNA-binding protein that is highly expressed in neurons. Absence of the protein results in fragile X syndrome, the most common form of inherited mental retardation, and, in a mouse knockout, the abnormal development of dendritic spines, which may result in deficits in long-term synaptic plasticity. Previous work has suggested that FMRP regulates the neuronal trafficking messenger RNAs (mRNAs) and represses translation of these mRNAs.

Two groups, Stefani *et al*. and Khandjian *et al*., describe the association of FMRP with polyribosomes—large, rapidly sedimenting granules containing mRNAs and ribosomes—and these appear to be actively translating conglomerates because Stefani *et al*. show that the ribosomes

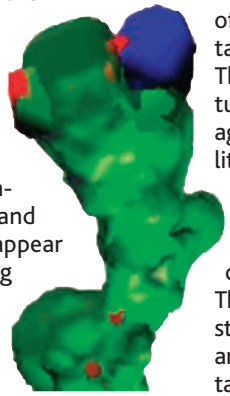

Reconstruction of a dendritic spine (green) showing FMRP granules (red) in the neck and head, and the presynaptic marker synapsin (blue).

can be released by the translational inhibitor puromycin. A clue to how FMRP might be involved in delivery, repression, and use of its mRNA cargo comes from results reported earlier by Antar *et al*. Using high-resolution fluorescence microscopy, they show that FMRP-containing granules are localized to dendritic spines and that stimulation, either through KCl depolarization or via metabotropic glutamate receptors, dynamically regulates FMRP localization in dendrites and at synapses. Thus, the apparently contradictory functions of FMRP may simply reflect where in the supply line one looks. — GJC

J. Neurosci. **24**, 7272 (2004); *Proc. Natl. Acad. Sci. U.S.A.* **101**, 13357 (2004); *J. Neurosci.* **24**, 2648 (2004).

BIOCHEMISTRY

A Neatly Pleated Sheet

Amyloid diseases such as Alzheimer's disease are characterized by a buildup of insoluble protein aggregates in tissues. These aggregates are formed by the conversion of normal soluble proteins into insoluble self-assembling fibrils via a soluble oligomeric intermediate that may be toxic to cells. An antibody that binds specifically to the oligomeric intermediates of several different amyloid proteins blocks toxicity, suggesting that the intermediates may share a common structure.

To identify what this structure might be, Armen *et al*. have modeled the conformational changes of four amyloid proteins under the low pH conditions that favor amyloid fibril formation. From their molecular dynamics simulations, they conclude that a key step in oligomeric intermediate formation is the acquisition of an α-pleated sheet that could be the target of the toxicity-blocking antibody. The α-pleated sheet, a secondary structural motif proposed more than 50 years ago by Pauling and Corey, has garnered little attention because it is rarely found in proteins. The α-pleated sheet has a residue length of 3.0 Å compared to 3.3 Å for the more common β-sheet conformation found in many proteins. The hunt is on to find this α-pleated sheet structure in the test tube; if it exists, such an unusual structure would be a valuable target for designing therapeutics. — OMS

Proc. Natl. Acad. Sci. U.S.A. **101**, 11622 (2004).

PALEOECOLOGY

Turning Over a New Leaf

Plants form the basis of most ecosystems, and understanding their turnover at the Cretaceous-Tertiary boundary is critical for determining the environmental effects of the large asteroid impact that seems to have triggered the mass extinction. Wilf and Johnson have studied in painstaking detail a section in North Dakota that spans the boundary and, when combined with other sections in North America that seemed to bear much of the brunt of the impact, helps document the effects of the extinction and earlier climate changes during the Cretaceous. Analysis of both leaf fossils and pollen shows that in all, about one-third to three-fifths of plant species in North America became extinct at the boundary, a bit lower than most previous estimates. Additional extinction occurred as a result of gradual global cooling during the latest Cretaceous. Most of the survivors were minor contributors to the Cretaceous ecosystem, yet they dominated the subsequent ecosystems in the Tertiary. — BH

Paleobiology **30**, 347 (2004).

CREDIT: ANTAR *ET AL*., *J. NEUROSCI.* **24**, 2648 (2004)

Published by AAAS

NetWatch

edited by Mitch Leslie

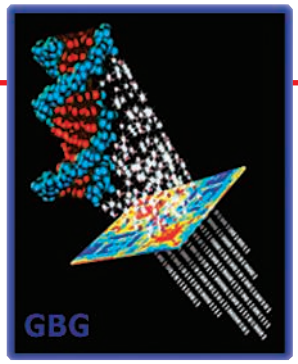

TOOLS

Getting More Out of Gene Chips

Microarrays yield prodigious amounts of data on gene activity, but the sheer volume can leave researchers asking, "What does it all mean biologically?" says molecular pharmacologist John Weinstein of the National Cancer Institute. This collection of tools crafted by Weinstein and colleagues can help the flummoxed winnow their results. For example, MatchMiner copes with what Weinstein calls genomics's "Tower of Babel": Different databases and gene chip–makers often apply different names to the same gene. Multilingual MatchMiner can translate between, say, GenBank and Unigene nomenclature. Another tool, GoMiner, helps collate and interpret genes by function. The site's newest offering, based on the team's paper last month in *Cancer Cell*, lets you download and analyze expression profiles for the ABC transporter genes. Some of these genes help tumors evade cancer drugs.

discover.nci.nih.gov

BIBLIOGRAPHY

Developing a Gut Reaction

If you've ever gotten sick after eating oysters, even smelling the shellfish can be revolting. This powerful reaction is a prime example of a conditioned taste aversion, in which animals learn to shun foods they associate with nausea. Round up the latest research in the field or delve into its history with this bibliography from researchers at American University in Washington, D.C. The collection lists nearly 2800 references (including the original description of taste aversion in a 1955 *Science* paper), many with abstracts or PDFs.

www.ctalearning.com

DATABASE

Down at the Frog Pond

The world's nearly 5700 amphibian species encompass baritone bullfrogs bellowing for a mate and wormlike caecilians slithering silently through tropical soils, tiny Brazilian frogs that could hide under a dime and lumbering salamanders big enough to tangle with an alligator. A clearinghouse of data on this multifarious group is AmphibiaWeb, sponsored by the University of California, Berkeley. The site is partway to its goal of posting a page for each amphibian species, with information on taxonomy, distribution, behavior, and conservation. Along with the more than 1000 species accounts, AmphibiaWeb holds recordings of nearly 100 frog calls and over 4000 photos. Above, the eastern newt (*Notophthalmus viridescens*), which lives from Nova Scotia to Florida.

www.amphibiaweb.org

IMAGES

Protozoans on Parade

Protist Image Data, hosted by the University of Montreal in Canada, holds information for everyone from students studying classification of algae to researchers hoping to cultivate parasitic amoebas. Visitors can explore the biology of some 20 genera of protozoa and algae, such as the ocean-dwelling photosynthesizer *Halosphaera* (left). An introductory page puts each group in evolutionary context. From there, you can study close-ups that delineate internal and external structures of the cells, get the latest on taxonomy and classification, or read about the creatures' form of reproduction (for *Halosphaera*, it's asexual). The site also lists sources that provide cultures of the organisms.

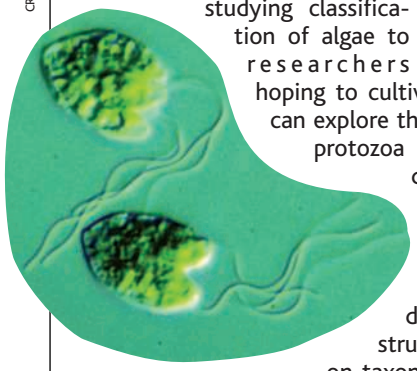

megasun.bch.umontreal.ca/protists

EDUCATION

Dust to Dust

You probably shouldn't drop by during lunch, but this Web site is worth visiting if you're curious about what happens to the body after death. Reflecting the ghoulish interests of ecologist Richard Major of the Australian Museum in Sydney, Decomposition lets you track the progress of decay with photos and time-lapse video. This piglet (below) has reached the sixth and final stage, with only hair and bones remaining, a point that usually takes 7 to 52 weeks. You can also read profiles of the "corpse fauna"—the waves of flies, moths, and bacteria that munch on and transform the cadaver.

Major disinters a wealth of intriguing factoids about our return to dust. For example, although brain cells usually perish within minutes of our demise, cells in the bones and skin can persist for days. And fat deposits can form "grave wax," or adipocere, a white substance that slows decay and has been found on 100-year-old corpses.

www.deathonline.net/decomposition/index.htm

Send site suggestions to netwatch@aaas.org. Archive: www.sciencemag.org/netwatch

CREDITS (TOP TO BOTTOM): JOHN WEINSTEIN/NCI; JOYCE GROSS; CHARLES O'KELLY; RICHARD MAJOR

Published by AAAS

This Week

PAGE 1548
Plankton and ocean warming

1551
Busquin leaves his mark

STEM CELL POLITICS

California Debates Whether to Become Stem Cell Heavyweight

President George W. Bush may end up doing California stem cell researchers a huge favor. Spurred by the Bush Administration's restrictions on funding for human embryonic stem (ES) cells, patient advocates, venture capitalists, and research leaders have launched a campaign to persuade California voters to pass an unprecedented ballot proposal, called Proposition 71, that would allocate $3 billion for the field over the next 10 years.

If the measure passes in November—and early polls say it's still too close to call (*Science*, 27 August, p. 1225)—California would spend nearly $300 million a year on human ES cell research, almost 50% more than the $214 million the National Institutes of Health (NIH) spent on all human stem cell research—both embryonic and nonembryonic—in 2003. "It will change the landscape of where this work is done," says Douglas Melton of Harvard University, who because of the White House's restrictions has had to set up a privately funded lab to derive new human ES cell lines. "California will become a hotbed of stem cell research."

Stem cell swing vote? Governor Arnold Schwarzenegger has stayed silent on the state's Proposition 71, which would fund human embryonic stem cell research.

Supporters of Proposition 71 have raised more than $11 million from donors such as Microsoft's Bill Gates and eBay founder Pierre Omidyar and his wife, Pamela. In the coming weeks, they plan to make their case for the measure with television, radio, and newspaper ads arguing that the investment will speed discovery of cures for dozens of diseases, cut health care costs, and boost California's economic recovery.

But some skeptics, including supporters of public funding for human ES cell research, say the plan is too expensive for a state facing multibillion-dollar budget deficits. A group called Doctors, Patients and Taxpayers for Fiscal Responsibility has led opposition to the measure, objecting to its cost as well as its focus on embryo-derived cells.

Proposition 71 at a Glance

- Establishes constitutional right to create and work with pluripotent stem cells, including those created by nuclear transfer.
- Allocates $3 billion in bond proceeds to stem cell research that NIH is not allowed to fund.
- Establishes California Institute for Regenerative Medicine to administer grants averaging $300 million per year for 10 years.

While Proposition 71 proponents say the opportunity for citizens to vote directly for science funding is an unprecedented chance for outreach, others worry that the political slogans could mislead voters and raise unrealistic expectations for miracle cures. "The argument that they use is that it's going to save lives. That's a good argument, politically, but in reality that's nuts," says George Annas, a bioethicist at Boston University. "Someday, hopefully, that's going to happen, but not in the next year or 2 or 10."

Proposition 71 is the brainchild of real estate developer Robert Klein II, whose son with juvenile diabetes and mother with Alzheimer's disease inspired his support for stem cell research. Following the decision that NIH funding for human ES cell research would be limited to cell lines created before 9 August 2001, California, like several other states, passed a bill explicitly allowing the derivation and use of new ES cell lines. But proponents soon realized that the measure meant little without any funding attached, says cell biologist Lawrence Goldstein of the University of California, San Diego.

Going further than the previous law, Proposition 71 would change the state's constitution, giving researchers the explicit right to conduct research with pluripotent stem cells, including cells created from embryos generated by couples undergoing fertility treatments or by somatic-cell nuclear transfer (SCNT). It would also authorize the state to issue $3 billion in bonds to establish the California Institute for Regenerative Medicine, a funding body that would disburse grants for buildings and research projects—an average of $300 million per year for 10 years.

The money would go to stem cell research that NIH cannot fund—namely, deriving or studying new human ES cell lines and working on human SCNT. It would potentially boost medical research funding in the state by 10% a year. (California scientists received about $3 billion from NIH last year, according to Goldstein.)

"I know these numbers seem immense," says Irving Weissman, a stem cell biologist at Stanford University and one of the initiative's main backers. "I'll just say that it shocked me" on first hearing, he says. But building buildings and conducting clinical trials—two of the tasks spelled out in the Proposition 71 proposal—can quickly consume tens of millions of dollars a year, he says. "Now it doesn't shock me at all."

The sums still stun some observers. "I think [$3 billion] is excessive in a state that is broke and cutting health services for their poor," says Annas, who notes that he nonetheless wholeheartedly supports federal funding for such research.

With respect to Annas's concern that the potential of stem cells is being oversold to voters, Weissman agrees that the nuances of the complicated field can get lost when distilled into a political slogan. "I say it all the time: 'Don't expect any cures from this in the next 5 years,' " he says. "Every time a public relations sort of person tries to talk about cures, I tell them you can't say that without qualifications. It's just not right."

What most excites scientists is hard to sell in a 30-second ad spot, says Fred Gage of the Salk Institute for Biological Studies in La Jolla. Although transplant therapies aren't likely to be ready within a decade, he says, stem cells will provide insights into many diseases. "Stem cell biology, and particularly human embryonic stem cells, will be a tool that every lab interested in biological sciences in the ▶

CREDIT: J. SCOTT APPLEWHITE/AP PHOTO

Published by AAAS

1552
Shaking up international health

1554
Skirmishing over salamanders

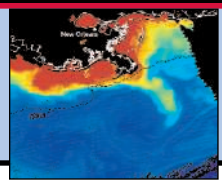

1557
Dead zone dispute

world will have to have" to test whether animal-based observations are true for human cells, says Gage. "We are asking the public of California to recognize the value that basic scientific discovery has on their lives. That's pretty 'out there.' We are giving the Californian voter credit for being smart enough to understand this."

Proponents of Proposition 71 also tout the potential economic boost the funding could give the economy. Cures for chronic diseases such as juvenile diabetes would save $1 billion a year in health care costs in the state, Goldstein says. And he and others argue that tax revenues and royalties from companies spun off from new discoveries will help offset the $6 billion it will cost to pay off the bonds over 30 years. "You could think of it as an intellectual stimulus package," Gage says.

But even if scientists develop a stem cell–based cure for diabetes, counters Annas, it would likely be so expensive that overall savings would be minimal.

The potential involvement of industry worries other observers. Richard Hayes of the Center for Genetics and Society in Oakland says that his group is concerned about the prominent role that industry representatives may have on the Institute for Regenerative Medicine's Independent Citizen's Oversight Committee. According to the proposition, the panel will include representatives from patient advocacy groups, universities, research institutes, and at least three biotech companies. "We're pro-science, pro-choice, and support public funding for stem cell research," he says. "But we're concerned that Prop 71 gives interested parties enormous power over a huge sum of public funds and restricts public accountability."

Whether voters will really understand such details before the election is far from clear, says Annas: "My guess would be that no one who is not directly involved will have read this initiative, and not more than a tiny percentage of voters really understand what this is about."

One wildcard is California's governor, Arnold Schwarzenegger. The state Republican party has come out against Proposition 71, but the pro-choice Republican governor has stayed quiet. The governor's support of either camp could decide the race, Weissman predicts. –GRETCHEN VOGEL

AIDS VACCINES

HIV Dodges One-Two Punch

In what has become a depressingly familiar story line, a leading AIDS vaccine strategy has failed to live up to expectations in human studies.

An international team led by Andrew McMichael, an immunologist at Oxford University in the U.K., reported last week at an AIDS vaccine meeting in Lausanne, Switzerland, that only 20% of 205 participants in the study had had the critical immune response the researchers had hoped to elicit. Like many who attended the meeting, Anthony Fauci, head of the National Institute of Allergy and Infectious Diseases (NIAID), says the meager response surprised him. "It was dreadfully low," says Fauci.

The 4-year-old study, funded by the New York City–based International AIDS Vaccine Initiative (IAVI), is taking place in five countries, but these preliminary results are from the United Kingdom, Kenya, and Uganda. Although many AIDS vaccines have focused on triggering production of antibodies that prevent HIV from infecting cells, this trial tested whether two vaccines in combination could stimulate the so-called cellular arm of the immune system, which clears cells that the virus manages to infect. The study built on provocative evidence from HIV-exposed but uninfected sex workers in Nairobi and the Gambia. McMichael and other researchers found that these subjects had developed cellular immune responses to the virus (*Science*, 23 June 2000, p. 2165).

The closely followed study has broad implications because several other research groups are pursuing similar approaches. Both vaccines rely on harmless vectors to shuttle an HIV gene (*gag*) and other small pieces of the virus into the body. The "priming" vaccine splices the viral components into a ring of bacterial DNA, and the researchers follow it with a "boost" that delivers the same HIV ingredients by means of an experimental smallpox vaccine called modified vaccinia Ankara (MVA).

Clinical study. Research in this Nairobi clinic found that HIV-exposed but uninfected sex workers had developed cellular immune responses to the virus. The vaccine failed to produce that response.

The McMichael team measured the ability of the prime-boost vaccination to turn up production of the biochemical messenger interferon γ in response to HIV, an indicator that the immune system has launched a cellular attack against the virus. The negative, preliminary results led IAVI to scotch plans to expand the MVA/DNA trials to other countries, but the researchers will complete those that are under way.

McMichael says their results may be disappointing in part because the team was very stringent in how it defined a positive interferon γ response. But he also suspects that the DNA prime, which works well in mouse experiments, didn't do its job. "I think DNA is a poor primer in humans," says McMichael, who notes that it has performed badly in other human studies. Yet there's no denying the new data call into question the worth of MVA. "Is this the death knell for all MVAs?" asks Cornell University's John Moore, a member of NIAID's AIDS Vaccine Research Working Group. "If other MVAs are no more immunogenic than McMichael's, this has major strategic impact." ▶

CREDIT: MALCOLM LINTON

Published by AAAS

"Before we throw away the platform, I think it's worth doing more studies with MVA," says IAVI's Emilio Emini, who formerly headed the AIDS vaccine program at Merck & Co., noting that IAVI has two new MVA projects in the works. "By this time next year, we'll know whether the whole platform is in trouble."

McMichael urges people to keep his group's data in perspective. "People have unreal expectations that a vaccine is just around the corner," says McMichael. "Getting the vaccine is going to be a slow building process. If something doesn't work, you have to reshape it. We want to regroup and keep going. And I don't think someone else is going to solve it in the next 3 months." His lab also plans to continue a small "therapeutic" study of the vaccines, intended to boost immune responses in HIV-infected people who are receiving antiretroviral drugs.

Seth Berkley, the head of IAVI, says it's critically important to pull the plug when confronted with disappointing results—a step that is all too often delayed in AIDS vaccine research. "The hardest decisions are going to be dropping things, not keeping things alive," says Berkley. "I'm quite proud that we took an idea that has been on the agenda since 1993 and got what would appear to be a definitive answer in a short period of time." **–JON COHEN**

JAPAN BUDGET

Science Ministry Puts In for Big Increases

TOKYO—Operating on the principle that it doesn't hurt to ask, Japan's Ministry of Education, Culture, Sports, Science, and Technology has submitted requests for sizable spending increases in next year's budget. That strategy, combined with the government's repeated promise to bolster research, helped make science one of the few winners in this year's budget. And policymakers predict it will work again.

"I don't know that [the overall 2005 science budget] will increase, but it may not decrease," says Reiko Kuroda, a chemist at the University of Tokyo and a member of the Council for Science and Technology Policy, which will vet the requests before they go to the Finance Ministry. That would be quite an achievement, she says, as "all other [spending categories] are likely going down" as the government tries to reduce a ballooning deficit. The ministry's current budget is $33 billion, and the council staff is still reviewing the 2005 requests submitted at the end of last month.

Those requests, for the fiscal year starting in April, include increases of 32% for life science research, 23% for environmental studies, and 46% for nanotechnology. The ministry also wants to pump up spending on competitive grants in a last-ditch effort to fulfill a promise to double such research over 5 years.

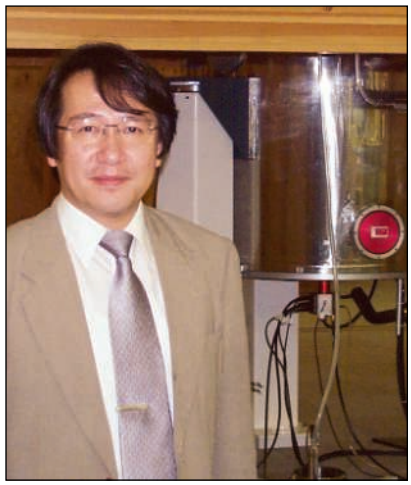

Unfolding story. RIKEN's Shigeyuki Yokoyama hopes protein project gets a raise next year.

CREDIT: D. NORMILE

Among the life sciences, the ministry is seeking a 48% boost, to $36 million, for a project headed by geneticist Yusuke Nakamura of the University of Tokyo to link single-nucleotide polymorphisms to diseases and adverse drug reactions, as a step toward tailoring medical treatments to an individual's genetic characteristics. It has also asked for an 18% hike, to $97 million, for the fourth year of a 5-year effort to resolve the structures of 3000 proteins in order to improve understanding of protein function and identify possible drug targets. "So far we have produced more than the promised number of protein structures," says Shigeyuki Yokoyama, a biophysicist at the RIKEN Genomic Sciences Center in Yokohama, who leads the project.

Japan's current 5-year science and technology plan pledged to double (from roughly $2.7 billion in 2000) the amount of money disbursed through competitive grants (*Science*, 27 June 2003, p. 2027). Although the government may get only halfway to that goal, planners at the Education and other ministries are emphasizing competitive grants in their 2005 requests. The bulk of the boost for nanotechnology and materials sciences, for example, would go to a $56 million competitive grants program, and the only major new program in the life sciences would provide $88 million to address emerging diseases (for example, SARS and avian influenza), molecular imaging, and other "social needs." **–DENNIS NORMILE**

ScienceScope

Big Bucks for Buck Rogers

NASA may need up to $32 billion more than it currently estimates for its proposed human exploration effort. The $127 billion figure, suggested this week by the Congressional Budget Office (CBO), is a third higher than what the agency envisions spending to return humans to the moon by 2020 and take the first steps toward Mars.

NASA managers have argued that they can keep the costs of the Bush Administration's exploration plan within the agency's current $15 billion annual budget by using robotic technologies while retiring the shuttle and space station. But the study by CBO, Congress's bipartisan accounting arm, expresses skepticism that those savings will materialize. Without huge funding increases, it warns, NASA will have to divert nearly half of planned aeronautics and science spending to exploration. Overall, CBO estimates that NASA may need a budget two-thirds larger than its current allocation by 2015 in order to meet its exploration schedule.

Such predictions may make it more difficult for NASA to persuade Congress, which returned from a summer recess this week, to begin funding its exploration program. **–ANDREW LAWLER**

CITES Withholds Caviar Quotas

Conservationists are welcoming a move by a United Nations agency that effectively suspends international trade in this year's caviar (sturgeon eggs) from the Caspian Sea region by delaying new export quotas.

Some scientists say that five Caspian states—which supply 90% of the world's caviar—have obscured overfishing by overstating the health of wild sturgeon stocks. Last March, a committee of the U.N.'s Convention on International Trade in Endangered Species of Wild Fauna and Flora (CITES) asked its secretariat to determine whether the exporters were complying with a global sturgeon conservation agreement (*Science*, 26 March, p. 1955). But the nations have yet to provide needed information, says James Armstrong, deputy secretary general of CITES. In particular, estimating levels of illegal fishing in order to set sustainable quotas has proved "difficult for them ... almost impossible," he says.

The 166 CITES members are now likely to bar Caspian caviar imports until the quotas are approved. Exporters, meanwhile, would like new numbers approved by November, so they can sell during the peak holiday season. Existing stocks will remain on the market.

–FIONA PROFFITT

Published by AAAS

CLIMATE CHANGE

Changes in Planktonic Food Web Hint At Major Disruptions in Atlantic

Land plants and animals are already responding to global warming. Cherry trees in Japan are blossoming ever earlier in the spring, for example, and some birds in northern Europe lay their eggs sooner than they used to. The oceans appear to be warming as well, and several groups are studying how the changes might be affecting marine organisms. Now two papers provide the most comprehensive, longest-term look at the impact of rising temperatures on ocean ecosystems.

On page 1609, Anthony Richardson, a numerical ecologist at the Sir Alister Hardy Foundation for Ocean Science (SAHFOS) in Plymouth, U.K., and marine ecologist David Schoeman of the University of Port Elizabeth in South Africa show that the abundance of plankton in the northeast Atlantic has shifted with water temperature over the past 45 years. And in the 19 August issue of *Nature*, Richardson and SAHFOS marine ecologist Martin Edwards reported that the timing of seasonal abundance of plankton has shifted in ways that already may have radically disrupted the food web. "These changes in the plankton will almost certainly have huge impacts on commercial fisheries and so will have accompanying economic implications," comments marine ecologist Graeme Hays of the University of Wales, Swansea.

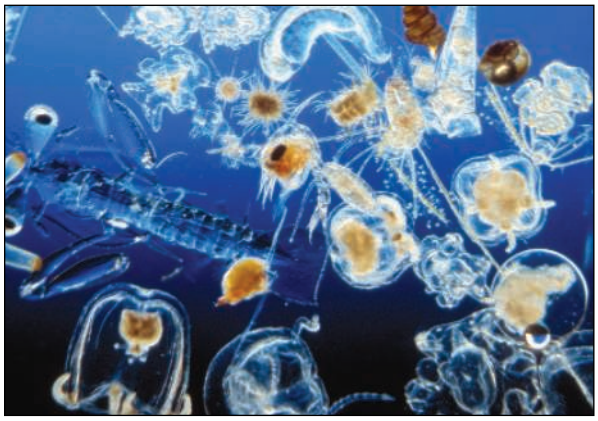

In flux. Plankton communities are changing radically in the northeast Atlantic, a broad new study has found.

Both sets of findings come from a unique monitoring effort called the Continuous Plankton Recorder survey, run by SAHFOS. Since 1931, researchers have hitched small sampling devices behind freighters that ply the North Atlantic, and since 1997, in the North Pacific as well. Every unit contains a long roll of silk that collects plankton as it slowly spools into an internal chamber. Each 10 centimeters of silk harvests about 18 kilometers' worth of plankton, which are identified in the lab. More than 9 million kilometers have been towed over the past 70 years. "It's only with data sets like this that we're going to be able to understand the impact of climate change," says biological oceanographer Charles Greene of Cornell University.

Using these data, SAHFOS researchers have previously discovered biological changes, such as the northward shift of some plankton species in parts of the northeast Atlantic (*Science*, 31 May 2002, p. 1692) and changes in the abundance of a few species. The new *Science* paper expands that effort by looking at more than a hundred taxa, including phytoplankton, such as diatoms and dinoflagellates; ▶

SCIENTIFIC PUBLISHING

NIH Proposes 6-Month Public Access to Papers

The National Institutes of Health (NIH) has released a draft policy aimed at increasing public access to the results of NIH-funded research. The proposal issued 3 September in the NIH Guide* would require grantees to deposit copies of their papers in NIH's free PubMed Central archive once they have been accepted by a journal. Manuscripts would be posted online 6 months after publication.

In July, a congressional spending panel recommended that NIH post NIH-funded manuscripts within 6 months of publication, or immediately if NIH grants were used to pay publication costs. The language, part of NIH's pending 2005 budget, triggered frenzied lobbying on all sides. Librarians, patient organizations, and scientists who think taxpayers should have easier access to NIH-funded research urged NIH to follow the House language. Commercial publishers and many scientific societies lobbied against a mandatory plan, saying it could bankrupt many journals.

Timed release. NIH's Elias Zerhouni sets limit for posting papers.

NIH Director Elias Zerhouni, who has held meetings recently with interested groups, told scientists last week that 6 months was "reasonable" (*Science*, 3 September, p. 1386). The draft policy is similar to the House language: Investigators will submit their final, peer-reviewed manuscript to PubMed Central. Journals can ask NIH to replace the manuscript with the published paper, sooner than 6 months if they wish. NIH plans to take comments for 60 days and will also post the draft policy in the *Federal Register*.

"We're strongly behind it," says Richard Johnson of the Scholarly Publishing and Academic Resources Coalition. His group "would have preferred immediate access, but we see this as an important step forward."

Scientific societies had a mixed reaction. Alan Leshner, executive director of AAAS (which publishes *Science*), calls the policy "a reasonable compromise" but says it "could pose significant risk for some scientific societies." And Martin Frank, executive director of the American Physiological Society, calls the plan "an unnecessary expenditure of federal funds for a redundant repository of peer-reviewed literature." He notes that most journals already provide back articles for around $5 to $30, or for free after a certain period. Frank also wonders how PubMed Central will keep track of manuscripts submitted separately by co-authors of the same paper. "It could be chaos out there," he warns.

The Association of American Publishers (AAP), which is also worried about the policy's impact on free markets, plans to take its objections to senators Arlen Specter (R–PA) and Tom Harkin (D–IA), chair and ranking member, respectively, of the Senate appropriations committee for NIH, which will take up the spending bill once it passes the House. "We think there are a lot of questions that should be answered," says Allan Adler, AAP vice president for legal and governmental affairs. However, last week Specter told *The Washington Post* that he does not intend to intervene. **–JOCELYN KAISER**

*grants1.nih.gov/grants/guide/notice-files/NOT-OD-04-064.html

CREDITS (TOP TO BOTTOM): PETER PARKS/IMAGEQUESTMARINE.COM; RICK KOZAK

Published by AAAS

herbivores, such as crustaceans called copepods; and carnivorous plankton, including arrow worms and voracious crustaceans called amphipods.

Comparing the counts with changes in sea surface temperatures in 20 regions of the northeast Atlantic, Richardson and Schoeman found two patterns. Phytoplankton tended to become more abundant when cooler regions warmed, probably because higher temperatures boost metabolic rates. But they became less common when already warm regions got even warmer, possibly because warm water blocks nutrient-rich deep water from rising to the upper layers, where phytoplankton live. That variable response suggests that climate change will have regional impacts on fisheries, Hays says.

Richardson and Schoeman also demonstrated effects further up the planktonic food chain. When phytoplankton bloomed, both herbivores and carnivores became more abundant. The pattern indicates that the planktonic food web is controlled from the "bottom up," by primary producers, rather than from the "top down," by predators. That means climate effects on primary producers could reach all the way to fisheries. "To date, we are not very good at detecting the consequences of plankton changes for fisheries production or for the rest of the marine ecosystem," says fisheries scientist Keith Brander of the International Council for the Exploration of the Sea in Copenhagen, Denmark.

In the *Nature* paper, Richardson and Edwards charted shifts in the timing of seasonal plankton blooms over the decades. Each species has an annual cycle, and herbivores and carnivores have evolved to exploit the phytoplankton bloom. Since 1987, however, the cycle's peaks have shifted out of synch. In places where waters have warmed, the peak bloom of phytoplankton occurs 3 weeks earlier, but zooplankton grazers peak only 10 days earlier. If the discrepancy causes herbivores to go hungry, they could provide less prey for fish larvae and carnivorous plankton. "These effects at the base of the food web are so dramatic that they're bound to have an effect on the whole North Atlantic ecology," Edwards says.

Measuring that impact will take a lot of work, Greene says, because marine food webs are extremely hard to untangle. Still, he says, ecologists should be concerned, because much more northeast Atlantic warming is predicted. Brander expects further changes in plankton abundance and timing as warming continues. Although some species should adapt, Edwards says, new communities will also likely emerge.

SAHFOS and others will be watching.

–ERIK STOKSTAD

NUCLEAR PROLIFERATION

South Korea Admits to Laser Enrichment Program

Another secret nuclear program on the Korean Peninsula is in the news, but this time it's the work of South Koreans that's drawing criticism. The International Atomic Energy Agency (IAEA) announced last week that South Korea had used a covert isotope-separation program to create a few hundred milligrams of highly enriched uranium. The technology, potentially an energy-saving way to separate bomb-worthy uranium-235 from its less dangerous sibling uranium-238, was tried and abandoned in the United States and Russia over the past few decades.

Few details about the nature of the program are available. However, faced with IAEA inspections, the Republic of Korea (ROK) admitted that several years ago its scientists had produced small quantities of near–weapons-quality uranium by using lasers, apparently at a nuclear facility in Taejeon, South Korea. Although the ROK government is claiming that the laser-separation project was run by a handful of rogue scientists, proliferation experts believe that the program must have been sanctioned by higher-ups.

"It's their main nuclear research site," says nuclear proliferation expert David Albright, president of the Institute for Science and International Security in Washington, D.C. "The scientists worked for a government-owned agency, and they had to report to their bosses." Furthermore, nuclear experts say, the technology is too costly and intricate for a small group of rogue scientists to have pursued on its own.

The method in question is known as atomic vapor–laser isotope separation (AVLIS). AVLIS exploits a subtle difference in how uranium-235 and uranium-238 absorb light. Because the two atoms have different masses, they absorb very slightly different colors of light. By shining a laser of precisely the right color on a beam of mixed-isotope uranium vapor, scientists can induce the uranium-235 in the beam to absorb a photon of light and fly in one direction while the uranium-238 in the beam remains unaffected. That's the theory, anyway.

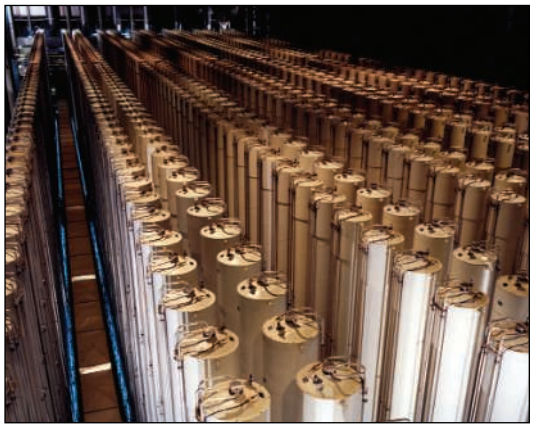

Spin control. Most countries have adopted nonlaser methods for enriching uranium, such as spinning it in gas centrifuges like these.

CREDIT: DOE

In practice, though, AVLIS hasn't proven useful for separating uranium on a large scale. "There are no commercial programs" that use lasers to separate uranium isotopes, says Thomas Cochran of the Natural Resources Defense Council in Washington, D.C. A diplomat who is knowledgeable about nuclear proliferation issues says the countries that have tried it concluded "it was too expensive; you could not produce enough [enriched uranium] quickly." In 1999, the United States killed its own AVLIS program, developed at Lawrence Livermore National Laboratory in California and run by a private firm based in Maryland.

Iraq and Iran also worked on laser-separation technologies, often with help from vendors in other countries. "Laser enrichment is not simple," says Kenneth Luongo, executive director of the Russian-American Nuclear Security Advisory Council in Washington, D.C. "In the Iranian case, they once had a deal with the Russians. In [the South Korean] case, it's not clear where the technology would have come from or whether it was developed indigenously."

Albright says he would be disturbed if the United States had been involved. "But I'd be even more worried if they'd made it themselves," he says, because it would mean that the technology isn't prohibitively difficult to develop. "It shows that, at the laboratory level, you can make nuclear materials."

The few hundred milligrams of enriched uranium are orders of magnitude less than what's needed to build a bomb. But producing even that amount is a serious violation of the nuclear nonproliferation treaty. "It's not so much the quantities but the fact that it wasn't declared," says the knowledgeable diplomat.

–CHARLES SEIFE

Published by AAAS

EUROPEAN UNION

The Commissioner Who Listened

BRUSSELS—Things didn't look auspicious for physicist Philippe Busquin when he was nominated for Europe's top science post in 1999. European scientists—many of whom equate Brussels with bureaucracy—knew next to nothing about the Belgian socialist and career politician. During a stormy confirmation hearing, conservative members of the European Parliament mounted a fierce attack, alleging that Busquin was tainted by corruption scandals in the party he chaired and unfit to be a credible manager. Busquin survived, but one thing was certain: The new European Commissioner for Research would have to work hard to make his term a success.

Now that his 5-year tenure has come to an end—Busquin is stepping down this week to take a seat in the European Parliament, ahead of the departure of the rest of the European Commission on 1 November—the skepticism has evaporated. "He really has done a remarkable job," says Thomas Östros, Sweden's minister of science and education. Östros credits Busquin with a skillful campaign to get science to the top of Europe's political agenda, crowned by an agreement, signed in Barcelona in 2002 by E.U. member states, to drive toward spending 3% of national income on research and development by 2010.

Busquin also launched the notion of a European Research Area (ERA)—Europe's scientific equivalent of a free trade zone—and maneuvered it into the text of the proposed European Constitution. He fought hard to fund stem cell research and threw his weight behind the creation of a European Research Council (ERC), which would fund basic research using no other criterion than excellence. "For the first time, we had a commissioner who was listening and who was responsive," says Kai Simons, director of the Max Planck Institute for Molecular Cell Biology and Genetics in Dresden.

Busquin had far better relations with the European Parliament than did Edith Cresson, his controversial predecessor, whose alleged fraud triggered the downfall of the entire commission in 1999. In part, this is because he's a "modest and unassuming man," says Eryl McNally, a former British member of the European Parliament. "Sometimes, it's the quiet ones who get things done."

In an interview with *Science* in his partly packed-up office last week, Busquin said he was proud of his tenure and a bit sad to leave a post that satisfied his passions of science and politics. He relished seeing top-notch research up close, he says, from the vast particle smashers near Geneva to Europe's mountaintop astronomical observatory at Paranal, Chile. And the European Molecular Biology Laboratory in Heidelberg is a "phenomenal place," he says. He devours its annual research report: "It's one of the most interesting books I know."

Busquin worries, however, that many Europeans fail to see science's beauty, let alone its potential to foster economic growth. Investment in research and development is lagging, compared to the United States and Japan, as young European researchers are moving overseas. At the same time, China is on the way to becoming a new scientific superpower. With Europe's aging population and few natural resources, the continent's survival is at stake, he warns, and only science and innovation will keep it competitive.

Science's cheerleader. Busquin sets out his policy on embryonic stem cells at a press conference in Brussels last year.

CREDIT: YVES LOGGHE/AP PHOTO

One response championed by Busquin is the ERA: It aims to forge a Europe-wide science policy, coordinate national funding agencies, and remove barriers between E.U. states that prevent researchers from relocating. Lining up political support among European leaders for an overall increase in spending was another. "The 3% really was his own idea," says Robert-Jan Smits, who heads a directorate under Busquin. But each country is responsible for its own R&D spending, and even Busquin acknowledges that many won't meet the target. Still, he says, using periodic scorecards produced by his staff, "we can now point the finger at countries that have not done their homework."

ERC was not one of Busquin's ideas. But once it arose in the scientific community, he was a skillful enough politician to sense its importance and embrace it, says Enric Banda, a former head of the European Science Foundation and director of the Catalan Research Foundation.

Still, there were problems that Busquin could not solve. Scientists often gave him an earful about the inescapable bureaucracy that comes with applying for grants from the E.U.'s gargantuan Framework research programs. Busquin acknowledges the problem but says it's difficult to amend, for various reasons. However, he agrees that the new ERC should keep paperwork to a minimum.

Another disappointment for Busquin was his failure to win support for using Framework money to fund research on human embryonic stem cells. Countries such as Germany, Austria, and Ireland, which have banned work that requires the destruction of embryos, fiercely opposed spending a single euro on such controversial studies and threatened to sink the entire $17.5 billion 6th Framework Program to make their point. "He took a very firm stand in the interest of science," says Peter Gruss, president of the Max Planck Society. The battle ended in a deadlock last year; for the moment, studies can be funded only after review by a special committee (*Science*, 12 December 2003, p. 1872).

Although he launched new initiatives to boost biotech, Busquin also acknowledges that the deep-seated public resistance to genetic engineering in Europe is hard to overcome—even though he finds it troubling sometimes. "When I see people uprooting trial fields, I find it completely unacceptable. And I think Europe should be a bit more clear and courageous in saying: 'No. Scientific progress is an important value for us.'"

Less glamorous times lie ahead. Busquin says he would have loved to stay on, but the Belgian government did not renominate him; instead, he was elected in June as one of the 730 members of the European Parliament, which sits a stone's throw from his current office. But because McNally and several other science experts have just stepped down, Busquin will stand out as the unrivaled heavyweight on science issues, and he says he will return to the fight with enthusiasm. Janez Potočnik, the Slovenian economist nominated to succeed him at the commission (*Science*, 20 August, p. 1089), is lucky, says McNally: "He has a very good legacy to work with." **–MARTIN ENSERINK**

Published by AAAS

U.S. official William Steiger has been criticized for making life harder for scientists in international health research and policymaking. He says he has strengthened the field

The Man Behind the Memos

It's not often that scientists at the bench or in the field battling diseases such as AIDS and malaria take note of a special assistant to the Secretary of Health and Human Services. But William R. Steiger, the point person on international health for HHS Secretary Tommy Thompson, has made a name for himself everywhere—from the National Institutes of Health (NIH) to the Centers for Disease Control and Prevention (CDC) to the halls of academia. Then again, not many bureaucrats would want the kind of attention he's received.

Steiger, 34, a political appointee who has close ties to the Bush family, has brought an unprecedented level of oversight to HHS's international activities—and it has made him a lightning rod for critics. When HHS clamped down on foreign travel by its scientists, Steiger began personally approving each trip. When industry groups criticized a World Health Organization (WHO) report on nutrition, Steiger slammed it as scientifically flawed. When the department declared that it would choose which U.S. scientists WHO could invite as expert advisers, Steiger signed the memo.

The critics complain that Steiger, who has a doctorate in Latin American history and is fluent in Spanish and Portuguese, has politicized a position traditionally held by an expert in public health. His command-and-control management style is demoralizing, they say. "I see an increasing and pervasive squeezing of academic freedom by bureaucratic control," says Gerald Keusch, who left as director of NIH's Fogarty International Center last December and recently endorsed a Union of Concerned Scientists critique of the Administration's science policy.

In a telephone interview with *Science*, Steiger brushed off the criticism, arguing that he has led a "major expansion" of HHS's international activities. His Office of Global Health Affairs' (OGHA's) management changes—part of Thompson's efforts to unite the department as "one HHS"—have shaken up the status quo; the scientists who complain, he says, "have axes to grind." He says too that "no HHS secretary in history has been as devoted to global health" as Thompson, who has traveled to 35 countries to see health problems firsthand and chairs the Global Fund, the international AIDS relief program.

Inside track

Steiger grew up in Washington, D.C., the son of Representative William A. Steiger from Oshkosh, Wisconsin, a moderate Republican who gave Vice President Dick Cheney his first political job. Representative Steiger died in 1978. Godson of former President George H. W. Bush, the younger Steiger completed a dissertation on Brazilian history in 1995 before he was tapped to be education policy adviser to then–Wisconsin governor Thompson. When Thompson became HHS secretary in 2001, he brought his protégé to Washington as part of his management team and gave him the job of overseeing international affairs.

Steiger was soon named Thompson's representative to the WHO board, the World Health Assembly, despite his lack of health experience. HHS also revamped the entire U.S. delegation, which in previous years had included representatives from the American Medical Association (AMA) and the American Public Health Association (APHA). They were not invited, although a nurse from the National Right to Life Committee was added. (Steiger explains that AMA and APHA "go anyway" on their own, and Thompson wanted to "include real people who might not have had a chance to go in the past.")

Meanwhile, scientists from CDC and NIH who took part in U.S. government delegations on specific health topics such as tobacco and nutrition were instructed to leave the talking to HHS officials, says Derek Yach, a former WHO chief of noncommunicable diseases and mental health who left for Yale earlier this year. "They weren't allowed to speak up."

Within WHO, Steiger's approach was to resolve disputes not by discussion but "by throwing [U.S.] power and authority around," charges Howard University College of Medicine senior associate dean Mohammed Akhter, a former executive director of APHA. Steiger advocated new policies that critics quickly labeled pro-industry. In May 2001, for example, he instructed Thomas Novotny, an epidemiologist and HHS career civil servant negotiating the U.S. position on a global treaty designed to curb tobacco use, to change course. Instead of endorsing a total ban on advertising, Novotny (now at the University of California, San Francisco) says he was told to oppose these restrictions, as well as proposed new tobacco taxes. This U.S. position caused an uproar among public health experts.

Nutrition research sparked another flap. Experts convened by WHO and the United Nations Food and Agriculture Organization (FAO) drafted a report on diet and disease that suggested that countries restrict junk-food ads. After the sugar industry tried to block the final April 2003 report, last January Steiger's office issued a scathing critique charging that the report was scientifically flawed, mixed science and policy, and departed from the U.S. position favoring "personal responsibility" for curbing unhealthy habits.

Although the critique included some valid scientific points, says Harvard epidemiologist Walter Willett, its emphasis on

> "I see an increasing and pervasive squeezing of academic freedom by bureaucratic control." —Gerald Keusch, assistant provost, Boston University

CREDIT: WORLD HEALTH ORGANIZATION

Published by AAAS

personal responsibility "is a political philosophy statement coming from Washington."

Steiger says all HHS scientists involved with the nutrition report "agreed with the message," and that the United States helped push through the tobacco treaty and an obesity strategy, yielding final WHO documents that were "strong" and "feasible."

Tough on travel

Steiger's aggressive style also has ruffled feathers in the AIDS research community. He has been a hard-nosed enforcer of the Administration's controversial emphasis on sexual abstinence in HIV prevention programs and its prohibition on using generic AIDS drugs for treatment until they are approved by the U.S. Food and Drug Administration. A decision to pull the plug on a proposed CDC AIDS partnership with Myanmar, claiming that Myanmar would not allow nongovernmental groups to perform voluntary testing and counseling, also rankled (*Science*, 19 September 2003, p. 1654).

This spring, Steiger ruled that HHS would send only 50 U.S. staff to the 2004 world AIDS conference in July in Bangkok, down from 236 sent to the previous meeting in Barcelona in 2002—keeping home many scientists scheduled to give talks (*Science*, 23 April, p. 499). HHS also slashed its support for the meeting to $500,000, compared to $3.6 million for Barcelona. The reason, Steiger says, is that "the scientific value of this conference is nowhere near what it used to be."

In April, Steiger decided that for the first time in 30 years HHS would not contribute funding for the annual meeting of the nonprofit Global Health Council, after conservatives complained that two participating groups supported abortion. HHS spokesperson William Pierce claimed the council could not ensure that the money would not be used to lobby Congress.

Steiger's crackdowns on travel have gotten attention in the scientific community. HHS's deputy director for management, Ed Sontag, announced in March 2001 that all foreign trips had to be cleared through the Secretary's office. Weeks-long delays and last-minute approvals have led some researchers to miss meetings, scientists say; in other cases, Steiger vetoed overseas trips and postings of CDC staff, overriding decisions made by scientific managers. Under orders from Steiger, NIH has trimmed staff participation in international meetings (*Science*, 23 July, p. 462). Even visits to offices of WHO and other United Nations agencies in downtown Washington now have to be cleared as foreign travel to help ensure "accountability," says Pierce.

CREDIT: WORLD HEALTH ORGANIZATION

Order in the ranks

Steiger's oversight, some critics suggest, is motivated more by political ideology than fiscal prudence. "He's been given far too much power without experience," says one former HHS scientist. "He feels like he's doing the bidding of the Administration, and he tends to overinterpret."

Keusch cites an example: Last fall, he says, he received a peremptory e-mail from Steiger as NIH was gearing up to co-host a November conference called Globalization, Justice, and Health. Steiger wrote, "I am very, very uncomfortable with this conference and our sponsorship of it, and I would like to discuss it with you." Steiger explains that some speakers, such as Columbia University economist Jeffrey Sachs, "were taking a particular point of view, which is not the department's point of view," on generic drugs and access to medicine. OGHA also asked to see Keusch's remarks in advance; he sent them afterward. "I didn't see any reason other than censorship," says Keusch, who now heads global health programs at Boston University.

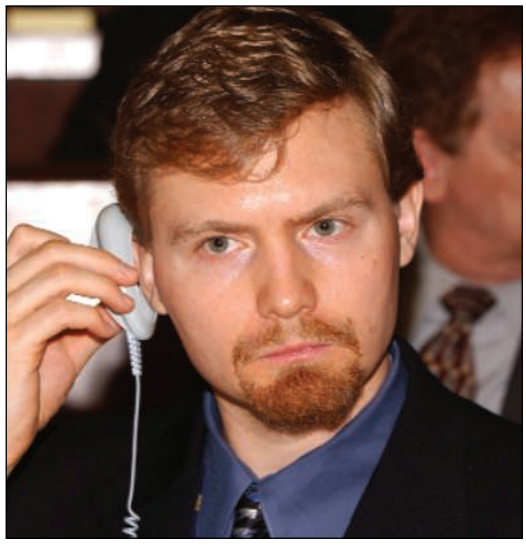

Enforcer. Steiger has imposed new strictures on U.S. scientists involved in international health programs, including limits on travel.

This spring, Steiger's office tightened the screws, scrutinizing staff involvement in WHO's scientific activities. In April, Steiger wrote WHO that invitations for HHS researchers to be consultants to WHO must go through his office, because WHO's choices "have not always resulted in the most appropriate selections." The letter drew angry editorials in the *Los Angeles Times*, the *Boston Globe*, and *The Lancet*, as well as criticism from health experts including smallpox expert D. A. Henderson and former CDC director Jeffrey Koplan, who called it a political move meant to suppress agency scientists.

WHO Assistant Director-General Denis Aitken at first challenged HHS's new position but has since reached a détente: WHO will send nominations to Steiger's office but will not accept substitutes. If HHS rejects WHO's choices, "there will be fewer and fewer requests for government scientists," says William Foege, a former CDC director now with the Gates Foundation in Seattle. Steiger's actions add up to a "tragedy," says Yach. "CDC and NIH are organizations like none other, and to have an Administration actively working to control how they work internationally is a loss to the U.S. and the world."

> "He's a very valuable guy now. And he's become more diplomatic with every meeting." —Thomas Loftus, WHO adviser

Steiger fiercely disagrees that he has suppressed HHS scientists. OGHA wants to weigh in on WHO consultations, he explains, because WHO may not identify some top experts and they needed to be briefed on related HHS activities. "Almost never are we going to say 'You've picked the wrong person,' " he says. His oversight of travel and overseas assignments, he says, has uncovered abuses and helped "our investments match a set of strategic priorities."

Moreover, such criticism overlooks what's been accomplished, Steiger says. OGHA has been elevated to a division at HHS, increasing its influence. More staff members are working overseas, including new "health attachés" added at embassies in places such as Beijing and South Africa. Steiger hopes to establish a "defined career path" for HHS staff interested in international health, like the State Department's Foreign Service.

A former Wisconsin Democratic leader, Thomas Loftus, says Steiger may have had a steep learning curve at WHO, but now he "knows this stuff." Loftus, special adviser to the WHO director-general, says, "He's a very valuable guy. And he's become more diplomatic with every meeting."

Even some of Steiger's fiercest critics say he is smart, can be likeable, and may mean well. But they also say his attempts to manage from the top down and enforce Administration priorities may do the opposite of what he intends by stifling scientists who have devoted their careers to international health.

–JOCELYN KAISER

With reporting by Jon Cohen.

Published by AAAS

Can California Ranchers Save The Tiger Salamander?

Scientists hope a very unusual conservation decision could preserve salamander habitat, but they worry that it might harm the most vulnerable populations

For some 5 million years, the California tiger salamander (*Ambystoma californiense*) has lived in grasslands surrounding pools that fill with water in the spring. Once a year, the salamanders emerge from burrows to lay eggs in these vernal oases. Over the past 150 years, however, three-quarters of the salamander's habitat has been lost, converted to housing tracts, vineyards, and row crops. Now, if the U.S. Fish and Wildlife Service (FWS) is correct, the 20-centimeter-long amphibians will have a new ally: ranchers.

On 4 August, FWS announced that it was protecting a vast swath of salamander habitat in the state. At the same time, the agency decided not to restrict what ranchers can do on that habitat—an unusual accommodation. That's because ranchers own the majority of salamander habitat—often prime real estate—and they maintain cattle ponds that the salamanders have adopted for breeding.

But although most scientists agree with FWS officials that a rancher-friendly approach could be crucial to preserving the habitat, they worry that some activities require closer scrutiny, especially where populations are most in jeopardy. The blanket exemption for ranching is "not scientifically based and may be harmful," says attorney Kassie Siegel of the Center for Biological Diversity, an environmental group that intends to take FWS to court over its August announcement in the *Federal Register*. At the same time, an industry group is challenging another aspect of that decision.

The California tiger salamander has been at the center of a political battle for more than a decade. In 1992, Bradley Shaffer, an evolutionary biologist at the University of California, Davis, and others began urging FWS to put the animals on the endangered species list. But the agency didn't move forward until environmentalists sued. Despite opposition from developers, in 2000, FWS declared a salamander population in Santa Barbara County to be in grave peril from loss of habitat and listed the animals as endangered. Shaffer's genetic studies showing that this group is a "distinct population segment" bolstered the rare, emergency listing. Three years later, facing another court-ordered deadline, FWS did the same for an even smaller salamander population in Sonoma County.

Geography lesson. Ranching could benefit central California tiger salamanders, but it might harm smaller populations along the coast.

The listing status matters. Under the law, "endangered" means that any activity that might harm the salamanders or their habitat requires a permit and a conservation plan. The requirement can be a paperwork headache. However, if a species is listed only as "threatened," FWS can exempt certain activities from permits. So it was a relief to ranchers when FWS exempted "routine ranching activities" in listing as threatened the state's largest population of the salamanders, spanning 20 counties.

The decision was based on the idea that ranching can be more compatible with salamander conservation than can other land uses, such as vineyards or housing. Like salamanders, cows need open grasslands and ponds. There's even evidence that grazing helps natural vernal pools persist, where grasslands are dominated by invasive grasses, ecologist Jaymee Marty of the Nature Conservancy has found.

But there are risks, too. Some routine ranching activities, such as creating firebreaks, may be deadly. The central population is a good place to examine those variables and determine proper guidance for ranchers, Shaffer says, because salamanders and their habitat are less critically endangered there. "We have more room to maneuver and more time to try creative solutions," he asserts.

That's not the case in Santa Barbara and Sonoma counties, Shaffer cautions. These populations are particularly vulnerable, he and others say, because they are small and face intense development pressure. And as genetically unique lineages, they're extremely valuable for conservation. "It seems obvious that they deserve more protection," says Carlos Davidson, a conservation biologist at California State University, Sacramento.

To exempt ranching statewide, FWS had to downgrade the populations in Santa Barbara and Sonoma counties from endangered to threatened. Normally, such an action only happens when populations are recovering and threats diminishing. Scientists say that's not the case with the two salamander populations. "There's no biological basis for downlisting," says Lawrence Hunt, a consulting herpetologist in Santa Barbara.

Some scientists also worry that the exemption could make it easier for ranchers who want to rid their land of salamanders—and the development restrictions that come with them—to do so through excessive use of routine practices. "It's basically a license to kill," says herpetologist Samuel Sweet of the University of California, Santa Barbara. Although scientists admit that there may be no way to eliminate cheating, they say the government should require permits to keep a closer eye on habitat in Santa Barbara and Sonoma counties.

Shortly after FWS issued its decision, environmentalists told the agency they plan to sue in federal court this fall to reverse the downlisting and remove the ranching exemption from Santa Barbara and Sonoma counties. And with industry challenging the listing of the central California population, the controversy over the tiger salamander seems certain to continue burning bright.

—ERIK STOKSTAD

CREDITS (TOP TO BOTTOM): P. TRENHAM/USGS; P. HUEY/*SCIENCE*; SOURCE: U.S. FISH AND WILDLIFE SERVICE

Published by AAAS

Archaeologist Leaves an Imprint On His Field—Without Research

Popularizer Brian Fagan argues that spreading the word about archaeological research is as important as doing it

SANTA BARBARA, CALIFORNIA—During the 1960s, archaeologist Brian Fagan was excavating at the Zambian site of Ingombe Ilede, famed for its gold-laden skeletons. Fagan was asked to date the burials and used indirect methods to place them around 1000 C.E. A few years later, however, another excavator showed conclusively that the skeletons had actually been laid to rest in the 16th century.

That miscalculation convinced Fagan of something he had long suspected: He was only a second-rate excavator. Reluctantly, he decided to abandon field research. But he did not give up archaeology. Instead, he traded in his trowel for a typewriter and later a computer, and launched an exceptional career as an academic popularizer.

Today British-born Fagan is arguably the best-known archaeologist in the United States, his adopted country, and the author of more than two dozen books, including an introductory archaeology textbook that has gone through 11 editions since its first printing in 1972. This year, Fagan, 68, won the Society for American Archaeology's public understanding of archaeology award for his latest book, *Before California*, and he is now finishing up his next book, on the archaeology of Chaco Canyon, New Mexico.

Last year Fagan retired from the faculty of the University of California, Santa Barbara (UCSB), where he had taught for 36 years. Unlike almost all other academics, however, Fagan has based his career entirely on general textbooks and popular archaeology books rather than on original research. He strongly defends his choice to be a generalist, and to do it from within the boundaries of academia. "Much of what we do in archaeology today is so arcane that it's of interest, at the most, to half a dozen people. We've forgotten that archaeology is of startling relevance to a contemporary society wrestling with issues of human diversity. We should take public outreach seriously—and do something about it," he says.

Many other academics, such as Jared Diamond and the late Stephen Jay Gould, have written popular books—but they usually have done so in addition to a successful research career. Some successful popularizers of science have even seen their scientific standing suffer as a result; the late Carl Sagan, whose nomination to the National Academy of Sciences was rejected in 1992, is the best-known example.

Perhaps surprisingly, Fagan's decision to eschew original research has not diminished his stature in the eyes of his colleagues. "He has been a very important person in the field," says anthropologist Margaret Conkey of UC Berkeley. "He is an excellent communicator of the fundamental principles, issues, and practices of the discipline."

Archaeologist Jeremy Sabloff, who recently stepped down as director of the University of Pennsylvania Museum in Philadelphia, agrees, adding that the kind of writing Fagan does is "part of our collective academic responsibility. Who better to explain the cutting edge of archaeological research than archaeologists themselves?"

It took a series of lucky breaks before Fagan found the popularizing path. He was considering working in his family's publishing business when an offer arrived from the University of Illinois, Urbana-Champaign, to teach for a year. This led to a tenured position teaching introductory archaeology at UCSB. Upon arriving, Fagan was surprised to find that there were no good introductory textbooks. So he wrote one himself.

During the earlier years of his career, Fagan says, his popular writings sometimes were not valued as highly as research papers. Skeptical promotion review committees wanted to see original contributions to archaeological journals—papers Fagan no longer produced. But most of this resistance came from "beyond the department," notes archaeologist Michael Glassow, the current chair of UCSB's anthropology department, adding that Fagan's anthropological colleagues gave him such strong support that he eventually rose to the university's "highest ranks" in terms of pay and prestige.

Fagan readily acknowledges this support and also credits the more experimental philosophy that existed at the relatively new Santa Barbara campus when he arrived there in 1967. "If I had gone to Berkeley or the University of Chicago, it would have been much harder to be a generalist," he says.

Nowadays, young archaeologists are often discouraged from following in Fagan's footsteps, says Sabloff. "Such activities don't help when it comes to tenure and promotion and might even count against them," he says. "Most scholars don't realize how strong one's grasp of relevant theory, method, and substance of a topic must be to produce a truly useful popular interpretation."

Fagan argues that popular writing should be considered a valid academic endeavor, especially because the preservation of often-threatened archaeological sites around the world requires public understanding of their importance. "You can define research many ways, but it's myopic to assume that it's all specialized inquiry," he says. "Startlingly few archaeologists are concerned with the big issues of early human history and diversity."

Enjoying the limelight. Popular acclaim hasn't tarnished Brian Fagan's academic reputation.

CREDIT: M. BALTER

He adds that today most digs are not university-supported research expeditions but "rescue" excavations of endangered sites, often reluctantly funded by developers. "Unless we take communicating with the wider audience seriously," he says, "there may be no archaeology for our grandchildren to study."

—MICHAEL BALTER

Published by AAAS

Dead Zone Fix Not a Dead Issue

Scientists debate how best to revive the Gulf of Mexico's oxygen-starved waters

Every summer, death stalks the waters of the northern Gulf of Mexico. A New Jersey–size swath of sea becomes depleted of oxygen, suffocating millions of crabs and other denizens of the sea floor. In 1999, the federal government diagnosed the cause of this seasonal dead zone: The hypoxia arises largely because of nitrogen pollution from the fertilizer-drenched farms in states along the Mississippi River. Two years later, the government released a plan to reduce nitrogen runoff and revive the gulf. Now a new government report says that because the original diagnosis was wrong, the costly prescription will fail.

Released last month to little public notice, the controversial report, issued by the Atlanta office of the U.S. Environmental Protection Agency (EPA), places increased blame for the dead zone on phosphorus pollution from factories and cities along the Mississippi River and recommends focusing the cleanup on phosphorus as well as nitrogen. Farm-industry groups seeking to delay the national plan have seized on an early draft of the report that challenged the use of any nitrogen reduction. Marine scientists have given the report, which has not yet been peer reviewed, a cooler reception. "I think it has some really serious deficiencies," says Donald Boesch, president of the University of Maryland Center for Environmental Science.

Scientists agree that factories, cities, and farms in the Mississippi River watershed have jacked up both phosphorus and nitrogen levels in the river. Each spring, those nutrients pour into the northern Gulf of Mexico and trigger blooms of phytoplankton, minuscule plants that float in the water. That sets off population booms in zooplankton, the tiny animals that consume them. Then sea-floor bacteria, which feed on dead zooplankton and their waste, multiply wildly and use up oxygen in the bottom waters.

In 1999, the National Oceanic and Atmospheric Administration (NOAA) released a comprehensive assessment of the causes and consequences of hypoxia in the gulf. It concluded that phytoplankton growth in the dead zone was primarily limited by the availability of nitrogen. Relying on that report, a state-federal partnership, the Task Force on Gulf Hypoxia, developed a national action plan with a single overarching goal: reduce nitrogen coming down the Mississippi River by 30% by 2015.

That prescription seemed simplistic to Howard Marshall, a veteran water-quality scientist at EPA's Atlanta regional office who was assigned to help implement the plan. By reexamining available data on dissolved nitrogen and dissolved phosphorus concentrations, Marshall and other EPA scientists determined that the lower Mississippi River contained a large excess of dissolved nitrogen relative to dissolved phosphorus. Although growing phytoplankton need more nitrogen than phosphorus—they usually accumulate the nutrients at a 16:1 ratio—the amount of nitrogen so exceeded the quantity of phosphorus that the latter nutrient had most likely limited the growth of phytoplankton there, the EPA group concluded. The same also held true for the northern gulf in the spring, when the dead zone typically forms, according to the group. "Wouldn't it be better to reduce phosphorus and starve the bastards?" Marshall asks.

That's "pretty naïve," argues biogeochemist Robert Howarth of Cornell University, who chaired a National Research Council committee in 2000 that examined hypoxia in coastal oceans. Last week, Howarth, Boesch, and Donald Scavia of the University of Michigan, Ann Arbor, sent EPA a letter criticizing the new report. They argue, for example, that the nutrient ratios in water don't necessarily reveal what's available to phytoplankton, because phosphorus is resupplied from organic debris in the sediment.

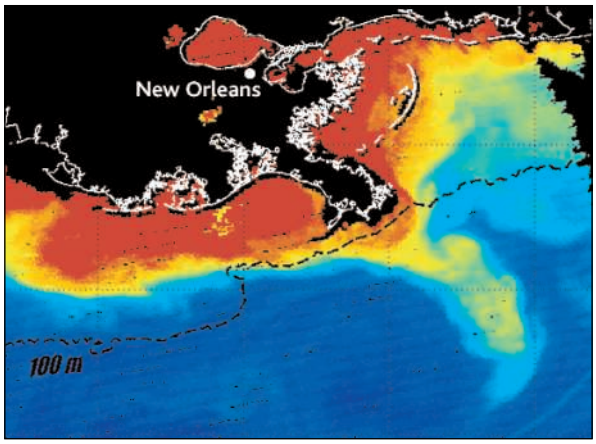

Enough already. Excess nutrients from the Mississippi River cause phytoplankton blooms (red and yellow) near the river's mouth.

CREDIT: STEVEN LOHRENZ/UNIVERSITY OF SOUTHERN MISSISSIPPI

But other oceanographers who have seen the report say that the EPA team has a point. "There's been this focus on nitrogen as the major culprit, even though we knew from early on that phosphorus played a role," says biological oceanographer Steven Lohrenz of the University of Southern Mississippi in Hattiesburg. And oceanographer Michael Dagg of the Louisiana Universities Marine Consortium in Cocodrie, who's worked in the gulf since the 1980s, says that Marshall "has done an extremely important service by scrutinizing these issues as intensely as he did. It should have been done 10 years ago."

Indeed, several recent lines of evidence support the idea that phosphorus can control phytoplankton growth in the gulf. In results presented in January at the American Geophysical Union's Ocean Sciences meeting, James Ammerman of Rutgers University and colleagues reported that nitrogen-to-phosphorus ratios greater than 380 occurred over the entire Louisiana continental shelf in the spring and early summer of 2001, indicating that phosphorus supplies may well constrain the plants' growth. Moreover, adding phosphorus but not nitrogen stimulated phytoplankton growth in bottles containing seawater from many of those locations. And phytoplankton from much of the shelf had high levels of an enzyme that they turn on to scavenge phosphorus when supplies are tight.

Overall, the data suggest that "there's this huge slug of water going into the gulf that's phosphorus-limited at its fresh end and nitrogen-limited at its salty end," says coastal ecologist Hans Paerl of the University of North Carolina, Chapel Hill. What remains unknown, he says, is how much phytoplankton growth at the fresh end contributes to hypoxia.

At last week's meeting of the gulf hypoxia task force, farm-industry interests lobbied to redo the NOAA-led science assessment and delay expensive efforts to reduce fertilizer runoff from farms. EPA's Ben Grumbles, acting assistant administrator in the Office of Water, says the task force is "committed to doing an independent peer review" of the new EPA report, and that the reviewers should include "fresh faces" who weren't involved in the 1999 NOAA assessment. But he emphasizes that the agency plans to continue its efforts to cut nitrogen pollution while exploring how to cut phosphorus. For the gulf, that may be just what the doctor ordered.

–DAN FERBER

Published by AAAS

Finding Reactions in a Haystack: Try 'em All, See What Works

PHILADELPHIA, PENNSYLVANIA—More than 10,000 chemists, physicists, and materials scientists gathered here from 22 to 26 August for the 228th national American Chemical Society meeting.

For synthetic chemists, improving on nature is, well, second nature. For over 150 years they have used new types of chemical reactions to craft molecules never seen before. "That strategy is very effective, particularly when you know what you're trying to make," says David Liu, a synthetic chemist at Harvard University in Cambridge, Massachusetts.

But is this goal-oriented approach the best way to find all the different types of possible chemical reactions under the sun? Liu suspected not. So he and his team set out to find new types of reactions by harnessing biology's prowess for synthesizing a diverse set of compounds. In Philadelphia, Liu unveiled an approach that shepherds molecules together with strands of DNA. The group has already spotted one new reaction with the technique and is casting its net wider to see what other reactions may be lying in wait.

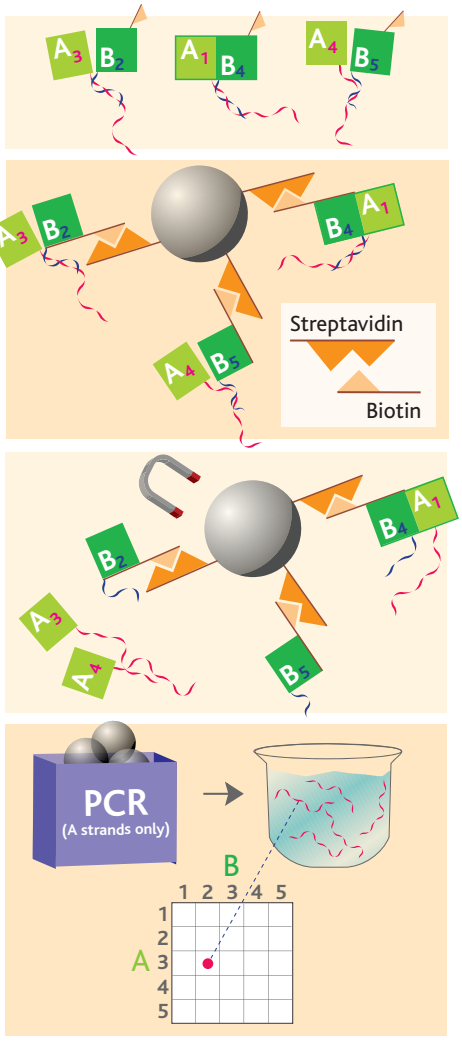

Making the cut. Coded DNA tags pick reactive molecules out of a host of also-rans.

Liu's talk was "pretty cool," says Kenneth Suslick, a chemist at the University of Illinois, Urbana-Champaign. "I was really taken with it." A chief goal of the new work is to discover novel reactions that chemists can then use in DNA-directed synthesis or with their traditional methods. But Suslick notes that not all reactions discovered by the new technique will make the jump: The DNA approach might prevent side reactions that would spoil the recipe in a conventional synthesis. So far, the technique has been used only to search for reactions that take place in water, but Liu says his team is expanding its search to include reactions in organic solvents.

Over eons of evolution, biological organisms generate a diversity of compounds and simply select those that work best. Liu and colleagues brought that kaleidoscopic approach to bear on the small organic molecules that synthetic chemists favor. They started with two flasks of small organic molecules, each tethered to a unique DNA snippet. Each DNA strand in flask A was designed to identify its own small-molecule cargo (A1, A2, and so on) and to attract a complementary DNA identity tag attached to one of the small molecules in flask B (B1, B2, etc.). Each B molecule also sported a molecular "hook" called biotin.

When the researchers poured the contents of the two flasks together, the complementary DNAs paired up, bringing their small molecules into close contact with one another in every possible combination of A's and B's. In the few cases in which conditions were right, the small molecules reacted to form larger molecules. To find which compounds had combined, the researchers weeded them out in several steps. First, they dropped in iron beads studded with streptavidin, a molecule that binds to biotin. The researchers then pulled the beads out again, dragging with them B molecules snagged by their biotin hooks, as well as other molecules entangled by their DNA, and washed the compounds in a solution that unzipped the intertwined DNA strands. Lone A molecules that had not reacted fell off and were washed away, leaving unreacted B molecules and the newborn AB compounds attached to the beads (see figure).

The researchers then used the polymerase chain reaction (PCR) to amplify trailing DNA strands containing a certain nucleic acid sequence—a sequence found only in the A strands. Because all the unattached A molecules had been left behind in a previous step, only the A strands that had formed new molecules survived to be amplified by PCR. The researchers read the amplified DNAs with a standard gene chip, which identified their full sequences and thus revealed which A and B molecules had paired off.

Liu reported that in one experiment, with 168 possible small-molecule products, his group found a new reaction that uses a palladium catalyst under mild conditions to link simple hydrocarbon molecules called alkenes and alkynes into a more complex group called a trans-enone. Using the setup, Liu says, a single researcher can scan thousands of possible combinations of small molecules and reaction conditions for new reactions in just days.

Enzyme Deactivates Heart-Friendly HDL

Not all "good" cholesterol in your bloodstream keeps good company. In patients with coronary artery–clogging plaques, as much as half of the high density lipoprotein (HDL), which carries the "good" cholesterol, is chemically altered, blocking its normal ability to combat the buildup of cholesterol deposits, researchers reported at the meeting. The new work, led by chemist and physician Stanley Hazen and graduate student Lemin Zheng of the Cleveland Clinic Foundation in Ohio, is expected to lead to novel drugs that help prevent atherosclerosis by blocking the damage to HDL. It may also spur better diagnostics for heart disease: At the meeting, another group reported preliminary progress on one such test.

"This is pretty exciting," says Ian Blair, a disease biomarker expert at the University of Pennsylvania in Philadelphia. "[They] seem to have a biomarker that is far better than existing biomarkers for cardiovascular disease." For the first time, he adds, the new work lays out a clear molecular mechanism that explains how HDL can become "dysfunctional" and why high HDL cholesterol levels may not always ward off heart disease.

The research grew out of efforts to find

CREDIT: K. BUCKHEIT/*SCIENCE*

Published by AAAS

better ways to track risk for heart disease. Last year, Hazen's team identified two new inflammation markers that were far better than existing tests for assessing a person's cardiac risks. The first of these was myeloperoxidase (MPO), an enzyme that immune cells use to fight bacterial and fungal invaders. MPO levels helped pinpoint the near-term risk of heart attacks, bypass surgery, or death among patients seeking emergency care for chest pain.

The second marker was a protein modification called nitrotyrosine, a byproduct of oxidative damage triggered by MPO and other compounds. At the time, however, Hazen's group didn't know whether MPO slapped nitrotyrosine groups on proteins indiscriminately or whether it had a primary target.

Using standard protein-tracking techniques, Hazen's group discovered that MPO targets apolipoprotein A1 (apoA1), the primary protein component of HDL, for oxidation. When the researchers looked at blood samples from 90 patients, half with cardiovascular disease and half without, they found that individuals with high levels of MPO-modified apoA1 had a 16-fold higher risk of heart disease. By contrast, patients with high levels of currently used clinical markers—total cholesterol and C-reactive protein—have less than double the risk. "This may help explain why not all persons with high HDL levels are protected from getting heart disease," Hazen says. He suggests that when MPO reacts with apoA1, it modifies the protein at one or more key sites, interfering with the protein's ability to ferry cholesterol out of cells and eventually leading to atherosclerosis. The findings also appear in the August *Journal of Clinical Investigation*. Hazen says his team's results have already prompted drug companies to work to develop compounds aimed at blocking MPO's ability to bind and react with HDL.

Last year Hazen's team also showed that patients at high cardiac risk have high levels of MPO in circulation, presumably released at sites of inflamed coronary vessels—a result that has spurred other researchers to track MPO levels to gauge heart attack and stroke risk.

At the meeting, for example, Alexei Bogdanov, a radiologist at Harvard Medical School in Boston, reported creating a new MPO-binding compound that can be used as a contrast agent for MRI tests. Bogdanov reported that the contrast agent gave off a clear MRI signal when added to petri dish materials designed to simulate real plaques. The contrast agent is now being tested in animals, Bogdanov says. Tracking high MPO levels in clots, Bogdanov explains, should show which atherosclerotic clots are at greatest risk of breaking apart and leading to a heart attack or stroke. If the test works in humans, it could give patients advance warning of a pending heart attack or stroke—a signal that could save thousands of lives.

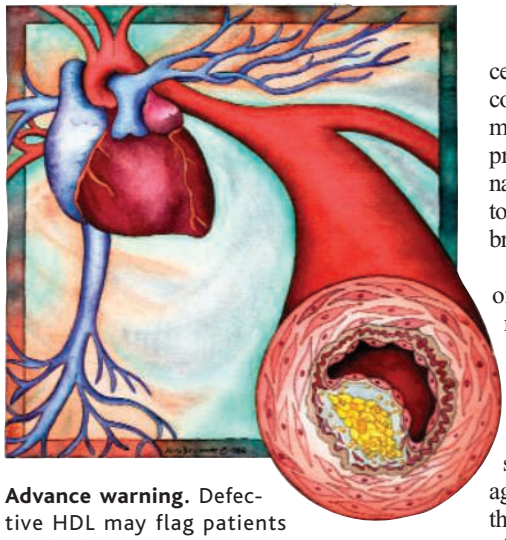

Advance warning. Defective HDL may flag patients with high cardiac risks.

CREDIT: CORBIS

Breaking a Barrier to New Brain Images

For more than 20 years, physicians have relied on magnetic resonance imaging's ability to peer inside tissues throughout the body to help them diagnose everything from torn ligaments to cancer. An offshoot of the technology, known as functional MRI, enables them to track the general metabolic activity level of tissues.

MRI researchers have beefed up the technique by developing MRI contrast agents that give off a strong MRI signal only when they bind to specific targets in the body—such as calcium, which indicates neuronal firing, or certain proteases, which are common in cancer cells. Tracking such processes in the brain could open new windows into brain development and point the way to diagnostics for depression and other brain diseases. Unfortunately, MRI contrast agents haven't been able to find their way across the protective membrane that surrounds the brain—until now.

At the meeting, chemist Thomas Meade of Northwestern University in Evanston, Illinois, reported that his student Matthew Allen synthesized a standard MRI contrast agent linked to stilbene, a small organic compound used to ferry radioactive compounds into the brain for positron emission tomography, another popular brain imaging technique. The Northwestern scientists then teamed up with chemist Russell Jacobs of the California Institute of Technology in Pasadena to test the compound on mice bred to serve as models for Alzheimer's disease. When the researchers injected the compound into the tail veins of mice, the stilbene-toting contrast agents found their way inside the brains of their mice and bound to amyloid plaques, which are typically found in the brains of Alzheimer's patients. If the new work pans out in further animal tests and humans, doctors might one day use noninvasive MRI imaging to track brain development and diseases from Alzheimer's to schizophrenia.

"It's a very exciting development," says Daryl Busch, a chemist at the University of Kansas, Lawrence. "You'll be able by [MRI] to see how the brain functions over a range of different conditions," he says. "That's heavy-duty."

Meade and colleagues are still studying how the stilbene-tethered compounds work. Meanwhile, they are seeing whether other contrast agents attached to stilbene will cross the blood-brain barrier as well.

–ROBERT F. SERVICE

Snapshots From the Meeting

Dendrimer splits water. Researchers from the University of Tokyo in Japan reported creating a starburst-shaped molecule called a dendrimer decorated with light-capturing compounds capable of splitting water molecules to make hydrogen gas, a valuable fuel. Previous water-splitting dendrimers were insoluble in water and therefore of little use. The new water-soluble dendrimers still can't match the water-splitting prowess of inorganic compounds, but because organic molecules are far easier to tailor, the Tokyo researchers expect the efficiency of the dendrimers to rise.

Heart failure help. Johns Hopkins University (JHU) researchers reported creating new compounds for treating heart failure. Nitroglycerin and other current heart failure medications deliver nitric oxide (NO), which helps the heart muscle relax. But the JHU researchers found in preliminary tests on dogs that novel compounds that deliver nitroxyl, or HNO, provide much the same benefit without the side effect of reducing the heart's ability to pump.

Cleaning water. Researchers at the University of Illinois, Urbana-Champaign, reported that cheap fibers made from polymer-coated fiberglass are eight times more effective at removing the herbicide atrazine from water than commercially available activated carbon. The new fibers could help combat increasing atrazine pollution. The popular herbicide contaminates the drinking water of millions of Americans.

–R.F.S.

Published by AAAS

Random Samples

Edited by Constance Holden

Betting on a Wave

The betting agency Ladbrokes stands to lose a bundle if scientists detect gravitational waves in the next 6 years.

Ladbrokes opened bets on this and four other scientific discoveries last month. After consulting experts, they set the odds of detecting gravitational waves—ripples in the fabric of spacetime produced by violent events such as black hole collisions—by 2010 at 500 to 1 because "80% of the people I spoke to were dismissive" of the possibility, says spokesperson Warren Lush. But other scientists are optimistic, and a flood of bets had Lush slashing the odds to 100, 25, 6, and, finally, 3 to 1. Physicist James Hough of the University of Glasgow, for example, has placed the maximum Internet bet of £25 ($45) on the discovery, noting that the Laser Interferometer Gravitational Wave Observatory in the United States is "now within a factor of 2 of its design sensitivity" and will be further upgraded by 2011—after which, he says, "detection is pretty well guaranteed."

Of the other developments for 2010, the lowest odds are on understanding the origin of cosmic rays (4:1), followed by finding the Higgs boson (6:1), creating a fusion power station (50:1), and finding "intelligent life" on Saturn's moon Titan (10,000:1).

Crashed dove imprint.

Reducing Bird Strikes

Every year, ornithologists say many millions of birds smack into North American windows, making glass a major player in feathered fatalities. But biologist Daniel Klem Jr. of Muhlenberg College in Allentown, Pennsylvania, says he's found a way to tilt the odds in the birds' favor. In this month's *Wilson Bulletin*, Klem and colleagues report that tilting windows toward the ground, so that they reflect earth and not sky, can dramatically decrease bird strikes.

Klem's group placed six windows along a forest edge near Allentown, randomly adjusting them to vertical or angled downward by 20° or 40°. Over 4 months there were 53 strikes, 12 fatal. Nearly 60% of the birds hit the vertical windows, but only 15% hit the 40°-angle panes.

Although tilted panes might not take suburbia by storm, Sandy Isenstadt of Yale University School of Architecture predicts that some architects—particularly "deconstructivists" who reject traditional forms—will now have a "strong practical justification for [their] aesthetics of fragmentation."

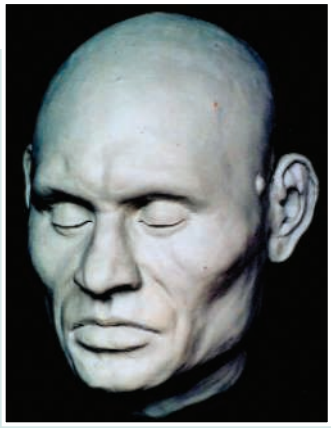

Mummy Revealed

A new reconstruction of Kennewick Man? No, this is Harwa, an Egyptian artisan who died 3000 years ago at about 45. His mummy resides in the Egyptian Museum in Turin, Italy. A team including anthropologists and forensic scientists from the University of Turin, led by physician Federico Cesarani, reconstructed Harwa's visage with 3D data gained from Multidetector CT, the latest advance in computed tomography. Virtual unwrapping of the mummy provided data on the original shape of the artisan's dehydrated nose, ears, and lips and even revealed a mole on his left temple. Harwa made his appearance in this month's *American Journal of Roentgenology*.

The Two Faces of Ginseng

Ginseng can have opposing effects on the body: Research has shown that the famed herbal palliative can both promote and curb the growth of blood vessels. Now scientists say they have figured out the two key ingredients behind ginseng's ambiguous nature.

Massachusetts Institute of Technology bioengineer Ram Sasisekharan and members of his lab, along with labs in England, the Netherlands, and Hong Kong, analyzed extracts from four ginseng varieties. Each had dramatically different levels of the herb's two most prevalent ingredients, steroid alcohols known as Rg1 and Rb1. In test tube studies, solutions high in Rg1 helped grow new blood vessels in human endothelial tissues, whereas solutions richer in Rb1 inhibited blood-vessel growth. The scientists got similar results from implanting sponges laden with Rg1 or Rb1 under the skin of mice, they report in the 7 September issue of *Circulation*.

The potent molecules could lead to new drugs for promoting healing or retarding cancer growth, Sasisekharan says. Herbal medicine expert Adriane Fugh-Berman of the Georgetown University School of Medicine says the work points to the need for testing such preparations. Sasisekharan agrees, noting that the way ginseng extracts are processed can alter the ratio of the two molecules.

Nanolander

Structural biologists at Purdue University in West Lafayette, Indiana, and the Institute of Bioorganic Chemistry in Moscow have made a tiny movie of a T4 virus attacking an *E. coli* bacterium. Using a cryo-electron microscope, Purdue's Michael G. Rossmann and colleagues put together images showing how the "baseplate" of the virus changes shape. Twelve legs touch down on the cell membrane, then the baseplate, composed of 16 types of protein molecules, opens like a flower to attach to the host. A paper on the work was published in the 20 August issue of *Cell*.

CREDITS (TOP TO BOTTOM): *AMERICAN JOURNAL OF ROENTGENOLOGY*; ROBERT MCCAW; PURDUE UNIVERSITY

Published by AAAS

PEOPLE

Edited by Yudhijit Bhattacharjee

JOBS

German museum head. The creator of the world's smallest hole has been named director of one of Europe's largest science museums. Nanoscientist Wolfgang Heckl of Munich's Ludwig Maximilians University will leave his lab to take charge of the 101-year-old Deutsches Museum in Munich next month, succeeding Wolf Peter Fehlhammer.

Heckl, 46, studied scanning probe microscopy with Nobel Prize winner Gerd Binnig. His lab's main focus has been self-assembly of organic molecules on surfaces, but the lab is perhaps best known for being listed in the *Guinness Book of World Records* for drilling the world's smallest hole, a one-atom prick in a molybdenum disulfide surface, using scanning tunneling microscopy.

Image not available for online use.

One of Heckl's challenges will be to fill the rather larger hole in the museum's $36 million budget, which has received flat or decreasing government support in recent years. His media savvy—he was named Germany's best science communicator in 2002—should serve him well for the task. "I'm not too proud to go knocking on doors" to potential museum donors, he told the German press last week. He told *Science* he'd like to build an open lab at the museum so visitors can observe and interact with researchers working with atomic force microscopes.

PIONEERS

The diversity business. Daryl Chubin has spent decades working to increase the participation of women and underrepresented minorities in science and engineering. Now the former vice president of the National Action Council for Minorities in Engineering and ex–federal science policy manager hopes to turn his knowledge into a business.

Chubin, 57, heads a new center that will help U.S. universities trying to attract and retain a greater number of U.S. citizens—especially women and minorities—in S&E disciplines. The Center for Advancing Science and Engineering Capacity is based at AAAS (which publishes *Science*) and funded for 3 years by the Alfred P. Sloan Foundation. "I have no doubt that universities committed to expanding and diversifying their student body will be willing to pay for these services," says Chubin, who's still working out a fee structure.

Cheers Down Under. A Danish-born biochemist has become the new chief of the Australian Research Council. Next month Peter Høj, who has headed the Australian Wine Research Institute in Adelaide since 1997, will succeed endocrinologist Vicki Sara, the council's inaugural CEO.

Høj, 47, created "an excellent model for bringing science and industry together" at the wine institute, says environmental physiologist Snow Barlow, president of the Federation of Australian Scientific and Technological Societies. He has also served on the Prime Minister's Science, Engineering, and Innovation Council.

Høj, who moved to Australia in 1987 for a postdoctoral fellowship, says he hopes to boost national spending on research by "demonstrating the benefits to society from R&D investment." Australia ranks in the lower half of industrialized countries in research spending as a percentage of its economy.

Got any tips for this page? E-mail people@aaas.org

DEATHS

Dr. Comet. Fred L. Whipple, a pioneer of modern planetary science, died 30 August in Cambridge, Massachusetts. He was 97.

In the early 1950s, Whipple single-handedly shifted the paradigm of comet science by proposing that the core of every comet is composed of a ball of ice and dust rather than a loose cloud of sand. In 1986, the Giotto spacecraft—protected from flying comet debris by Whipple's 1946 invention, the meteor bumper—confirmed the "dirty snowball" theory over the "flying sandbank" by imaging comet Halley's icy nucleus during a close flyby.

Image not available for online use.

"He was an idea man," says comet researcher Donald Yeomans of the Jet Propulsion Laboratory in Pasadena, California. During a 65-year career spent at Harvard University and the Smithsonian Astrophysical Observatory in Cambridge, his work encompassed a half-dozen areas and creations including a device for slicing aluminum into strips that fooled German radar and the only observing network prepared to track Sputnik I. "He was a kind, respectful gentleman," says Yeomans, "and such a nice guy."

Air collision. An aircraft accident investigator and systems safety professor at Embry-Riddle Aeronautical University in Prescott, Arizona, was one of two pilots killed on 28 August when their stunt planes collided during a rehearsal for a local air show.

Robert Sweginnis, 64, was head of the university's aeronautical science department. The pilot of the second plane, 55-year-old Michael Corradi, was the chief flight instructor on campus. Neither plane carried any passengers.

CREDITS (TOP TO BOTTOM): ACMC; SOURCE: LMU; HARVARD-SMITHSONIAN CENTER FOR ASTROPHYSICS

Published by AAAS

Letters to the Editor

Letters (~300 words) discuss material published in *Science* in the previous 6 months or issues of general interest. They can be submitted through the Web (www.submit2science.org) or by regular mail (1200 New York Ave., NW, Washington, DC 20005, USA). Letters are not acknowledged upon receipt, nor are authors generally consulted before publication. Whether published in full or in part, letters are subject to editing for clarity and space.

Extinction Rates and Butterflies

RATES OF POPULATION EXTINCTIONS IN BRITISH invertebrates have now been measured in several different ways [(*1*), "Comparative losses of British butterflies, birds, and plants and the global extinction crisis," J. A. Thomas *et al.*, Reports, 19 March, p. 1879] and may have relevance to estimating global extinction rates (*2*). We (*1*) have used the rate of extirpation of species from the whole of the British Isles, measured over the 20th century from the British Red Data Book (RDB), whereas Thomas *et al.* use distribution changes in the last 20 to 40 years measured in about 3000 map grid cells by 20,000 volunteers. There are notable consistencies and differences in the conclusions of these two approaches.

The extinction of species from the whole of the British Isles is likely to be relatively accurately recorded: Rare species are actively sought, and only one of the 43 species recorded as likely extinct in the RDB has since been rediscovered (with a low and local population). The national extinction rate per century ranges from 0.4% overall for the 14,000 insect species covered in the RDB to over 5% for the 60 species of butterflies and 7% for the 40 species of Odonata (the two best-recorded taxa).

Both studies find the rate of loss of selected invertebrate taxa to be roughly the same order of magnitude as the rate of loss of plants and birds. In both studies, butterflies have a notably higher rate of loss than plants or birds, which is not a recording artifact, because these three taxa are well studied.

Given the relatively high local extinction rates of butterflies recorded by these and other studies, we disagree with the conclusion of Thomas *et al.* that butterflies represent good indicators for losses of other taxa. Rather, Thomas *et al.*'s study supports our suggestion (*2*, *3*) that butterflies (being mostly warmth-loving and herbivorous) are atypical invertebrates that are relatively sensitive to climatic fluctuations and thus give a potentially misleading guide to extinction rates and human impacts.

CLIVE HAMBLER AND MARTIN R. SPEIGHT
Department of Zoology, University of Oxford, South Parks Road, Oxford OX1 3PS, UK.

References
1. C. Hambler, M. R. Speight, *Conserv. Biol.* **10**, 892 (1996).
2. C. Hambler, *Conservation* (Cambridge Univ. Press, Cambridge, 2004).
3. C. Hambler, M. R. Speight, *Br. Wildlife* **6**, 137 (1995).

Response

HAMBLER AND SPEIGHT SUGGEST THAT butterflies have experienced amplified extinction rates in Britain, and thus their widespread use as indicators of change in insects (*1*, *2*) is inappropriate. We consider this argument to be flawed, because of an artifact of recording.

It is widely accepted that comparisons of the proportion of species believed to have become extinct in different taxonomic groups will be biased if the groups being compared experienced different levels of past recording (*1*, *3*). This occurs because the early species lists for undersampled groups contain a disproportionately high representation of common widespread species (*4*), and it is the rare and local species in a taxon, which tended not to have been recorded in the first place, that are especially prone to extinction (*1*, *3*). McKinney (*5*) quantified this artifact in six groups (mammals, birds, molluscs, crustaceans, insects, and marine invertebrates) and obtained a strong correlation between the proportion of species recorded as being globally extinct against the proportion of species that was estimated to have been discovered (r^2 = 0.82). We can extend this analysis to different groups of British insects using, like Hambler and Speight, the British RDBs as the main data source (see figure).

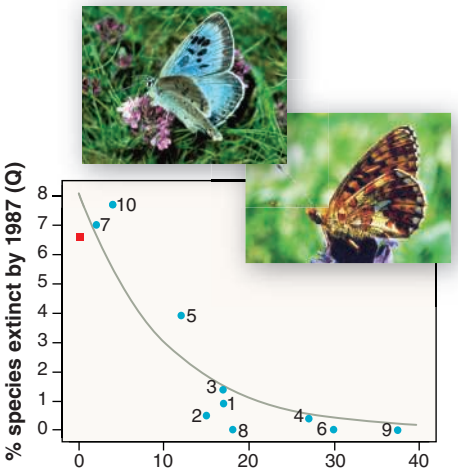

Percentage (*Q*) of insect (+ spiders) groups considered to have become extinct in circa 1900–87 in relation to the percentage (*U*) of native species in current British lists that were unknown in circa 1900. Least squares fitted line: $Q = 8.13e^{-0.0996U}$, $r^2 = 0.92$, $P < 0.001$. Squares, butterflies; circles, other groups: 1, other Macrolepidoptera (n = 900); 2, spider (n = 622); 3, weevil (n = 612); 4, hoverfly (n = 266); 5, macro-Brachyra (n = 154); 6, ant (n = 47); 7, dragonfly (n = 43); 8, grasshopper-cricket (n = 38); 9, mosquito (n = 32); 10, bumblebee species (n = 26).

The figure, which represents change in 9.2% of all known British insect species plus spiders, shows a similar relationship to McKinney's, indicating that for groups in which "only" 90% of species had been listed a century ago, recorded national extinction rates were less than half those of groups in which 100% of species had been known. Given the rigor of early butterfly recording, their documented declines were not unusual.

Nor are British butterflies atypically thermophilous, as Hambler and Speight claim. The immature, not adult, stages define climatic constraints on insects (*6*), and distribution maps show that higher proportions of aculeate Hymenoptera and Orthoptera species than butterflies are restricted to the warmest regions of Britain; moths and dragonflies are similar to butterflies, while staphilinid beetles and woodlice are less confined to warm spots (*7*). Furthermore, because of climate warming, those butterfly species that are thermophilous experienced population increases in Britain that frequently mitigated the effect of habitat degradation (*8*). Only four of the ten most rapidly declining butterfly species could be classed as thermophilous: The majority include alpine species.

We are also surprised that Hambler and Speight consider phytophagous insects to be unduly sensitive to environmental change. This contradicts their earlier statements (*9*), with which we agree (*6*), that specialists, such as taxa inhabiting rotting trees, are more threatened; moreover, the (well-recorded) taxa with the highest reported extinction rates in Britain have different lifestyles: carnivorous aquatic (dragonflies) and social terrestrial (bumblebees). In theory, parasitic species are the most vulnerable of all to change (*10*). Parasitoids are too poorly described to assess critically, but social parasites of ants have a disproportionately high representation in RDBs (*6*).

In conclusion, we do not claim that butterflies are ideal indicators of other insect changes, but they appear to be suffi-

ciently representative to be employed usefully, due to their comprehensive recording levels, as the only invertebrate taxon for which it is possible to estimate rates of decline in many parts of the world (*1*, *2*).

JEREMY A. THOMAS* AND RALPH T. CLARKE
Natural Environment Research Council (NERC) Centre for Ecology and Hydrology, Dorset Laboratory, Winfrith Technology Centre, Dorchester DT2 8ZD, UK.
*To whom correspondence should be addressed. E-mail: jat@ceh.ac.uk

References and Notes

1. R. M. May, J. H. Lawton, N. E. Stork, in *Extinction Rates*, J. H. Lawton, R. M. May, Eds. (Oxford Univ. Press, Oxford, 1995), pp. 1–24.
2. P. R. Ehrlich, *Philos. Trans. R. Soc. London B Biol. Sci.* **344**, 99 (1994).
3. G. M. Mace, W. Kunin, *Philos. Trans. R. Soc. London B Biol. Sci.* **344**, 91 (1994).
4. K. J. Gaston, T. M. Blackburn, N. Loder, *Biodivers. Conserv.* **4**, 119 (1995).
5. M. L. McKinney, *Conserv. Biol.* **13**, 1273 (1999).
6. J. A. Thomas, M. G. Morris, *Philos. Trans. R. Soc. London B Biol. Sci.* **344**, 47 (1994).
7. N. Loder, *Invertebrate Geographic Ranges and Climate* (Institute of Terrestrial Ecology, Huntingdon, UK, 1991).
8. M. S. Warren *et al.*, *Nature* **414**, 65 (2001).
9. C. Hambler, M. R. Speight, *Conserv. Biol.* **10**, 892 (1996).
10. M. E. Hochberg, in *Parasitoid Population Biology*, M. E. Hochberg, A. R. Ives, Eds. (Princeton Univ. Press, Princeton, NJ, 2000), pp. 266–277.
11. We thank A. Stubbs, M. G. Morris, and J. Davy-Bowker for data included in the figure.

Noguchi's Contributions to Science

THE RANDOM SAMPLES ITEM "ON THE money" (4 June, p. 1443) states that Hideyo Noguchi discovered the syphilis-causing microbe *Treponema pallidum* and that he was trying to develop a vaccine for yellow fever. Both of these statements are incorrect.

Noguchi proved that the neurological disease called tabes dorsalis was due to late stage syphilis infection. He demonstrated the presence of *Treponema pallidum* in some sections from the spinal cord of a patient with tabes dorsalis.

He became interested in yellow fever, and because of his experience with *Treponema*, he thought that this disease was also caused by some spirocheta-like organisms. He went to Merida, Mexico, to study yellow fever. A local physician introduced him to a patient who had Weil disease, which also produced jaundice but was caused by *Leptospira icterohemorrhagiae*, a spirocheta-like organism. Noguchi discovered this organism and published it as the cause of yellow fever. Many competent microbiologists failed to repeat his findings, and his statement was considered a mistake. He went to Ghana to study yellow fever once more, and he died there from the disease. He never realized that this disease was caused by a virus, which was eventually discovered by Walter Reed.

PINGHUI V. LIU
533 NE Wavecrest Court, Boca Raton, FL 33432, USA.

Networks by Design: A Revolution in Ecology

ENVIRONMENTAL CHANGE AND ANTHRO-pogenic activities threaten biodiversity and compromise essential ecosystem services at local to global scales (*1*, *2*). Despite this, current ecological understanding derives mainly from site-specific research and measurements at scales of ≤10 m^2 and at durations of ≤5 years (*2–4*). Several new [e.g., Conservation International's TEAM, the National Park Service Vital Signs, and SAEON (South African Environmental Observatory Network) (*5–7*)] or proposed [e.g., the U.S. National Science Foundation's NEON and ORION) (*8*, *9*)] initiatives for continental and global-scale research and monitoring networks represent unprecedented new funding in support of ecological research. These programs promise to expand scales of ecological understanding and transform ecology into a more mechanistic and predictive science.

Some assume that such networks should be assembled by locating a single site in each of a number of ecoregions, biomes, or biodiversity hotspots [e.g., (*10*)], or that by developing large networks employing standard methods, many questions will be answered by brute force. However, the high degree of variability inherent in large-scale systems makes it difficult to disentangle exogenous and endogenous sources of change and may compromise the efficacy of network designs. Designing an effective, large-scale ecological network is remarkably complex. In particular, ensuring appropriate levels of integrated sampling to achieve adequate statistical power at multiple spatial and temporal scales is extremely demanding. Previous efforts, often involving substantial expense (*11–15*), have been limited by several recurring problems: absence of clear questions underlying the design, sampling inadequacy and bias, inadequate statistical power, heterogeneity of measurement, incomplete and unstructured metadata, lack of tools for integration and analysis of heterogeneous data, and cultural or institutional impediments to data sharing.

By tradition, ecology has been a grassroots discipline in which individual investigators drive the scientific enterprise in an

uncoordinated and serendipitous fashion. Transforming this paradigm to one that will advance large-scale, mechanistic understanding across multiple spatial and temporal scales that reflect critical environmental gradients will require a revolutionary change in approach and in the culture of the discipline.

SANDY J. ANDELMAN[1] AND MICHAEL R. WILLIG[2]

[1]National Center for Ecological Analysis & Synthesis, University of California, Santa Barbara. 735 State Street, Suite 300, Santa Barbara, CA 93101, USA. [2]Ecology Program, Department of Biological Sciences and The Museum, Texas Tech University, Lubbock, TX 79409–3131, USA.

References and Notes

1. M. Palmer *et al.*, *Science* **304**, 1251 (2004).
2. *NEON: Addressing the Nation's Environmental Challenges* (National Research Council, Washington, DC, 2003).
3. P. Kareiva, M. Anderson, in *Community Ecology*, A. Hastings, Ed. (Springer, New York, 1989), pp. 35–50.
4. P. Keddy, L. Fraser, in *Modern Trends in Applied Aquatic Ecology*, R. Ambasht, N. Ambasht, Eds. (Kluwer Academic/Plenum Publishers, New York, 2003), pp. 21–42.
5. See www.teaminitiative.org.
6. See http://science.nature.nps.gov/im/monitor.
7. See www.nrf.ac.za/saeon/.
8. See www.nsf.gov/bio/neon/start.htm.
9. See www.nsf.gov/pubs/2004/nsf04003/start.htm.
10. Rationale, Blueprint and Expectations for the National Ecological Observatory Network (American Institute of Biological Sciences, Washington, DC, 2003).
11. Review of EPA's Environmental Monitoring and Assessment Program (National Research Council, Washington, DC, 1995).
12. J. Sauer *et al.*, *The North American Breeding Bird Survey, Results and Analysis 1966 - 2002. Version 2003.1* (U.S. Geological Survey Patuxent Wildlife Research Center, Laurel, MD, 2003).
13. J. Hobbie, Ed., A special section on U.S. Long Term Ecological Research Network, *BioScience* **53** (no. 1), 17–67 (2003).
14. R. Condit, *Tropical Forest Census Plots: Methods and Results from Barro Colorado Island, Panama and a Comparison with Other Plots* (Springer-Verlag, New York, 1998).
15. D. Burslem *et al.*, *Science* **291**, 606 (2001).

CORRECTIONS AND CLARIFICATIONS

Reports: "Indian Ocean climate and an absolute chronology over Dansgaard/Oeschger events 9 to 13" by S. J. Burns *et al.* (5 Sept. 2003, p. 1365). The chronology for the climate time series presented in this Report has been found to be ~2.3 ky too old, due primarily to a systematic standardization error in measurement of the thorium isotopes. A new age model for stalagmite M1-2 based on 19 new Th/U analyses measured by thermal ionization mass spectrometry (TIMS) at the Heidelberg Academy of Sciences and 6 new measurements by induction-coupled plasma mass spectrometry at the University of Bern is shown in fig. S1 (see Supplementary Online Material available at www.sciencemag.org/cgi/content/full/305/5690/1567a/DC1). A simple linear fit through the data was used to recalculate ages for individual data points in the stable isotope time series. The slope of this line (7.59 year/mm) is nearly identical to the slope of a linear fit through the original age model (7.60 year/mm). Thus, the pattern of climate change observed in the oxygen isotopic time series does not change with the new age model. The climate record, however, is moved forward by 2290 years. On the revised time scale, the ages of climate events found in the record, specifically the Dansgaard/Oeschger cycles, match well with two other independently dated records (fig. S2): Hulu Cave stalagmites [Y. J. Wang *et al.*, *Science* **294**, 2345 (2001)] and the most recent chronology for the GRIP Greenland ice core [S. J. Johnsen *et al.*, *J. Quat. Sci.* **16**, 299 (2001)].

TECHNICAL COMMENT ABSTRACTS

COMMENT ON "Managing Soil Carbon" (I)

K. Van Oost, G. Govers, T. A. Quine, G. Heckrath

The assessment of the potential carbon sequestration benefits of no-till agriculture presented by Lal *et al.* (Policy Forum, 16 April 2004, p. 393) is overly optimistic, because the carbon dynamics of water erosion remain poorly understood and because Lal *et al.* have not accounted for carbon storage as a result of tillage-induced soil redistribution.

Full text at www.sciencemag.org/cgi/content/full/305/5690/1567b

COMMENT ON "Managing Soil Carbon" (II)

W. H. Renwick, S. V. Smith, R. O. Sleezer, Robert W. Buddemeier

Based on erosion and sediment budgets for the United States, we contend that the estimates of oxidation for eroded soil carbon by Lal *et al.* are too high. Such overestimates have important implications for estimates of fluxes involved in the atmospheric carbon dioxide budget in the context of the missing carbon sink.

Full text at www.sciencemag.org/cgi/content/full/305/5690/1567c

Response to Comments on "Managing Soil Carbon"

R. Lal, M. Griffin, J. Apt, L. Lave, M. G. Morgan

Although eroded soil carbon is a major contributor to atmospheric carbon dioxide, Renwick *et al.* and Van Oost *et al.* are correct that the emission from eroded soil carbon is uncertain, with a range of 0 to 100% and with some values at about 20%. Erosion and tillage destroy structure, alter temperature and moisture, and expose soil carbon to microbial action that increases carbon dioxide emission (estimated at 1 gigaton of carbon per year). Deep burial may stabilize carbon, but the labile fraction in the surface layer is mineralized following tillage. Despite uncertainties, no-till farming and retaining crop residues and cover cropping are certain to increase soil carbon storage and enhance productivity.

Full text at www.sciencemag.org/cgi/content/full/305/5690/1567d

Comment on "Managing Soil Carbon" (I)

Lal *et al.* (*1*) recently argued that no-till agriculture is a viable strategy for restoring on-site soil carbon, for reducing soil erosion and sediment yields, and, consequently, for enhancing soil quality. We believe, however, that their statements regarding the relation between soil erosion and increases in atmospheric CO_2 do not take into account all relevant aspects of agricultural soil erosion. Failure to correctly assess the role in the carbon cycle of soil erosion—in particular, tillage erosion—on arable land may lead to an overoptimistic view of the potential benefits of no-till farming.

The first issue that requires attention is the fate of eroded soil carbon and rapid carbon replacement at eroded sites. Lal *et al.* (*1*) identified soil erosion by water as an important source of atmospheric CO_2, on the order of 1 gigaton (Gt) C/year. This assessment assumes that 20% of the C that is displaced by water erosion is emitted into the atmosphere, mostly due to the breakdown of aggregates and subsequent C mineralization during transport by overland flow (*2*). However, C mineralization during transport is not the only process that affects the C balance of the water erosion process. The admixture of carbon-poor subsoil at eroding, carbon-depleted sites leads to rapid C replacement through roots and litter input in the soil, whereas the carbon that is buried at depositional sites is slowly mineralized. Thus, ultimately, soil erosion and deposition may lead to carbon sequestration. Some authors estimate that 0.6 to 1.5 Gt C/year may be sequestered globally through deposition in terrestrial environments (*3*). The mobilization of terrestrial C during erosion events may indeed have a significant effect on the global carbon budget; however, whether that erosion creates an atmospheric sink or source is still highly uncertain, as the various fates of eroded soil organic carbon (SOC) are poorly understood.

The second issue that demands attention is that Lal *et al.* (*1*) did not consider carbon storage due to tillage-induced soil redistribution. Over the past decade, a paradigm shift in erosion research has occurred with the identification and growing acceptance of the dominant role of tillage in redistributing soil within rolling arable fields (*4*). Tillage erosion redistributes soil in amounts that often dwarf the effect of water erosion at the field scale, and the process is now identified as a major contributor to the formation of colluvial deposits in agricultural landscapes. In contrast to the sediment mobilized by water erosion, the soil eroded by tillage erosion is deposited within the same field and no transport-related mineralization of organic matter occurs. Therefore, tillage erosion results in high carbon inventories at depositional sites (Fig. 1). Because part of the eroded carbon is dynamically replaced at eroding sites as a result of increased humification, tillage erosion and deposition lead to carbon sequestration on arable land. For example, assuming a tillage erosion rate of 10 Mg/ha per year, a carbon content of 2%, and that only 50% of the eroded carbon is replaced at eroding sites (*3*), tillage erosion leads to an annual carbon sequestration rate of 10 g C/m^2.

Recognizing and understanding the magnitude and dynamics of the tillage erosion–induced carbon sink is crucial, given that the sink would be lost with a change to no-till agriculture. In the United States and Europe, conversion from conventional tillage to no-till or minimal-tillage agriculture is considered to be the practice with the highest carbon sequestration potential for arable land (*5*,*6*). Yet tillage erosion leads to C sequestration rates that are of the same order of magnitude as the projected annual potential carbon sequestration rate of 10 to 40 g C/m^2 from the conversion of agricultural land to no-till (*6*, *7*). The carbon sequestration benefit of no-till practices on sloping land may, therefore, be considerably less than expected.

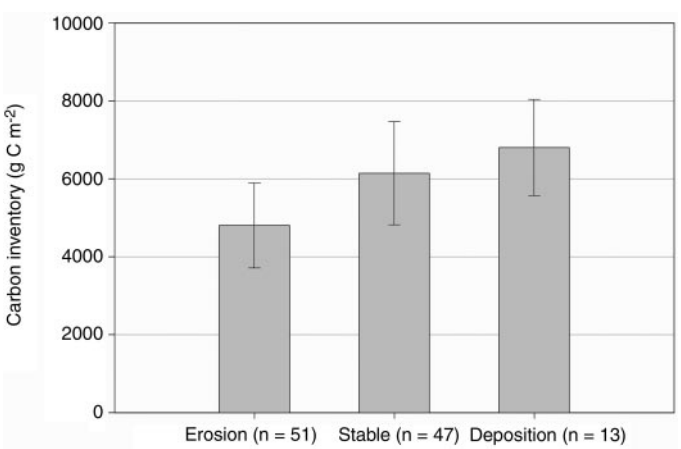

Fig. 1. Spatial differences in carbon storage due to tillage erosion. Soil carbon inventories (g C/m^2) for the 0 to 0.45 m soil layer were measured at an eroding agricultural field in Denmark (57°20′N, 10°31′E). Erosion classes are based on the measured ^{137}Cs activity; values significantly lower or higher than the ^{137}Cs reference value (at the 0.05 level) were classified as erosion and deposition, respectively. The ^{137}Cs reference value was determined by sampling an uneroded site in the area. *n* indicates the number of samples in each class. Error bars represent 1 SD. There is a significant difference in the measured SOC inventories between eroding, stable, and aggrading sites ($F = 29.46$, $P < 0.0001$ in one-way analysis of variance).

K. Van Oost
Physical and Regional Geography Research Group
K. U. Leuven
Redingenstraat 16b, 3000 Leuven, Belgium
E-mail: k.vanoost@exeter.ac.uk
and
Department of Geography
University of Exeter
Amory Building, Rennes Drive
EX4 4RJ, UK

G. Govers
Physical and Regional Geography Research Group
K. U. Leuven

T. A. Quine
Department of Geography
University of Exeter

G. Heckrath
Department of Agroecology
Danish Institute for Agricultural Sciences
8830 Tjele, Denmark

References
1. R. Lal *et al.*, *Science* **304**, 393 (2004).
2. R. Lal, *Environ. Int.* **29**, 437 (2003).
3. R. F. Stallard, *Global Biogeochem. Cycles* **12**, 231 (1998).
4. G. Govers, D. A. Lobb, T. A. Quine, *Soil Tillage Res.* **51**, 167 (1999).
5. R. Lal *et al.*, *J. Soil Water Conserv.* **54**, 374 (1999).
6. P. Smith, *Eur. J. Agron.* **20**, 229 (2004).
7. P. Smith, D. S. Powlson, M. J. Glendining, J. O. U. Smith, *Global Change Biol.* **4**, 679 (1998).

13 May 2004; accepted 29 July 2004

Comment on "Managing Soil Carbon" (II)

Lal *et al*. have recently argued (*1*, *2*) that restoring soil carbon levels worldwide is important for a number of purposes, including reducing atmospheric CO_2 concentrations. We agree, but we question how much eroded soil C is ultimately delivered to the atmosphere. Previous estimates of the proportion of eroded soil carbon oxidized range from 0% to near 100% (*3*, *4*). We believe that the true value is nearer the extreme low end of that range, because much of this soil carbon is deposited in depressions, water impoundments, and floodplains, where oxidation rates are lower than in the original soils (*5*, *6*). Therefore, erosion-related emissions of C are probably much smaller than the ~1 gigaton (Gt) C/year estimated by Lal *et al*. We have argued previously (*7*) that erosion and subsequent deposition represent an apparent sink of ~1 Gt/year.

Our published estimates suggest that soil erosion globally mobilizes ~1.4 Gt carbon annually (*7*), based on a robust budgetary estimate for the United States of 0.05 Gt C mobilization per year from erosion. Further, we demonstrated that U.S. river discharge of total organic C is about 20% of soil C erosion. We identified storage compartments for bulk sediment on land—large (inventoried) impoundments, smaller (uninventoried) impoundments, and (by difference) alluvium—and estimated the organic carbon buried in each. The carbon not associated with any storage compartment was assigned to oxidation. Within the uncertainties in our bulk sediment budget, there was no evidence of net carbon oxidation, although we cited the basis on which our estimates could be raised from 0 to 20% oxidation. This estimate was based on budgetary calculations, not an assumption, as stated by Lal *et al*. (*1*, *3*). Although the Lal *et al*. value of 20% is not inconsistent with that range, we believe that this high-end value is extreme for the United States and that higher percentages are well outside the constraints imposed by the budget. Indeed, the Lal *et al*. estimate of 1 Gt yearly carbon loss to the atmosphere is itself based on two unsubstantiated assumptions: 20% C oxidation in the erosion/transport process and 3% C content of soils (*8*).

We have also demonstrated that deposition in artificial impoundments is the largest single sink for eroded soil in the United States (*9*, *10*). The carbon content of this sediment is similar to that of the soil from which it was derived, which in turn indicates that there is little or no loss in transport (11).

In terms of effect on the CO_2 budget, the most important issue is how the oxidation rates for eroded and uneroded soil carbon compare. Rice (*5*) points out that soil C, at field moisture capacity, is more rapidly reactive than C in either water-saturated sediments or dry soil. If both our budgetary model and the assertions of Rice are valid, then erosion decreases the net rate of soil carbon oxidation by moving soil C from relatively reactive to relatively unreactive sites. However, the combination of tillage and erosion in fields does increase the C oxidation from soils in situ. The magnitudes of these counterbalancing processes are unknown or, at least, poorly quantifiable.

With respect to mass balance, a smaller source term (for example, less oxidation of eroded soil C) is equivalent to a net sink. The general equation is that net ecosystem production (NEP) equals net primary production (NPP) minus respiration (R). Soil C oxidizes, whether it is in place or not. Eroded soil carbon continues to oxidize, but we contend that the erosion and redistribution to buried, submerged, waterlogged, or even dry environments lowers the net oxidation rate. Thus, eroding soil C raises NEP by lowering R. We have estimated (*4*) that the difference between the Lal *et al*. estimate of soil C oxidation and our estimate corresponds to an apparent erosion-associated soil carbon "sink" of about 1 Gt/year. This virtual sink has gone unrecognized because it is passive (less oxidation than expected) rather than active (photosynthetic fixation).

Loss of soil C from an individual field represents a complex admixture of local translocation, local oxidation, and "downstream" oxidation and is difficult to describe at the field scale. Although our analysis differs in an important detail from that of Lal *et al*. (*1*), we fully support their call for the development and adoption of tools such as conservation tillage agriculture. This would not only increase the carbon content of soils, but also preserve storage capacity in impoundments where eroded soil and carbon are accumulating.

W. H. Renwick
Department of Geography
Miami University
Oxford, OH 45056, USA
E-mail: renwicwh@muohio.edu

S. V. Smith
Centro de Investigación Científica y de Educación Superior de Ensenada, Ensenada, BC, Mexico
E-mail: svsmith@cicese.mx

R. O. Sleezer
Earth Science Department
Emporia State University
Emporia, KS 66801, USA
E-mail: sleezerr@emporia.edu

Robert W. Buddemeier
Kansas Geological Survey
University of Kansas
Lawrence, KS 66047, USA
E-mail: buddrw@ku.edu

References

1. R Lal *et al*., *Science* **304**, 393 (2004).
2. R. Lal, *Science* **304**, 1623 (2004)
3. R. Lal, *Environ. Int.* **29**, 437 (2003)
4. W. H. Schlesinger, in *Biotic Feedback in the Global Climatic System: Will the Warming Feed the Warming?*, G. M. Woodwell, F. T. MacKenzie, Eds. (Oxford Univ. Press, New York, 1995), pp. 159–168.
5. C. Rice, *Geotimes* **47**, 14 (2002).
6. S. Liu *et al*., *Global Biogeochem. Cycles* **17**, 1074 (2003).
7. S. V. Smith *et al*., *Global Biogeochem. Cycles* **15**, 697 (2001).
8. R. Lal, in *Soils and Global Change*, R. Lal *et al*., Eds. (CRC/Lewis, Boca Raton, FL, 1995), pp. 131–142.
9. S. V. Smith *et al*., *Sci. Total Environ.* **299**, 21 (2002).
10. W. H. Renwick, S. V. Smith, J. D. Bartley, R. W. Buddemeier, *Geomorphology*, in press.
11. J. C. Ritchie, *Water Resour. Bull.* **25**, 301 (1989).

18 May 2004; accepted 29 July 2004

Response to Comments on "Managing Soil Carbon"

We agree with Renwick *et al*. (*1*) and Van Oost *et al*. (*2*) that the magnitude of organic carbon lost from cultivated soils by erosion and mineralization processes is uncertain. The uncertainty is especially large with respect to the fate of carbon transported, redistributed over the landscape, and deposited in depressional sites; resolving that uncertainty will require additional site-specific data from properly designed experiments. Little uncertainty exists, however, about the benefits of no-till agriculture: It slows water and wind erosion and stops tillage erosion, preserving land fertility and productivity and sequestering carbon.

Renwick *et al*. highlight the importance of understanding the pathways of carbon displaced by erosion and of quantifying the magnitude of erosion-induced emission of CO_2, CH_4, and N_2O into the atmosphere. In response, we point out that soil erosion exacerbates carbon emission from ecosystem in five ways.

1) Soil erosion increases soil degradation and reduces biomass production on-site. Crop yields in eroded soil can be drastically reduced, even with high fertilizer input (*3*, *4*), which itself increases emission of CO_2 and N_2O. Yield reduction is especially severe in tropical soils of low inherent fertility (*5*, *6*). Erosion reduces production through adverse effects on soil structure, aeration, effective rooting depth, available water-holding capacity, and nutrient reserves; the reduced production, in turn, further reduces the soil carbon pool. Erosion decreases net primary productivity (NPP) on eroded sites, increases oxidation of soil organic matter, and reduces net ecosystem productivity (NEP). The gains in the soil carbon pool in depressional sites rarely compensate for losses on eroded sites in view of reduced NEP and increased mineralization.

2) Erosion causes the breakdown of macroaggregates into microaggregates and, possibly, complete soil dispersion, exposing hitherto encapsulated organic matter to microbial processes. The outer layer of macroaggregates has more soil organic matter than the inner core (*7*); that outer organic matter is progressively peeled off and transported with the sediments, because aggregation and soil structure control decomposition of organic matter in soil (*8*). Changes in soil moisture and temperature also increase the rate of decomposition of the remaining organic matter at the eroded site. Eroded soils have different radiative and thermal properties, leading to increased soil temperature (*9*), an important factor controlling CO_2 emission from soil (*10*).

3) Sediments are often enriched in soil organic carbon (SOC), because SOC has low density and is concentrated in the vicinity of the soil surface. The enrichment ratio of carbon in the sediments can be 5 to 32 times (*11*, *12*) as high as that for the field soil. Most of C transported with sediment is the labile fraction, which is easily mineralizable (*13*); the mineralizable fraction in translocated organic matter may range from 29% to as high as 70% (*14*–*16*). Thus, assuming that the mineralizable fraction in eroded and redeposited material is close to zero (*17*) can lead to erroneous conclusions. In most cases, sediment deposited may lead to higher emissions (CO_2, CH_4, and N_2O) from depositional sites. Overall, soil erosion is a net source of CO_2 and other gases, and in many watersheds a 20% oxidation rate is rather conservative (*14*–*16*). Taking into consideration the enrichment ratio and the delivery ratio of total soil displaced, emission of 1 gigaton (Gt) C/yr is possible.

4) In truncated soil profiles characterized by carbonaceous subsoil horizons, exposed carbonates may react with acidiferous material, such as fertilizers, and release CO_2 into the atmosphere.

5) The fate of carbon deposited in burial and depressional sites is governed by complex processes. The deposition may decrease the rate of mineralization by reaggregation of dispersed clay and silt (*18*) and burial of carbon-rich material and calciferous layer. On the other hand, the rate of mineralization may also be increased in depressional sites because of the high proportion of mineralizable fraction (*19*). Depending on soil moisture and temperature regimes, depositional sites may also undergo methanogenesis with release of CH_4 and denitrification with release of N_2O. The rate of mineralization on erosional phases strongly depends on soil temperature (*19*).

On the whole, as these mechanisms suggest, accelerated erosion reduces the ecosystem carbon pool, accentuates carbon emissions, and must be controlled effectively. Still, despite success in modeling erosion-induced loss of soil carbon, the fate of the displaced carbon remains largely unresolved (*20*), as both Renwick *et al*. and Van Oost *et al*. suggest.

Van Oost *et al*. also comment on tillage translocation—soil movement during tillage, which in turn leads to soil loss from convex slopes and soil gain by concave slopes. A net downslope displacement of soil on the hillslope by tillage, called tillage erosion, has been discussed as a soil degradation process since the 1940s (*21*–*23*). In general, the soil flux increases with increase in slope gradient and tillage intensity, and strongly depends on the antecedent soil conditions (*24*). Soil degradation and its adverse effects on productivity on convex slopes are as pronounced in tillage erosion as in water erosion, and both forms of erosion accentuate spatial variability in soil quality.

Yet there are some notable differences between tillage-induced and water-induced erosion. For one, soil erosion by water preferentially removes the light fraction, so sediments thus removed are generally enriched in SOC and other elements. Also, the deposition of sediments in the water erosion process follows Stokes' law: The sequence and the rate of fall depends on the particle size. Further, the depositional site for water erosion, being preferentially enriched in soil C, may have different soil properties and different gaseous flux than concave slopes receiving soil translocated by tillage operations. And tillage erosion generally causes soil loss in the shoulder position, whereas water erosion causes soil loss on mid and lower backslope positions (*25*).

Any tillage and related soil disturbance enhances the rate of mineralization of soil organic matter (*26*) and thus leads to emission of CO_2 into the atmosphere. The losses of carbon can be especially high if the depositional sites, where the labile fraction is concentrated in the top 10 to 20 cm, is tilled frequently. Tillage decreases the humification rate compared with no-till techniques (*27*) and leads to depletion rather than sequestration of soil carbon. Further, tillage operations involve fossil fuel consumption of as much as 30 to 40 kg C/ha/season (*28*). Rather than providing a sink, tillage accentuates the capacity of soil as a source of CO_2 to the atmosphere. If tillage-induced erosion reduces crop productivity and the amount of residue returned to the soil is also thus reduced, it is extremely difficult to stabilize or increase the SOC pool (*29*). As with the data in figure 1 of Van Oost *et al*. (which does not provide the least significant difference, with which to compare means), extensive research from the midwestern United States (*30*) and from Canada (*31*) also show a higher SOC pool in depositional sites. Yet the total SOC pool in the eroded and deposited landscapes is

lower than in uneroded landscapes because of losses by mineralization.

Because the global C budget cannot be balanced, the so-called missing sink or unknown residual sink lumps in all the uncertainties. The magnitude of unknown sink could be 2 to 4 Gt C/yr (*32*) or more because of unaccounted-for erosion-induced effects and other sources. Further, accelerated soil erosion is a threat to world food security, water quality, and health of coastal ecosystems (hypoxia). Although there is indeed uncertainty concerning how much carbon no-till agriculture is preventing from being emitted to the atmosphere, there is no doubt of the value of no-till agriculture in preserving cropland for the benefit of people today and in the future. The latter benefit is sufficient reason to promote no-till extensively, even as the uncertainty about carbon emissions rates is being resolved. No-till agriculture and soil carbon sequestration are win-win options, both locally and globally.

R. Lal
Carbon Management and Sequestration Center
The Ohio State University
Columbus, OH 43210, USA

M. Griffin
Tepper School of Business
Carnegie Mellon University
Pittsburgh, PA 15213, USA

J. Apt
L. Lave
Tepper School of Business
Department of Engineering and Public Policy
Carnegie Mellon University

G. Morgan
Department of Engineering and Public Policy
Carnegie Mellon University

References

1. W. H. Renwick, S. V. Smith, R. O. Sleezer, R. W. Biddemeier, *Science* **305**, 1567 (2004); www.sciencemag.org/cgi/content/full/305/5690/1567c.
2. K. Van Oost, G. Govers, T. A. Quine, G. Heckrath, *Science* **305**, 1567 (2004); www.sciencemag.org/cgi/content/full/305/5690/1567b.
3. C. J. Gantzer *et al*., *Soil Water Conserv*. **45**, 641 (1990).
4. C. M. Monreal *et al*., *Can. J. Soil Sci*. **77**, 553 (1997).
5. R. Lal, *Geoderma* **25**, 215 (1980).
6. M. A. Stocking, *Science* **302**, 1356 (2003).
7. H. Ghadiri, C. W. Rose, *J. Environ. Qual*. **20**, 628 (1991).
8. J. A. Vanveen, P. J. Kuikman, *Biogeochemistry* **11**, 213 (1990).
9. C. Wagner-Riddle *et al*., *Agric. For. Meteorol*. **78**, 67 (1996).
10. P. C. Mielnick, W. A. Dugas, *Soil Biol. Biochem*. **32**, 221 (2000).
11. T. M. Zobeck, D. W. Fryrear, *Trans. ASAE* **29**, 1037 (1986).
12. G. Sterk *et al*., *Land Degrad. Dev*. **7**, 325 (1996).
13. W. H. Schlesinger, in *Biotic Feedback in the Global Climatic System: Will the Warming Feed the Warming?*, G. M. Woodwell, F. T. MacKenzie, Eds. (Oxford Univ. Press, New York, 1995), pp. 159–168.
14. P. A. Jacinthe *et al*., *Soil Tillage Res*. **66**, 23 (2002).
15. H. Oskarsson *et al*., *Catena* **56**, 225 (2004).
16. L. Beyer *et al*., *J. Plant Nutr. Soil Sci*. **156**, 197 (1993).
17. S. V. Smith *et al*., *Global Biogeochem. Cycles* **15**, 697 (2001).
18. E. G. Gregorich *et al*., *Soil Tillage Res*. **47**, 291 (1998).
19. R. Bajracharya *et al*., *Soil Sci. Soc. Am. J*. **64**, 694 (2000).
20. V. Polyakov, R. Lal, *Environ. Intl*. **30**, 547 (2004).
21. S. J. Mech, G. A. Free, *Agric. Eng*. **23**, 379 (1942).
22. Z. Martini, *Rocz. Nauk Roln*. **66C**, 97 (1953).
23. M. Wienblum, S. Stekelmacher, Special Bulletin No. 52, Soil Conservation Division, Ministry of Agriculture, Israel (1963).
24. W. van Muysen *et al*., *Soil Tillage Res*. **51**, 303 (1999).
25. T. E. Schumacher *et al*., *Soil Tillage Res.* **51**, 331 (1999).
26. D. R. Morris *et al*., *Soil Sci. Soc. Am. J*. **68**, 817 (2004).
27. S. W. Duiker, R. Lal, *Soil Tillage Res.* **52**, 73 (1999).
28. R. Lal, *Environ. Int*. **30**, 981 (2004).
29. W. A. Dick, E. G. Gregorich, *Managing Soil Quality: Challenges in Modern Agriculture* (CAB International, Wallingford, UK, 2004), pp. 103–120.
30. P. R. Fahnestock *et al*., *J. Sustain. Agric*. **7**, 63 (1996).
31. E. G. Gregorich *et al*., *Soil Tillage Res*. **47**, 291 (1998).
32. D. S. Schimel *et al*., *Nature* **414**, 169 (2001).

8 June 2004; accepted 13 August 2004

TECHNOLOGY

The Value of Things to Come

Domenico Grasso

Human-Built World
How to Think about Technology and Culture
by Thomas P. Hughes
University of Chicago Press, Chicago, 2004. 235 pp. $22.50, £16. ISBN 0-226-35933-6.

Rudyard Kipling's poem "The Sons of Martha," often cited by engineering societies and organizations, uses the parable of Jesus's visit to Mary and Martha to set the stage for the role of Martha's sons for eternity. Martha's sons will forever serve the sons of Mary. They will do so in many gifted ways; they will move mountains, part seas, and so forth. But no matter how talented they may be, they will nonetheless be serving the sons of Mary. Except through the execution of their orders, they will not be determining their own or the world's fate. For a good part of the 20th century, this is precisely the role that engineers played, one of directed performance—marginalized from many policy- and decision-making tables (both in government and industry).

However, this is not the role engineers have always played. Thomas P. Hughes's new book, *Human-Built World*, describes a time when these masters of technology were thought to be imbued with "godlike powers" or, at a minimum, promethean ingenuity. Rather than being relegated to a vocational category of education, the study of the mechanical or technological arts was formerly elevated to the status of the liberal arts. Hughes goes on to provide a compelling story of how engineering was thought to have the capability, and indeed the destiny, of providing a second (and better) edenic creation.

To the extent that this remains a commonly held belief, we are assured of falling short of this lofty goal. No doubt technology must have a major part to play in opening the doors to paradise. Yet until technology is born out of and imbued with broad-based cultural values that help direct its creation, we will forever be the proverbial dog chasing its tail. But what, after all, is technology? Hughes (an emeritus professor in the history and sociology of science at the University of Pennsylvania) begins his book with the statement that "technology is messy and complex." Indeed it is, so much so that most well-educated people would be hard pressed to provide a succinct definition. In Hughes's own definition, technology is process and product inextricably tied together. It is designer and craftsman, scientist and engineer, inventor and mechanic using knowledge and tools to create and control the human-built world. This definition has some very attractive features: Technology is no longer inanimate but becomes a reflection and embodiment of the human essence. Technology has intrinsic value and purpose; it is not an innocent product of its creator, waiting to be put to some use—good or bad. Just as Victor Frankenstein had to take responsibility for his creation, so must today's technologists be responsible for what they produce. It is unacceptable to create solely because you can. The ostensible requirements of a high-tech work force have often relegated the study of the humanities in engineering schools to a second-order importance. It is interesting that the modern-day technological wizards often practice their art without being well grounded in the human condition or the human record. Perhaps these are some reasons that they have lost their influence over the direction and uses of their own intellectual labors.

Hughes discusses technology's role in and impact on culture, as reflected through machines. He implicitly poses the question of what is driving what: is culture a result of technology or is technology responding to culture? In a clever juxtaposition, Hughes then moves to consider technology as systems (control systems and information systems). Here he proffers an implicit answer—technology and culture are interdependent—through a description of the nature of feedback mechanisms and control loops. Technology and its relation to society are indeed messy and complex. In the last half of the previous century, we moved into the information age, a time when minds displace machines. Hughes does a very nice job weaving together a discussion of information as manifested in molecular biology, computer chips, weapons systems, and ecosystems.

In the book's climax, Hughes turns to technology and culture together. This exciting and stimulating chapter focuses on technology as reflected primarily through architecture. Much of what Hughes discusses in it seems embodied in the protagonist of Ayn Rand's *The Fountainhead*, Howard Roark. (Though the book's only reference to the novel is a brief mention, in a subsequent chapter, of Gary Cooper's portrayal in the film version.) Indeed, Roark could have been talking about the Bauhaus school when he mused that "most people build as they live—as a matter of routine and senseless accident. But a few understand that building is a great symbol. We live in our minds, and existence is the attempt to bring that life into physical reality, to state it in gesture and form" (*1*). Compare this with how Hughes describes the fusion of art and technology: "Artists turned to technological symbols and metaphors to represent a modern world and human characteristics." It is clear that in literature as well as in art and architecture, technology is a vehicle to set the soul free.

Technology celebrated. Medieval monks accorded the mechanical arts the same status as the liberal arts of antiquity. The grinding of grain is depicted in *Le Moulin mystique* (The Mystic Mill), carved on a nave capital at Ste. Madeleine, Vezelay, France.

CREDIT: SCALA/ART RESOURCES, NY

The reviewer is at the Picker Engineering Program, Smith College, 51 College Lane, Northhampton, MA 01063, USA. E-mail: dgrasso@email.smith.edu

Published by AAAS

Hughes's coda does a nice job of closing the circle by bringing in the dimension of ecotechnology. Although he never uses the s-word (sustainability)—probably because it is as much of a cliché in engineering as postmodernism is in literature—he does allude to many of the tenets that are encompassed by its various definitions. It is clear technology and culture are not separate and competing elements of the human-built world. Rather, they must be thought of together and transcended if we are to realize a civilization that can survive for the centuries to come.

Human-Built World offers an excellent overview of how to think about culture and technology. The book should be required reading for anyone who aspires to participate meaningfully in our technological society. It also serves to remind us that returning engineers to the policy- and decision-making tables will move us closer to fully realizing technology's potential and promise.

References

1. A. Rand, *The Fountainhead* (Bobbs-Merrill, Indianapolis, IN, 1943).

HISTORY OF SCIENCE

Building Circuits of Trust

Sungook Hong

The 19th-century British physicist William Thomson (later Lord Kelvin) proclaimed in 1883 that "when you cannot measure it, when you cannot express it in numbers, your knowledge is of a meager and unsatisfactory kind." Not simply a theoretical physicist, Thomson was also a great experimenter, a proponent for standardization, and the designer of various precise electrical instruments.

In recent years, historians of science and technology have paid increasing attention to measurement. Because quantification and standardization characterized the practices of electrical measurements from Coulomb into the 20th century, measurement and measuring instruments in electrical science and technology have been extensively discussed. Some argue that quantification provided a basis for the objectivity of science. Standardization functioned as a sort of common language, one which facilitated the communitarian characteristics of science. Due to these traits, scientific knowledge became easily moved and shared. Such institutions as Cambridge University's Cavendish Laboratory (which each year measured the value of the standard resistance ohm), Berlin's Physikalische-Technische Reichsanstalt, and the United Kingdom's National Physical Laboratory established imperial standards and dißstributed them to the world. They were, according to the French sociologist Bruno Latour, the "centers of calculation" and embodied power in the Foucauldian sense.

The Morals of Measurement
Accuracy, Irony, and Trust in Late Victorian Electrical Practice
by Graeme J. N. Gooday
Cambridge University Press, Cambridge, 2004. 357 pp. $85, £55.00. ISBN 0-521-43098-4.

Missing from these previous historical and sociological discussions on measurement is the complex net of relationships between theory and practice, between practitioners and instruments, and among practitioners from diverse backgrounds. This net is the subject of Graeme Gooday's *The Morals of Measurement*. As Gooday, a historian of science at the University of Leeds, aptly argues, electrical units and standards were continuously contested through the last quarter of the 19th century. Without universal standards, physicists and electrical engineers (though generally trusting their instruments) disputed the values obtained from measuring various quantities.

When and why did practitioners come to trust the measurements? A simple answer would be that they did so when the measurements became sufficiently accurate. But this begs the crucial question, because they employed the language of accuracy to set the limits within which they could trust others' (and their own) measurements. They could have trusted the results obtained by others when they believed in the honesty and integrity of the measurer. However, this criterion does not provide a sufficient condition for trustworthiness either, because honest and credible practitioners could produce inaccurate data if their measuring instruments were not correctly calibrated.

Gooday's book highlights the moral dimensions involved in measurement, and it suggests the advantages of considering the history of measurement from the perspective of morals and trust rather than that of power. Measurements of electrical properties comprise several moral factors: the practitioner's assumption of the integrity of previous measurers; the trustworthiness of the measurer's

The reviewer is in the Department of Biological Sciences, College of Natural Sciences, Seoul National University, Gwan-Ak Gu, Seoul 151-742, South Korea. E-mail: comenius@snu.ac.kr

Published by AAAS

skill and experimental practices; the trustworthiness of the theory, instruments, and substances used in the measurement; the honest reporting of results; and the benefits of the quantitative data for others. When practitioners accepted measurements obtained by others, all these factors formed a net of credibility and simultaneously contributed to the formation of trust. However, when one or two of these factors were in doubt, the entire measurement and its data tended to be seen as suspect. As a result, the history of electrical measurement that Gooday explores is accurately characterized in terms of dispute and contest rather those of harmony and consensus.

The first of the book's six chapters provides a detailed analysis of the role of trust in measurement. Rather than placing excessive emphasis on standardization carried out by the imperialistic laboratories, Gooday argues that consideration of the bonds of trust provides a better grounds for understanding whose measurement was trusted and why. The second chapter, which discusses the notion of accuracy, highlights the interesting difference between German and British practitioners over the best method for maximizing measurement accuracy. The Germans favored taking a great number of measurements in order to employ a method of error analysis, whereas the British preferred paying sufficient care to decrease the error in individual measurements. In the subsequent chapters, Gooday discusses the aforementioned moral dimensions involved in the measurement of resistance, current, self-induction, and domestic electrical consumption. For the difficult task of measuring the self-induction of electrical machinery, no consensus was established until early in the 20th century. Gooday also shows, however, that even a seemingly simple measurement of electrical current was not universally standardized during the Victorian era, because scientists and engineers employed different amperemeters at different sites and for different purposes.

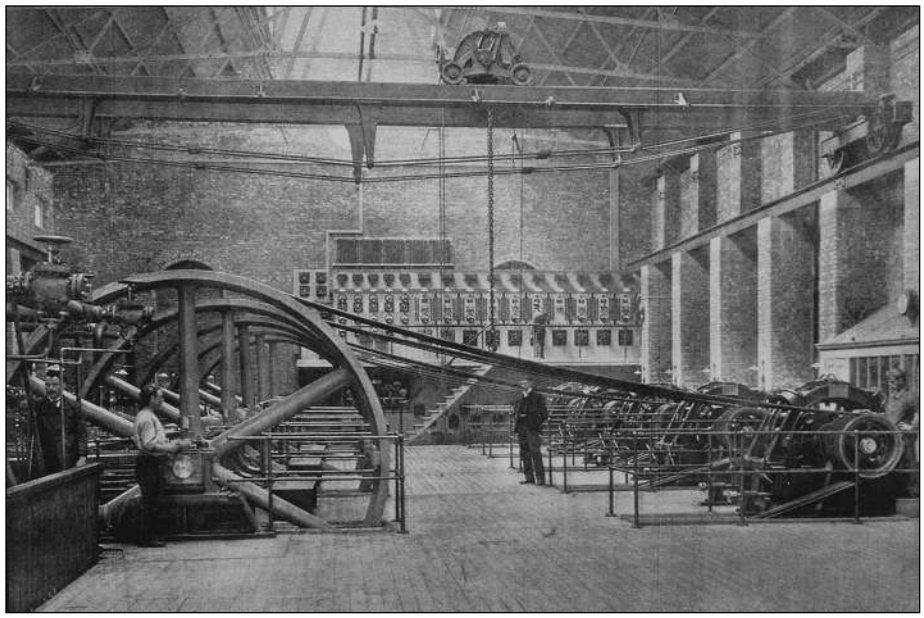

Coupled problems. The issue of quantifying self-induction came to prominence in efforts to commercially run alternating-current generators (alternators) in parallel, as was done with the belt-linked alternators and steam generators at this Electric Lighting Station in West London (circa 1893).

Because Gooday's work tightly focuses on the moral and social dimensions of electrical measurements, those who wish to explore how the technologies and techniques were developed and functioned should also refer to other books and articles. Nonetheless, there is no doubt that *The Morals of Measurement* is a timely contribution to the history, as well as the historiography, of measurement. It complements recent scholarship, which has emphasized the universalizing tendency of standardization, and will draw historians' attention to the importance of morals and trust.

BROWSINGS

Brick. A World History. *James W. P. Campbell; photographs by Will Pryce.* Thames and Hudson, London, 2003. 320 pp. $70, £39.95. ISBN 0-500-34195-8.

Sun-dried mud bricks are easily made but suffer from a susceptibility to rains and floods. Although fire-hardening requires an ample supply of fuel as well as the skills to select appropriate clays and maintain steady kiln temperatures, the result is a waterproof and resilient material. Campbell and Pryce offer lay readers a profusely illustrated introduction to the diverse uses of brick in building and engineering. Their personal survey ranges from the earliest common use of fired brick (in Mesopotamia, circa 3000 B.C.) to contemporary housing in Amsterdam. Among the highlights is the Tomb of the Saminids, circa 900 C.E., at Bukhara, Uzbekistan (left), which has been immaculately preserved largely because it had been buried under sand for much of its existence. The book focuses on architecture, but it also reveals the variety in sizes and shapes of bricks and discusses the techniques of brickmakers and bricklayers.

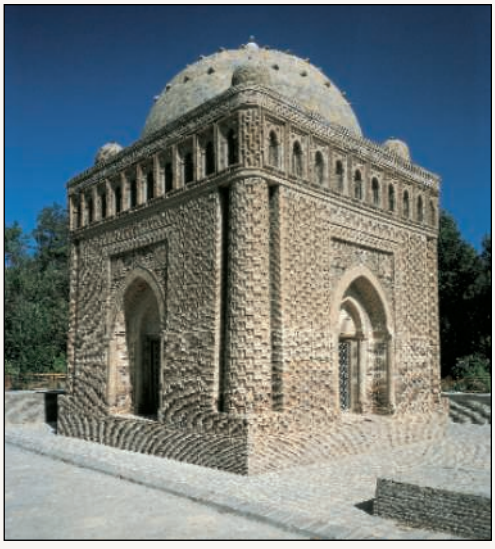

Inventing for the Environment. *Arthur Molella and Joyce Bedi, Eds.* MIT Press, Cambridge, MA, 2003. 320 pp. $29.95, £19.95. ISBN 0-262-13427-6. Lemelson Center Studies in Invention and Innovation.

The contributors explore the variety of ways in which technological innovations affect interactions between humans and nature. Each of the volume's sections examines a particular environmental topic, such as urban landscapes or alternative energy sources. Each section comprises three parts: an essay by a historian, a perspective by someone working on the issue, and a biographical portrait of an individual who has contributed a creative approach to the problem. The dialogue among historians, inventors, architects, and planners is meant to provide part of the foundation for a sustainable future.

CREDITS: (TOP) FROM *ENGINEER* **75**, 523 (1893)/COURTESY G. J. N. GOODAY (BOTTOM) WILL PRYCE/COURTESY THAMES AND HUDSON

Published by AAAS

POLICY FORUM

BIOTECHNOLOGY

Japanese Controversies over Transgenic Crop Regulation

Kazuo N. Watanabe,[1,2]* Mohammad Taeb,[3] Haruko Okusu[3]

The Cartagena Protocol on Biosafety was enacted in 2003 to regulate transboundary movement of genetically modified organisms or LMOs (living modified organisms, the legal term defined by the protocol) (*1*). The Japanese Diet approved a bill that made drastic changes to existing national guidelines to fulfill the requirements of the Cartagena Protocol (*2*). Ministries associated with aspects of biosafety discussed the bill and its integration with the overall system for environmental and laboratory safety (*3*), and the Japanese law entered into force in February 2004.

This law has made legal procedures more comprehensive and consistent. However, operational details have not yet been digested by stakeholders, especially commercial traders and academic researchers. Furthermore, Japan is at a critical stage in dealing with negative public reaction to modern biotechnology and its products.

Under the new law, there are specific legal procedures required for exchange of transgenic organisms with Japan. For importation, it is necessary to document prior informed consent (PIC) between exporter and importer. The shipment must clearly indicate on the package and in accompanying documentation that transgenic materials are included. For Japanese scientists, importation of transgenic materials is allowed only after the certification of experiments as safe by the research institution or, if the risk level is high, by the Ministry of Education, Culture, Sports, Science, and Technology (MEXT).

For exportation, a PIC document is required from the importer to protect Japanese research institutions from foreign claims. International scientists should be aware, for example, that transport of recombinant microorganisms and seeds from transgenic plants could be rejected for lack of documentation. For those who are accustomed to a more relaxed system, the new laws require attention to avoid delays or blocked shipments. This applies to materials for basic research or commerce.

There is domestic confusion as well over the new rules. To focus attention on this issue, officials at MEXT (*4*) have held tutorials for the academic community and basic research institutions on risk minimization and the new legal system. This is to avoid procedural failures that might result in domestic legal prosecution and penalties, as well as any international perception that Japan has problems with compliance.

Importation of transgenic crops is skyrocketing in Japan. For example, the combined value of imported transgenic soybean, maize, and canola was nearly US$ 3.5 billion in 2003 (*5*). However, against the backdrop of food safety concerns and distrust of government authorities in the wake of bovine spongiform encephalopathy, avian influenza, and fraudulent food labeling scandals, public anxiety has been increasing (*6*). One result is that local prefectures in Shiga, Iwate, Hokkaido, and Ibaraki are considering instituting their own regulations (*7–10*) on the general release of transgenic organisms, in an attempt to regulate crops that have already been approved by the central Japanese government. There is concern that public reaction will adversely affect local farmers and the tourism industry, as well as fear that products derived from genetic engineering are not safe and that transgenic crops could contaminate neighboring fields.

Elsewhere in Asia, national efforts to promote testing and use of transgenic crops have increased. For example, China has nearly 7 million acres of Bt cotton (which has *Bacillus thuringiensis* toxin genes), and India and Pakistan have developed commercial products from their research (*11–13*). However, the paradigm shift toward comparable developments in Japan may not occur because of extreme feeling against transgenic crops (*14*). Although hundreds of experiments on transgenic plants are being conducted yearly, they could be shut down by fragmented and preventive regulations, as is happening in the United Kingdom (*15*).

The biggest problem may be that discussions on transgenic organisms have never been seen as a long-term, trust-building, and collaborative exercise among stakeholders. Organizations such as the Japan Bioindustry Association; the Society for Techno-Innovation of Agriculture, Forestry, and Fish; and the International Life Science Institute (ILSI) Japan have met to discuss public education (*6*, *16*, *17*). However, their sessions have not had follow-up. Approaches to risk communication need to be re-examined (*18*).

Although academic societies have tried to promote public awareness, there has been little consensus within or between organizations. Individual scientists have made public statements, adding to the confusion (*19*). The Japanese Society for Plant Cell and Molecular Biology and the Japanese Society of Breeding have begun to hold discussions on transgenic crops with consumer groups, stakeholders, and governmental organizations. This is a step in the right direction, but sustained effort will be needed if plant biotechnology is to prosper in Japan.

[1]Gene Research Center, University of Tsukuba, Ibaraki, 305-8572, Japan. [2]International Plant Genetic Resources Institute, Rome, Italy. [3]Institute of Advanced Studies, United Nations University, Yokohama, 220-0012, Japan.

*To whom correspondence should be addressed. E-mail: nabechan@gene.tsukuba.ac.jp

References and Notes

1. See www.biodiv.org/biosafety.
2. K. N. Watanabe, *Nature* **421**, 689 (2003).
3. Law Concerning the Conservation and Sustainable Use of Biological Diversity through Regulations on the Use of Living Modified Organisms (Law No. 97 of 2003), available at www.biodic.go.jp/cbd/biosafety/sps.html.
4. MEXT, see www.mext.go.jp/a_menu/shinkou/seimei/.
5. Ministry of Agriculture, Forestry, and Fisheries of Japan, 30 April 2004, available at www.maff.go.jp/www/info/bun09.html.
6. Questionnaire on GM crops and food, 6 April 2004, available at http://web.staff.or.jp/.
7. K. Watanabe *et al.*, *Nature Biotechnol.* **22**, 943 (2004).
8. Mainichi Newspapers, "Trends in GM crops in prefectures," 31 July 2004, available at www.mainichi-msn.co.jp/kagaku/news/20040731k0000m070175000c.html.
9. "Shiga Prefecture examines the need for regulating GM crops," *Kyoto Shimbun News*, 11 June 2004, available at www.kyoto-np.co.jp/article.php?mid=P2004061100213&genre=G1&area=S10.
10. For example, Guideline on planting GM crops in Hokkaido, 5 March 2004, available at www.pref.hokkaido.jp/nousei/ns-rtsak/shokuan/conf.html.
11. C. James, *Global Status of Commercialized Transgenic Crops: 2003* (ISAAA Briefs. No. 30, International Service for the Acquisition of Agri-biotech Applications, Ithaca, NY, 2003); available at www.isaaa.org.
12. P. Menon, *Frontline* **19**, 22 June 2002; available at www.hinduonnet.com/fline/fl1913/19130900.htm.
13. I. A. Rao, www.pakissan.com/english/advisory/the.use.shtml.
14. K. N. Watanabe, A. Komamine, in *Intellectual Property Rights in Agricultural Biotechnology*, F. H. Erbisch, K. M. Maredia, Eds. (Michigan State Univ., East Lansing, and C.A.B. International, Wallingford, UK, ed. 2, 2004), pp. 187–200.
15. Department for Environment, Food, and Rural Affairs, "Genetic modification," available at www.defra.gov.uk/environment/gm/index.htm.
16. Japan Bioindustry Association, "Biotechnology Q & A," available at www.jba.or.jp/index_e.html.
17. ILSI Japan, see http://japan.ilsi.org/.
18. A. Kapuscinski *et al. Nature Biotechnol.* **21**, 599 (2003).
19. No! GMO Campaign, see www.no-gmo.org.

20. K.N.W. acknowledges the Japanese Society for the Promotion of Science, grant no. JSPS-RFTF-00L01602.

STRUCTURAL BIOLOGY

The Atomic Architecture of a Gas Channel

Mark A. Knepper and Peter Agre

"Form ever follows function." Penned in 1896 by the renowned architect Louis Henri Sullivan in reference to the first tall office buildings, this sentence also applies to the structure of cell membrane proteins. Although high-resolution structures of protein channels that allow passage of ions, uncharged solutes, and even water have been solved, the precise mechanisms by which gases cross biological membranes have remained enigmatic. On page 1587 of this issue, Khademi *et al*. (*1*) provide a quantum leap forward in our understanding of gas transport. They resolve the crystallographic structure of a bacterial ammonia transport channel, AmtB, to 1.35 Å—an unprecedented resolution for an integral membrane protein.

Ammonia (NH_3) is a gas, but when dissolved in water it exists predominantly as the ammonium ion (NH_4^+) with a pK_a of about 9 under physiological conditions. For a bacterium, NH_3 is an important nutrient that must be taken up from the surroundings to provide a source of nitrogen for amino acid synthesis. AmtB is a transport protein present in the bacterial inner membrane between the cytoplasmic and periplasmic spaces that facilitates NH_3 uptake (see the figure). Interestingly, AmtB proteins are genetically related to the structural components of the Rh blood group antigens of mammalian red blood cells. The Rh-related proteins are a family of membrane proteins reported to facilitate the transport of ammonia (*2*) and carbon dioxide across eukaryotic cell membranes (*3*). Human Rh-related proteins are thought to be important in critical physiological processes and, when defective, may result in impairment of systemic pH regulation or central nervous system dysfunction due to ammonium toxicity. The structure of Rh antigens has long been pondered. Now, the trimeric structure of AmtB revealed by Khademi and colleagues suggests a simple explanation for how the three Rh polypeptides of red blood cells—RhAG, RhD, and RhCE—form the Rh antigen complex in the erythrocyte plasma membrane (*4*). In addition, the Khademi *et al*. study reveals a mechanism of ammonia permeation in bacteria that is likely to be similar in eukaryotic cells.

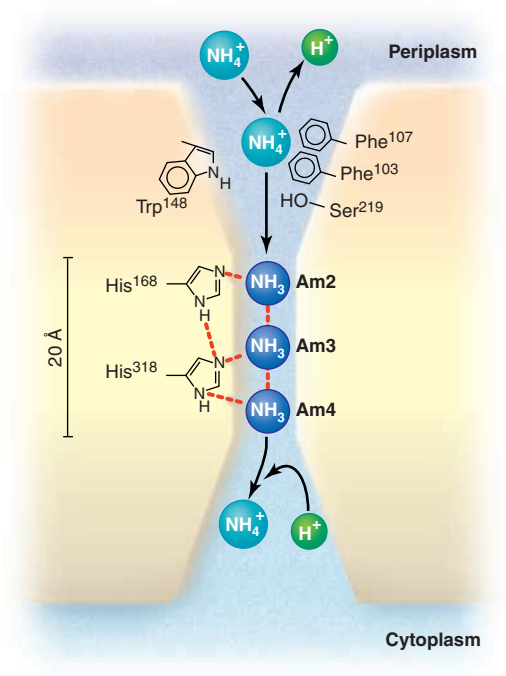

The AmtB ammonia channel of *E. coli*. Resolution of the structure of the bacterial integral protein AmtB reveals a wider vestibule at the top and bottom of the channel. The amino acid residues that line the pore of the outer vestibule—Trp^{148}, Phe^{107}, Phe^{103}, and Ser^{219}—stabilize NH_4^+ (Am1). Midway through the membrane, the channel narrows over a 20 Å span. Here, two pore-lining residues, His^{168} and His^{318}, stabilize three NH_3 molecules (Am2, Am3, and Am4) through hydrogen bonding (red dashed lines). The molecules return to equilibrium as NH_4^+ in the inner vestibule.

Databases of solved protein structures are burgeoning with structural maps of both intracellular and extracellular proteins. However, structures of integral proteins with their many membrane-spanning loops are just now beginning to emerge. A common strategy, and one adopted by Khademi *et al*., is to express paralogous genes from multiple bacterial species, prepare three-dimensional crystals of the proteins they encode, and select the crystal producing the highest resolution x-ray diffraction pattern for analysis. The structures of a few eukaryotic integral proteins have been determined by cryo-electron microscopy of membrane crystals or by molecular modeling using coordinates determined from x-ray analysis of prokaryotic paralogs. Khademi *et al*.'s success with AmtB, an integral membrane protein from *Escherichia coli* with 11 membrane-spanning α helices, foreshadows continued progress with other integral membrane proteins whose structures have been elusive.

Elements of the AmtB structure reveal how this protein channel transports ammonia (see the figure). AmtB has the same structure when crystallized in both the absence and presence of ammonia, leading the authors to conclude that it is a channel rather than a transporter that would be expected to have flexible elements involved in translocation of the substrate. At the two ends of the pore, broader vestibules contain NH_3 in equilibrium with NH_4^+. AmtB has at its center a narrow hydrophobic pore element about 20 Å in length, which allows the passage of NH_3 but not the monovalent ion NH_4^+. This distinction is important because the structure must prevent ions such as K^+ from crossing the inner membrane. Thus, AmtB is an NH_3 channel that does not mediate the net transfer of protons and does not directly alter the membrane potential. Although these conclusions appear contrary to those of prior studies in which biophysical techniques indicated that ammonia translocation is affected by pH and voltage gradients (*5*), Khademi and colleagues argue persuasively that their model (see the figure) is compatible with most of the biophysical data reported so far.

Simple membrane bilayers have moderate intrinsic NH_3 permeability (*6*), so the necessity of ammonia channels could be questioned. Ammonia channels, however, may serve to accelerate ammonia transport at sites where the diffusion of NH_3 through the lipid bilayer is too slow for physiological needs, or may provide a molecular target for regulating the passage of NH_3. Both functions may be important in the mammalian kidney collecting duct where two

M. A. Knepper is in the Laboratory of Kidney and Electrolyte Metabolism, National Institutes of Health, Bethesda, MD 20892, USA. E-mail: kneperm@nhlbi.nih.gov P. Agre is in the Departments of Biological Chemistry and Medicine, Johns Hopkins University School of Medicine, Baltimore, MD 21205, USA. E-mail: pagre@jhmi.edu

Rh-related proteins are expressed—RhBG in the basolateral plasma membrane and RhCG in the apical plasma membrane (*5*). Regulated excretion of NH_4^+ by the kidneys is a crucial mechanism for controlling systemic pH (*7*). Synthesized in the proximal tubule, NH_4^+ accumulates in the renal medulla by active transport from the loop of Henle. The final step in NH_4^+ excretion involves rapid NH_3 diffusion across the collecting duct epithelium in parallel with active H^+ secretion. Although it has been assumed that NH_3 diffuses into the collecting duct lumen through the lipid bilayer, the structure of AmtB predicts that the entry of NH_3 is mediated by the Rh-related proteins expressed there. It remains to be seen whether NH_3 penetration through these proteins may be a point where systemic acid-base balance is regulated, or whether Rh-related proteins are involved in clinical disorders such as renal tubule acidosis.

Another site where rapid ammonia transport may be critical to homeostasis is the liver where RhBG is present (*8*). NH_4^+ is produced during the catabolism of amino acids and is also delivered to the portal circulation by intestinal bacteria that break down urea. NH_4^+ is a neurotoxin and must be efficiently cleared from the portal blood by hepatocytes and converted to urea and glutamine to prevent serious systemic consequences. Central nervous system dysfunction occurs if NH_4^+ concentrations are elevated as seen in hepatic encephalopathy, a common but ominous manifestation of advanced liver failure. RhBG is expressed selectively in the pericentral hepatocytes, just before the portal blood is delivered to the systemic circulation. Thus, RhBG may be important to the process that normally clears the last vestiges of ammonia from the portal blood.

The structural determination reported by Khademi *et al*. provides great insight into the important process of gas transport. As with the transport of water, glycerol, and other uncharged solutes, the phenomenon of gas transport now has a molecular identity and an advanced level of understanding. Thus, physiologists may now be able to ask specific scientific questions about ammonia transport with great precision.

References

1. S. Khademi *et al.*, *Science* **305**, 1587 (2004).
2. A.-M. Marini *et al.*, *Nature Genet.* **26**, 341 (2000).
3. E. Soupene, W. Inwood, S. Kustu, *Proc. Natl. Acad. Sci. U.S.A.* **101**, 7787 (2004).
4. J. P Cartron, *Bailleres Clin. Haematol.* **12**, 655 (1999).
5. N. L. Nahkhoul, L. L. Hamm, *Pflugers Arch.* **447**, 807 (2004).
6. A. Walter, J. Gutknecht, *J. Membr. Biol.* **90**, 207 (1986).
7. M. A. Knepper, R. Packer, D. W. Good, *Physiol. Rev.* **69**, 179 (1989).
8. I. D. Weiner, R. T. Miller, J. W. Verlander, *Gastroenterology* **124**, 1432 (2003).

PHYSICS

Visualizing the Dynamics of the Onset of Turbulence

Friedrich H. Busse

The transition to turbulence in fluid flow is an everyday experience. As a faucet is slowly opened, the initially laminar flow of water changes into an irregular chaotic flow. As a result, friction is much increased and, for the same discharge, a higher pressure head must be applied than in the laminar case. This transition is of fundamental importance in engineering problems dealing with fluid flows. On page 1594 in this issue, Hof *et al.* (*1*) present the first observation of a basic dynamical property of the transition.

The study of the onset of turbulence has a long history. In 1839, Hagen first noted the existence of two distinct flow regimes in the discharge from pipes (*2*). Some 50 years later, Reynolds (*3*) realized that the transition between these regimes only depends on a dimensionless number, $Re = UD/\nu$, where U denotes the mean velocity averaged over the circular cross section of the pipe, D is its diameter, and ν is the kinematic viscosity of the fluid.

In pipe flows, disturbances of finite amplitude are responsible for the transition to turbulence. Reynolds noticed as much when he reported that the transition was delayed to higher values of Re when a particularly smooth entrance region of the pipe was used. However, theoretical studies can treat easily only infinitesimally small disturbances, and this is one reason why theoretical understanding of the transition to turbulence in shear flows has been slow to emerge. For laminar flow in a channel between parallel plates, such analysis suggests that laminar flow should become unstable at $Re = 7696$, but experiments indicate a much lower value of ~1500 for the transition (*4*). For flow between two parallel plates sliding relative to each other with speed U (plane Couette flow) and for flow through a circular pipe (see the figure), the discrepancies are even larger: No growing infinitesimal disturbances could be found theoretically at any Reynolds number.

With today's powerful computers, it is not difficult to simulate turbulent fluid flows at Reynolds numbers of several thousands. Good agreement between statistical properties of turbulence in experiments and in numerical simulations has been found (*5*), but a detailed understanding of the transition process is still lacking.

For configurations other than plane parallel flow, theoretical studies have been more successful. For example, when the circularly symmetric flow between differentially rotating coaxial cylinders becomes unstable, axisymmetric vortices are formed, the amplitude of which increases smoothly with the Reynolds number. This is a typical example of a supercritical bifurcation (*6*), in

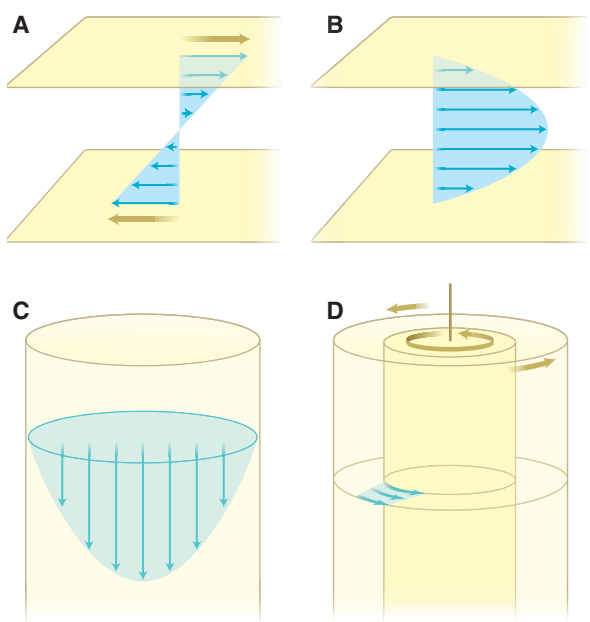

Simple laminar shear flows. (**A**) Plane Couette flow; (**B**) channel flow (Poiseuille flow); (**C**) pipe flow; (**D**) circular Couette flow.

CREDIT: PRESTON HUEY/*SCIENCE*

The author is at the Institute of Physics, University of Bayreuth, 95440 Bayreuth, Germany. E-mail: busse@uni-bayreuth.de

Published by AAAS

contrast to the unstable subcritical bifurcations that occur in plane parallel shear flows in the absence of rotation.

For plane Couette flow and pipe flow, theoretical studies have not found evidence for bifurcation at finite values of *Re*. Nevertheless, the belief in the existence of relatively simple solutions describing states of fluid flow distinct from the basic states of plane Couette flow or pipe flow has persisted. These solutions must be expected to be unstable; therefore, numerical methods are usually not capable of producing them, just as experiments do not exhibit them.

One way of accessing these solutions is by considering the plane Couette or pipe flow problem as a special case of a more general problem, with an additional parameter as a function of which instabilities or bifurcations can be found. The desired solutions are searched by following one or the other of the bifurcating solution branches through secondary bifurcations. For plane Couette flow, the small-gap limit of circular Couette flow provides such an additional parameter in the form of the mean rate of rotation (*7*), which vanishes only in the special case of plane Couette flow. Alternatively, one may consider plane Couette flow between horizontal plates, the lower of which is heated, and the upper of which is cooled. The basic state of flow is not changed by this procedure, but additional instabilities driven by thermal buoyancy become available (*8*). Or an artificial forcing can be applied to gain a point of bifurcation from which a solution branch can be followed to the place of vanishing forcing (*9*). This method has been applied to the case of pipe flow (*10*, *11*).

With these methods, steady solutions are obtained for plane Couette flow and traveling wave solutions for pipe flow. These "tertiary solutions" are separated from the basic states by two bifurcations. They are thus characterized by two wave numbers, in the streamwise and in the transverse directions.

A dominant component of the tertiary solutions are the roll-like eddies with axes parallel to the mean flow. These rolls redistribute momentum and tend to flatten the profile of the mean flow. As a result, the slope of the profile close to the solid boundary steepens, thereby increasing viscous stress. To obtain the same mass flux through the pipe as in the laminar case, a higher pressure gradient is thus needed. Similarly, in the plane Couette case, a stronger force must be applied to keep the plates moving relative to each other with velocity *U*.

The two-dimensional roll-like eddies would decay if they were not sustained by the three-dimensional components of the tertiary solutions. Streamwise oriented roll-like structures or "streaks" are commonly observed in wall-bounded turbulent shear flows, but the relationship to the tertiary solutions is tenuous at best. There has been little hope to observe the latter solutions in the laboratory because they are almost always unstable.

It thus came as a surprise when Hof *et al.* (*1*) observed the predicted patterns of tertiary solutions in their experiments. Using special disturbances in carefully prepared pipe flow (*12*) and sophisticated visualization techniques, they demonstrate that the tertiary solutions can be realized at least as a transient phenomenon. They find surprisingly close agreement between experimentally observed structures and their theoretical counterparts (*1*).

The puzzle of the visibility of unstable solutions may be explained as follows. The changing state of fluid flow can be considered as a trajectory in the high-dimensional solution space of the basic equations of motion. The tertiary solutions (and the more complex ones bifurcating from them) are unstable in particular directions, but they attract trajectories from most other directions. The trajectories therefore spend much of their time in the neighborhood of those solutions before they are ejected. These solutions may thus be regarded as virtual traffic arteries, which become visible as they attract parcels of momentum and transport them for a while until they deliver them to another artery and decay.

The achievement reported by Hof *et al.* (*1*) stems from a collaboration between engineers, physicists, and mathematicians. It opens the door not only to a full understanding of the transition problem, but also to possibilities for influencing and controlling transitions, with far-reaching engineering implications. The new results also demonstrate that it is never too late to attack an old problem, especially if it is done as an interdisciplinary effort.

References and Notes

1. B. Hof *et al.*, *Science* **305**, xxxx (2004).
2. G. H. L. Hagen, *Pogg. Ann.* **46**, 423 (1839).
3. O. Reynolds, *Proc. R. Soc. London A* **35**, 84 (1883).
4. Here the same definition of the Reynolds number is used as for pipe flow except that *D* now refers to the width of the channel.
5. J. G. M. Eggels *et al.*, *J. Fluid Mech.* **268**, 175 (1994).
6. "Bifurcation" is a mathematical term used when a secondary solution branches from a primary one.
7. M. Nagata, *J. Fluid. Mech.* **217**, 519 (1990).
8. R. M. Clever, F. H. Busse, *J. Fluid Mech.* **234**, 511 (1992).
9. F. Waleffe, *Phys. Rev. Lett.* **81**, 4140 (1998).
10. H. Faisst, B. Eckhardt, *Phys. Rev. Lett.* **91**, 224502 (2003).
11. H. Wedin, R. R. Kerswell, *J. Fluid Mech.* **508**, 333 (2004).
12. Measurement in the same 30-m-long pipe clearly demonstrated the influence of the Earth's rotation on the laminar flow profile (*13*).
13. A. A. Draad, F. T. M. Nieuwstadt, *J. Fluid Mech.* **361**, 297 (1998).

CHEMISTRY

Multidimensional Snapshots of Chemical Dynamics

Albert Stolow and David M. Jonas

Chemical reactions involve the concerted motions of both atoms and electrons as bonds rearrange on the way from reactant to product. Elementary models use a single, one-dimensional (1D) reaction coordinate to describe motion across a transition state separating reactants from products. However, internal molecular motions along other coordinates tend to prevent molecules from following this lowest energy reaction coordinate. These other motions are not mere energetic reservoirs that may aid or deter motion along the reaction coordinate. Rather, they are intimately involved in the complex flow of electronic charge and vibrational energy during reaction. Recent advances in femtosecond (10^{-15} s) laser and detector technologies are enabling a new generation of experiments that provide true multidimensional views of the dynamics of chemical reactions (*1*).

One emerging approach is based on time-resolved diffraction from crystals that have been photochemically excited by a femtosecond pulse of light, allowing multidimensional measurements of the ensuing atomic motions. For example, Moffat (*2*) and Anfinrud and co-workers (*3*) have performed time-resolved crystal diffraction experiments that yield the time-dependent positions of all atoms during a biochemical photoreaction. The reaction is initiated by a 100-picosecond pulse of light and then probed by measuring the diffraction pattern

A. Stolow is at the Steacie Institute for Molecular Sciences, National Research Council Canada, 100 Sussex Drive, Ottawa, Ontario K1A 0R6, Canada. E-mail: albert.stolow@nrc.ca D. M. Jonas is in the Department of Chemistry and Biochemistry, University of Colorado, Boulder, CO 80309, USA. E-mail: david.jonas@colorado.edu

with a delayed x-ray pulse of the same duration. Large-scale structural rearrangements in proteins (such as the side-chain motions in myoglobin upon carbon monoxide undocking) or at surfaces are almost impossible to observe in another way. Nanosecond time resolution reveals several distinct intermediate structures (*2*), with evidence of driven motions at faster time scales (*3*). New instruments that aim for even higher time resolution using either x-ray or electron scattering are being developed by several groups (*4*–*8*).

Femtosecond two-dimensional infrared (2D IR) spectroscopy is being explored as a way to gain information about transient molecular structures in disordered materials. Bredenbeck and Hamm have used transient femtosecond 2D infrared spectra, which are sensitive to distances between the carbonyl groups in peptides (*9*), to monitor the progress of photoinduced peptide folding. To follow peptide folding on a picosecond time scale, an octapeptide is covalently bound to both ends of an azobenzene conformational switch. First, a femtosecond ultraviolet pulse electronically excites the azobenzene molecule and induces isomerization from the cis to the trans form, triggering the folding of the peptide backbone into its new equilibrium conformation. The time evolution of the azobenzene electronic spectrum, observed in a conventional pump-probe experiment, monitors peptide folding indirectly, because the unfolded peptide inhibits complete isomerization of the switch (*10*). In the new experiments, the femtosecond 2D infrared spectra are sensitive to distances between the carbonyl groups in the peptide itself.

The 2D infrared spectra are recorded by hitting the peptide with a "single-frequency" infrared excitation pulse and then detecting changes in the frequency-resolved infrared absorption spectrum as a function of the initial infrared excitation frequency. When two carbonyl groups in the peptide are within 0.3 nm, their vibrations are coupled so that excitation of either one shifts the absorption frequency of the other, producing a cross-peak in the 2D spectrum. This is analogous to how the coupling between spins produces cross-peaks in 2D nuclear magnetic resonance (NMR) (*11*, *12*).

Although 2D infrared spectroscopy has a much faster time scale than 2D NMR (*10*), vibrational transitions also have larger linewidths. In the octapeptide, the number of carbonyl groups prevents the resolution of individual cross-peaks. Peptide dynamics were therefore probed only through the overall 2D line shape (see the figure), which changes rather dramatically and continues to change even after the infrared spectrum of the peptide and electronic spectrum of the azobenzene have relaxed to equilibrium. The reduction in the homogeneous linewidth of the 2D infrared spectrum has been interpreted as reflecting more restricted conformational fluctuations around the minimum free energy folded conformation.

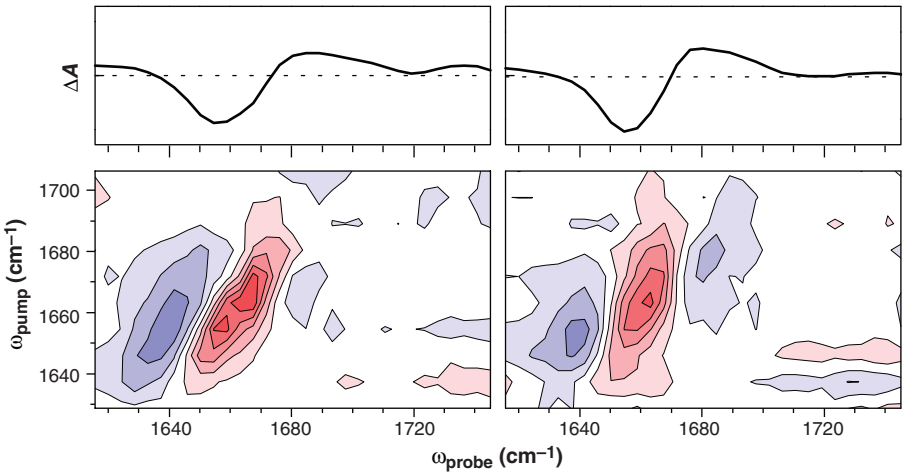

Tracking complex reactions. Polypeptide conformational dynamics observed via transient changes in the 1D (**top**) and 2D IR spectra (**bottom**) of an octapeptide as a function of pump frequency (ω_{pump}) and probe frequency (ω_{probe}). The spectra show differences between the spectra of the intermediates and the reactants at 20 ps (left) and 1.7 ns (right) after cis-trans photoisomerization of the azobenzene bound to both ends of the octapeptide. Blue indicates that the UV photoisomerization pulse and IR pump pulse reduce IR probe absorption, whereas red indicates increased IR probe absorption. While the 1D spectra apparently cease to evolve beyond 20 ps, the 2D spectra continue to reveal changes caused by peptide folding for more than 200 ps. [Data from (*9*)].

A third approach, sensitive to both electronic and atomic motions, is based on photoionization. This approach applies in the gas phase and on surfaces. Because ionization techniques are sensitive to electronic structure and require only that the photon energy exceed the ionization potential, time-resolved photoelectron spectroscopy (*13*–*15*) has been used to probe the coupled redistribution of charge and energy in gas-phase photochemical reactions all the way from reactants to products. Hayden and co-workers have combined time-resolved photoelectron spectroscopy with new coincidence and imaging techniques in "coincidence-imaging spectroscopy" (CIS) (*1*). As a result of developments in charged-particle detector technology, miniaturized versions of the "crossed wire" detector famous in particle physics now allow 3D measurements of a single particle emitted from a chemical event (*16*). The CIS technique measures the energy and 3D angular distributions of ions and electrons in coincidence and as a function of time, thus removing orientational and product channel averaging (*17*). This is important because chemistry occurs in the randomly oriented frame of the molecule, whereas measurements are made in the frame of the laboratory, leading to a loss of information.

In the experiments of Hayden and coworkers, a femtosecond pump pulse initiates a photodissociation reaction, a delayed probe laser pulse ionizes the reacting molecule, and a pair of 3D particle detectors measures the emitted positive ion and electron from a single molecular dissociation/ionization event in coincidence, building up sets of "coincidence maps" that reveal detailed correlations. Because the ion recoil distributions relate to the molecular orientation, the correlated electron distributions reveal details of both charge and energy flow in the reacting molecule. In the photodissociation of the atmospherically important nitrogen dioxide molecule ($NO_2 \rightarrow NO + O$), CIS was used to directly observe the evolving rearrangement of the electron cloud (*1*) on the NO molecule as its O atom partner breaks its bond and leaves (*17*).

The elucidation of complex chemical processes rests on the availability of femtosecond laser sources. To do the same for correlated electron dynamics of strongly bound electrons requires pulses that are 1000 times as fast—that is, attosecond (10^{-18} s) pulses. Attosecond pulses have been demonstrated, and a new approach to time-resolved electron dynamics has been reported by Krausz and co-workers (*18*). In an alternate approach, attosecond measurements based on correlation techniques in a strong laser field were reported by Corkum and co-workers (*19*). These first results open up yet another frontier for the time-resolved measurement of the ultrafast processes that occur during chemical reactions.

References and Notes

1. Many of these approaches were recently discussed in the symposium on *Emerging Ultrafast* Spectroscopies: From Chemistry to Biophysics, 227th National Meeting of the American Chemical Society, Anaheim, CA, 28 March to 1 April 2004.
2. K. Moffat, *Faraday Discuss.* **122**, 65 (2003).
3. F. Schotte *et al.*, *Science* **300**, 1944 (2003).
4. F. Benesch, T. Lee, Y. Jiang, C. G. Rose-Petruck, *Opt. Lett.* **29**, 1028 (2004).
5. M. F. Decamp *et al.*, *Phys. Rev. Lett.* **91**, 165502 (2003).
6. S. L. Johnson *et al.*, *Phys. Rev. Lett.* **91**, 157403 (2003).
7. B. J. Siwick, J. R. Dwyer, R. E. Jordan, R. J. D. Miller, *Science* **302**, 1382 (2003).
8. C. Y. Ruan *et al.*, *Proc. Natl. Acad. Sci. U.S.A.* **101**, 1123 (2004).
9. J. Bredenbeck *et al.*, *J. Phys. Chem. B* **107**, 8654 (2003).
10. S. Spörlein *et al.*, *Proc. Natl. Acad. Sci. U.S.A.* **99**, 7998 (2002).
11. D. M. Jonas, *Science* **300**, 1515 (2003).
12. D. M. Jonas, *Annu. Rev. Phys. Chem.* **54**, 425 (2003).
13. V. Blanchet, M. Zgierski, T. Seidemann, A. Stolow, *Nature* **401**, 52 (1999).
14. A. Stolow, A. E. Bragg, D. M. Neumark, *Chem. Rev.* **104**, 1719 (2004).
15. L. Lehr *et al.*, *Science* **284**, 635 (1999).
16. K. A. Hanold, M. C. Ganer, A. E. Continetti *Phys. Rev. Lett.* **77**, 3335 (1996).
17. J. A. Davies, R. E. Continetti, D. W. Chandler, C. C. Hayden, *Phys. Rev. Lett.* **84**, 5983 (2000).
18. R. Kienberger *et al.*, *Nature* **427**, 817 (2004).
19. H. Niikura *et al.*, *Nature* **421**, 826 (2003).

MICROBIOLOGY

Pathogenic Bacteria Prefer Heme

Tracey A. Rouault

Almost all cells and organisms require iron to facilitate basic cellular processes such as respiration and DNA biosynthesis. Diverse and complex iron-uptake systems have evolved throughout the biological world to provide iron for numerous proteins, particularly those involved in energy capture and oxygen transport. Indeed, in parts of the great oceans, a complete lack of iron profoundly limits bacterial growth (*1*, *2*). In most environments, however, iron uptake is limited not by its absence, but by the fact that it is insoluble and inaccessible. To facilitate iron uptake, free-living bacteria and fungi have adopted several strategies. Some secrete compounds known as siderophores that solubilize and bind to an external source of iron with high affinity; the iron-siderophore complexes are then imported into the bacteria by specific transporter proteins. Others have uptake systems that import free iron salts directly (*3*, *4*). To combat microbial infections, animals strictly limit the availability of free iron in their blood and tissues. They do this by ensuring that iron in blood and secretions is carried by the high-affinity iron-binding proteins transferrin and lactoferrin, which create a primary line of defense against infection termed the "iron blockade" (*5*). The two ferric iron-binding sites of transferrin are rarely fully saturated, and an excess of unsaturated transferrin (apo-transferrin) ensures that free iron is virtually eliminated from blood. Pathogenic microorganisms, therefore, must overcome major obstacles if they are to acquire iron and thrive in their animal hosts. On page XXXX of this issue, Skaar and colleagues (*6*) explore how the pathogenic bacterium *Staphylococcus aureus* acquires the iron that it needs for growth in two different animal hosts. By growing the bacteria in the presence of the two principal iron sources found in mammals—diferric transferrin and the iron-porphyrin heme—the investigators show that most of the iron taken up by *S. aureus* during the initial phases of infection is obtained from heme.

Enhanced online at www.sciencemag.org/cgi/content/full/305/5690/1577

Although most bacteria are unable to grow in media in which the only iron sources are transferrin-iron and heme, some bacteria have developed strategies that enable them to obtain iron from these two sources (*7*, *8*). To determine whether *S. aureus* prefers transferrin-iron or heme as a source of iron, Skaar and colleagues labeled heme with ^{54}Fe and transferrin with ^{57}Fe, two rare and stable iron isotopes (*9*). After establishing that *S. aureus* grew well in medium supplemented with equimolar amounts of ^{54}Fe heme and ^{57}Fe transferrin, they analyzed the isotope content of cells using inductively coupled plasma–mass spectrometry (ICP-MS) at various times during growth. They discovered that *S. aureus* markedly prefers a source of iron derived from heme. Analysis of the *S. aureus* genome revealed that it encodes seven putative membrane transporter proteins that have some homology to known bacterial iron transporters. Using mutational inactivation and ICP-MS to monitor uptake of heme iron, the investigators identified a heme transport system in *S. aureus* composed of three genes

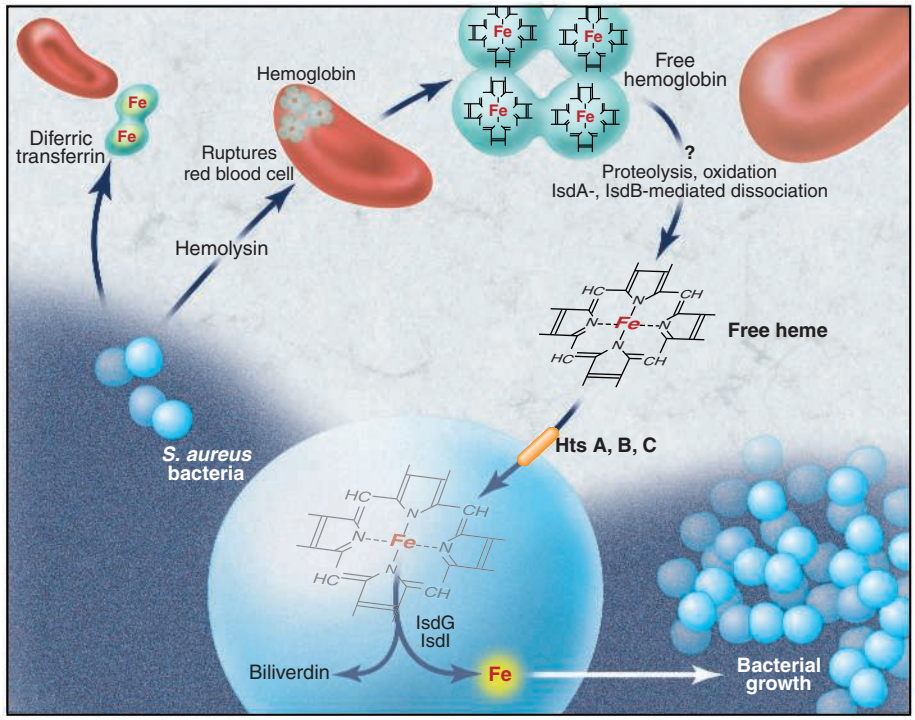

Bloodletting explained. *S. aureus* bacteria obtain most of the iron (Fe) that they need for growth in mammalian hosts from an iron-containing porphyrin ring called heme. *S. aureus* produces hemolysins that lyse red blood cells containing heme in the form of hemoglobin. It is unclear how the bacteria break down the released hemoglobin to heme, but the bacterial enzymes IsdA and IsdB may be involved. The bacteria then import heme via transporter proteins encoded by the *hts* ABC operon. The heme is then catabolized by the heme oxygenase-like enzymes, IsdG and IsdI, with the release of iron and biliverdin (a breakdown product of the porphyrin ring). The free iron released from heme is used to fuel further bacterial growth. The practice of bloodletting in the pre-antibiotic era may have been an attempt to starve pathogenic bacteria of the iron that they need for growth.

CREDIT: KATHARINE SUTLIFF/*SCIENCE*

The author is in the Section on Human Iron Metabolism, Cell Biology and Metabolism Branch, the National Institute of Child Health and Human Development, National Institutes of Health, Bethesda, MD 20892, USA. E-mail: trou@helix.nih.gov

(*hts* A, B, and C) that show homology with known heme transporter genes in other bacteria (*Yersinia enterocolytica* and *Corynebacterium diphtheriae*). Moreover, they identified a binding site for the bacterial ferric-uptake repressor protein, Fur, immediately upstream of the *Hts*A initiation codon, implying that the *hts* system is switched on in response to iron deficiency.

Although a heme-uptake system is of potential value, it would be of little use if *S. aureus* did not also possess mechanisms for liberating heme from the red blood cells where it is packaged in the form of hemoglobin (see the figure). *S. aureus* produces multiple hemolysins that breach the red cell membrane, promoting osmotic lysis of the cells (*10*). Once hemoglobin is released, it is not clear whether *S. aureus* liberates heme from hemoglobin with specific IsdB and IsdA enzymes (*11*), by secreting proteases like *Vibrio vulnificus* (*12*), or by oxidizing hemoglobin to promote its spontaneous dissociation into globin and heme (*13*). The bacteria then import the free heme, which is catabolized by the bacterial enzymes IsdG and IsdI in the same way as mammalian heme oxygenases catabolize heme, resulting in the release of iron from the heme porphyrin ring (*14*). Thus, *S. aureus* is a versatile pathogen that liberates heme from a vast erythrocyte repository, imports heme across its bacterial membrane, and degrades it to yield free iron (see the figure).

If the ability to take up iron is a potent virulence factor and the *hts* system is a major determinant of iron uptake, then mutational inactivation of the *hts* genes should attenuate *S. aureus* virulence. The authors analyze the pathogenicity of mutant and wild-type *S. aureus* in two model systems: the worm *Caenorhabditis elegans* and the mouse. Mutations in the *Hts* B and C genes markedly decreased mortality in worms infected 48 hours previously, and abscess formation markedly decreased in the livers and kidneys of mice 96 hours after intravenous injection of mutant compared to wild-type *S. aureus*. These results strongly imply that heme is the major source of nutrient iron in the critical early stages of *S. aureus* infection.

In response to bacterial infection and inflammation, humans restrict iron uptake and sequester iron within macrophages throughout the body. The peptide hormone hepcidin orchestrates these changes and causes a substantial decrease in serum iron levels (*15*). This hypoferremic response may be important for host defense by making iron even less available than usual to invading pathogens. The protective effects of hypoferremia may explain the mystery of why physicians embraced bloodletting as a therapeutic procedure for more than 2500 years. As recently as 1942, Sir William Osler's highly regarded medical textbook advocated bloodletting as a treatment for acute pneumonia: "To bleed at the onset in robust healthy individuals in whom the disease sets in with great intensity and harsh fever is good practice" (*16*). The development and widespread use of antibiotics in the mid-20th century obviated the need to employ questionable treatments such as bloodletting. However, the discovery that *S. aureus* depends on heme iron for growth in its animal hosts suggests that bloodletting in the pre-antibiotic era may have been an effective mechanism for starving bacterial pathogens of iron and slowing bacterial growth.

Bacteria continue to discover new ways to combat antibiotics and the race is on to discover new therapeutic targets to combat bacterial infection. The heme-uptake proteins of *S. aureus* may represent a new target for molecular therapy. Efficient lysis of erythrocytes increases the concentration of iron available to *S. aureus* by 100-fold compared to the normal concentration of transferrin-iron in serum. This liberated heme-iron apparently fuels the rapid growth of virulent *S. aureus* infection. Thus, pathogenic *S. aureus* applies principles of logic similar to those of accomplished bank robbers: They go for the heme, because that's where the iron is.

References

1. M. M. Mills, C. Ridame, M. Davey, R. J. La, R. J. Geider, *Nature* **429**, 292 (2004).
2. P. W. Boyd *et al.*, *Nature* **428**, 549 (2004).
3. S. C. Andrews, A. K. Robinson, F. Rodriguez-Quinones, *FEMS Microbiol. Rev.* **27**, 215 (2003).
4. V. Braun, *Front. Biosci.* **8**, s1409 (2003).
5. K. H. Rohde, D. W. Dyer, *Front. Biosci.* **8**, d1186 (2003).
6. E. P. Skaar, M. Humayun, T. Bae1, K. L. DeBord, O. Schneewind, *Science* **305**, xxx (2004).
7. C. N. Cornelissen, P. F. Sparling, *Mol. Microbiol.* **14**, 843 (1994).
8. B. C. Lee, *Mol. Microbiol.* **18**, 383 (1995).
9. T. Walczyk, F. von Blanckenburg, *Science* **295**, 2065 (2002).
10. M. M. Dinges, P. M. Orwin, P. M. Schlievert, *Clin. Microbiol. Rev.* **13**, 16 (2000).
11. S. K. Mazmanian *et al.*, *Science*, **299**, 906 (2003).
12. Y. Nishina, S. Miyoshi, A. Nagase, S. Shinoda, *Infect. Immun.* **60**, 2128 (1992).
13. G. B. Brittenham, in *Iron Metabolism in Health and Disease* (Saunders, New York, 1994), pp. 31–62.
14. E. P. Skaar, A. H. Gaspar, O. Schneewind. *J. Biol. Chem.* **279**, 436 (2004).
15. T. Ganz, *Blood* **102**, 783 (2003).
16. N. G. Schneeberg, *Trans. Stud. Coll. Physicians Phila.* **24**, 157 (2002).

MICROBIOLOGY

Noninherited Resistance to Antibiotics

Bruce R. Levin

As notorious as they may be, bacteria with inherited resistance to antibiotics are not the only reason that antibiotics fail and may not even be the major reason, at least not yet. A contribution to the humbling of these "wonder drugs" is the fact that growing populations of bacteria do not just die off when confronted with bactericidal antibiotics. Instead, their rates of mortality decline with time, and viable antibiotic-sensitive cells can be recovered even after hours of exposure to the drug (see the figure, panel A) (*1*). This phenomenon of declining sensitivity (noninherited resistance) is well established for different species of bacteria and for different classes of antibiotics (*2*–*4*). Variously called "bacterial persistence" (*5*), "phenotypic tolerance" (*6*), or "adaptive resistance" (*7*), the phenomenon remains a mystery with respect to its mechanism as well as its contribution treatment failure.

One mechanism postulated to account for the declining sensitivity and survival of bacteria confronted with bactericidal antibiotics is that growing populations of genetically identical bacteria continually generate subpopulations that are less sensitive to killing by antibiotics because they either are not growing or are dividing at very low rates (*8*). On page XXXX of this issue, Balaban *et al*. provide evidence for the existence of these refractory bacterial subpopulations and explain how they may account for the persistence of antibiotic-sensitive bacteria (*9*). Meanwhile, on page YYYY, Miller *et al*. present a mechanism by which this kind of noninherited resistance to antibiotics can be generated. This mechanism unexpectedly involves the SOS response, which blocks cell division during the repair of DNA damage (*10*).

Balaban and colleagues used a really cool combination of microfluidics and optical microscopy to make intimate movies of the replication of individual *Escherichia coli* bacteria, under normal conditions and when treated with the antibiotic ampicillin. In this way, the investigators were able to distinguish at least two distinct cell types in exponentially growing clones of *E. coli*: "nor-

The author is in the Department of Biology, Emory University, Atlanta, GA 30322, USA. E-mail: blevin@emory.edu

mal" rapidly dividing cells and slowly dividing "persisters." By combining mathematical modeling, data fitting, and competition experiments, they present a compelling argument that the decline in the mortality rate of growing populations of *E. coli* exposed to ampicillin can be attributed to switching from a normal to a persister phenotype. Ampicillin treatment enriches the more antibiotic-tolerant persister subpopulations, thereby reducing the average susceptibility of the population to ampicillin.

In a complementary study, Miller and co-workers used classy molecular genetics to show that ampicillin (as well as some, but not all, other β-lactam antibiotics) induces an SOS response in *E. coli* that halts cell division. They demonstrate that ampicillin induces a temporary block in *E. coli* cell division by inactivating a penicillin-binding protein, thereby activating the DpiBA two-component signal transduction system that regulates not only transcription but also DNA replication. The result is the production of an ampicillin-tolerant subpopulation of bacteria that is functionally similar to the persisters observed by Balaban and colleagues.

Although both sets of experiments used *E. coli* and ampicillin, I don't believe the two sets of results present different aspects of a single process. Rather, I propose that they describe two mechanisms that could operate synergistically to produce the same result: bacterial subpopulations that are tolerant to antibiotics. In accord with the phenotypic switch hypothesis (but unlike SOS induction), tolerant subpopulations can be generated in the absence of ampicillin. Whether these processes are in fact different could be tested genetically by ascertaining whether the genes needed for induction of the SOS response—*dpiA*, *recA*, and *lexA*—are required for the production of the Balaban *et al.* persisters. Of course, it is possible that these bacterial persisters are the product of stochasticity (leakiness) in the induction process (*11*). Whether produced constitutively or stochastically, persister populations should be enriched by all bactericidal antibiotics that are ineffective against slowly dividing or nondividing cells.

From the perspective of classical genetics, phenotypic variation in genetically homogeneous populations of the sorts considered in these studies is an inconvenience. Who wants to deal with characters that are leaky, incompletely penetrant, or variable in their expressivity? On the other hand, from a clinical, ecological, and evolutionary perspective, such characters raise important as well as intriguing questions.

Although the phenomena of bacterial persistence in vitro and antibiotic tolerance in vivo are well established (*12*), they have been largely ignored in the "rational" design of antibiotic treatment protocols (*13*). In theory, the declining rates of mortality and the "tail" observed in antibiotic kill curves (see the figure, panel A) could have a substantial effect on treatment efficacy. Initially, the density of a susceptible bacterial population is cut back by the antibiotic treatment, but, as time elapses, increasing fractions of the population become refractory to that drug. When the concentration of the antibiotic wanes between doses, the bacterial population becomes increasingly sensitive, but that may not be sufficient for the antibiotic to clear the infection. This can be seen with a computer simulation of a simple model of antibiotic treatment (*3*, *4*) that includes the phenotypic switching modeled by Balaban *et al*. (see the figure, panel B**)**. Similar results have been obtained with a model of antibiotic-mediated induction of the tolerant state in bacteria akin to that observed by Miller *et al.* (*1*).

The reports by Balaban, Miller, and their colleagues remind us once again that eukaryotes and little-studied bacteria, such as streptomyces and myxobacteria, are not the only organisms that undergo cellular differentiation. Spores and the stationary phase of growth are differentiated cellular states that enable bacteria to survive resource deprivation and other hardships. One interpretation of the two new studies is that cellular differentiation survival mechanisms akin to those induced during times of famine operate during times of feast.

It is easy to concoct just-so stories to explain the evolution of a mechanism that, like the SOS response, produces quiescent cells that are refractory to lethal agents. Yet it seems unlikely that ampicillin was the original selective force responsible for the evolution of the induction mechanism observed by Miller and colleagues. A bigger challenge to those in the evolution business is to account for the generation of lower fitness cell types in the absence of antibiotics, when, like the persisters of Balaban *et al*., they do not provide an advantage to the collective. Then again, just like people, bacteria do some seemingly perverse things that are not easy to account for by simple stories of adaptive evolution (*14*).

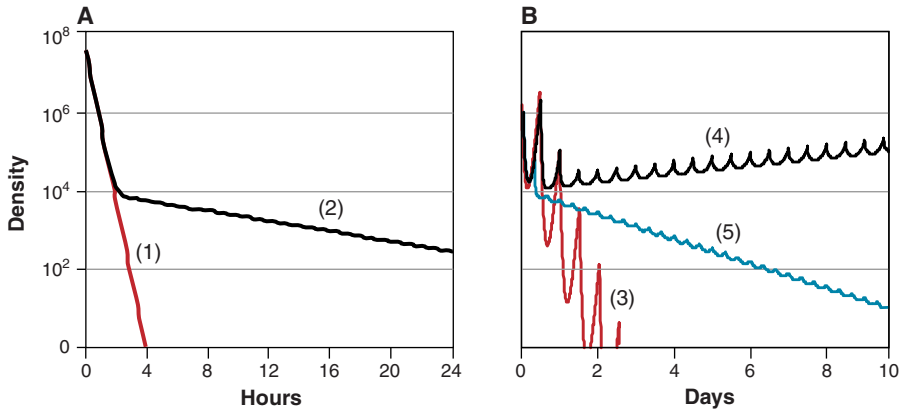

Bugs bite back. Computer simulations map changes in the density of a viable bacterial population exposed to an antibiotic. (**A**) Kill curve over time for a sensitive bacterial population confronted with a constant concentration of a bactericidal antibiotic: (1) the exponential decline we would like, (2) the declining rate of mortality and tail-off that actually occur. (**B**) Simulation of antibiotic treatment of a bacterial infection with the kill curve depicted in (A) but with an exponentially decaying antibiotic that is periodically replenished by a fixed dose every 8 or 12 hours: (3) no phenotypic switching, (4 and 5) phenotypic switching with antibiotic doses administered every 12 and 8 hours, respectively.

References and Notes

1. The mathematical models, computer simulations, and parameter values used to generate these figures and explore these dynamics are described at www.eclf.net (Tolerance models). The Berkeley Madonna software package used for these simulations can also be accessed from this Web site.
2. E. Gradelski, L. Valera, B. Kolek, D. Bonner, J. Fung-Tomc, *Int. J. Antimicrob. Agents* **18**, 43 (2001).
3. R. R. Regoes *et al.*, unpublished data.
4. C. Wiuff *et al.*, unpublished data.
5. W. B. Bigger, *Lancet* **244**, 497 (1944).
6. E. Tuomanen, A. Tomasz, *Scand. J. Infect. Dis. Suppl.* **74**, 102 (1990).
7. M. L. Barclay, E. J. Begg, S. T. Chambers, *Antimicrob. Agents Chemother.* **36**, 1951 (1992).
8. R. C. Massey, A. Buckling, S. J. Peacock, *Curr. Biol.* **11**, 1810 (2001).
9. N. Q. Balaban, J. Merrin, R. Chait, L. Kowalik, S. Leibler, *Science* **305**, XXXX (2004); published online 12 August 2004 (10.1126/science.1099390).
10. C. Miller *et al.*, *Science* **305**, YYYY (2004); published online 12 August 2004 (10.1126/science.1101630).
11. M. B. Elowitz, A. J. Levine, E. Siggia, P. Swain, *Science* **297**, 1183 (2002).
12. H. Eagle, R. Fleischman, A. D. Musselman, *Ann. Intern. Med.* **33**, 544 (1950).
13. G. L. Drusano, *Nature Rev. Microbiol.* **2**, 289 (2004).
14. K. Lewis, *Microbiol. Mol. Biol. Rev.* **64**, 503 (2000).

15. Dedicated to the memory of John A. Barrett, a friend and the founder of the *Ec*LF (*E. coli* Liberation Front). I thank R. Regoes, C. Wiuff, and D. Rozen for helpful comments. Supported by NIH grants GM33782 and AI40662 and by the British Wellcome Trust (IPRAVE project).

Asymmetric Cochlear Processing Mimics Hemispheric Specialization

Y. S. Sininger[1]* and B. Cone-Wesson[2]

The left hemisphere generally takes precedence over the right in processing of speech sounds and performance of sophisticated language functions, whereas the right hemisphere is primary in the processing of tonal stimuli and music. Converging evidence from diverse methodologies has revealed that left and right auditory regions may be individually specialized for processing of sounds based on acoustic properties. Rapidly changing signals are processed preferentially in auditory areas of the left hemisphere because of enhanced temporal resolution, and tonal stimuli are best processed in auditory areas of the right, reflecting specialized abilities for spectral resolution (*1*). Behaviorally, reaction time is faster and stimulus identification is more accurate when a subject's right ear is presented with speech-type stimuli or when the left ear is presented with tonal information (*2*). The strength of crossed pathways from the ear to the auditory cortex is credited with the ear-advantage phenomenon. Asymmetry of function at the level of the ear has not generally been considered in this process.

Otoacoustic emissions (OAEs) reflect activity from active mechanisms of the outer hair cells that serve to amplify acoustic energy in the cochlea (*3*). OAEs require no innervation, but they are modulated by the medial olivocochlear efferent system in the brainstem (*4*). A transducer fit into the ear canal provides sound to activate an OAE. Energy generated in the cochlea is transmitted back into the middle ear and ear canal and is measured by a microphone in the transducer-probe assembly. Transient-evoked otoacoustic emissions (TEOAEs) are stimulated by clicks presented in rapid succession. Distortion-product otoacoustic emissions DPOAEs) are evoked by pairs of continuous tones. The amplitudes or signal-to-noise ratios (SNRs) of TEOAEs and DPOAEs reflect the magnitude of active cochlear amplification mechanisms, although by slightly different processes (*5*).

DPOAEs to a set of tone pairs and TEOAEs generated by clicks (80/s) were obtained from a pool of 3011 infants. Data were further selected to include only those infants from whom clear TEOAE and DPOAE responses (with an average SNR of 3 dB or greater) were obtained in both ears. This reduced the pool to 1593 infants for whom data was analyzed. Details of our methods have been published (*6*, *7*) and are available online (*8*). The test order for ear and OAE type was randomized. SNRs from frequency regions from 1500 through 4000 Hz were averaged for both types of OAE.

Figure 1 reveals that the average TEOAE SNR generated by clicks was larger when elicited in right ears, and the average DPOAE generated by tones was larger from left ears. This pattern of TEOAE result was seen in 855 (53.6%) of infants, and the DPOAE pattern was seen in 825 (51.75%). When the two measures are combined, 324 infants demonstrate the average trend and 241 demonstrate the opposite (larger TEOAEs in the left ear and DPOAEs in the right). The remaining infants showed mixed trends. Repeated measures analysis of variance (*8*) revealed significant ear-by-OAE-type interaction ($P < 0.0001$). No significant interaction was found between ear and sex. Post hoc tests found significant ear effects for DPOAEs ($P = 0.0010$) and for TEOAEs ($P = 0.0013$). The results indicate a tendency for the cochlea to provide greater amplification to stimuli that will also be preferentially processed in the auditory areas of the contralateral hemisphere. Others have found larger average TEOAEs in the right ear of neonates (*9*), but no clear ear difference has been reported for DPOAEs.

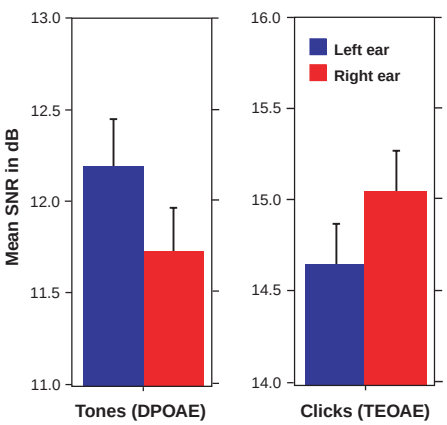

Fig. 1. Mean OAE SNR in response to tone pairs (f1 and f2) presented with f1 = 65 and f2 = 50 dB sound pressure level (SPL) tones, and in response to 80-dB peak SPL clicks. Error bars represent the 95th percentile range.

Both speech and tonal stimuli have been shown to elicit larger evoked potential activity over the left hemisphere in 4-month-old infants (*10*). This study indicates that stimulus-guided asymmetry is present at the level of the cochlea before it is evident in the auditory cortex. The developmental time course of ascending and descending neural pathways connecting the ear to the auditory regions of the cortex is complex. Moore (*11*) has found that afferent connections in the auditory system between the brainstem and cortex are immature at birth. The time of development of descending neurons from the cortex to inferior colliculus is not established. Olivocochlear efferent neurons in the brainstem, however, are mature before birth (*12*) and have been shown to modulate the OAE in newborns (*13*). The stimulus-guided asymmetrical nature of OAEs in infants suggests that, at the early stages of auditory system development, initial processing of sound in the auditory system at the level of the cochlea and brainstem may serve to facilitate later development of hemispheric specialization for sound processing.

References and Notes

1. R. J. Zatorre, P. Belin, V. B. Penhune, *Trends Cognit. Sci.* **6**, 37 (2002).
2. D. Kimura, *Q. J. Exp. Psychol.* **16**, 355 (1964).
3. D. T. Kemp, *J. Acoust. Soc. Am.* **64**, 1386 (1978).
4. E. Veuillet, L. Collet, R. Duclaux, *J. Neurophysiol.* **65**, 724 (1991).
5. C. A. Shera, *Ear Hear.* **25**, 86 (2004).
6. S. J. Norton *et al.*, *Ear Hear.* **21**, 425 (2000).
7. M. P. Gorga *et al.*, *Ear Hear.* **21**, 400 (2000).
8. Materials and methods are available as supporting material on *Science* Online.
9. D. Aidan *et al.*, *Acta Oto-Laryngol.* **117**, 25 (1997).
10. G. Dahyaene-Lambertz, *J. Cognit. Neurosci.* **12**, 449 (2000).
11. J. K. Moore, *Ann. Otol. Rhinol. Laryngol. Suppl.* **189**, 7 (2002).
12. D. D. Simmons, Y Guan. J. K. Moore, *Audiol. Neurootol.* **4**, 311 (1999).
13. T. Morlet *et al.*, *Acta Oto-Laryngol.* **113**, 271 (1993).
14. We thank E. Ma, E. Guckert, and A. Schaedler for data collection and analysis and J. Moore, J. Jerger, M. Hyde, and T. Glattke for critical review. We also appreciate the participation of consortium members and of S. Norton and M. Gorga in the initial study design. Supported by the National Institute on Deafness and Other Communication Disorders.

Supporting Online Material
www.sciencemag.org/cgi/content/full/305/5690/1581/DC1
Materials and Methods
SOM Text
Tables S1 and S2
References and Notes

24 May 2004; accepted 27 July 2004

[1]Division of Head and Neck Surgery, University of California–Los Angeles, David Geffen School of Medicine, 62-132 Center for Health Science, Los Angeles, CA 90095–1624, USA. [2]Department of Speech, Language, and Hearing Sciences, University of Arizona, Post Office Box 210071, Tucson, AZ 85721, USA.

*To whom correspondence should be addressed. E-mail: ysininger@mednet.ucla.edu

Jupiter's Atmospheric Composition from the Cassini Thermal Infrared Spectroscopy Experiment

V. G. Kunde,[1]* F. M. Flasar,[2] D. E. Jennings,[2] B. Bézard,[3] D. F. Strobel,[4] B. J. Conrath,[5] C. A. Nixon,[1] G. L. Bjoraker,[2] P. N. Romani,[2] R. K. Achterberg,[6] A. A. Simon-Miller,[2] P. Irwin,[7] J. C. Brasunas,[2] J. C. Pearl,[2] M. D. Smith,[2] G. S. Orton,[8] P. J. Gierasch,[5] L. J. Spilker,[8] R. C. Carlson,[6] A. A. Mamoutkine,[6] S. B. Calcutt,[7] P. L. Read,[7] F. W. Taylor,[7] T. Fouchet,[3] P. Parrish,[7] A. Barucci,[3] R. Courtin,[3] A. Coustenis,[3] D. Gautier,[3] E. Lellouch,[3] A. Marten,[3] R. Prangé,[3] Y. Biraud,[3] C. Ferrari,[9] T. C. Owen,[10] M. M. Abbas,[11] R. E. Samuelson,[1] F. Raulin,[12] P. Ade,[13] C. J. Césarsky,[14] K. U. Grossman,[15] A. Coradini[16]

The Composite Infrared Spectrometer observed Jupiter in the thermal infrared during the swing-by of the Cassini spacecraft. Results include the detection of two new stratospheric species, the methyl radical and diacetylene, gaseous species present in the north and south auroral infrared hot spots; determination of the variations with latitude of acetylene and ethane, the latter a tracer of atmospheric motion; observations of unexpected spatial distributions of carbon dioxide and hydrogen cyanide, both considered to be products of comet Shoemaker-Levy 9 impacts; characterization of the morphology of the auroral infrared hot spot acetylene emission; and a new evaluation of the energetics of the northern auroral infrared hot spot.

Jupiter serves as an analog for the numerous extrasolar planets that have been detected; the formation and evolution of these are not well understood. The primary paradigm is Jupiter, which had a pronounced effect on the evolution of our system. An understanding of the processes governing the composition and distribution of chemical species in Jupiter's atmosphere is required to successfully understand the chemical composition of extrasolar planets. Additionally, it is important to study Jupiter in its own right, as a key member of the solar system. In the deep atmosphere, where pressures and temperatures are high, Jupiter's thermochemical furnace processes the approximately solar elemental composition by converting H atoms into molecular form (H_2) and reactive atoms (e.g., C, N, and O) into saturated hydrides (methane, CH_4; ammonia, NH_3; water, H_2O). Convection transports these molecules upward into the cooler regions, where H_2O, NH_4SH, and NH_3 condense to form clouds. Jupiter's chemical composition is also influenced by external sources of material. The most dramatic illustrations of this were the multiple impacts of comet Shoemaker-Levy 9 (SL9) in July 1994 (*1*–*5*).

The Composite Infrared Spectrometer (CIRS) (*6*) on the Cassini spacecraft is particularly well suited to study this broad range of gas molecules, whose origins are linked to internal thermochemistry, photochemistry, and impactor chemistry. During the Cassini spacecraft flyby of Jupiter between October 2000 and March 2001, CIRS remotely sensed the atmosphere of that planet with an unprecedented combination of spatial and spectral resolutions. CIRS consists of a pair of Fourier transform spectrometers, which together cover the spectral range from 10 to 1400 cm^{-1} with a spectral resolution up to 0.5 cm^{-1}. The far-infrared interferometer, covering 10 to 600 cm^{-1}, has a 4-mrad field of view on the sky; at Jupiter's closest approach (138 Jupiter radii), it subtended 0.3 of the planetary diameter.

The mid-infrared interferometer, covering 600 to 1400 cm^{-1}, consists of two 10-element linear arrays of 0.3-mrad pixels; at closest approach, they each subtended 0.02 of the planetary diameter, equivalent to 2.4° of latitude near the equator. A typical low-latitude jovian thermal emission spectrum, from observations centered between 20°S and 20°N, is shown in fig. S1. A summary of the major and minor atmospheric gases that have been detected in the CIRS spectra is given in table S1; included are the spectral regions where the gaseous signatures occur and brief comments on global characteristics of the gas.

Two new hydrocarbon species detected in Jupiter's stratosphere in the north and south auroral infrared hot spots are the methyl radical (CH_3) and diacetylene (C_4H_2) (Fig. 1). Both species are important to Jupiter's stratospheric photochemistry. The self-recombination of CH_3 leads to the formation of C_2H_6, whereas its reaction with H atoms re-forms CH_4. Thus, the efficiency of CH_4 photochemical destruction is governed by the fate of CH_3 (*7*). C_4H_2 is produced from C_2H_2 photochemistry and is a potential precursor molecule for stratospheric haze. CIRS has also detected a broad spectral feature in the 693 to 707 cm^{-1} region, at both high northern and southern polar latitudes (fig. S2). The origin of this feature is unknown. It has also been observed on Titan and may be due to haze from condensation of a stratospheric gas (*8*). The first identification of the rotational lines of CH_4, an already known species, is illustrated in fig. S3; these lines allow an independent estimate of the jovian tropospheric CH_4 abundance.

Stratospheric Hydrocarbons C_2H_6 and C_2H_2

In nonauroral regions of Jupiter's upper atmosphere (stratosphere), methane photolysis and ensuing photochemical processes create numerous short- and long-lived hydrocarbon species. The most abundant are C_2H_6 and C_2H_2. Until now, only one-dimensional models constrained by disk-averaged observations have been used to study photochemistry and vertical transport (*9*, *10*). These models

[1]Department of Astronomy, University of Maryland, College Park, MD 20742, USA. [2]NASA/Goddard Space Flight Center, Code 693, Greenbelt, MD 20771, USA. [3]LESIA, CNRS-UMR8109, Observatoire de Paris, 5 place Jules Janssen, F-91925 Meudon Cedex, France. [4]Johns Hopkins University, Department of Earth and Planetary Science, Baltimore, MD 21218, USA. [5]Department of Astronomy, Cornell University, Ithaca, NY 14853, USA. [6]Space Science and Applications, Inc., 5900 Princess Garden Parkway, Suite 300, Lanham, MD 20706, USA. [7]Atmospheric, Oceanic, and Planetary Physics, Clarendon Laboratory, Parks Road, University of Oxford, Oxford OX1 3PU, UK. [8]Jet Propulsion Laboratory, 4800 Oak Grove Drive, Pasadena, CA 91109, USA. [9]CEA Saclay, Service d'Astrophysique, 91191 Gif-sur-Yvette Cedex, France. [10]University of Hawaii, Institute of Astronomy, 2680 Woodlawn Drive, Honolulu, HI 96822, USA. [11]NASA/Marshall Space Flight Center, SD50, Huntsville, AL 35812, USA. [12]LISA, Université de Paris 7 and 12, CNRS–UMR 7583, 61 Avenue General de Gaulle, 94010 Creteil Cedex, France. [13]School of Physics and Astronomy, Cardiff University, 5 The Parade, Cardiff CF24 3YB, UK. [14]European Southern Observatory, Karl-Schwarzschild-strasse 2, 85748 Garching bei Muenchen, Germany. [15]Gesamthochschule Wuppertal, Department of Physics, Gausstrasse 20, 5600 Wuppertal 1, Germany. [16]Instituto di Astrofisica Spaziale–CNR, Area della recerca di Tor Vergata, via del Fosso del Cavaliere 100, Rome, I-00133 Italy.

*To whom correspondence should be addressed. E-Mail: Virgil.G.Kunde.1@gsfc.nasa.gov

indicate that ethane is mostly produced by the self-recombination of methyl radicals (CH_3), directly formed from methane photolysis. C_2H_6 is relatively unreactive and efficiently shielded by CH_4 from photolysis, so it has a long photochemical lifetime, exceeding 100 years in the stratosphere. This makes it an excellent chemical tracer of atmospheric motion. To first order, its vertical distribution is a balance between photochemical production and downward transport to the troposphere.

Acetylene is produced mainly from the photodissociation of ethylene and is lost through photolysis and H-atom reaction. Its photochemical lifetime is approximately a year, much shorter than that of ethane. The variations of C_2H_6 and C_2H_2 abundances with latitude depend on photochemical and dynamical processes. These variations give insight into meridional transport in the stratosphere, which is poorly understood. Observations of Jupiter by the thermal infrared spectrometers (IRIS) (*11*, *12*) on the Voyager spacecraft were used in an early attempt to obtain latitudinal distributions of C_2H_6 and C_2H_2.

CIRS spectra of Jupiter, with much better sensitivity and spatial resolution than Voyager, have been analyzed for the latitude variations of these species. The C_2H_6 and C_2H_2 line intensities in the stratosphere are functions of the abundance profiles of the species, the temperature profile, and the air-mass factor [1/cos (emission angle)] (*13*). The line intensities (Fig. 2) have been corrected to first order for the last two effects. To properly model the optical thickness of the lines, the corrections for air-mass variations were made with a radiative transfer model. The derived C_2H_6 line intensities, roughly proportional to column abundance, are essentially constant with latitude, which indicates a uniform C_2H_6 profile from equator to pole. As the C_2H_6 production rate declines toward the poles, the constancy of the abundance profile suggests that meridional transport is much faster than the loss of C_2H_6 by vertical transport (>100 years). In contrast, the C_2H_2 Q-branch intensity is reasonably symmetric in latitude but drops appreciably from the equator to 70°N or S; the corresponding decrease of the C_2H_2 column abundance reaches a factor of ~3 [corresponding to a factor of 2 in intensity (*13*)] and varies with the local solar flux (Fig. 2). This result suggests that the latitudinal distribution of C_2H_2 is mostly governed by local photochemistry and that its lifetime (~1 year) is much shorter than the characteristic time for horizontal transport. The differences between the latitude structure of the two hydrocarbons thus reflect the large difference in their lifetimes and indicates that the characteristic time constant for horizontal transport is on the order of 10 years.

Hydrogen Cyanide and Carbon Dioxide

In July 1994, SL9 injected large quantities of N-, O-, and, S-bearing molecules into Jupiter's stratosphere near 45°S. Substantial amounts of hydrogen cyanide (HCN), carbon monoxide (CO), and carbon monosulfide (CS), were produced in the ensuing shock chemistry and subsequent photochemistry (*1*–*4*). Carbon dioxide (CO_2), presumably a secondary product of the SL9 collision

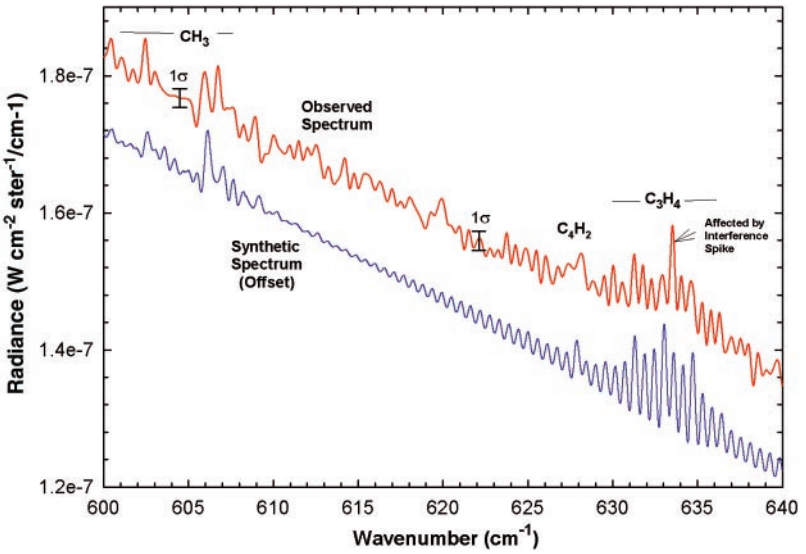

Fig. 1. Observed and synthetic average spectra from the north auroral infrared hot spot showing the two new gaseous detections in Jupiter's stratosphere, the methyl radical (CH_3) and diacetylene (C_4H_2). The spectral resolution is 0.26 cm^{-1} unapodized. This average consists of 2228 individual spectra at high emission angle from 10 detectors for the time period December 2000 to January 2001. For comparison, a synthetic Jupiter spectrum (offset from the observed spectrum) containing the two species is also shown to aid in validating the identifications. The CH_3 signature is most evident in its strong Q branch at 606 cm^{-1}, supported by several weaker Q branches from 603 to 606 cm^{-1}. The 1σ error bar indicates detection at the 2σ to 3σ level. CIRS has also detected C_4H_2 via its Q branch at 628 cm^{-1}, at the 1σ to 2σ level.

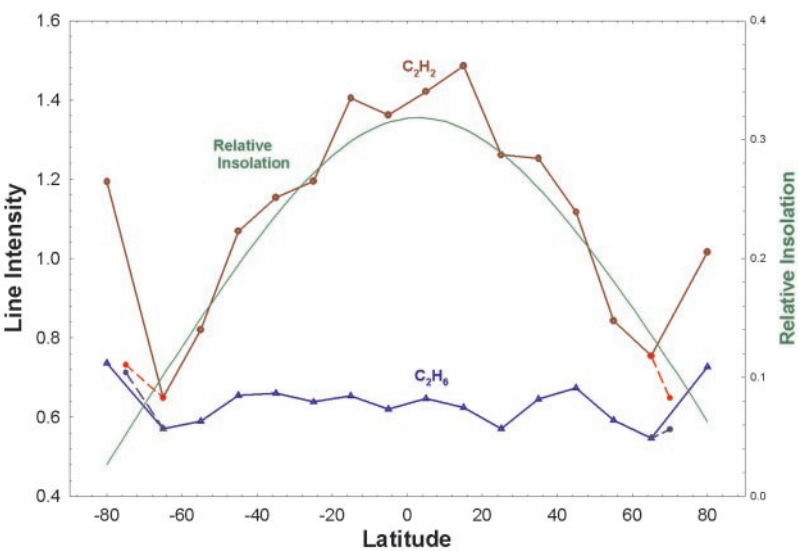

Fig. 2. Latitudinal variation of the mean line intensity (12 Q-branch multiplets selected in the range 806 to 836 cm^{-1}) for C_2H_6 and of the Q-branch intensity at 729.3 cm^{-1} for C_2H_2. High spectral resolution data sets (0.26 cm^{-1} unapodized) were averaged for 10° wide latitude bins. These stratospheric line intensities have been corrected for limb brightening and thermal effects, and are increasing functions of the column abundance of the species (*13*). Exceptions are the data points at the highest latitudes (80°S and 80°N), which are enhanced by the temperature increase in the auroral regions, especially as concerns C_2H_2. The dashed line corresponds to smaller selections, which exclude the auroral longitudes and do not show this enhancement as much. The CIRS data indicate that the C_2H_6 stratospheric column abundance is approximately constant from 70°S to 70°N, whereas the C_2H_2 column abundance decreases uniformly from the equator to high latitudes by a factor of about 3.

formed from the photochemical evolution of CO and H_2O, was detected by the Infrared Space Observatory (ISO) Short-Wavelength Spectrometer observations of the 667 cm^{-1} band of CO_2, also at low spatial resolution (*14*). Millimeter observations have tracked the subsequent transport of HCN, CS, and oxygen-bearing compounds from the impact sites, albeit with limited spatial resolution (*5*).

CIRS has mapped the Q-branch emission features of HCN and CO_2 at 712 and 667 cm^{-1} (figs. S4 and S5), at a much higher spatial resolution than ISO. These emissions are optically thin, and the line intensities are proportional to the column abundance of the species, the air-mass factor, and the Planck function value at the average pressure levels where they reside [~0.2 mbar; (*5*)] (*13*). The observed HCN and CO_2 intensities, corrected for the last two effects, are thus proportional to the column densities (Fig. 3). Because the emissions are optically thin, information on their vertical distribution cannot be directly inferred.

The distributions of HCN and CO_2 with latitude are very different (Fig. 3 and fig. S6). HCN peaks near 45°S and has a broader distribution. It decreases smoothly toward the north up to ~50°N; at latitudes higher than 50°N and 50°S, the abundance falls off abruptly to one-third as much at 65° as at 45°(N or S). This is consistent with ground-based infrared observations of individual HCN lines, which exhibit a maximum abundance around 45°S and a smooth decrease northward to 60° N (*15*). The latitudinal distribution of CO_2, however, is much narrower, and its maximum lies southward of 60°S, decreasing abruptly northward of 50°S. Northward of 30°S, it is only marginally detectable, except at high northern latitudes (70°N to 90°N). The polar enhancements suggest a link with the auroral regions.

HCN latitudinal distribution. Once produced by shock chemistry during the SL9 impacts, HCN is stable (*4*, *15*, *16*) and almost inert in the stratosphere, so that it is a tracer of atmospheric motions (*5*). In fact, the peak abundance is still at the impact latitude, and the total HCN mass in Jupiter's stratosphere observed between 1995 and 2000 (*5*, *15*) is comparable to what was inferred right after the SL9 impacts in 1994 (*2*). The sharp falloff of HCN observed at high latitudes cannot be due to chemistry driven by particle bombardment in the auroral regions. Ion chemistry does not break the CN bond but only efficiently recycles HCN (*17*, *18*). Thus, a dynamical explanation is the most logical explanation, and HCN should provide a powerful constraint on mixing at mid-latitudes in the southern hemisphere by meridional winds and horizontal wave-induced diffusion. The CIRS observations yield a maximum 5° latitudinal shift in the location of peak abundance from the impact latitude, a behavior consistent with a meridional velocity of zero and a spreading due to diffusion. The equatorward spread of HCN is then mostly by diffusive transport.

If horizontal diffusion were constant with latitude, the SL9-produced HCN would maximize at the south pole (*14*). The most probable dynamical reason for the southward decrease is the inhibition of wave-induced diffusive mixing of HCN in the presence of strong circumpolar winds (vortices) in Jupiter's polar regions. This effect is analogous to the polar vortex that produces a confinement vessel for the Antarctic ozone hole from mid-latitude air in Earth's stratosphere and dynamically isolates polar regions from lower latitudes (*19*). Latitudinal temperature gradients measured by CIRS in Jupiter's upper stratosphere indicate the existence of strong polar vortices near 65°N and 65°S (*20*), yielding jet streams with eastward velocities of about 20 m s^{-1} or higher near 1 mbar. Ground-based observations at the Infrared Telescope Facility (*21*) confirm the presence of a north polar vortex.

CO_2 latitudinal distribution. If the CO_2 is simply a product of the SL9 impacts, the observed shift of its maximum column abundance from the SL9 impact sites (45°S) to latitude 60°S over 6.5 years (the time between the impacts and the CIRS observations) suggests a southward velocity of ~12 cm s^{-1} and/or constant horizontal diffusion. However, if both HCN and CO_2 have an SL9 origin and are similarly distributed in altitude, this is difficult to reconcile with the constraint on meridional transport implied by the HCN distribution. Under these assumptions, HCN and CO_2 would exhibit the same latitudinal behavior. This strongly suggests that some non-SL9 or post-SL9 chemistry is involved. One possible chemical explanation for the high-latitude abundances of CO_2 is the precipitation of energetic oxygen ions in the auroral regions (*22*), leading to the formation of H_2O, OH, and eventually CO_2 from the OH oxidation of CO. The low abundance in the northern auroral region relative to the southern auroral region suggests that SL9 is the origin of the CO, which is converted partially to CO_2.

The difference in the latitude variation of these two species is surprising and difficult to understand. Atmospherics dynamics clearly play a role in how these two species are distributed with latitude; other effects, such as auroral particle precipitation, different photochemistry, and/or different altitude distributions, may help explain why the latitude variation of these species differs. Unraveling the seemingly inconsistent latitudinal distributions of HCN and CO_2 will require knowledge of their vertical profiles, as well as the height-latitudinal distributions of both CO, the primary carrier of SL9 elemental oxygen (O), and H_2O, which photolytically yields the OH that oxidizes CO to CO_2.

Auroral Infrared Hot Spots

Jupiter's polar auroral stratosphere is driven by the deposition of energetic magnetospheric electrons and ions, which heats the atmosphere, enhances the abundances of some hydrocarbons by ion-induced chemistry, and increases the visibil-

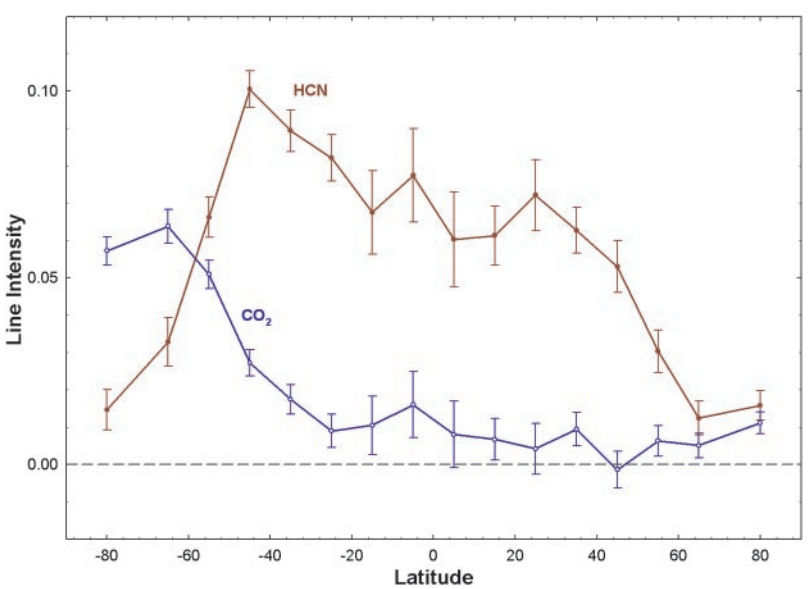

Fig. 3. Latitudinal distribution of the HCN and CO_2 column abundances as determined from the intensity for the Q-branch features at 712 and 667 cm^{-1}, respectively. High spectral resolution data sets (0.26 cm^{-1} unapodized) were averaged for 10° wide latitude bins. The intensities are proportional to the column abundances of the species. The original source of these two species is thought to be the SL9 impact in 1994, around 45°S. The differences in the latitudinal variation of these two species are unexpected and not understood.

ity of all stratospheric species in the thermal infrared by elevating the ambient temperatures (*23*–*26*). Spatial variations in the constituent emissions within the auroral region reflect the complex interaction of charged particle impact processes, ion and neutral chemistry, the intense heating associated with direct particle energy deposition and Joule dissipation, and the dynamical transport that it generates. The high spectral and spatial resolution measurements of the auroral regions obtained by CIRS show that the emissions of many hydrocarbons (e.g., C_2H_2, C_6H_6, C_2H_6, CH_4 in Fig. 4; CH_3, C_4H_2, C_3H_4 in Fig. 1; C_2H_4; in fig. S7) within the auroral infrared hot spots are enhanced relative to the surrounding ambient polar atmosphere. These spectral enhancements arise as a result of differences in temperature and/or composition in the hot spot relative to its surroundings.

These enhancements in the CH_4 band (Fig. 4B) are due to differences in temperature; the CIRS temperature enhancement is of the order 20K at 1 mbar (*20*), which could produce the emission enhancement. The enhancements shown in Fig. 4A for the derivative hydrocarbons arise because of differences in temperature and/or composition. A large temperature enhancement in the upper stratosphere, along with a small variation in the hydrocarbon abundances, has been found to fit the Voyager data (*25*).

Auroral infrared hot spot morphology—C_2H_2. The global emission enhancement associated with C_2H_2 has been mapped from the strong Q-branch emission feature at 729 cm^{-1} (Fig. 5). The two localized regions of enhanced emission that stand out at high northern and southern latitudes correspond to the auroral infrared hot spots that have been observed by ground-based telescopes (*23*) and Voyager IRIS (*24*). The north hot spot C_2H_2 emission peaks at 73°N latitude and 180°W longitude and covers an area of about 2.5×10^8 km^2 (at half maximum), with the same morphology as the CH_4 emission enhancement (*20*). Although the vertical extent of the heated regions is not precisely determined, temperature retrievals from CIRS spectra indicate that the warm anomalies associated with the auroral hot spots lie above the 4-mbar level (*20*).

The morphology of the CIRS C_2H_2 spots differs from that of the jovian aurorae described at ultraviolet, visible, and near infrared wavelengths (*27*–*31*). Instead, the CIRS auroral hot spots coincide with the footprints of the jovian polar cusps identified with the Hubble Space Telescope in the far ultraviolet (FUV) at very high latitude (*32*, *33*) and are also detected by x-ray emissions with the Chandra observatory (*34*). These features are fixed in magnetic local time near noon and are localized (5×10^5 to 5×10^6 km^2), but they display a slow motion as Jupiter rotates, which may explain the larger extent of the infrared spot. In addition, the extinction by hydrocarbon absorption of the FUV spectra is much larger in the polar cusp (spot) than in any other auroral feature, especially shortward of ~145 nm (*33*), which indicates large CH_4 column densities, up to several times 10^{17} cm^{-2}, above the auroral source. This indicates that the charged particles responsible for the FUV auroral polar cusps penetrate deeply into the CH_4/C_2H_2 hydrocarbon layer and may trigger the C_2H_2 auroral hot spots (Fig. 5). Based on the FUV spectra, either the emissions in the C_2H_2 auroral hot spots are excited by very energetic charged particles (200 keV if electrons, tens of MeV if protons), which deposit the bulk of their energy in the ~2 to 5 μbar pressure level, or the energy deposition in the upper atmosphere is so large (100 ergs cm^{-2} s^{-1}) that upward vertical mixing of the CH_4/C_2H_2 hydrocarbon layer is appreciably increased. In both cases, this is expected to result in changed chemical reactions and/or heating near or below pressure levels of a few microbars.

Auroral infrared hot spot energetics. The higher spectral and spatial resolution of the CIRS spectra allows an accurate analysis of the outgoing infrared power from the northern auroral infrared hot spot. The northern auroral hot spot spectra were obtained on 8 January 2001, at the highest spatial resolution, during the closest approach to Jupiter. The geometrical parameters associated with the average auroral spectrum inside the north hot spot, and the average nonauroral spectrum from the surroundings outside the spot, are summarized in table S2. The spectra selected to average inside the hot spot represent the maximum outgoing infrared hydrocarbon emissions observed by CIRS during the Ju-

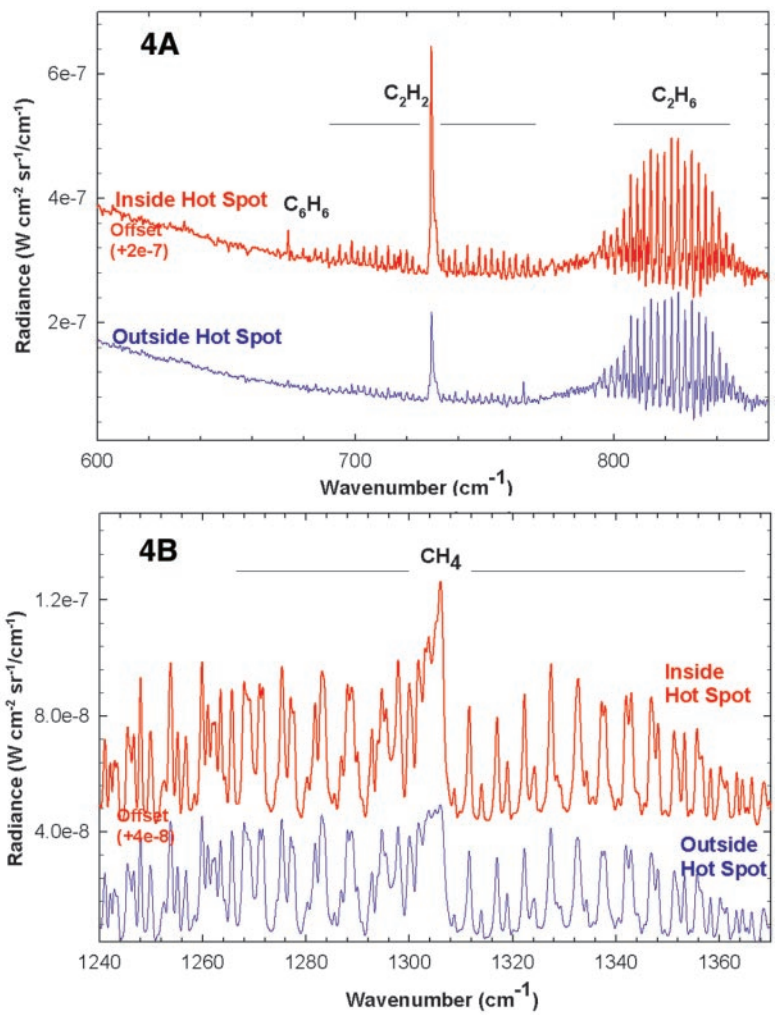

Fig. 4. Comparison of high spectral resolution (0.52 cm^{-1} apodized) radiance measurements in the northern auroral infrared hot spot to those outside the spot, showing enhanced hydrocarbon emissions. Both spectral averages correspond to the same latitude range (65°N to 85°N). These spectral emissions originate in the warm stratosphere, at altitudes from ~5 mbar to ~1 μbar. These enhancements arise as a result of differences in temperature and/or composition from the hot spot to its surroundings. (**A**) Enhanced emissions are evident for the stratospheric hydrocarbons C_6H_6, C_2H_2, and C_2H_6. The number of spectra in the average is 98 inside the hot spot and 277 outside. (**B**) Enhanced emissions are evident for stratospheric CH_4. The number of spectra in the average is 64 inside the hot spot and 197 outside.

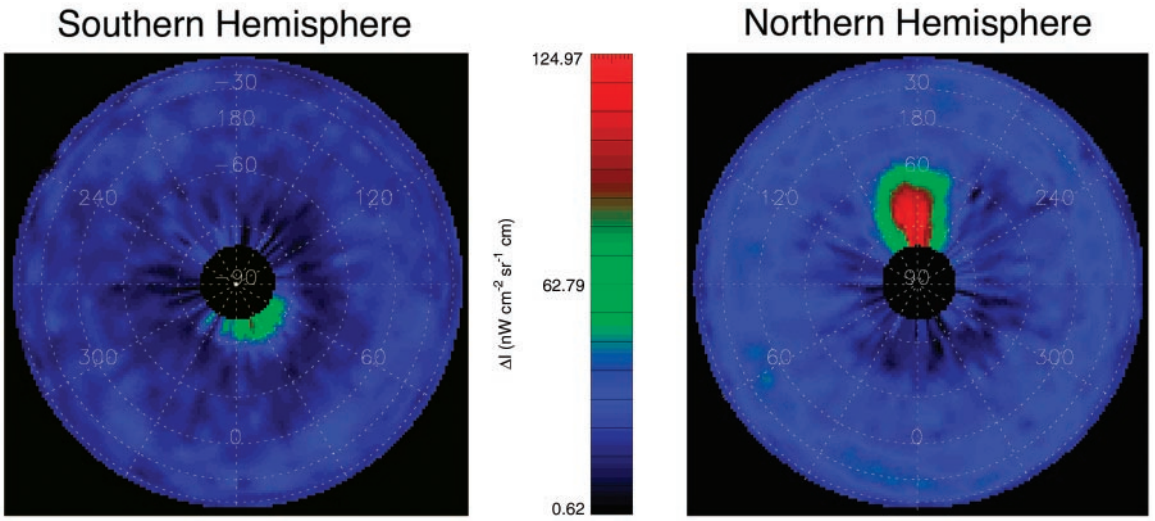

Fig. 5. Polar projection maps of emission from the strong Q branch of C_2H_2 at 729 cm^{-1}. These 3 cm^{-1} data were obtained between 31 December 2000 and 1 January 2001, a time period centered on Jupiter's closest approach. The north infrared auroral hot spot (right panel) is seen in the 65°N to 85°N (planetographic) latitude and 160°W to 190°W longitude ranges. The south infrared auroral hot spot (left panel) is seen in the 75°S to 85°S and 0°W to 70°W ranges. The locations of the enhancements coincide approximately with the Hubble Space Telescope FUV features identified as the footprints of the jovian polar cusps.

piter flyby. Integration over the radiance differences (fig. S8, A and B) yields an average infrared excess flux of 6 to 11 $\times$ 10^{-6} W cm^{-2} for a total excess outgoing spot power of 1.5 to 3 $\times$ 10^{13} W, similar to the determination from Voyager IRIS (*25*). For the hot spot energy balance, the excess outgoing power needs to be compared with the incoming energy flux. The power input due to precipitating energetic particles, as derived from the FUV spectra, is at most $\sim 10^{12}$ W (*35*–*37*), well below the total outgoing infrared auroral power derived above.

Previous work has also suggested that direct heating from particle precipitation alone cannot account for the infrared emissions (*25*). Joule heating is a viable alternative to supply the missing outgoing power. To account for the high energy suggested by FUV and x-ray observations, the polar cusp precipitating particles need to be strongly accelerated before they penetrate the atmosphere. This suggests that strong field-aligned (Birkeland) currents may flow along cusp magnetic field lines and close as a Pedersen current across field lines in the ionosphere near the altitude of maximum ion conductivity (which is approximately the altitude of maximum energy deposition and ionization and thus within the hydrocarbon layer). Because the ionosphere has finite resistivity, significant Joule heating accompanies the precipitation process. An estimate of the Joule power released exists for another auroral feature, the main oval (*38*). If we assume that similar currents can flow along cusp field lines, and if we scale by the relative size of the features, some 0.5 to 5 $\times$ 10^{13} watts of Joule heating could be released in the cusp. On the other hand, using predictions from a new model of the jovian cusp processes (*39*), one can estimate this power to vary in the range 10^{11} to 10^{15} watts, depending on solar wind conditions and on the nature of the precipitating particles. Therefore, a time-averaged Joule heating power of a few times 10^{13} watts in the polar cusp is not an unreasonable value, possibly accounting for the missing infrared output power.

References and Notes

1. K. S. Noll, H. A. Weaver, P. D. Feldman, Eds., *The Collision of Comet Shoemaker-Levy 9 and Jupiter* (Cambridge Univ. Press, 1996).
2. B. Bézard *et al.*, *Icarus* **125**, 94 (1997).
3. E. Lellouch *et al.*, *Nature* **373**, 592 (1995).
4. A. Marten *et al.*, *Geophys. Res. Lett.* **22**, 1589 (1995).
5. R. Moreno, A. Marten, H. E. Matthews, Y. Biraud, *Planet. Space Sci.* **51**, 591 (2003).
6. V. Kunde *et al.*, *SPIE Proceedings, International Society for Optical Engineering* **2803**, 162 (1996).
7. D. F. Strobel, *Int. Rev. Phys. Chem.* **3**, 145 (1983).
8. A. Coustenis, B. Schmitt, R. K. Khana, F. Trotta, *Planet. Space Sci.* **47**, 1305 (1999).
9. G. R. Gladstone, M. Allen, Y. L. Yung, *Icarus* **119**, 1 (1996).
10. J. I. Moses *et al.*, in *Jupiter: Planets, Satellites, and Magnetospheres* (Cambridge Univ. Press, in press).
11. R. A. Hanel *et al.*, *Science* **204**, 972 (1979).
12. R. A. Hanel *et al.*, *Science* **206**, 952 (1979).
13. The line intensities are proportional to $[(I_{Emission} - I_{Continuum})/B(T)]$, where B(T) is the Planck function at the average pressure level, where the contribution functions peak, and are increasing functions of the air mass and gas abundances. The correction for air mass variations within the samples has been made with a radiative transfer model of the limb brightening. This model indicates that the C_2H_2 Q-branch emission (line minus nearby continuum) doubles when the air mass (or the column abundance) is increased by a factor of 3, whereas the C_2H_6 line emissions are multiplied by a factor of 2.6. In the case of CO_2 and HCN, the emission is proportional to the air mass. The raw intensities of the emission features are first corrected for this effect and then divided by the Planck function at 5 mbar (C_2H_2 and C_2H_6) or 1.0 mbar (CO_2 and HCN) (normalized at 45°S), taken from the zonal mean temperature maps derived from CIRS data (*20*). This approximately corrects the dependence of the emission upon temperature, given that the contribution functions peak around 5 mbar for the two hydrocarbons and around 0.2 mbar for CO_2 and HCN.
14. E. Lellouch *et al.*, *Icarus* **159**, 112 (2002).
15. C. Griffith *et al.*, *Icarus* **170**, 58 (2004).
16. J. I. Moses, in *The Collision of Comet Shoemaker-Levy 9 and Jupiter*, K. S. Noll, H. A. Weaver, and P. D. Feldman, Eds. (Cambridge Univ. Press, 1996).
17. V. G. Banaszkiewicz *et al.*, *Icarus* **147**, 386 (2000).
18. V. G. Anicich, W. T. Huntress Jr., *Astrophys. J. Suppl. Ser.* **62**, 553 (1986).
19. M. R. Schoeberl, L. R. Lait, P. A. Newman, J. E. Rosenfield, *J. Geophys. Res.* **97**, 7859 (1992).
20. F. M. Flasar *et al.*, *Nature* **427**, 132 (2004).
21. G. Orton, *Bull. Am. Astron. Soc.* **35,** (2003).
22. N. Gehrels, E. C. Stone, *J. Geophys. Res.* **88**, 5537 (1983).
23. J. Caldwell, A. T. Tokunaga, F. C. Gillett, *Icarus* **44**, 667 (1980).
24. S. J. Kim, J. Caldwell, A. R. Rivolo, R. Wagener, G. S. Orton, *Icarus* **64**, 233 (1985).
25. P. Drossart *et al.*, *J. Geophys. Res.* **98**, 18803 (1993).
26. G. S. Orton *et al.*, *Science* **252**, 537 (1991).
27. J. T. Clarke *et al.*, *Nature* **415**, 997 (2002).
28. R. Prangé *et al.*, *J. Geophys. Res.* **103**, 20195 (1998).
29. A. P. Ingersoll *et al.*, *Icarus* **135**, 251 (1998).
30. C. C. Porco *et al.*, *Science* **299**, 1541 (2003).
31. J. E. P. Connerney, R. Baron, T. Satoh, T. Owen, *Science* **262**, 1035 (1993).
32. L. Pallier, R. Prangé, *Planet. Space Sci.* **49**, 1159 (2001).
33. L. Pallier, R. Prangé, *Geophys. Res. Lett.* **31**, L06701 (2004).
34. G. R. Gladstone *et al.*, *Nature* **415**, 1000 (2002).
35. R. Prangé, L. Pallier, American Geophysical Union Fall Meeting, abstract #4098, San Francisco, 8 to 12 December (2003).
36. D. Rego, R. Prangé, J. C. Gérard, *J. Geophys. Res.* **99**, 17075 (1994).
37. J. H. Waite Jr. *et al.*, *J. Geophys. Res.* **88**, 6143 (1983).
38. T. W. Hill, *J. Geophys. Res.* **106,** 8101 (2000JA000302) (2001).
39. E. W. Bunce, S. W. H. Cowley, T. K. Yeoman, *J. Geophys. Res.*, in press (2004).

40. M. H. Elliott, J. S. Tingley, and F. Carroll assisted with instrument commanding and data processing. P. J. Schinder computed the pointing geometry files for the CIRS observations during the Jupiter swing-by. We acknowledge the assistance of many individuals in the planning and execution of the Jupiter science sequences. This work was supported by funding from the NASA Cassini Project for U.S. coauthors. British coauthors at Oxford and Cardiff Universities acknowledge support of the Particle Physics and Astronomy Research Council. French coauthors acknowledge financial support from the Centre National d'Etudes Spatiales (CNES) and the Institut National des Sciences de l'Univers (CNRS/INSU). Comments by two reviewers substantially improved the manuscript.

Supporting Online Material

www.sciencemag.org/cgi/content/full/1100240/DC1
SOM Text
Figs. S1 to S8
Tables S1 and S2
References

12 May 2004; accepted 4 August 2004
Published online 19 August 2004;
10.1126/science.1100240
Include this information when citing this paper.

Mechanism of Ammonia Transport by Amt/MEP/Rh: Structure of AmtB at 1.35 Å

Shahram Khademi, Joseph O'Connell III, Jonathan Remis, Yaneth Robles-Colmenares, Larry J. W. Miercke, Robert M. Stroud*

The first structure of an ammonia channel from the Amt/MEP/Rh protein superfamily, determined to 1.35 angstrom resolution, shows it to be a channel that spans the membrane 11 times. Two structurally similar halves span the membrane with opposite polarity. Structures with and without ammonia or methyl ammonia show a vestibule that recruits NH_4^+/NH_3, a binding site for NH_4^+, and a 20 angstrom–long hydrophobic channel that lowers the NH_4^+ pK_a to below 6 and conducts NH_3. Favorable interactions for NH_3 are seen within the channel and use conserved histidines. Reconstitution of AmtB into vesicles shows that AmtB conducts uncharged NH_3.

The transport of ammonia/ammonium is fundamental to nitrogen metabolism throughout all domains of life (*1*–*4*). In what follows, Am refers to (NH_3 + NH_4^+), and MA to (CH_3NH_2+ $CH_3NH_3^+$). The so-called ammonia transporters (Amt proteins), whose paralogs in yeast are called methylammonium/ammonium permeases (MEP proteins) (*5*, *6*) are typically >420 amino acids in length and are assembled as trimers of proteins (*7*). The transport rates of most Amt/MEP proteins can be conveniently measured by transport of radioactive ^{14}C–labeled MA (*8*).

Plant, bacterial Amt, and yeast MEP family members show a range of concentration dependence for Am conductance up to "high affinity," as reflected in their ability to grow on very low concentrations (<5 μM) of ammonium salts as sole nitrogen source. The "response K_m" (the concentration that evokes half-maximal conductance) for Am is ~5 to 10 μM for MEP1 and 1 to 2 μM for MEP2. MEP3 is of much lower affinity, K_m ~ 2 mM (*6*). *amtB* and *glnK* located on the same operon, are cotranscribed in bacteria (*9*) and archaea, and GlnK plays a dynamic role in the regulation of nitrogen uptake (*10*) by binding to AmtB (*11*, *12*). In humans, the Rhesus (Rh) family of proteins, both erythroid (RhAG, RhD, and RhCE) and nonerythroid (RhCG, RhBG, and RhGK), also share conservation with the Amt/MEP family throughout their sequence (*13*) (Fig. 1).

Our structural analysis is based on crystals grown in the absence or presence of Am or MA. It reveals a recruitment vestibule for cations such as NH_4^+ or neutral NH_3, a site that can bind $CH_3NH_3^+$ or NH_4^+ using π-cation interactions, and a hydrophobic channel that incorporates NH_3 using weak interactions with C-H hydrogen bond donors. Our assays carried out on reconstituted vesicles show that the protein conducts NH_3 because addition of Am salts outside raises internal pH. This is therefore the first structure of a transmembrane channel family that can conduct unhydrated molecules that in isolation would be gaseous.

Department of Biochemistry and Biophysics, S412C Genentech Hall, University of California–San Francisco, 600 16th Street, San Francisco, CA 94143–2240, USA.

*To whom correspondence should be addressed. E-mail: stroud@msg.ucsf.edu

Structure Determination

We cloned two orthologs of AmtB, from *Aquifex aeolicus* (AmtB_AQFX) (*14*) and *Escherichia coli* (AmtB_*Ecoli*) (*4*, *7*). Twenty amino acids were excised from the N terminus of AmtB_AQFX and 22 were excised from AmtB_*Ecoli*, as established by matrix-assisted laser desorption/ionization mass spectroscopy (MALDI-MS) and N-terminal amino acid sequencing. This and the prediction of signal peptide cleavage sites through neural network approaches (*15*) led to the identification of these regions as signal sequences, which are removed upon insertion of the proteins into the cell membrane (Fig. 1). Crystals of AmtB_*Ecoli*, grown in the presence of 25 mM $AmSO_4$ at pH 6.5, diffract to a resolution of 1.35 Å (Table 1). Crystals of AmtB_AQFX diffracted to 4.5 Å and have not yet been pursued.

A Trimer of Three Channels

AmtB crystallizes as the physiological threefold symmetric trimer of channel-containing proteins (Fig. 2, A and B). The trimer extends ~65 Å parallel to the threefold axis and is 81 Å in diameter in the plane of the membrane. Eleven transmembrane-spanning α-helices (M1 to M11) form a right-handed helical bundle around each channel. Residues from M1, M6, M7, M8, and M9 of one monomer interact with helices M1, M2, and M3 of the neighboring monomer, with a total interacting surface area of 2716 $Å^2$. As described for other membrane proteins, polar aromatic side chains of residues Tyr^{62} at the periplasmic (termed extracellular) side and Tyr^{180}, Trp^{250}, and Trp^{297} at the cytoplasmic side would lie in the membrane-aqueous phase interface. The trimer has a net negative charge of –7.5 (13.5 positive + 21 negative) on the outer surface and a net positive charge of +9 (42

Table 1. Crystallographic statistics to 1.35 Å resolution. Crystals of SeMet AmtB (used for all crystallography) were in space group $P6_3$. Data were collected at the ALS beamline 8.3.1, with a CCD detector (Quantum 4), and integrated and scaled with DENZO, SCALEPACK (Native), and MOSFILM (MAD data). Phases were calculated with CCP4. After solvent flattening and phase extension to 2.0 Å, the model was refined with CNS to 1.8 Å and SHELX to 1.35 Å.

Data set	With 25 mM $AmSO_4$	With 100 mM $MASO_4$	Without Am/MA	SeMet MAD remote	SeMet MAD peak
Cell dimensions (*a* Å, *c* Å)	96.5, 94.6	95.7, 94.6	95.8, 94.7	95.8, 94.7	95.8, 94.7
Wavelength (Å)	1.1159	1.1159	1.1159	1.0080	0.9797
Resolution (Å)	1.35	1.85	2.0	2.5	2.5
Multiplicity	14.3	13.3	19.6	7.3	6.6
Completeness %*	97.3 (90.4)	99.7 (99.3)	87.4 (48.3)	99.7 (99.6)	99.7 (99.6)
I/σ	20.4 (1.6)	19.3 (1.9)	25.8 (2.0)	10.6 (3.3)	9.4 (2.8)
R_{sym} (%)	5.8 (62.1)	6.4 (80.0)	6.4 (69.5)	11.4 (81.0)	12.5 (87.0)
Phasing power				0.7	0.34
Figure of merit (after solvent flattening)				0.265 (0.877)	
R_{cryst}/R_{free} (%)	13.3/16.8	19.5/20.5	18.2/20.5		
RMSD bond length (Å)	0.007	0.007	0.013		
RMSD bond angle (°)	1.3	1.3	1.8		
Mean B factor ($Å^2$)	24.6	37.5	43.2		

*Numbers in parenthesis refer to the high-resolution shell for data refinement (1.45 to 1.40 with $AmSO_4$, 1.92 to 1.85 for $MASO_4$, and 2.07 to 2.00 for without substrate).

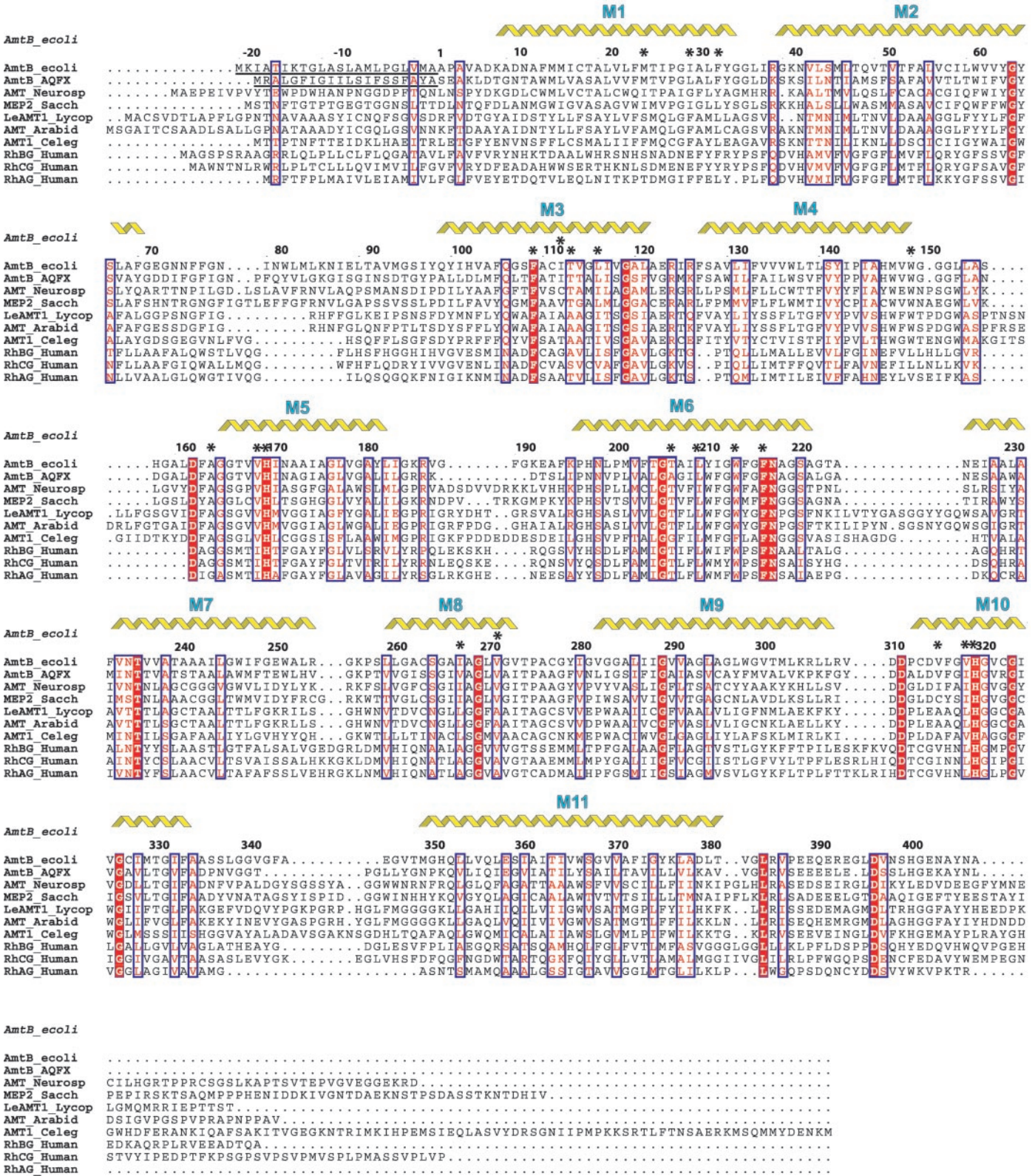

Fig. 1. The amino acid sequence alignments of AmtB/MEP/Rh homologs from *E. coli* (AmtB_*E. coli*), *A. aeolicus* (AmtB_AQFX), Neurospora (AMT_Neurosp), *Saccharomyces cerevisiae* (MEP2_Sacch), *Lycopersicon esculentum* (LeAMT1_Lycop), *Arabidopsis thaliana* (AMT_Arabid), *Caenorhabditis elegans* (AMT1_Celeg), and human Rh factors (RhBG, RhCG, and RhAG). The numbering is that of *E. coli* AmtB. Conserved amino acids are in white in red-filled rectangles. Similar residues are in red surrounded by blue lines. The signal sequences in *E. coli* and *A. aeolicus* are underlined. Residues that line the lumen of the channel are labeled with asterisks above. Eleven transmembrane helices are identified by helical motifs above the sequence, labeled by transmembrane helix numbers M1 to M11.

positive + 33 negative) on the cytoplasmic side, as is the trend in membrane proteins.

At the extracellular side, the threefold axis is surrounded by three closely packed copies of just M1 of each monomer, which seal the central axis against passage. Toward the cytoplasmic side, the three M1s (+16° to each other) veer away from the threefold axis to leave an open pocket ~10 Å across, formed by three copies of M1 and M6. M1 has a kink (22°) in the helix secured by the only cis-proline (Pro^{26}) in AmtB, a residue not conserved in the superfamily. M1 and M6 are not long enough to span the bilayer, consistent with the trimer being the stable physiological quaternary structure. The interfaces between subunits are almost as hydrophobic as the exterior, suggesting that a monomer could be transiently stable in the membrane upon synthesis, before forming trimers. An isolated square planar arrangement of four water molecules, each hydrogen-bonded to each other (average hydrogen bond length 3.0 Å), makes two hydrogen bonds to carbonyl oxygens of Cys^{56} and Ala^{102} in an otherwise hydrophobic cavity in the interface.

An 11-Crossing Membrane Protein with a Quasi-Twofold Axis in the Plane of the Membrane

We found that AmtB from *E. coli* and AmtB from *A. aeolicus* each begin with a signal sequence that is cleaved during synthesis. The topology of AmtB was correctly determined by a careful series of PhoA and LacZ insertions, and the C terminus was shown to be cytoplasmic (*4*). Within each AmtB channel, M1 to M10 diverge outward from the central plane in a right-handed helical bundle to generate a vestibule on each surface. Their inter helix angles are +26° to –58°. Within the trans-bilayer region, there are three glycine Cα-H. . .O=C hydrogen bonds (between the Cα hydrogen of glycine and a main chain carbonyl oxygen of a neighboring α-helix) between M1 and M6 (Gly^{204}, Gly^{211}, and Gly^{34}) and one between M8 and M10 (Gly^{325}). Cys^{109} and Cys^{56}, found only in *E. coli* AmtB, are close enough to form a disulfide in the transmembrane region.

The fold is not homologous to any other membrane protein structure previously reported. Although there is no evidence for any gene duplication in the family, the structure of M1 to M10 reflects a quasi-twofold axis in the midplane of the membrane that intersects the trimer threefold axis. It relates the structural context of the M1 to M5 region to that of M6 to M10. M11 is an additional ~50 Å–long straight helix, inclined at –50° to the perpendicular to the membrane plane that surrounds the lipid accessible side of each monomer (Fig. 2, B and C). This type of structural duplication with opposite polarity with respect to the membrane plane is seen in a number of membrane proteins, including AmtB, GlpF and all aquaporins, the SecY pro-

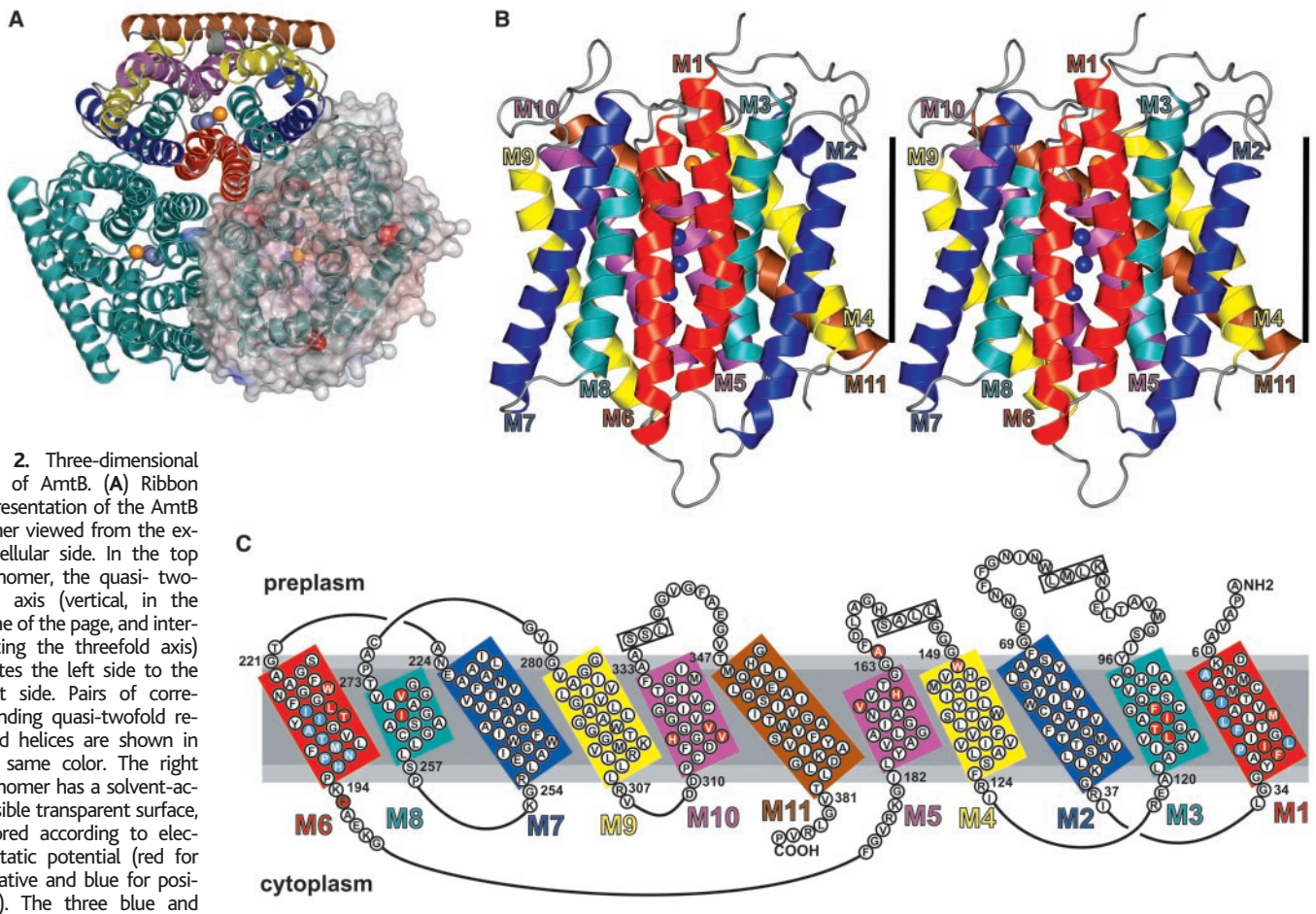

Fig. 2. Three-dimensional fold of AmtB. (**A**) Ribbon representation of the AmtB trimer viewed from the extracellular side. In the top monomer, the quasi- twofold axis (vertical, in the plane of the page, and intersecting the threefold axis) relates the left side to the right side. Pairs of corresponding quasi-twofold related helices are shown in the same color. The right monomer has a solvent-accessible transparent surface, colored according to electrostatic potential (red for negative and blue for positive). The three blue and one orange spheres are potential ammonia molecules and an ammonium ion, respectively. (**B**) A stereoview of the monomeric ammonia channel viewed down the quasi-twofold axis. In this and all subsequent figures, the extracellular side is uppermost. The vertical bar (35 Å) represents the inferred position of the hydrophobic portion of the bilayer. Three NH_3 molecules seen only when crystallized in the presence of ammonium sulfates, are shown as blue spheres. (**C**) The amino acid sequence of AmtB is arranged topologically as in the structure, with helices viewed as if from inside the channel looking away from the threefold axis. The quasi-twofold axis is perpendicular to the center of the figure. Five helices compose each segment, labeled M1 to M5 and M6 to M10. Related helices M1 and M6, M2 and M7, etc., are boxed in similar colors. Side chains of residues in red circles contribute to the substrate-contacting walls of the channel. Residues in blue circles contribute side chains to the inter-monomer contacts that immediately surround just the threefold axis of the trimer, because many oligomeric membrane proteins either need to insulate against passage of alternate molecules there or use this special location for stability, as in the aquaporins, or for conductance as in K^+ channels. The deduced location of the cell membrane is illustrated in gray (35 Å) with light gray for the head group region (to 40 Å thickness).

tein of the translocon, and the ClC chloride channel. However, of these, only in the aquaporin family were the vestiges of duplication recognized in the gene sequences (*16*). The sparse vestiges of duplication now apparent in sequence after the structure imply that they should be identifiable in other proteins when conservation among multiple sequences is taken into account. Because of the opposite polarity of the duplicated segments relative to the membrane, the primordial gene duplication event of such membrane proteins must have occurred before generation of enough functional surroundings to support any transport of molecules from one side of the membrane to the other.

The Mechanism of Transport or Conductance

We sought to define any preferred sites for Am or MA and the mechanism for transport or conductance of these molecules by comparison of the structure in the absence of any ammonium derivative, in 25 mM $AmSO_4$ at pH 6.5, and in 100 mM $MASO_4$ at pH 6.5. These concentrations are in ~1000-fold excess relative to the response K_m (Am, $K_m \sim 10$ μM; MA, $K_m \sim 50$ μM). There is no significant overall conformational change of the protein with Am or MA, consistent with AmtB as a channel rather than as an ammonia transporter that would harness alternating conformational states. Therefore, from now on, we refer to this family of molecules as channels.

The quasi-twofold (i.e., up to down) symmetric channel generated within each monomer by the structural antiparallel duplication begins with an extracellular vestibule. This is followed by one of two most constricted hydrophobic regions (Fig. 3A). The mid-membrane center of the pathway has two in-line histidines followed by the second constricted hydrophobic region and the intracellular vestibule. Between the two hydrophobic constrictions the channel wall is narrow and mostly nonpolar throughout its ~20 Å length, consistent with conduction of uncharged NH_3.

The outer vestibule contains 30 ordered water molecules. Am has similar density to that of H_2O; thus, if it replaces H_2O, it is difficult to identify unambiguously as Am. The density for MA is clearly distinguished from that of H_2O/Am, and the difference can uniquely mark a site. Because the Am and the MA crystals have slightly different unit cells and so were not isomorphous, Fo-Fo maps were not useful; thus, we cite Fo-Fc maps. One such MA site (60% ordered, where this order parameter represents the integrated electron content, referenced to the highest occupied water molecule) is located against both aromatic rings of Trp^{148} and Phe^{107} (Fig. 3B). The $-NH_3^+$ moiety is a hydrogen bond donor to the O_γ of Ser^{219}. This provides a favorable two π-cation interaction for NH_4^+ and for $CH_3NH_3^+$, stabilized by ring currents, and is accessible to solvent. MA displaces two separate peaks (Am1, 67% ordered) and a water peak in the Am structure (Fig. 3C), very similar to two water peaks in the H_2O structure (60% ordered). The order parameter we use primarily reflects movement in the site and secondarily statistical occupation.

Mutation of conserved Asp^{160} to Ala^{160} completely destroys transport of MA, implying that Asp^{160} plays a key role (*12*), and Merrick proposed that it might provide a primary binding site for NH_4^+. However, there is no peak of density against Asp^{160} even in the presence of 25 mM $AmSO_4$ or 100 mM $MASO_4$. Conserved Asp^{160} is a helix-capping residue for M5 (Fig. 4A), being a hydrogen bond acceptor at its Oδ2 from the Oγ H (2.51 Å) and N-H of Thr^{165} (2.8

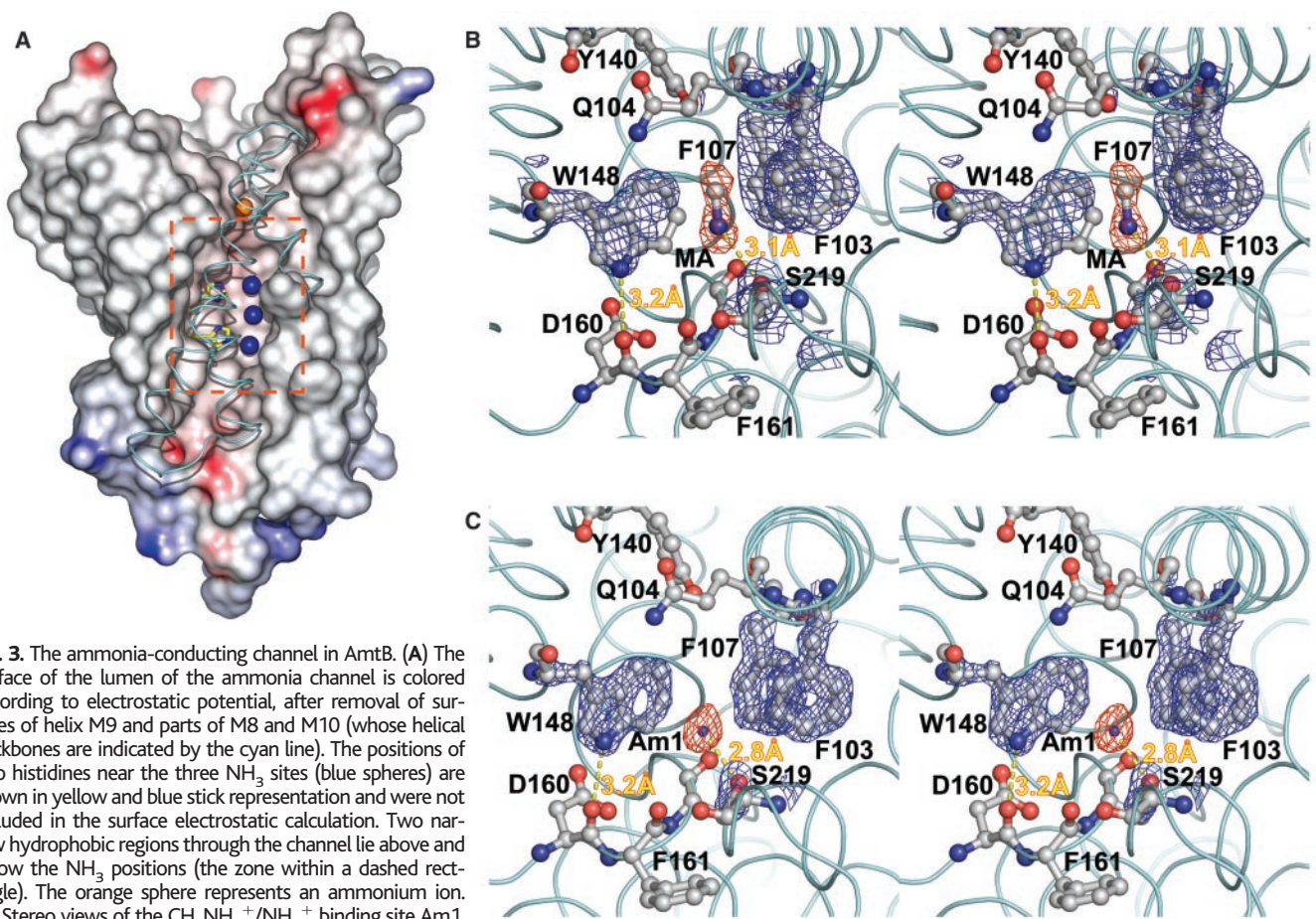

Fig. 3. The ammonia-conducting channel in AmtB. (**A**) The surface of the lumen of the ammonia channel is colored according to electrostatic potential, after removal of surfaces of helix M9 and parts of M8 and M10 (whose helical backbones are indicated by the cyan line). The positions of two histidines near the three NH_3 sites (blue spheres) are shown in yellow and blue stick representation and were not included in the surface electrostatic calculation. Two narrow hydrophobic regions through the channel lie above and below the NH_3 positions (the zone within a dashed rectangle). The orange sphere represents an ammonium ion. (**B**) Stereo views of the $CH_3NH_3^+/NH_4^+$ binding site Am1. The electron density map (2Fo-Fc) is contoured at 2σ for the protein (blue), and the (Fo-Fc) $CH_3NH_3^+$ omit map is contoured at 4.5σ (red) for AmtB in 100 mM $MASO_4$ at pH 6.5. The MA order is 67% occupancy for each (CH_3 and NH_3) group. Hydrogen bonds between the NH of $CH_3NH_3^+$ and Oγ of Ser^{219} and between the Nε1H of Trp^{148} and O of Asp^{160} are indicated by yellow dashed lines, with bond distance in yellow. (**C**) As in (B), for AmtB in 25 mM Am SO_4 at pH 6.5. Am order is 67% occupancy (6.7 electrons).

Å) and at its Oδ1 from the N-H of Gly^{164} (2.7 Å) and the N-H of Gly^{163} (2.8 Å) at the N-terminal end of M5. Thus, the Asp^{160} carboxyl orients the carbonyls of Asp^{160}, Phe^{161}, and Ala^{162} that, along with carbonyls of Ser^{68}, Ser^{219}, Val^{147}, and Trp^{148} from the outside ends of helices M2, M4, and M6, line the vestibule and make it cation-attracting. Asp^{160} itself is not accessible to bulk solvent and is conserved across the superfamily, underlying its key role that appears to be primarily structural. Cys^{326} shields one planar face of Asp^{160}. The indole ring of Trp^{148} is interposed between Asp^{160} and the MA site and shields Asp^{160} from solvent. Trp^{148} is conserved among the Amt/MEP subfamilies. The lowest polar carbonyl oxygen is for Ala^{162} at z = 8.5 Å. The first hydrophobic constriction in the channel formed by Trp^{148}, Phe^{103}, Phe^{161}, and Tyr^{140}, all of which are conserved only in Amt's, and everywhere conserved Phe^{107} and Phe^{215} suggests possible π-cation interactions for NH_4^+ on entry to the channel. The diameter is 1.2 Å; thus, the side chains of Phe^{107} and Phe^{215} must move dynamically during any conduction event.

In 25 mM $AmSO_4$, the crystal structure shows three additional peaks (Am2, Am3, and Am4 of order 20%, 15%, and 20%, respectively), not present without AmSO4 adjacent to two quasi-twofold, related, conserved imidazoles of His^{168} and His^{318} at the center of the narrow hydrophobic channel (Fig. 4, A and B). The partial order indicates that these Am-specific peaks are poorly ordered, consistent with there being no good localizing hydrogen bonds in the channel or with their being occupied alternately with each other, or conceivably partially occupied such that at higher concentration they might be fully occupied. This latter reason seems very unlikely, because Am is already at 1000-fold the K_m. At this resolution (1.35 Å), C, N, and O in AmtB are clearly distinguished. The orientation and hydrogen bonding of the imidazoles are unambiguously determined. The OH of conserved Thr^{273} is a hydrogen donor to the C=O of Leu^{269} and therefore an acceptor of the hydrogen bond from Nε2H of His^{168}. Unprotonated His^{168} Nδ1 and His^{318} Nδ1H are fixed by hydrogen bond to each other. They provide two Cε1-H hydrogen bond donors (*17*) to the N of Am2 and the N of Am3 (3.2 Å and 3.4 Å between heavy atoms, respectively), and one Nε acceptor for the N-H of Am4. The other surrounding side chains are all hydrophobic. π-cation stabilization is possible at Am2 from side chains of Phe^{215} and Trp^{212}. In this low dielectric environment, the imidazole Cε1-Hs will appear more acidic than imidazole in aqueous solution, because the effective dielectric constant (ε) is much lower. Therefore, coulombic attraction forces will increase as 1/ε.

Whereas imidazole nitrogens might act as a hydrogen donor N-H or an acceptor N at the lone pair of electrons on an unprotonated nitrogen, the Cε1–Hs can only be donors, easing passage of a molecule that is an acceptor, as is NH_3 but not NH_4^+. Thus, this signature structure harnesses all of its hydrogen-bonding potential to accommodate the passage of hydrogen bond–accepting molecules. The pK_a of NH_3 must be lowered to below 6 at sites Am3 and Am4, because peaks clearly reflect NH_3 at a pH of 6.5 in the crystals. At some point close to the aromatic constriction, NH_4^+ gives up its proton, leaving it predominantly on the side of entry, and NH_3 is transported. The cation-selective vestibule, possibly down to the Am2 site, can recruit NH_4^+. This and the aliphatic hydrophobic channel compatible with NH_3 can explain many of the seemingly inconsistent observations of function.

Phe^{31}, Tyr^{32}, and Val^{314} surround the second cytoplasmic constriction. Asp^{310}, the conserved quasi-twofold relative of Asp^{160}, similarly acts as a helix cap for M10. The first exit-peak of density within the channel pathway is hydrogen-bonded to Asp^{313} and could be close to where NH_3 would reacquire a proton on the inside to become NH_4^+.

Ammonia Conductivity by AmtB

In order to determine the substrate specificity and rates of conductance of AmtB, we adapted a fluorescence-based assay to measure the influx of ammonia into vesicles (liposomes or proteoliposomes) by monitoring the pH-sensitive fluorescence of 5-carboxy fluorescein (CF) (*18*, *19*). Rapid mixing of CF-loaded vesicles with ammonium chloride (0.5 mM or 5 mM) was initiated at pH 6.8. The internal pH rose, reflecting influx of NH_3 through the lipids and through AmtB, which subsequently acquires a proton from H_2O inside, to give NH_4^+ and OH^- (Fig. 5A).

The rate constant of ammonia influx indicated by the rate of pH change, 115.6 ± 13.2 s^{-1} (average of n = 6 determinations, typical curve fitting error in a single curve), for 5 mM NH_4Cl outside is 10-fold faster than for protein-free liposomes, 12.8 ± 0.7 s^{-1} (n = 6). The rate of pH change for 0.5 mM NH_4Cl (one tenth the concentration) is 70 s^{-1} (60% of the rate). Substitution of 5 mM NH_4Cl by 5 mM NaCl did not lead to any detectable change in fluorescence even after 10 s, showing that changes in CF fluorescence are due to ammonia influx and not, for example, to any water efflux due to change in osmolarity. As a further control, ammonia conductivity for proteoliposomes reconstituted with the aquaglyceroporin GlpF was measured at 11.4 ± 0.06 s^{-1} (n = 6), the same as for liposomes, consistent with there being no leakage due to the reconstitution procedure per se. Thus, when the ammonium concentration drops 10-fold, the rate drops only

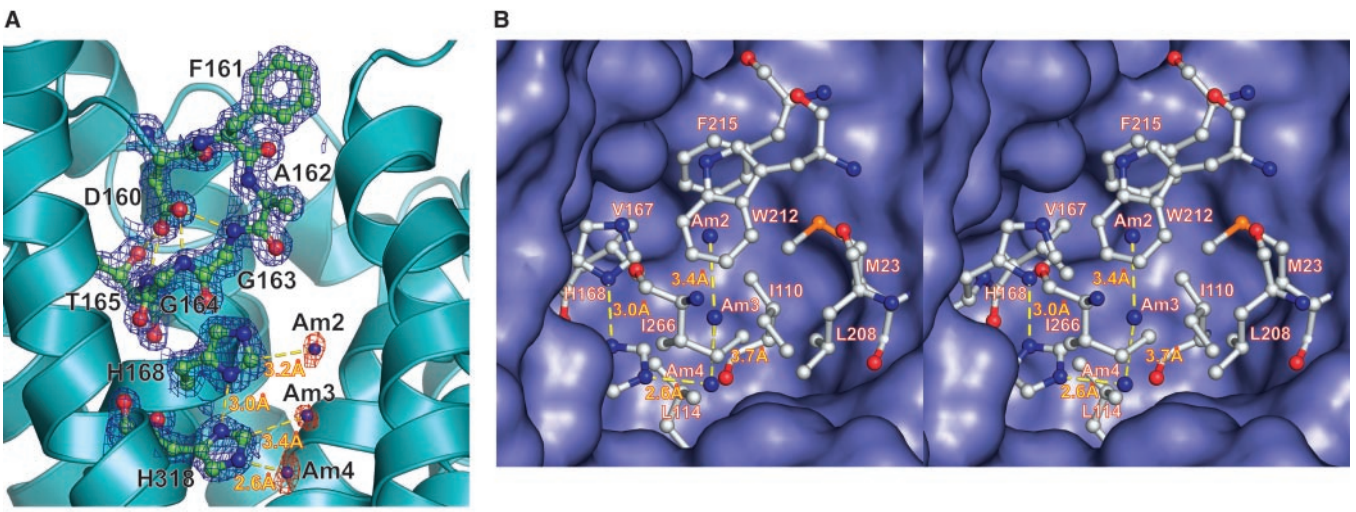

Fig. 4. (**A**) Electron density (2Fo-Fc) contoured at 1.5σ (blue) for the two-histidine region and surrounding structure, including conserved Asp^{160} that accepts four short hydrogen bonds (dashed yellow). Additional peaks Am2, Am3, and Am4 seen when crystallized with 25 mM ammonium sulfate are defined in the Fo-Fc omit map at 1.5σ (in red), indicating putative NH_3 molecule positions (blue spheres). The hydrogen-bonding network shows interactions between His^{168} and His^{318} and NH_3 peaks in yellow (distances in red). (**B**) Stereo view of the two-histidine center of the channel. Surrounding hydrophobic residues are shown in ball and stick representation. The surface representation covers other surrounding amino acids. Three ammonia-dependent sites are shown (blue spheres) with associated distances (dashed yellow line and yellow labels).

40%, generally consistent with the fact that the K_m for transport is below 500 μM Am.

To assess possible water conductivity by AmtB, osmotic permeability of water was measured by concentration-dependent self-quenching of vesicular CF with an aliquot of the same batch of AmtB proteoliposomes (*19*) (Fig. 5B), and also by light scattering as a monitor of vesicle shrinkage and swelling (*20*). By the fluorescence assay, when vesicles were mixed with sucrose to a final concentration of 250 mM sucrose outside, water efflux was 7.85 ± 0.08 s^{-1} ($n = 6$) for liposomes, versus 8.78 ± 0.07 s^{-1} ($n = 6$) for AmtB proteoliposomes, indicating no additional water conductivity in AmtB proteoliposomes, versus ~150 s^{-1} for a water channel AqpZ in the proteoliposomes. Thus, AmtB does not conduct water.

Likewise, the structure of AmtB without $(NH_4)_2SO_4$ showed no ordered water in between the hydrophobic constricted regions of the channel. Thus, the channel removes water of hydration from NH_4^+ and a proton, as NH_3 passes through the channel. The channel is narrow and the cost of dehydration of H_2O itself is not compensated by oxygen in the lumen of the channel, and no line of waters can be supported within the channel. This implication was also challenged by molecular mechanics simulation with NAMD, which after 2 ns of simulation confirmed that no water enters the channel (*21*).

The Mechanism: Recruitment of NH_4^+ and Filtered Passage of NH_3

The mechanism suggested by the atomic resolution structures, difference maps for Am/MA, and NH_3 conductivity in proteoliposomes involves a vestibular recruitment of total Am, a site that can bind NH_4^+, and a channel for NH_3 that lowers its pK_a to <6 (Fig. 6). This mechanism of conductance can reconcile many, but not yet, all data that lead to the seemingly inconsistent proposals of how members of the Amt/MEP family work.

Soupene *et al*. have maintained that the Amt/MEP family conducts NH_3 bidirectionally (*22*, *23*), with which our findings are consistent. On the basis of experiments, it has also been proposed that the Amt/MEP family variously transports NH_4+ (*9*, *24*–*26*), cotransport 26 and exchanges NH_3/H^+ (*26*), and exchanges NH_4^+/H^+ in Rh proteins (*27*, *28*). We attempt to address these data here.

pH-dependent effects. NH_4^+ (or $CH_3NH_3^+$) becomes less basic in the channel as it becomes progressively desolvated, until it reaches the Am2 position. At Am3, it is deprotonated and becomes uncharged (pK_a < 6). Entry of the uncharged NH_3 or CH_3NH_2 species into the hydrophobic channel at pHs above the new pK_a could eliminate all dependence of rate on pH and hence any dependence on concentration of the uncharged species in the bulk solution. Correspondingly, the solution equilibrium between NH_3 and NH_4^+ has little to do with the mechanism, because both species can enter the vestibule to become NH_3 at the Am2/3 site. If at all, lower pH might contribute to reduce the rate of Am conductance, not by reducing the level of NH_3 in bulk solution, but by opposing proton release from NH_4^+ in the vestibule. The vestibule may also have some preference for NH_4^+ or NH_3 that could be reflected as an indirect effect of pH in either direction; a tendency to recruit NH_4^+ would favor a small increase in rate at lower pH.

In *Coryne bacterium glutamicum*, two ammonia channels are present, Amt and AmtB. MA uptake has an apparent K_m ($CH_3NH_3^+$) of 53 ± 11 μM at pH 6.0 that is unchanged at pH 8.5, leading to the conclusion that NH_4^+ is the transported species, because NH_3 concentration in bulk solution would change 300-fold over this pH range, whereas NH_4^+ concentration is little changed (*25*, *29*). Likewise, the K_m for transport by *Arabidopsis* AMT2 is not pH-dependent between pH 5.0 and 7.5 (*30*). However, recruitment of Am to the vestibule can be completely pH-independent. Therefore, the inference that NH4$^+$ is conducted is incorrect; all Am will become NH_3 as it reaches the Am2/3 sites.

Effects of pH on transport of Am or MA by the human Rh factor RhAG show that the rate of inward transport of (external) $^{14}CH_3NH_3^+$ increases as external pH rises from 5.5 to 8.5 (*27*), tending to suggest that the neutral species may be conducted, because its concentration increases exponentially as pH is raised. However, a lack of effect of changes in membrane potential on conductance of MA, and a small decrease in conductance as internal pH rises, led to the conclusion that transport was electrically net neutral. Westhoff and colleagues reasoned that an increase in the outward-directed proton gradient might drive transport of ammonium ion, the predominant species in solution, and so suggested that RhAG might be a $H^+/CH_3NH_3^+$ antiporter. However, in light of our conclusions, it is of note that the increase in conductance was much more strongly dependent on the external pH than on internal pH, and it can equally be interpreted as transport of uncharged CH_3NH_2 as

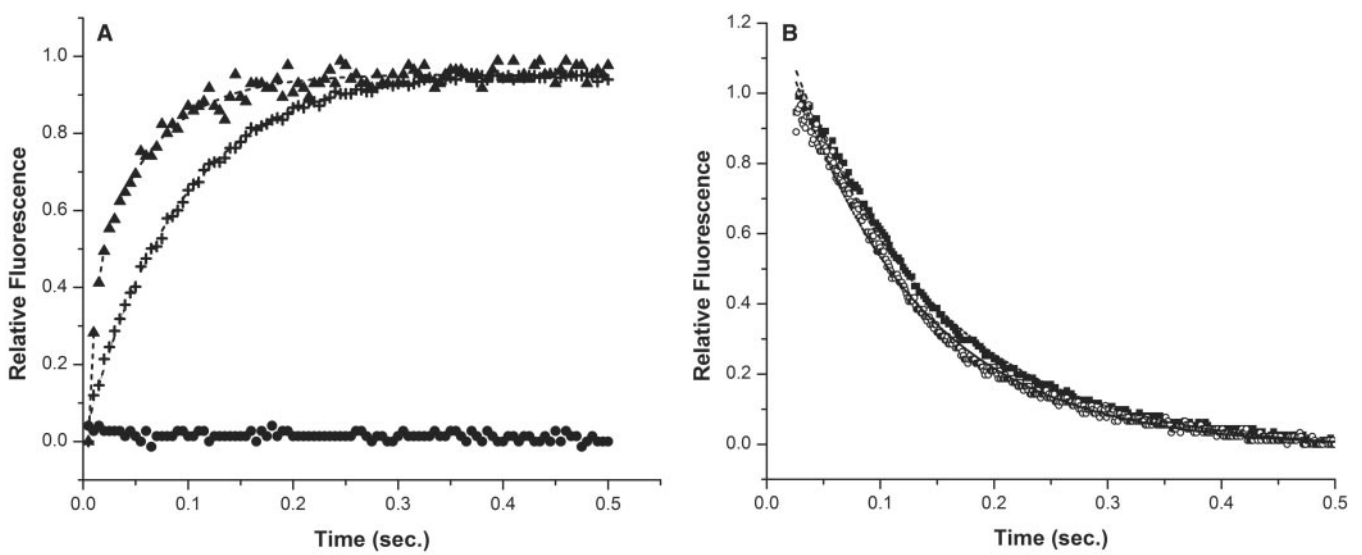

Fig. 5. Channel conductance in proteoliposomes. (**A**) The time course of change in pH inside of vesicles containing CF buffered by 20 mM Hepes as detected by fluorescence change. Initial pH was 6.8 both inside and outside. To initiate flux, 5 mM NH_4Cl was added externally to protein-free liposomes (+) and to AmtB-containing proteoliposomes (solid triangles) (protein to lipid ratio was 1:200 by weight) (*36*). To control for possible osmotic effects, instead of 5 mM NH_4Cl, 5 mM NaCl was added to proteoliposomes (solid circles). The dashed lines are exponential fits to the data. (**B**) Water conductance assessed by concentration-dependant self-quenching of CF-containing liposomes (solid squares) and proteoliposomes (open circles) upon addition of 500 mM sucrose at $t = 0$. The osmotic change leads to conductance of water through the lipids or through protein. The dashed lines are exponential fits to the data.

implied by our mechanism, in which the deprotonation of $CH_3NH_3^+$ in the vestibule might well become easier as pH is raised.

Soupene *et al*. show that growth in minimal nitrogen-limiting conditions of Am (≤1 mM) is especially deleterious at pH values below 7, where the effect of AmtB/MEP disruptions are profound (*22*). The bulk solution concentration of NH_3 decreases as pH is lowered, one reason that they propose that the Amt/MEP proteins increase the rate of equilibration of the uncharged species NH_3 across the membrane, rather than actively transporting the charged species NH_4^+ (*23*). Although our results are consistent with this conclusion, and with their findings that conductance is bidirectional, we contend that the effect of pH is not by effect on solution concentration of NH_3. Any pH dependence could be consistent with a possible pH effect on H^+ release from NH_4^+ in the vestibule. Consistent with this conclusion, the increase in rates of transport of MA versus pH do not increase by a factor of 10 per unit increase in pH as would be expected for a bulk pH effect, but increase by a factor of ~2 per pH unit (*27*).

Competitive inhibition. Ammonia channels conduct Am and MA but no larger secondary or tertiary amines. However, seemingly inconsistently, dimethylamine and ethylamine were found to inhibit the uptake of CH_3NH_2 by Amt and AmtB from *C. glutamicum*, whereas trimethyl- and tetramethyl amine did not (*25*). Although the channel is too small to accommodate these molecules, competition for the smaller cationic forms can take place at the Am1 site in the vestibule. This inhibition of MA conductance by Am in RhAG is pH-independent, surprisingly because their pK_as are different (*27*). However, we now would expect this pH independence because competition is between total MA and Am.

Transmembrane potential. Transmembrane potential accentuated conductance by the channel has been noted because K_m for MA decreases as transmembrane voltage (negative in the direction of conductance) increases, interpreted as indicating that NH_4^+ is conducted (*26*). However, the electric field will concentrate NH_4^+ on the NH_4^+ rich side of the membrane and in the vestibule, increasing the local concentration there and so explaining this effect. Thus, K_m (apparent) appears to be lower because the local concentration of MA/Am is higher in the vestibule than in the bulk solution.

Westhoff *et al*. show by expression of human RhAG in oocytes that the rate of conductance of MA remains constant even when membrane potential is modulated from –35 mV to –9 mV (inside the oocyte), concluding that transport is not electrogenic (*27*). This could be consistent with an electrically neutral NH_4^+/H^+ antiport mechanism as these authors suggest, but it is also consistent with net transport of uncharged CH_3NH_2 as our results imply.

All the observations noted so far are reconciled by the recruitment of NH_4^+, reduction of its pK_a and conductance of NH_3 as the primary mechanism. However, observations of ammonium-dependent currents through ammonia channels are not and demand further examination. A two-electrode voltage clamp was used to vary the transmembrane potential in oocytes transiently expressing the tomato paralog LeAMT1. Inward currents increased with voltage and with external ammonium ions from ~3 μM Am upward. The currents show a Hill coefficient of 1, implying that there is no cooperative effect of one conducted molecule of Am on another and suggesting a single binding site (*26*), which we presume could be Am1. This electrogenic behavior suggests that the channel transports ammonium ions (NH_4^+, or NH_3 plus a H^+) rather than uncharged NH_3. The measured currents are the same from pH 5.5 to 8.5 (*26*), consistent with conductance of NH_4^+ ions rather than with NH_3 and H^+, which might have showed some pH dependence. Although we have shown that AmtB conducts predominantly NH_3 (assayed in proteoliposomes), we have not shown that it does not conduct any occasional nonstoichiometric NH_4^+/H^+ ions that could give rise to these currents. A stoichiometric measure of conductance of each species NH_3/NH_4^+ will be required to establish whether this takes place at some low level. We do not see any hydrogen-bonded pathway that could act as a conductor for H^+, nor any change in conformation of AmtB determined in the presence of Am/MA. Given with these observations, one possibility is therefore that an occasional NH_4^+ ion can reach Am2, stabilized by ring currents of the rich aromatic environment at the constriction, and pass through the two-histidine region, possibly using the acid/base properties of the imidazole nitrogens to assist in proton transfer. This would require a transient conformational change that could be induced. The structure can clearly guide experimental measures of the ratio of conductances. Alternatively, the currents could be carried by another ion or another Am dependent pathway in the oocytes.

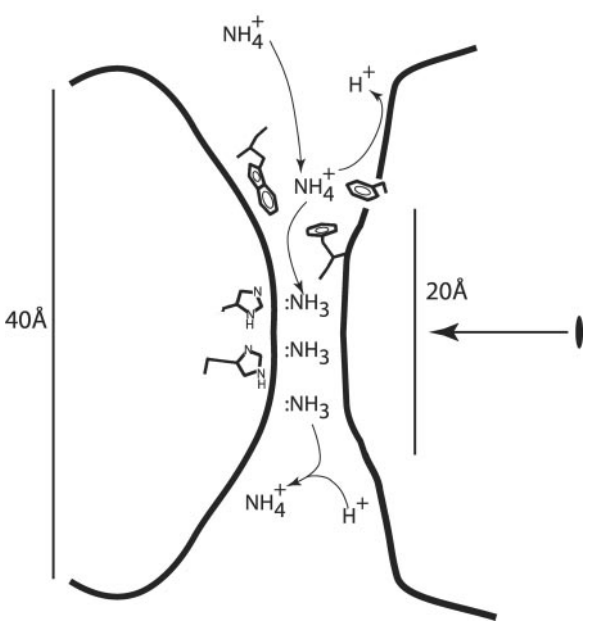

Fig. 6. The deduced mechanism of conductance is summarized. The low electron density for NH_3 may represent substitutional interchange or relative freedom of NH_3 within the hydrophobic channel. NH_3 normally undergoes rapid inversion. This may be impeded against the weak hydrogen bond C-H donors of imidazole.

The Mechanisms of Rh Factors

In light of the AmtB structure, the sequence of Rh factors can now be mapped onto the three dimensional structure of AmtB to address questions of Rh function. Variabilities in the Rh factors versus Amt/MEPs are seen in lengthened N- and C-terminal domains and in Rh-specific internal changes. The Rh proteins complement mutants in which all three of the yeast MEP proteins are inactivated (*mep1*Δ, *mep2*Δ, and *mep3*Δ), showing that the theRh proteins can provide similar function in the transport of Am to support the growth of yeast (*13*, *28*, *31*).

The rate of MA uptake in RhAG was saturable and well fitted by a Michaelis Menten equation with a K_m = 1.6 mM for the ionic species. NH_4^+ competed with MA (*27*). However, K_m for RhaG is 300-fold higher than for AtB and the Am1 site differs in lacking some of the π-cation stabilizing rings. Trp^{148} is Leu or Val in Rh factors; Phe/Tyr^{103} is Ile in Rh; Phe^{107} is conserved. This is consistent with low affinity for cations.

Based on several lines of evidence, Soupene *et al*. speculate that certain Rh factors, prominent in mammals and found alongside Amt in, for example, green algae, may function physiologically as channels for CO_2 (*32*, *33*). The stoichiometry of Rh factor associations in erythrocytes and their impact on the maternal immune response to fetal Rh are not known. Thus, the structure allows docking of models of the various Rh factors against each other to define this heterotrimeric assembly.

Biological Relevance of This Mechanism

Conductance of uncharged NH_3, versus NH_4^+ ion, can solve several biological problems. First, because K^+ channels conduct the very similarly sized NH_4^+ ion, there is the reverse possibility that an NH_4^+ ion channel could "leak" potassium and hence leak membrane potential in eukaryotes. Amt/MEP proteins are not permeable to any other ions (*26*). Transport of only uncharged NH_3 and not NH_4^+ assures this selectivity against all ions that would require replacement for their hydration shell while in the narrow portion of the channel. The energetic cost of removing even a single water of hydration from an ion is prohibitive. Second, NH_4^+ or any other ion is progressively energetically unstable as it approaches the center of the hydrophobic bilayer, whereas NH3 is much less so because it is electrically neutral. Potassium channels for example, have solved the problem by providing 16 carbonyl oxygens, 8 around each K^+ ion position on the way into the channel (*34*). Each oxygen offers a partial charge of 0.4 electrons to stabilize each K^+ ion. The KcsA channel also provides a water-filled cavity in the most energetically costly position at the center of the bilayer (*35*). The narrow hydrophobic channel of AmtB solves this energetic problem, as it also selects against the ionic form of NH_4^+ or any organic molecule larger in cross section than a single NH_3. Third, passage of uncharged NH_3 versus NH_4^+ would not leak proton motive force in conduction. Thus, neither energy nor any counter ion would be needed to accumulate ammonia.

Note added in proof: In a recent publication (*37*), it is shown that Am conductance by RhBG in oocytes is electroneutral, in contrast to the currents reported by the same group for another homolog (*26*), and can explain observations of electric currents in oocytes by an indirect mechanism. If general to the Amt/MEP/Rh family (Fig. 1), this would eliminate the only data that we discuss as potentially inconsistent with the mechanism we deduce.

References and Notes

1. J. Broach *et al.*, *J. Bacteriol.* **128**, 86 (1976).
2. M. A. Knepper *et al.*, *Physiol. Rev.* **69**, 179 (1989).
3. M. H. Saier Jr. *et al.*, *Biochim. Biophys. Acta* **1422**, 1 (1999).
4. G. H. Thomas *et al.*, *Mol. Microbiol.* **37**, 331 (2000).
5. A. M. Marini *et al.*, *EMBO J.* **13**, 3456 (1994).
6. A. M. Marini *et al.*, *Mol. Cell. Biol.* **17**, 4282 (1997).
7. D. Blakey *et al.*, *Biochem. J.* **364**, 527 (2002).
8. S. L. Hackette *et al.*, *J. Biol. Chem.* **245**, 4241 (1970).
9. R. Tate *et al.*, *Mol. Plant Microbe Interact.* **11**, 188 (1998).
10. M. R. Atkinson, A. J. Ninfa, *Mol. Microbiol.* **29**, 431 (1998).
11. G. Coutts *et al.*, *EMBO J.* **21**, 536 (2002).
12. A. Javelle *et al.*, *J. Biol. Chem.* **279**, 8530 (2004).
13. A. M. Marini *et al.*, *Trends Biochem. Sci.* **22**, 460 (1997).
14. E. Soupene *et al.*, *J. Bacteriol.* **184**, 3396 (2002).
15. H. Nielsen *et al.*, *Protein Eng.* **10**, 1 (1997).
16. J. H. Park, M. H. Saier Jr. *J. Membr. Biol.* **153**, 171 (1996).
17. Z. S. Derewenda *et al.*, *J. Mol. Biol.* **252**, 248 (1995).
18. A. Roos, W. F. Boron, *Physiol. Rev.* **61**, 296 (1981).
19. N. A. Priver *et al.*, *Biochemistry* **32**, 2459 (1993).
20. D. Fu *et al.*, *Science* **290**, 481 (2000).
21. S. Khademi *et al.*, unpublished data.
22. E. Soupene *et al.*, *Proc. Natl. Acad. Sci. U.S.A.* **95**, 7030 (1998).
23. E. Soupene *et al.*, *Proc. Natl. Acad. Sci. U.S.A.* **99**, 3926 (2002).
24. M. Y. Wang *et al.*, *Plant Physiol.* **103**, 1259 (1993).
25. J. Meier-Wagner *et al.*, *Microbiology* **147**, 135 (2001).
26. U. Ludewig *et al.*, *J. Biol. Chem.* **277**, 13548 (2002).
27. C. M. Westhoff *et al.*, *J. Biol. Chem.* **277**, 12499 (2002).
28. C. M. Westhoff *et al.*, *J. Biol. Chem.* **279**, 17443 (2004).
29. R. M. Siewe *et al.*, *J. Biol. Chem.* **271**, 5398 (1996).
30. C. Sohlenkamp *et al.*, *Plant Physiol.* **130**, 1788 (2002).
31. A. M. Marini *et al.*, *Nature Genet.* **26**, 341 (2000).
32. E. Soupene *et al.*, *Proc. Natl. Acad. Sci. U.S.A.* **99**, 7769 (2002).
33. E. Soupene *et al.*, *Proc. Natl. Acad. Sci. U.S.A.* **101**, 7787 (2004).
34. J. H. Morais-Cabral *et al.*, *Nature* **414**, 37 (2001).
35. Y. Jiang *et al.*, *Nature* **417**, 523 (2002).
36. Materials and methods are available as supporting material on *Science* Online.
37. U. Ludewig, *J. Physiol. (London)*, in press; published online 29 July 2004 (10.1113/jphysiol.2004.067728).

38. We thank J. Finer-Moore for her enlightened counsel, J. Holten for his assistance at the Advanced Light Source (ALS) beamline 8.3.1, and M. Mann for assistance in molecular biology. E. Soupene and S. Kustu suggested structure determination of an AmtB, and we thank them for providing an *Aquifex amtB* clone pJES1331, a solubilized cell pellet, and partially purified *Aquifex* protein. Supported by NIH grant no. GM24485 (R.M.S.). Coordinates (accession codes: apo, 1U77; Am, 1U7G; and MA, 1U7C) and structure factors (accession codes: apo, RCSB023331; Am, RCSB023340; and MA, RCSB023336) of the structures have been deposited in the Research Collaboratory for Structural Bioinformatics Protein Data Bank.

Supporting Online Material

www.sciencemag.org/cgi/content/full/305/5690/1587/DC1
Materials and Methods
References and Notes

24 June 2004; accepted 5 August 2004

REPORTS

Experimental Observation of Nonlinear Traveling Waves in Turbulent Pipe Flow

Björn Hof,[1]*† Casimir W. H. van Doorne,[1]* Jerry Westerweel,[1] Frans T. M. Nieuwstadt,[1] Holger Faisst,[2] Bruno Eckhardt,[2] Hakan Wedin,[3] Richard R. Kerswell,[3] Fabian Waleffe[4]

Transition to turbulence in pipe flow is one of the most fundamental and longest- standing problems in fluid dynamics. Stability theory suggests that the flow remains laminar for all flow rates, but in practice pipe flow becomes turbulent even at moderate speeds. This transition drastically affects the transport efficiency of mass, momentum, and heat. On the basis of the recent discovery of unstable traveling waves in computational studies of the Navier-Stokes equations and ideas from dynamical systems theory, a model for the transition process has been suggested. We report experimental observation of these traveling waves in pipe flow, confirming the proposed transition scenario and suggesting that the dynamics associated with these unstable states may indeed capture the nature of fluid turbulence.

Turbulence is one of the most common examples of complex and disordered dynamical behavior in nature. Typically, the motion of clouds, weather patterns, river flows, and even the flow from a faucet are turbulent. Yet the way in which turbulence arises and sustains itself is not understood even in laboratory experiments with well-controlled boundary conditions. The first study of this kind was undertaken by Reynolds (*1*) in 1883. He investigated the transition to turbulence in pipe flow and his observations have posed a riddle ever since. Whereas stability theory predicts that pipe flow will remain laminar for all flow rates (*2*), in practice pipe flow becomes turbulent even at moderate speeds. In contrast to other laminar-turbulence transitions, where primary and secondary instabilities of the laminar flow provide guidance, the transition process in pipe flow has remained a near total mystery. In pipes, turbulence sets in suddenly and fully, with no intermediate states and without a clear stability boundary.

Pipe flow can be described by a single dimensionless parameter, the Reynolds number $Re = UD/\nu$, where U is the mean (or bulk) flow speed, D the pipe diameter, and ν the kinematic viscosity of the fluid. In the laminar state, the flow profile is parabolic and the flow rate is proportional to the pressure

gradient. This picture changes markedly when the flow rate is increased and turbulent flow commences. The ensuing flow is temporally and spatially highly disordered and viscous drag and dissipation are strongly increased. In typical pipe flows, turbulence sets in spontaneously at Reynolds numbers as low as 2000; however, in carefully designed experiments the transition point can be delayed to Reynolds numbers as large as 100,000 (*3*). On the basis of the recent discovery of traveling wave and periodic solutions to the governing Navier-Stokes equation (*4*–*10*), a new transition scenario for pipe and related shear flows has been suggested (*11*–*13*). All of the observed solutions are believed to be unstable and cannot persist individually in practical flows because of the inevitable presence of ambient noise. Yet as the Reynolds number is increased, more and more of these unstable solutions are believed to arise. In their multitude they can support long-lived disordered flows in which the flow state transiently visits these unstable solutions before returning to the laminar state. In mathematical terms, the unstable states form a chaotic repellor in phase space (*11*), which gives rise to long-lived turbulent transients. As the Reynolds number is increased further, this chaotic repellor is believed to evolve into a turbulent attractor, i.e., an attracting region in phase space, dynamically governed by the large number of unstable solutions, which sustains disordered turbulent flow indefinitely. The laminar state is still stable, but it is reduced from a global to a local attractor. As the Reynolds number increases, the basin of the turbulent attractor grows, whereas that of the laminar state diminishes (i.e., the number of initial conditions that lead to turbulent flow markedly increases). Consequently, smaller and smaller perturbations to the laminar flow are sufficient to cause a transition to turbulence. Some consensus between theoretical ideas and actual experimental observations has been found in that the stability boundary, and hence the basin of attraction of the laminar state, indeed decreases in proportion to $1/Re$ (*14*). However, direct evidence that unstable traveling waves are relevant for turbulent flows in practice is missing.

For the dynamics of flow patterns in shear flows, Waleffe (*8*, *9*, *15*–*17*) has proposed a self-sustaining process. Vortices with a streamwise orientation move fast fluid from the center toward the wall and simultaneously lift slow fluid from the walls to the center, creating local anomalies in the streamwise velocity called streaks. These streaks become inflexionally unstable. Nonlinear self-interaction of the unstable modes regenerates the streamwise vortices closing the feedback loop, thus sustaining these flow states against viscous decay. The traveling waves reflect this process. Hence, the most important structural features of these traveling waves are the streamwise vortices and streaks. The wavy nature of these states can most readily be identified in the periodic modulation of the low-speed streaks. The waves travel in the streamwise direction at a phase speed typically slightly larger than the bulk velocity (*4*, *5*). Because all of the numerically observed traveling waves are (most likely) unstable, they cannot persist in practical pipe flows but may be observable as transients, if indeed they are relevant to the turbulent flow. The aim of this study is to identify these traveling waves in experimental turbulent pipe flow.

A schematic of the experimental set-up is shown in Fig. 1 (supporting online material text) (*18*, *19*). For the present measurements, fully developed laminar pipe flow [i.e., for which the velocity profile was parabolic (fig. S3)] was destabilized 350 pipe diameters from the inlet by means of injecting an impulsive jet for 1.5 s ($\sim 1.9D/U$) through a hole of 1-mm diameter in the pipe wall. The jet was injected orthogonally to the main flow with a volume flux of approximately 50% of the flux in the pipe. The so-created turbulent flow region was inspected 150 pipe diameters downstream of the injection point with a 500-Hz high-speed stereoscopic particle image velocimetry system. As found in our own studies and in agreement with previous observations (*20*, *21*), a distance of $150D$ is more than sufficient to allow all transients inflicted by the perturbation mechanism to subside. Hence, the observations presented here can be regarded as typical flow structures representative for turbulent pipe flow at the particular Reynolds number. For visualization purposes, the water was seeded with 10-μm tracer particles that were neutrally buoyant, and a radial cross-sectional plane of the pipe was illuminated by a frequency-doubled pulsed neodymium-doped yttrium lithium fluoride laser. This plane was viewed by two cameras positioned in forward scatter on opposite sides of the light sheet at 45° to the observation plane (figs. S1 and S2). The full three-component velocity field at about 2600 points in the observation plane was reconstructed from the displacement of the tracer particles between subsequent images recorded by the cameras (*22*). The passage of turbulent structures was recorded in a series of 1000 contiguous measurements at sampling frequencies between 60 and 500 Hz. A high degree of precision (figs. S4 to S8) was achieved with the use of a test section that minimizes optical distortion and an optimized calibration procedure to align the stereoscopic camera set-up (fig. S2) (*19*).

Our first investigation is concerned with localized turbulent structures, called "puffs" (*21*), which occur at relatively low Reynolds numbers ($1800 < Re < 2500$). Puffs are isolated patches of turbulent flow, which are advected downstream at ~95% of the bulk velocity. Turbulent puffs typically extend 5 to ~20 pipe diameters, depending on the Reynolds number. The transition regions between the laminar flow and the turbulent flow at either end of the puff are referred to as the downstream and upstream edge, and these can be identified by the characteristic velocity change during the passage of a puff (*20*, *21*). A velocity field in a cross-sectional plane close to the upstream edge of a puff measured at $Re = 2000$ is shown in Fig. 2A. Here, the laminar flow profile is subtracted from the measured downstream velocity component. Regions of high velocity relative to the lam-

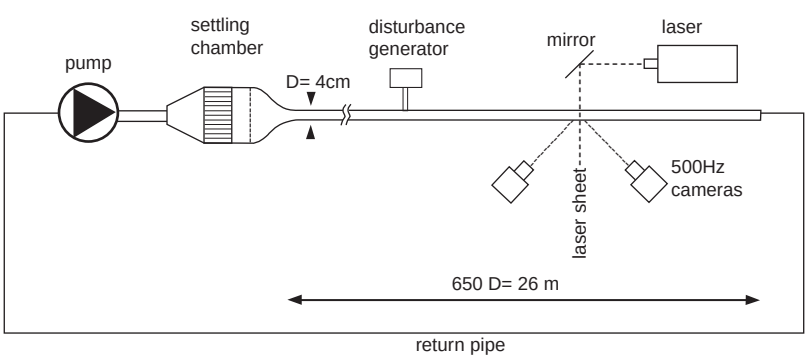

Fig. 1. Experimental apparatus: Water is pumped by way of a settling chamber into a 26-m-long straight pipe that has a diameter of $D = 4$ cm. The settling chamber as well as the inlet shape were designed to minimize disturbances from the inlet (*13*). The entire pipe is thermally insulated to avoid heat convection, which would distort the flow profile. The fully developed laminar flow is perturbed $350D$ from the inlet, and particle image velocimetry measurements are performed another $150D$ downstream.

[1]Laboratory of Aerodynamics and Hydrodynamics, Delft University of Technology, Leeghwaterstraat 21, 2628 CA Delft, Netherlands. [2]Fachbereich Physik, Philipps-Universität Marburg, 35032 Marburg, Germany. [3]Department of Mathematics, University of Bristol, Bristol, BS8 1TW, UK. [4]Departments of Mathematics and Engineering Physics, University of Wisconsin, Madison, WI 53706, USA.

*These authors contributed equally to this work.
†To whom correspondence should be addressed. E-mail: b.hof@wbmt.tudelft.nl

inar profile are shown in red, regions of low velocity relative to the laminar profile are shown in blue, and transverse components are indicated by arrows. Whereas the wall region contains six distinct high-speed streaks, the central region is occupied by a large low-speed streak extending three arms in the radial direction. This streak configuration is in notable agreement with a C_3 symmetric traveling wave (C_m specifies an m-fold rotational symmetry) found by Faisst and Eckhardt (*4*) (Fig. 2B). Generally, the flow is dominated by the streaks, and the spanwise motions are critical but much weaker. The cross-stream motions are therefore more quickly overwhelmed by fluctuations resulting from the inherent instabilities of the traveling waves. Although the experimentally observed state does not display a full periodic cycle in the streamwise direction, certain features of the state persist over a large portion of the turbulent puff. In particular, we observed that the high-speed streaks are considerably more static than the low-speed streaks, which was also observed numerically (*4*, *5*). To quantify the persistence of the symmetry features, we calculated an azimuthal correlation of the streamwise velocity component in the vicinity of the pipe wall. A correlation calculated from the measurements close to the upstream end of the puff is shown in Fig. 3A. Peaks at 60°, 120°, and 180° manifest the presence of six distinct high-speed streaks in the near-wall region. The correlation curve in Fig. 3B, measured close to the downstream (leading) edge of the puff, only has a peak at 120°. The flow pattern observed here consists of three high-speed streaks close to the wall spaced at 120° and a low-speed region in the central part of the pipe. Traveling wave modes with a C_3 symmetry containing three high-speed streaks in the near-wall region have also been calculated numerically (*5*). The resulting correlations measured along the entire puff are shown in Fig. 3C. Throughout the downstream end of the puff, a single correlation peak was found. At a distance of about 4D, the single peak bifurcates into three peaks (at about 60°, 120°, and 180°), which persist throughout the upstream part of the turbulent puff. Visual inspection of the velocity fields confirms that indeed three high-speed streaks are present throughout the downstream section of the puff and six

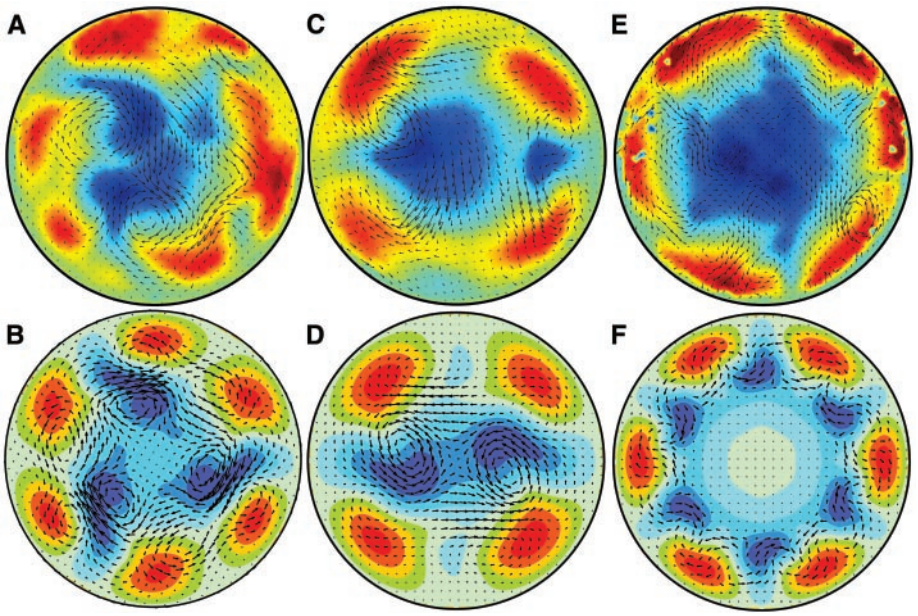

Fig. 2. Comparison of experimentally (top) and numerically (bottom) observed streak patterns. Velocity components in the plane are indicated by arrows, and the downstream component is indicated by color coding, where red or blue signifies velocities faster or slower than the parabolic profile, respectively. The color coding for the experimental flow patterns (top row) ranges from plus (dark red) to minus (dark blue) 0.6U; the numerical flows (bottom row) range from plus (dark red) to minus (dark blue) 0.4U. The maximum in-plane velocities are one order of magnitude smaller than the maximum out-of-plane components. (**A**) Experimentally observed state in turbulent puff at $Re = 2000$. (**B**) Cross-sectional slice through a C_3 symmetric streamwise traveling wave observed numerically at $Re = 1250$ (*4*, *5*). (**C**) C_2 symmetric state observed in a turbulent puff at $Re = 2500$. (**D**) Corresponding numerical C_2 traveling wave ($Re = 1360$). (**E**) C_6 symmetric state found in the experiment at $Re = 5300$ for fully turbulent flow. The streak configuration in the near-wall region resembles that of a numerical C_6 traveling wave (**F**) ($Re = 2900$). The dominance of the low-speed streak in the central part of (E) is more characteristic of a C_3 traveling wave, suggesting that (E) may result from nonlinear interactions of C_3 and C_6 traveling waves.

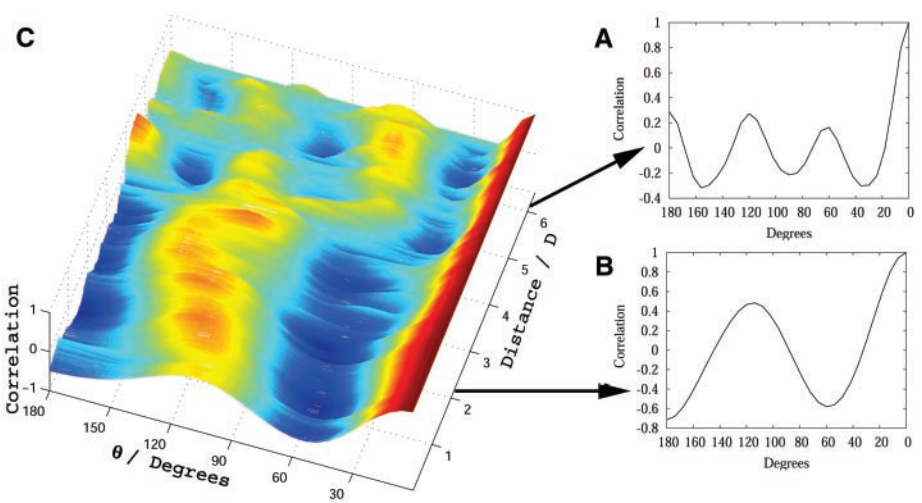

Fig. 3. (**A**) Azimuthal correlation close to the upstream edge of a puff ($Re = 2000$). (**B**) Azimuthal correlation close to the downstream edge of the puff. (**C**) Display of the azimuthal correlations from 500 consecutive measurements, taken while a turbulent puff traveled through the measurement plane. Distances are measured with respect to the first measurement, which was taken at the downstream end of the puff. The temporal spacing of the measurements was converted into a spatial one by multiplication with the advection speed (Taylor's hypothesis). This approximation is justified because the puff advection speed is more than an order of magnitude larger than the in-plane velocity components. Colors represent the amplitude of the correlation ranging from dark red (+1) for maximal correlation to dark blue (–1) for anticorrelated data. A single correlation peak is observed for distance <4, which then splits up into three peaks for distance >4, indicating a change in the streak pattern from three to six high-speed streaks in the near-wall region. Correlations were calculated according to $C(\phi,r)=\int_0^{2\pi} U(\phi,r)U(\phi+\theta,r)d\theta$ for five radii in the interval $0.9 \geq r/(D/2) \geq 0.7$, where r is the radial distance from the pipe centerline, and for each measurement plane the radius showing the maximum correlation (largest difference between the maxima and minima) was selected.

streaks are present for the remainder of the puff. Qualitatively, the same result has been found for all puffs investigated at this Reynolds number. This result is surprising, in that features of the turbulent puff—i.e., the number and spacing of high-speed streaks—appear to be determined by a small number of unstable states.

The C_2 traveling wave, shown in Fig. 2C, has been observed at $Re = 2500$. Again, the streak pattern is in excellent agreement with that of its numerical counterpart (Fig. 2D). The numerically calculated traveling waves in Figs. 2 and 4 are shown for lower Reynolds numbers than the experimentally observed traveling waves. As pointed out by Wedin and Kerswell (*5*), the change in the form of the numerical solutions for an increasing Reynolds number is very small, and the main features and symmetry properties remain unchanged. The flow state (Fig. 2E) was observed in a turbulent slug (*21*) at $Re = 5300$. The streak/vortex configuration in the near-wall region resembles a numerically observed C_6 traveling wave (Fig. 2F). Overall, the measured structure is more likely to be a combination of C_6 and C_3 modes (Fig. 2), which is in accord with the increased complexity of the observed structures at higher Reynolds numbers. In this Reynolds number regime, excellent agreement was found for statistical quantities such as the mean velocity and root mean square velocity fluctuations between the experimental measurements and numerical simulations of turbulent flow (figs. S6 to S8) (*19*, *23*, *24*). For plane Couette and channel flow, the exact traveling waves in the numerical model already capture turbulence statistics (*17*) remarkably well, which can be seen as an indication of the intrinsic role of the traveling wave states to the turbulent flow.

Finally, we observed a C_4 symmetric traveling wave at $Re = 3000$ (Fig. 4).This wave transient showed a periodic modulation similar to that of a C_4 symmetric wave over several periods and allowed us to estimate its wavelength ($\pm$SD) to $(1.1 \pm 0.15)\ D$. The periodic modulation is most evident in the up and down motion of the left low-speed streak shown in Fig. 4A. The three figures show half of one periodic cycle. The corresponding C_4 traveling wave (Fig. 4B) has an optimal wavelength of $0.97D$, which is in excellent agreement with the experimentally determined value. As in Fig. 2E, the central low-speed region of the experimental traveling wave is more pronounced than that of its numerical counterpart.

The experimental observation of unstable states can be rationalized by comparing the characteristic time scales. The experimental observation time is about $10D/U$ and the largest unstable Lyapunov exponent is about 0.07, implying a characteristic time scale for the decay of a traveling wave transient of about $14D/U$. Thus, if the experimentally observed turbulent state is close to a three-dimensional traveling wave at one instance, the observation time is not long enough for it to evolve far away.

In conclusion, signatures of unstable traveling wave modes have been observed in surprising clarity and agreement with numerical studies (*4*, *5*). Spatial features of these wave states persist over large time intervals in turbulent pipe flow. These insights into the dynamics and symmetry of streaks open up further avenues for application of turbulent and chaos control (*25*, *26*) strategies.

These observations support a theoretical scenario in which the turbulent state is organized around a few dominant traveling waves. Although such a proposal is in line with dynamical systems ideas (*27*), there has been no experimental or theoretical evidence for its applicability to shear flow turbulence before the present study. The observation of the traveling wave states shows that concepts from dynamical systems theory can contribute greatly to our understanding of turbulence. Indeed, because unstable solutions have been calculated for a variety of shear flows (*4*–*10*), we speculate that these states play a universal role in shear flow turbulence.

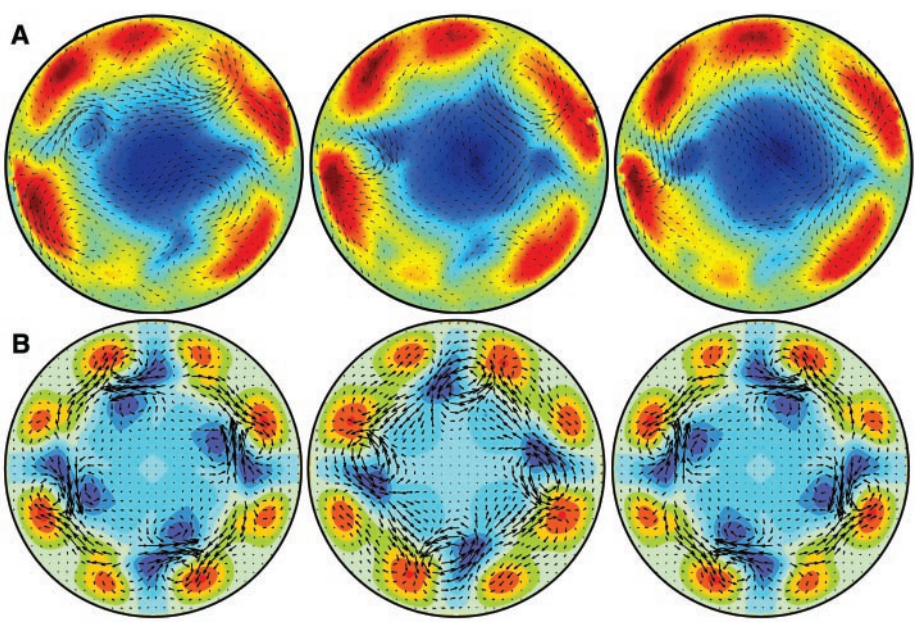

Fig. 4. Velocity scales and color coding are the same as for Fig. 2. (**A**) Half a wavelength of a C_4 traveling wave transient observed in fully turbulent flow at $Re = 3000$. The frames are spaced by $\lambda/4$ where the wavelength ($\pm$SD) was measured as $\lambda = 1.1D \pm 0.15$. The low-speed streak on the left-hand side shows the clearest modulation. (**B**) Exact C_4 traveling wave ($Re = 1650$) as observed in the numerical simulations. Again, the frame spacing is $\lambda/4$ and the wavelength is $\lambda = 0.97D$. The strong low-speed streak at the center of the experimental traveling wave is not found in the numerical traveling wave and is more characteristic for a C_2 traveling wave. In analogy to the C_6 symmetric wave in Fig. 2E, this suggests that the experimental state may result from interactions of C_4 and the C_2 traveling waves.

References and Notes

1. O. Reynolds, *Proc. R. Soc. London* **35**, 84 (1883).
2. P. G. Drazin, W. H. Reid, *Hydrodynamic Stability* (Cambridge Univ. Press, Cambridge, 1981).
3. W. Pfenniger, in *Boundary Layer and Flow Control*, G. V. Lachman, Ed. (Pergamon, Oxford, 1961), pp. 970–980.
4. H. Faisst, B. Eckhardt, *Phys. Rev. Lett.* **91**, 224502 (2003).
5. H. Wedin, R. R. Kerswell, *J. Fluid Mech.* **508**, 333 (2004).
6. M. Nagata, *J. Fluid Mech.* **217**, 519 (1990).
7. R. M. Clever, F. H. Busse, *J. Fluid Mech.* **344**, 137 (1997).
8. F. Waleffe, *Phys. Rev. Lett.* **81**, 4140 (1998).
9. F. Waleffe, *J. Fluid Mech.* **435**, 93 (2001).
10. G. Kawahara, S. Kida, *J. Fluid Mech.* **449**, 291 (2001).
11. H. Faisst, B. Eckhardt, *J. Fluid Mech.* **504**, 343 (2004).
12. A. Schmiegel, B. Eckhardt, *Phys. Rev. Lett.* **79**, 5250 (1997).
13. B. Eckhardt, A. Mersmann, *Phys Rev. E* **60**, 509 (1999).
14. B. Hof, A. Juel, T. Mullin, *Phys. Rev. Lett.* **91**, 244502 (2003).
15. J. M. Hamilton, J. Kim, F. Waleffe, *J. Fluid Mech.* **287**, 317 (1995).
16. F. Waleffe, *Phys. Fluids* **9**, 883 (1997).
17. F. Waleffe, *Phys. of Fluids* **15**, 1517 (2003).
18. A. A. Draad, G. D. C. Kuiken, F. T. M. Nieuwstadt, *J. Fluid Mech.* **377**, 267 (1998).
19. C. W. H. van Doorne, thesis, Delft University of Technology (2004).
20. A. G. Darbyshire, T. Mullin, *J. Fluid Mech.* **289**, 83 (1995).
21. I. J. Wygnanski, F. H. Champagne, *J. Fluid Mech.* **59**, 281 (1973).
22. A. K. Prasad, *Exp. Fluids* **29**, 103 (2000).
23. J. G. M. Eggels *et al.*, *J. Fluid Mech.* **268**, 175 (1994).
24. C. W. H. van Doorne, J. Westerweel, F. T. M. Nieuwstadt, *Proceedings of the EUROPIV 2* (Springer-Verlag, Zaragoza, Spain, 2003).
25. T. Shinbrot, C. Grebogi, E. Ott, J. A. Yorke, *Nature* **363**, 411 (1993).
26. H. Choi, P. Moin, J. Kim, *J. Fluid Mech.* **262**, 75 (1994).
27. I. Procaccia, *Nature* **333**, 498 (1988).

28. Supported by the European Union network on stirring and mixing (B.H.), the Foundation of Fundamental Research on Matter (B.H., C.W.H.v.D., F.T.M.N., and J.W.), Deutsche

F.T.M.N., and J.W.), Deutsche Forschungsgemeinschaft (H.F. and B.E.), the Engineering and Physical Sciences Research Council (H.W. and R.R.K.) and the NSF (F.W.). Part of the experimental equipment was supplied by La Vision GmbH.

Supporting Online Material
www.sciencemag.org/cgi/content/full/305/5690/1594/DC1
Materials and Methods
Figs. S1 to S8
Tables S1 and S2
References

17 May 2004; accepted 30 July 2004

Mesophase Structure-Mechanical and Ionic Transport Correlations in Extended Amphiphilic Dendrons

B.-K. Cho,[1]* A. Jain,[1]* S. M. Gruner,[2] U. Wiesner[1]†

We have studied the self-assembly of amphiphilic dendrons extended with linear polyethylene oxide (PEO) chains and their ion complexes. Keeping the dendron core and linear PEO chain compatible allows for the combination of dendritic core-shell and conventional block copolymer characteristics for complex mesophase behavior. An unexpected sequence of crystalline lamellar, cubic micellar ($Pm\bar{3}n$), hexagonal columnar, continuous cubic ($Ia\bar{3}d$), and lamellar mesophases is observed. Multiple phase behavior within single compounds allows for the study of charge transport and mechanical property correlations as a function of structure. The results suggest an advanced molecular design concept for the next generation of nanostructured materials in applications involving charge transport.

The generation of supramolecular structures by self-assembly of molecular building blocks has become a powerful tool in designing enhanced material properties (*1*, *2*). Molecular engineering of the interface in microphase-separated domains is believed to be a key to the precise manipulation of supramolecular structures. To this end, a variety of molecular building blocks with rod (*3*), disk (*4*), and linear (*5*) type architecture have already been combined. Recently, dendrimers and their segments, dendrons, have fostered scientific interest as another class of building blocks. They are attractive because their particular shape introduces curved interfaces and because large numbers of functional groups can be readily introduced into a single molecule (*6*–*8*). Their unique structural features might lead to phase behavior that is quite different from that of conventional linear building blocks (*9*). Indeed, the dendrimer/dendron-periphery interface has been systematically controlled by either tethering different generations or periphery groups (*10*–*12*), and micellar structures with complicated lattices have been found in benzyl ether–based dendrons as a function of temperature (*13*, *14*). Despite theoretical predictions of a rich phase behavior (*15*), observed phases to date reveal only lamellar, columnar, or micellar packing. In particular, the existence of three-dimensional (3D) cubic network structures important for potential applications has not been demonstrated.

Here we report on third-generation amphiphilic dendrons extended by linear polyethylene oxide (PEO) chains synthesized as described in (*16*). Although several molecules with varying PEO molecular weights were studied, we will focus on two compounds, **1** and **2** (Fig. 1), which exhibit multiple phases that combine the behavior of linear block copolymers with that of dendritic systems. The mesophases were accessible through temperature changes and include crystalline lamellar (k_1, k_2), micellar (mc), hexagonal columnar (hex), continuous cubic (cc), lamellar (lam), and disordered (dis). Molecular masses of compounds **1** and **2** were determined to be 4600 and 7500 g/mol by matrix-assisted laser desorption ionization time-of-flight (MALDI-TOF) mass spectrometry. Based on these molecular masses and the density of each block, the hydrophilic volume fractions (f) were calculated to be 0.41 and 0.62 for **1** and **2**, respectively. Polydispersities (M_w/M_n) from MALDI-TOF mass spectrometry and gel permeation chromatography (GPC) were found to be less than 1.05. In contrast to most previous combinations of coil-dendron systems, the interface of these linearly extended dendrons is modeled in the middle of the dendritic structure rather than at the focal point (*17*–*20*). The hydrophilic part is composed of linear PEO plus a PEO-like dendritic core, whereas the hydrophobic fraction consists of eight docosyl peripheries (*21*, *22*). In this way, structural features of phase-separated dendritic core-shell architectures are combined with the ability to fine tune volume fractions through simple linear chain extension. Furthermore, linear and branched chain topologies are combined within one domain of the microphase-separated material.

Thermal behavior of compounds **1** and **2** was studied by differential scanning calorimetry (DSC) and transitions corroborated by dynamic mechanical spectroscopy (DMS) and temperature-dependent small-angle x-ray scattering (SAXS). The results are summarized in Table 1. DSC was run at a rate of 10°C/min, and transition temperatures were determined at peak maxima. Isochronal temperature step measurements at a frequency of 0.5 rad/s and shear amplitude in the linear regime (<2%) were performed on an advanced rheometrics expansion system (ARES) to identify the melting temperatures of the docosyl peripheries, order-order transitions (OOTs), and order-disorder transitions (ODTs). In DSC data, **1** and **2** show two

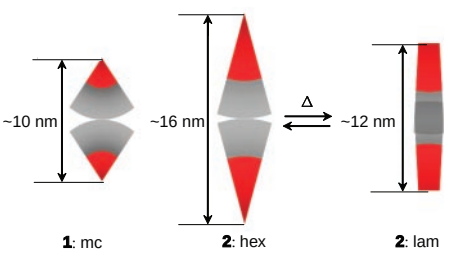

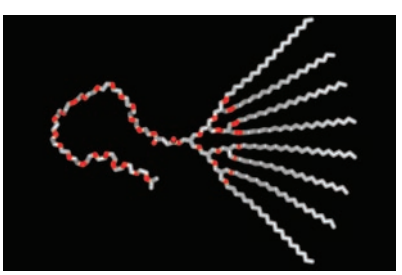

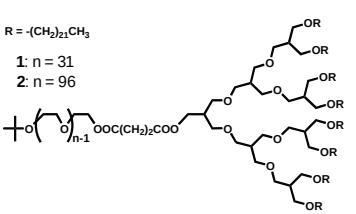

Fig. 1. Molecular architecture of extended amphiphilic dendrons **1** and **2**. Oxygen-containing segments are shown in red. (**Top**) Schematics of the type of molecular packing in different mesophases along with the respective dimensions consistent with SAXS data analyses and molecular models (red, hydrophilic parts; gray, hydrophobic parts). The schematics are meant to illustrate aspects of the local packing behavior only.

Department of Materials Science and Engineering and [2]Department of Physics, Cornell University, Ithaca NY 14853.
*These authors contributed equally to this work.
†To whom correspondence should be addressed. E-mail: ubw1@cornell.edu

distinct transitions corresponding to melting of the linear PEO chains and docosyl peripheries. Upon further heating, both **1** and **2** form ordered mesophases and subsequently disordered liquids.

All ordered microstructures were characterized using temperature-variable SAXS experiments. A summary of measured distances and corresponding indexation for each mesophase is given in Table 2. The extended amphiphilic dendrons are all consistent with lamellar structures in the crystalline states (Fig. 2B). After PEO (12°C) and periphery (63°C) melting and before isotropization, the SAXS pattern of **1** shows a large number of reflections (Fig. 2A). They can be indexed consistently as a cubic structure with $Pm\bar{3}n$ symmetry. After melting (45°C PEO, 63°C periphery), **2** shows three distinct mesophases as a function of temperature before isotropization. For the first mesophase, the SAXS pattern shows five reflections, consistent with a hexagonal mesophase (Fig. 2C). As the temperature increases, two intense and several weak reflections appear (Fig. 2D), consistent with a cubic structure of $Ia\bar{3}d$ symmetry. Upon further heating, **2** displays two reflections with a q-spacing ratio of 1:2. Although only two peaks are seen, the equal spacing between the peaks and the occurrence at relatively large angles are suggestive of a lamellar mesophase (Fig. 2E).

Despite an intermediate hydrophilic volume fraction $f = 0.41$ of **1**, the cubic mesophase with $Pm\bar{3}n$ symmetry is expected to be a micellar structure (Fig. 3A). This is consistent with the observation that **2,** with higher $f = 0.62$, shows a columnar mesophase after melting (Fig. 3C). In the micellar mesophase, the hydrophilic parts occupy the core encapsulated by the hydrophobic peripheries, as expected from the inherent interfacial curvature. Cubic structures with $Pm\bar{3}n$ symmetry have been found in only a few bulk systems with other molecular structures such as taper-shaped small amphiphiles and cone-shaped dendrons (*23*–*25*), and have recently been predicted for branched block copolymer type systems (*15*).

Most notable, however, is the cubic mesophase with $Ia\bar{3}d$ symmetry at intermediate temperatures of **2**. In Fig. 3D, this symmetry is represented by a gyroidlike continuous structure, consistent with conductivity measurements and theoretical predictions for linear-branched block copolymers (*15*). In contrast, dendrimers/dendrons have mostly been shown to self-organize into columnar or micellar structures due to their taper/cone-shaped molecular architecture (*24*–*27*). Furthermore, the mesophase sequence in which the $Ia\bar{3}d$ phase is observed upon heating—i.e., hexagonal, $Ia\bar{3}d$, lamellar, disordered—is quite unusual for block copolymers. It is not readily understood in the context of simple diblock copolymer phase diagrams (*15*, *28*). The sequence is likely due to a larger expansion parallel to the interface as a function of temperature of the linear PEO/branched (dendritic) section of the molecules versus the hydrophobic docosyl section. The effect thus may be explained by similar arguments governing packing of surfactant molecules (Fig. 1) (*29*).

The linear viscoelastic properties of soft materials are sensitive to morphology. Measurements of the temperature dependence of the elastic shear modulus (G') with a dynamic mechanical spectrometer are in good agreement with the results of DSC and SAXS studies. In Fig. 4A, after a large drop from the crystalline lamellar phase, the cubic mesophase with $Pm\bar{3}n$ symmetry of **1** shows high G' values ($\sim 10^6$ Pa), which can be attributed to the 3D cubic symmetry (*30*). Upon heating into the disordered state, the modulus drops precipitously. In the case of **2**, G' values nicely follow the transitions as observed by DSC and/or SAXS and, after melting, are highest for the intermediate $Ia\bar{3}d$ cubic structure, which shows elastic behavior similar to that of the $Pm\bar{3}n$ phase of **1** (Fig. 4B). Despite the lower temperatures, the hexagonal phase exhibits almost an order of magnitude lower G' values. At higher temperatures, values drop more than two orders of magnitude into the lamellar phase, before they finally plummet upon heating into the disordered phase.

A powerful tool for elucidating structural features like dimensionality and connectivity is measuring the transport behavior within one domain of the phase-separated material (*31*, *32*). To this end, we prepared ion-doped extended amphiphilic dendrons **1-Li$^+$** and **2-Li$^+$**, adding lithium triflate salt that is selectively soluble in the hydrophilic parts. To ensure minimal deviations in volume fraction from undoped **1** and **2**, we chose Li^+ concentrations per ethylene oxide to be 0.02. The transition temperatures of ion-doped materials were first characterized by DSC, DMS, and SAXS (Table 1). Whereas the melting transitions, as observed by DSC, were essentially unchanged, ion-doping stabilized the mesophases, resulting in a high-temperature shift of the transition temperatures (Fig. 4, A and B). The stabilization of both the mc phase of **1** and the hex phase of **2** by about 50°C can be attributed to the increased interaction parameter, χ, upon doping with lithium salts. It may also be due to the rigidifying of the PEO chains upon Li^+ addition. Surprisingly, for **2-Li$^+$** at temperatures above 170°C, SAXS diffractograms are obtained that are consistent with a cubic mesophase with $Ia\bar{3}d$ symmetry (Fig. 2F). This is in marked contrast to the case of linear block copolymers (*33*), in which even small amounts of polar ions have been shown to force the system into a stronger segregation regime, causing a switch from an $Ia\bar{3}d$ bicontinuous cubic phase to a hexagonal columnar mesophase. The lamellar mesophase and isotropic liquid phase of **2** are not reached because ion-doped extended dendrons begin to degrade near 195°C, as observed by thermal gravimetric analysis (*34*).

Ionic conductivity was measured with an impedance analyzer in the frequency range of 10^1 to 10^6 Hz. Direct conductivity was obtained by extrapolation to zero frequency (*35*). In Fig. 4C, the changes in conductivity as a function of temperature for ion-doped

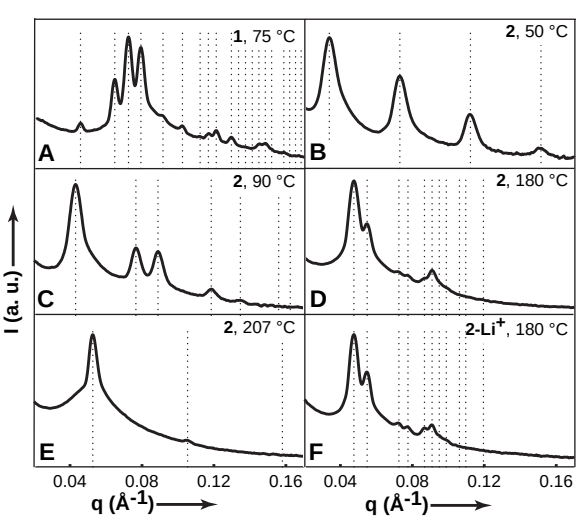

Fig. 2. SAXS spectra for **1** (**A**), **2** (**B** to **E**), and **2-Li$^+$** (**F**) at different temperatures plotted against the scattering wave vector, q ($= 4\pi\sin\theta/\lambda$). The vertical dotted lines correspond to the expected peaks for $Pm\bar{3}n$ cubic (A), lamellar (B and E), hexagonal columnar (C), and $Ia\bar{3}d$ cubic (D and F) lattices.

Table 1. Phase behavior of **1**, **2**, **1-Li$^+$**, and **2-Li$^+$**. k, crystalline; mc, micellar; hex, hexagonal columnar; lam, lamellar; cc, continuous cubic; dis, disordered; dec, decomposition.

Compound	Phase transitions (°C)
1	k_1 12 k_2 63 mc 93 dis
2	k_1 45 k_2 63 hex 114 cc 190 lam 226 dis
1-Li$^+$	k_1 16 k_2 63 mc 139 dis
2-Li$^+$	k_1 44 k_2 63 hex 170 cc 195 dec

compounds **1-Li**$^+$ and **2-Li**$^+$ are in excellent agreement with the temperature-dependent behavior as observed by DSC (Table 1) and DMS (Fig. 4, A and B). For **1-Li**$^+$, the most interesting feature in the conductivity curve occurs at the docosyl periphery melt transition where the conductivity drops from 4.6 $\times 10^{-6}$ to 1.2 $\times 10^{-9}$ S/cm. This large reduction in the conductivity is consistent with the interpretation of a 2D layer structure melting into a micellar structure in which hydrophilic micelles are embedded in a hydrophobic matrix (Fig. 3, A and B). Thus, lithium ions are preferentially confined in micelles, preventing fast long-range transport. The huge conductivity drop by more than three orders of magnitude at the transition can potentially be used as a supramolecular on-off switch. Indeed, the mechanical properties (G′ $\sim 10^6$ Pa) of this micellar mesophase are sufficient to encourage such an application (Fig. 4A). Interestingly, no discontinuity is observed for **1-Li**$^+$ upon disordering at 139°C. This is consistent with recent studies of the order-disorder transition (ODT) in sphere-forming diblock copolymer melts, demonstrating that at the transition, the long-range order (or lattice) of micelles disappears whereas micelles persist up to much higher temperatures (*36*, *37*).

The most complex transport behavior is found for **2-Li**$^+$, with four different conductivity regimes strongly correlated to the mesophase behavior of this compound. At the first melting transition (PEO), conductivity rises by one to two orders of magnitude, whereas at the second (periphery melting), it drops by about an order of magnitude, going from a crystalline lamellar into the hexagonal mesophase. At the onset of the *Ia*$\bar{3}$*d* cubic mesophase, it rises again by an order of magnitude and finally reaches values of about 1.5 $\times$ 10^{-4} S/cm at the highest temperatures measured. The observation of a distinct step in conductivity upon PEO melting for **2-Li**$^+$, which was not observed for **1-Li**$^+$, is consistent with a substantially increased degree of crystallinity for this compound due to the longer PEO chains. All other transition behavior can be rationalized by assuming that the hydrophilic parts responsible for ion transport form cylinder cores in both the hexagonal and cubic mesophases, because the conductivity in the present nonaligned microstructures is then expected to be roughly proportional to the dimensionality of the structure (*38*). Following this argument, periphery melting leads to a transition from a 2D lamellar to a 1D hexagonal columnar phase, resulting in a sharp decrease in the ion conductivity. The transition into the cubic phase increases the dimensionality to three, resulting in the highest conductivity values of about 1.5 $\times$ 10^{-4} S/cm. This analysis also reveals that the *Ia*$\bar{3}$*d* cubic structure is continuous. We note that the present conductivity values of the cubic structure without macroscopic orientation efforts are comparable to those of aligned lamellar structures at similar temperatures and lithium concentrations (*39*, *40*). Furthermore, this mesophase shows outstanding mechanical properties (G′ $\sim 10^6$ Pa for **2-Li**$^+$) as expected for a continuous structure (Fig. 4B), making it particularly attractive for applications involving charge transport.

In conclusion, we have demonstrated that the present extended amphiphilic dendrons self-assemble into an unexpected sequence of crystalline lamellar, *Pm*$\bar{3}$*n* micellar cubic, hexagonal columnar, *Ia*$\bar{3}$*d* continuous cubic, and lamellar mesophases as a function of volume fraction and temperature. We revealed local core-shell topologies by monitoring the ion conductivity of ion-doped samples, which is strongly correlated to mesophase behavior and mechanical properties. We were thus able to study charge transport within a nanostructured material in which the conducting medium is confined to either micelles (zero-dimensional), cylinders (1D), or lamellae (2D), or is a continuous (3D) network throughout the entire macroscopic sample (Fig. 3). These results may

Table 2. The measured distances ($d_{meas} = 2\pi/q$; see Fig. 2 legend) and corresponding (*hkl*) indexation data of the observed SAXS reflections for each mesophase. d_{calcd} is the calculated distance based on the lattice parameter of each structure. Depending on the strength of the peak, the accuracy of measurement is generally better than 0.5 Å.

hkl	d_{meas} (Å)	d_{calcd} (Å)
Pm$\bar{3}$*n cubic structure with lattice parameter of 194.0 Å in Fig. 2A*		
110	137.2	137.2
200	97.0	97.0
210	86.8	86.8
211	79.2	79.2
220	69.0	68.7
310	61.5	61.4
320	53.7	53.8
321	51.9	51.9
400	48.5	48.5
420	43.4	43.4
421	42.3	42.3
2D hexagonal structure with lattice parameter of 162.2 Å in Fig. 2C		
100	140.5	140.5
110	81.1	81.1
200	70.1	70.3
210	53.1	53.1
Ia$\bar{3}$*d cubic structure with lattice parameter of 324.4 Å in Fig. 2D*		
211	132.3	132.3
220	114.9	114.7
321	87.4	86.7
400	81.6	81.1
420	72.4	72.5
332	69.2	69.1
Lamellar structure with lattice parameter of 119.2 Å in Fig. 2E		
100	119.2	119.2
200	59.9	59.6

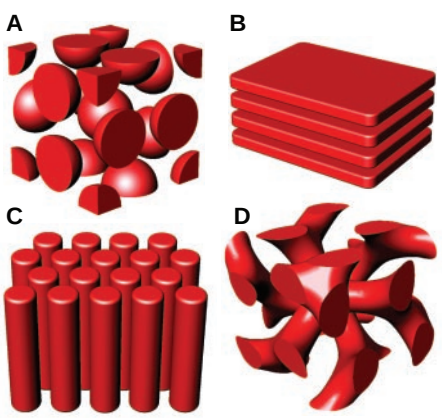

Fig. 3. Schematic illustration of supramolecular architectures of self-assembled extended amphiphilic dendrons consistent with the various lattice symmetries: *Pm*$\bar{3}$*n* cubic (micelles) (**A**), lamellar (2D layers) (**B**), hexagonal columnar (1D cylinders) (**C**), and *Ia*$\bar{3}$*d* continuous cubic (3D network) (**D**) structures. The red-colored parts represent the hydrophilic domains consisting of PEO chains and dendritic cores in which, for lithium-doped compounds, the ion transport takes place.

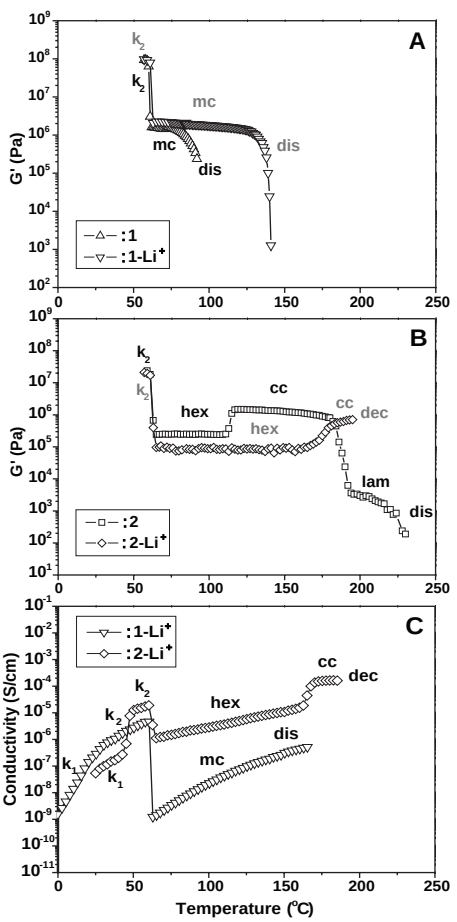

Fig. 4. Elastic modulus G′ (**A** and **B**) and ionic conductivity (**C**) as a function of temperature for extended amphiphilic dendrons **1** and **2** and their ion-doped **1-Li**$^+$ and **2-Li**$^+$. Mesophase nomenclature is given in Table 1.

have significant implications in areas where charge transport in nanostructured materials and devices is becoming increasingly important, such as ion conductors, photovoltaics or electroluminescence, for which the present extended amphiphilic dendrons may provide an advanced molecular design concept.

References and Notes

1. J. M. Lehn, *Supramolecular Chemistry* (VCH, Weinheim, Germany, 1995).
2. V. Percec *et al*., *Nature* **417**, 384 (2002).
3. S. I. Stupp *et al*., *Science* **276**, 384 (1997).
4. D. Demus, J. Goodby, G. W. Gray, H. W. Spiess, V. Vill, *Handbook of Liquid Crystals* (Wiley-VCH Verlag, Weinheim, Germany, 1998).
5. M. A. Hillmyer *et al*., *Science* **271**, 976 (1996).
6. C. J. Hawker, J. M. J. Fréchet, *J. Am. Chem. Soc.* **112**, 7638 (1990).
7. D. A. Tomalia *et al*., *Polym. J.* **17**, 117 (1985).
8. E. W. Buhleier, W. Wehner, F. Vögtle, *Synthesis* 155 (1978).
9. A. W. Bosman, H. M. Janssen, E. W. Meijer, *Chem. Rev.* **99**, 1665 (1999).
10. V. S. K. Balagurusamy, G. Ungar, V. Percec, G. Johansson, *J. Am. Chem. Soc.* **119**, 1539 (1997).
11. K. Lorenz, H. Frey, B. Stühn, R. Müllhaupt, *Macromolecules* **30**, 6860 (1997).
12. J. H. Cameron, A. Facher, G. Lattermann, S. Diele, *Adv. Mater.* **9**, 398 (1997).
13. G. Ungar, Y. Liu, X. Zeng, V. Percec, W. D. Cho, *Science* **299**, 1208 (2003).
14. X. Zeng *et al*., *Nature* **428**, 157 (2004).
15. G. M. Grason, B. A. DiDonna, R. D. Kamien, *Phys. Rev. Lett.* **91**, 58304 (2003).
16. B.-K. Cho *et al*., *J. Am. Chem. Soc.* **126**, 4070 (2004).
17. I. Gitsov, K. L. Wooley, C. J. Hawker, P. T. Ivanova, J. M. J. Fréchet, *Macromolecules* **26**, 5621 (1993).
18. M. A. Johnson, J. Iyer, P. T. Hammond, *Macromolecules* **37**, 2490 (2004).
19. C. Román, H. R. Fischer, E. W. Meijer, *Macromolecules* **32**, 5525 (1999).
20. M. E. Mackey *et al*., *Macromolecules* **35**, 8391 (2002).
21. M. Jayaraman, J. M. J. Fréchet, *J. Am. Chem. Soc.* **120**, 12996 (1998).
22. B.-K. Cho *et al*., *Macromolecules* **37**, 4227 (2004).
23. K. Borisch, S. Diele, P. Göring, C. Tschierske, *Chem. Commun*. 237 (1996).
24. S. D. Hudson *et al*., *Science* **278**, 449 (1997).
25. V. Percec *et al*., *Nature* **391**, 161 (1998).
26. S. M. Grayson, J. M. J. Fréchet, *Chem. Rev.* **101**, 3819 (2001).
27. D. Tsiourvas, K. Stathopoulou, Z. Sideratou, C. M. Paleos, *Macromolecules* **35**, 1746 (2002).
28. I. W. Hamley, *The Physics of Block Copolymers* (Oxford Univ. Press, New York, 1998).
29. J. N. Israelachvili, D. J. Mitchell, B. W. Ninham, *J. Chem. Soc. Faraday Trans.* **1**, 72, 1525 (1976).
30. J. Zhao *et al*., *Macromolecules* **29**, 1204 (1996).
31. P. P. Soo *et al*., *J. Electrochem. Soc.* **146**, 32 (1999).
32. P. V. Wright, Y. Zheng, D. Bhatt, T. Richardson, G. Ungar, *Polym. Int.* **47**, 34 (1998).
33. T. H. Epps, T. S. Bailey, R. Waletzko, F. Bates, *Macromolecules* **36**, 2873 (2003).
34. B.-K. Cho, A. Jain, S. M. Gruner, U. Wiesner, data not shown.
35. H. Kosonen *et al*., *Macromolecules* **35**, 10149 (2002).
36. E. E. Dormidontova, T. P. Lodge, *Macromolecules* **34**, 9143 (2001).
37. X. Wang, E. E. Dormidontova, T. P. Lodge, *Macromolecules* **35**, 9687 (2002).
38. J. Ruokolainen *et al*., *Science* **280**, 557 (1998).
39. T. Ohtake *et al*., *Chem. Mater.* **12**, 782 (2000).
40. K. Kishimoto *et al*., *J. Am. Chem. Soc.* **125**, 3196 (2003).

41. This work was supported by the Postdoctoral Fellowship Program of Korea Science and Engineering Foundation (KOSEF), the NSF (DMR-0312913), and the Cornell Center for Materials Research (CCMR), a Materials Research Science and Engineering Center (MRSEC) of the NSF (DMR-0079992). Financial support of Philip Morris, USA, is gratefully acknowledged. The SAXS x-ray facility is supported by Department of Energy Biological and Environmental Research (BER) grant DE-FG02-97ER62443. This work made use of the CCMR Hudson mesoscale facility, supported through the NSF MRSEC Program (DMR-0079992). We thank H. J. Räder and S. Türk (Max-Planck Institute for Polymer Research) for the MALDI-TOF measurements on the extended dendrimers and S. Mahajan (Cornell University) for help with PEO synthesis.

28 May 2004; accepted 12 August 2004

DNA-Templated Organic Synthesis and Selection of a Library of Macrocycles

Zev J. Gartner, Brian N. Tse, Rozalina Grubina, Jeffrey B. Doyon, Thomas M. Snyder, David R. Liu*

The translation of nucleic acid libraries into corresponding synthetic compounds would enable selection and amplification principles to be applied to man-made molecules. We used multistep DNA-templated organic synthesis to translate libraries of DNA sequences, each containing three "codons," into libraries of sequence-programmed synthetic small-molecule macrocycles. The resulting DNA-macrocycle conjugates were subjected to in vitro selections for protein affinity. The identity of a single macrocycle possessing known target protein affinity was inferred through the sequence of the amplified DNA template surviving the selection. This work represents the translation, selection, and amplification of libraries of nucleic acids encoding synthetic small molecules rather than biological macromolecules.

Nature generates functional biological molecules by subjecting libraries of nucleic acids to iterated cycles of translation, selection, amplification, and diversification (*1*–*4*). Compared with analogous synthesis and screening methods currently used to discover synthetic molecules with desired properties, these evolution-based approaches are attractive because of the much larger numbers of molecules that can be simultaneously evaluated, the minute quantities of material needed, and the relatively modest infrastructure requirements for library synthesis and processing (*1*–*4*).

Despite these attractions, evolution-based approaches can only be applied to molecules that can be translated from amplifiable information carriers. We previously described the generality of DNA-templated organic synthesis (DTS) and explored its potential for translating DNA sequences into corresponding synthetic products by using DNA hybridization to modulate the effective molarity of DNA-linked reactants (*5*). DTS can generate products unrelated in structure to the DNA backbone in a sequence-specific manner (*5*, *6*), does not require functional group adjacency to proceed efficiently (*5*, *7*), can mediate sequence-programmed multistep small-molecule synthesis (*8*), and can enable reaction pathways that are difficult or impossible to realize with the use of conventional synthetic strategies (*9*).

These features of DTS raise the possibility of translating single-solution libraries of DNA sequences into corresponding libraries of synthetic small molecules conjugated to their respective templates. Because each member of a DNA-templated synthetic library is linked to an encoding nucleic acid, these libraries are suitable for in vitro selection (*10*), polymerase chain reaction (PCR) amplification, and DNA sequence characterization to reveal the identity of synthetic library members possessing functional properties (Fig. 1). Below, we describe the integration of these concepts into the DNA-templated synthesis of a library of macrocycles (Fig. 2A), the selection of this pilot library for affinity to a target protein, and the identification of a functional library member through the amplification and characterization of DNA sequences surviving the selection.

Although macrocycles can be challenging targets for conventional synthesis (*11*), the compatibility of DTS with nM reactant concentrations, aqueous solvents (*12*), and purification methods not available to conventional synthesis (*8*) suggested that macrocycle synthesis might proceed efficiently in this format. We subjected a 48-base DNA-linked lysine derivative (**1a**, the "template," analogous to an mRNA during protein biosynthesis) to three successive DNA-templated amine acylation reactions (*6*) with building blocks conjugated to DNA 10-mer or 12-mer oligonucleotides (**2a**, **3a**, or **4a**, the "re-

Department of Chemistry and Chemical Biology, Harvard University, 12 Oxford Street, Cambridge, MA 02138, USA.

*To whom correspondence should be addressed. E-mail: drliu@fas.harvard.edu

agents," analogous to tRNAs) (Figs. 2B and 3). Each reagent oligonucleotide complemented one of three unique coding regions in the template sequence. The reagent oligonucleotides were biotinylated to allow products from each DNA-templated step (**5a**, **6a**, and **7a**) to be purified by capture with, and release from, streptavidin-linked magnetic beads (*8*) (Fig. 2, A and B). This direct selection for bond formation facilitates multistep synthesis by enabling the one-pot purification of products independent of their structure.

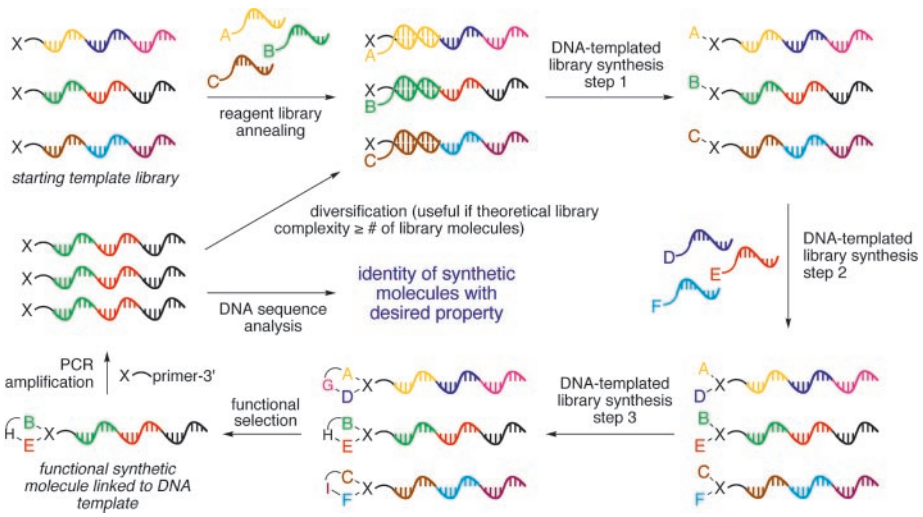

Fig. 1. Scheme for the translation, selection, and amplification of libraries of DNA templates encoding synthetic small molecules. When the number of different possible library structures approaches or exceeds the number generated, template diversification after selection can be added to evolve the pool of synthetic molecules toward structures possessing desired properties. X is a starting material common to all library members.

The diol group in the captured product of the third DNA-templated reaction (**7a**) was oxidatively cleaved with $NaIO_4$ to reveal an aldehyde. The phosphonium group was then deprotonated by elevating the pH of the buffer to 8.5, which induced Wittig olefination and macrocyclization. Because macrocyclization results in the cleavage of the reagent oligonucleotide-product bond, the desired macrocyclic fumaramide (**8a**) self-eluted in pure form from the streptavidin-linked magnetic beads (Fig. 2, A and B). The generality of this reaction was examined by assaying the macrocyclization of 11 molecules related to **7a** (fig. S1) (*13*). Macrocyclization was efficient for a wide variety of precyclized structures (60 to 90% yields with no contaminating uncyclized material). Control reactions lacking $NaIO_4$ confirmed that the cyclization reaction required the presence of an aldehyde group (fig. S1) (*13*).

The progress of each DNA-templated step during the transformation of **1a** to **8a** was followed by denaturing polyacrylamide gel electrophoresis (PAGE) (Fig. 2C) and by matrix-assisted laser desorption/ionization–time-of-flight (MALDI-TOF) mass spectrometry (Fig. 4A) after endonuclease-catalyzed removal of all but seven nucleotides at the 5′ end of the template. The presence of

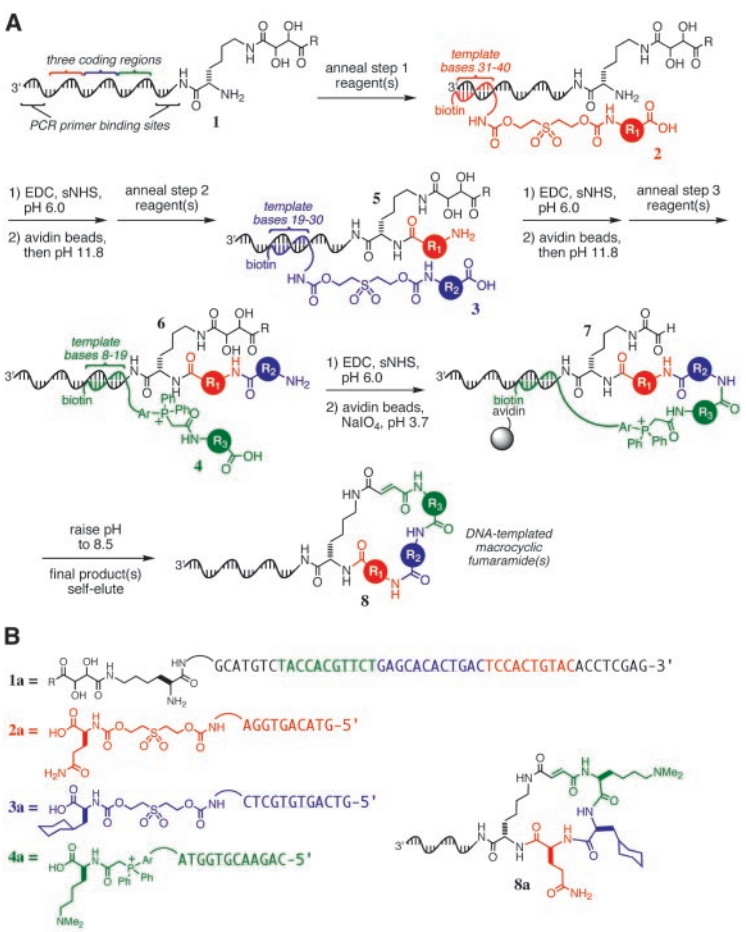

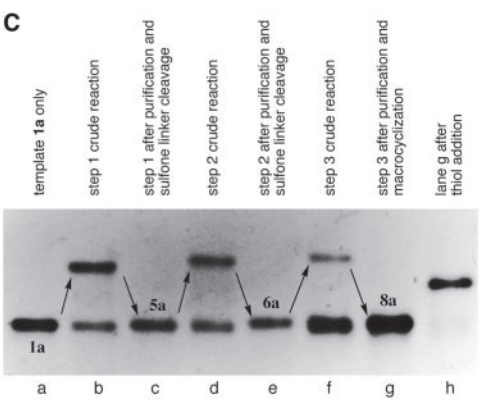

Fig. 2. (**A**) DNA-templated macrocycle library synthesis scheme. R is $NHCH_3$ where R is $NHCH_3$ or tryptamine; Ar, –(*p*-C_6H_4)–. The macrocyclization reaction is confirmed to give predominantly *trans* alkene stereochemistry for one library member (fig. S4) (*13*) but may give other outcomes for different macrocyclic structures. (**B**) Template and reagents used in the DNA-templated synthesis of **8a**. (**C**) Denaturing PAGE of each step in the DNA-templated synthesis of **8a**. Lane h is the product of a DNA-templated thiol addition to the product shown in lane g, confirming the formation of the fumaramide group during macrocyclization.

the electrophilic fumaramide group in the final product was confirmed by mass spectrometry and by its ability to accept a thiol nucleophile during a DNA-templated conjugate addition (Figs. 2C and 4A). Macrocycle **8a** (expected mass is 2908.8 daltons; observed mass is 2910.4 ± 6 daltons) was synthesized with high purity in 1 to 5% overall yield for three DNA-templated steps, the macrocyclization, and all associated purifications. To verify that the reaction conditions do not induce epimerization of the amino acid–derived chiral centers, we performed large-scale amine acylation reactions of analogous non–DNA-linked substrates under conditions that mimicked steps 1 to 3. The stereochemical integrity of the resulting products was confirmed by comparison to authentic diastereomeric standards (figs. S2 and S3) (*13*). In addition, exposure of a non–DNA-linked version of **7** to the above macrocyclization conditions provided the corresponding macrocycle (a non–DNA-linked version of **8**) containing a predominantly *trans* alkene (*14*) by nuclear magnetic resonance analysis (figs. S4 and S5) (*13*).

In addition to the multistep DTS of one synthetic small molecule, implementation of the scheme in Fig. 1 requires that DTS proceed in a sequence-specific manner in a library format in which multiple templates and multiple reagents are present in the same solution. Although DNA-templated reactions have been shown to be sequence-specific (*5*, *9*), library-format DTS to generate multistep small-molecule products has not been previously achieved.

We chose unique template "codons" to encode four or five reactants for each of the three DNA-templated steps in the macrocycle synthesis (13 codons total) (Fig. 3A). Each of the 13 codons was assigned to encode a different building block. The building blocks were chosen to include diverse functionalities, stereochemistries, and backbone lengths (Fig. 3A). Four different templates (**1a** to **1d**) (Fig. 3B), each containing three codons, were prepared such that the maximum number of 12 different codons (complementing reagents **2a** to **2d**, **3a** to **3d**, and **4a** to **4d**) were represented within the four templates. The corresponding reagents, each consisting of an amino acid building block conjugated through the linkers shown in Fig. 2A to a decoding DNA "anticodon," were also prepared (Fig. 3A).

We tested the sequence specificity of DTS in the presence of multiple reagents by exposing template **1a**, **1b**, **1c**, or **1d** separately to a mixture of all step 1 reagents except the reagent complementing the step 1 codon present in each template. As a positive control, each of the four templates was also separately reacted with its complementary step 1 reagent. These two DNA-templated reactions were repeated for each of the four step 2 codons and for each of the four step 3 codons. In contrast with the positive control, the reaction lacking the complementary reagent in all 12 cases did not generate significant product (Fig. 3C). These results indicate that templates do not react with mismatched reagents under the conditions in Fig. 2, even in the absence of complementary reagents.

To examine the sequence specificity of true library-format DNA-templated synthesis involving multiple templates and multiple reagents in a single solution, we reacted templates **1a** to **1d** in one solution with the four step 1 reagents (**2a** to **2d**). After reagent-linker cleavage (Fig. 2, A and C), the solution containing the step 1 products was reacted with the four step 2 reagents (**3a** to **3d**), and the resulting purified products were then reacted with the four step 3 reagents (**4a** to **4d**) before undergoing Wittig macrocyclization.

In all cases, the major products observed by MALDI-TOF mass spectrometry after each step consisted of all four of the sequence-programmed products (Fig. 4B). If the 12 reagents used to synthesize **8a** to **8d** reacted with templates randomly, rather than in a sequence-programmed manner, up to 64 different macrocycles would have been synthesized rather than the exclusive formation of the four observed products. The faithful translation of four DNA templates (**1a** to **1d**) into four sequence-programmed macrocyclic fumaramides (**8a** to **8d**) indicates a one-to-one correspondence between the DNA sequence that enters the above process and the structure of the resulting macrocycle.

After developing a robust multistep DNA-templated macrocycle synthesis and establishing

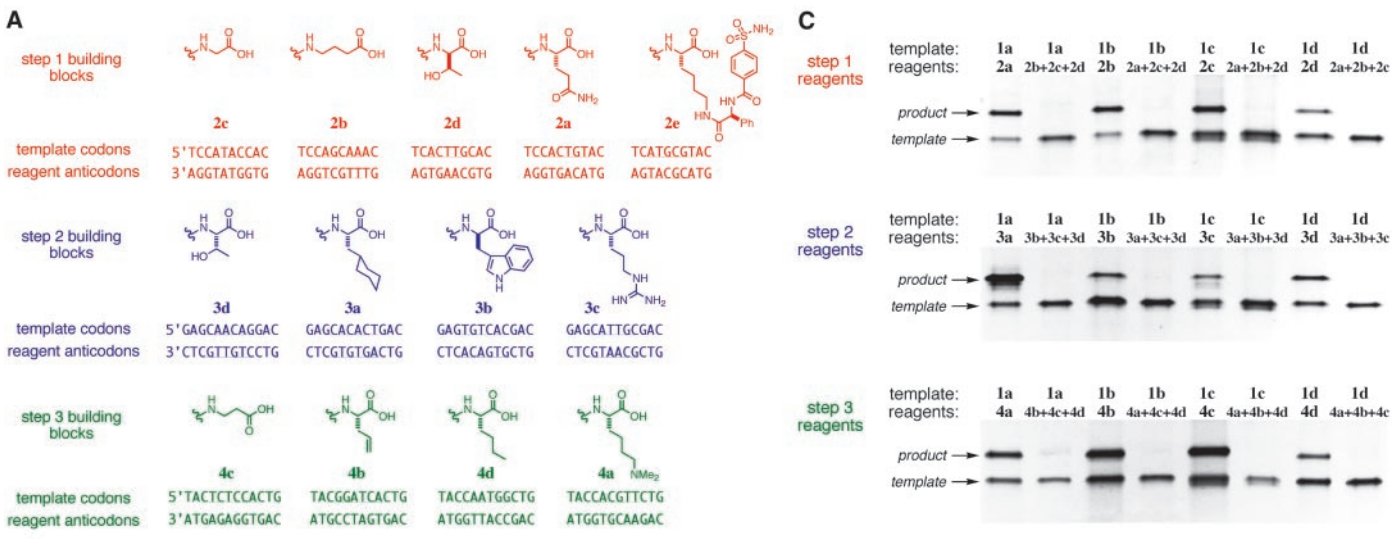

Fig. 3. (**A**) Building blocks and anticodons used in reagents for DNA-templated macrocycle library synthesis. The variable regions within each anticodon are underlined. The *Nla*III cleavage site within template **1e** is shown in lower case. (**B**) Representative DNA templates used in macrocycle library synthesis. Templates **1a** to **1e** (R is $NHCH_3$ or tryptamine) collectively call for each of the reagents in (A). (**C**) Denaturing PAGE analysis confirming the sequence specificity of each template-reagent combination used in the macrocycle library synthesis. The listed template and reagent(s) were combined under the conditions shown in Fig. 2A, and the reactions were analyzed before reagent-linker cleavage. Products appear as bands of higher molecular weight above templates.

the sequence specificity of library-format DNA-templated reactions, we prepared a library of 65 templates (**1**) that contained all 64 possible combinations of the four codons at each coding region and a 65th template (**1e**) that uniquely contained a step 1 codon encoding a phenyl sulfonamide building block (Fig. 3A). Because carbonic anhydrase is known to bind phenyl sulfonamides with high affinity [dissociation constant K_d = ~1 nM (*15*)], the macrocycle encoded by the 65th template serves as a positive control to evaluate the ability of a DNA-templated small molecule library to be selected in vitro for target protein affinity (see below).

The single-solution library of 65 equimolar DNA templates was translated into 65 corresponding macrocyclic fumaramides through the scheme shown in Fig. 2A. Each of the three coupling steps was executed in a single solution containing all 65 templates (typically 500 pmol total) and all five (step 1) or four (steps 2 and 3) reagents as described above. Denaturing PAGE analysis of each library synthesis step indicated yields similar to those of the single-template and four-template cases. MALDI-TOF mass spectrometry was used to observe the formation of the four major step 1 small-molecule products (all but the product encoded by **1e**, which is expected to be 16-fold less abundant than the four major step 1 products). After step 2, mass spectrum peaks consistent with the presence of all mass-resolvable step 2 small-molecule products were also observed (Fig. 4C).

After step 3 and macrocyclization, exposure of the completed 65-member library to a DNA-linked thiol reagent efficiently (84% yield) converted the library to higher molecular weight species. This result is consistent with the formation of the fumaramide group during the macrocyclization (Fig. 4D). Beginning with 0.1 to 3 nmol of starting template (**1**), the multistep DNA-templated library synthesis described above provided sufficient final product to undergo many in vitro selections (*10*) for library members with protein binding properties. Taken together, these results represent the translation of a library of DNA templates into a library of corresponding synthetic molecules.

Each member of a DNA-templated synthetic library of the type described in Fig. 1 is associated with an amplifiable DNA strand that not only encodes but has actually directed that molecule's synthesis. DNA-templated libraries, like libraries made by DNA display (*16*), are conceptually analogous to genetically encoded protein libraries (*2*, *4*) except that the structures generated are not limited to those that can be biosynthesized by the ribo-

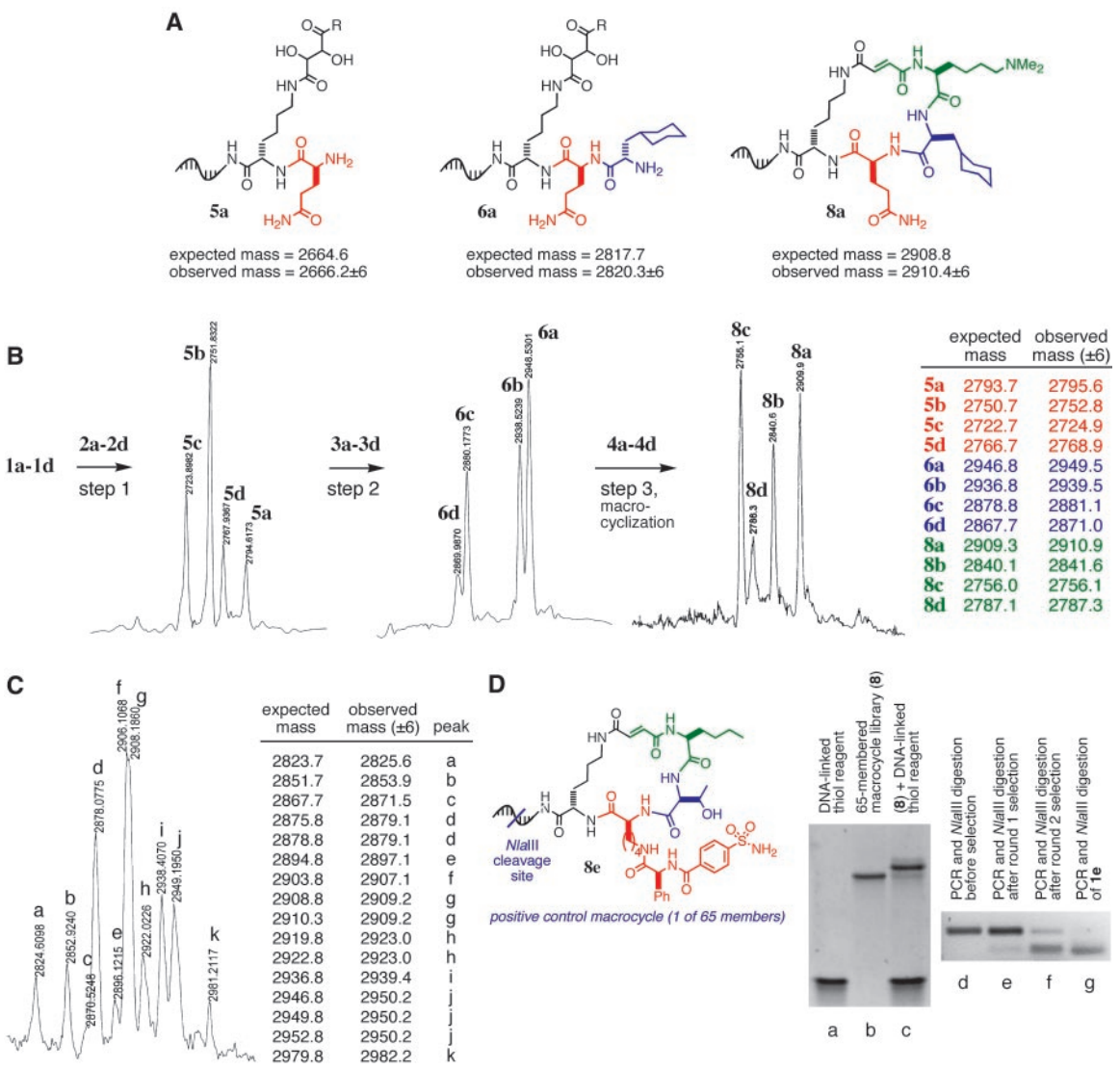

Fig. 4. MALDI-TOF mass spectrometric analyses (M–H negative ion mode) of (**A**) the multistep DNA-templated synthesis of **8a** starting from **1a** (R is $NHCH_3$), (**B**) the translation of four templates (**1a** to **1d**; R is tryptamine) into four corresponding macrocycles (**8a** to **8d**), and (**C**) step two of the translation of 65 templates (the 64 templates containing all possible combinations of codons complementing **2a** to **2d**, **3a** to **3d**, **4a** to **4d**, plus template **1e**) into 65 corresponding macrocycles. (**D**) Analysis of the DNA-templated 65-member macrocyclic fumaramide library by denaturing PAGE (lanes a to c) and agarose gel electrophoresis (lanes d to g). Lane a, DNA-linked thiol reagent complementing the constant 5′ region of all macrocycle template sequences; lane b, the 65-member library of template-linked macrocycles (**8**); lane c, the library after DNA-templated thiol addition, confirming the presence of the fumaramide group formed during macrocyclization; lane d, *Nla*III digestion of PCR-amplified templates from the 65-member macrocycle library before selection; lanes e and f, *Nla*III digestion of PCR-amplified templates from the 65-member macrocycle library after one and two rounds of selection for carbonic anhydrase affinity, respectively; lane g, *Nla*III digestion of authentic PCR-amplified template **1e** that directs the synthesis of **8e**.

some. Similar to nucleic acid–templated protein libraries, DNA-templated synthetic libraries, in principle, can be selected for desired properties such as target binding affinity or specificity (*10*).

To test this possibility, we subjected a minute quantity (100 fmol) of the 65-member DNA-templated macrocyclic fumaramide library to an in vitro selection for binding carbonic anhydrase, a well-studied protein (*17*). Carbonic anhydrase was immobilized by reaction with *N*-hydroxysuccinimide ester–linked agarose beads, combined with 100 fmol of the 65-member macrocyclic fumaramide library, and washed with buffer. Bound molecules were eluted and subjected to a second iteration of the selection. The DNA templates encoding macrocycles surviving each round of selection were amplified by PCR and digested with the restriction endonuclease *Nla*III. The 65th template (**1e**) uniquely contains a 5′-CATG-3′ sequence in the coding region of the phenyl sulfonamide building block that is cleaved by *Nla*III (Fig. 3B).

Before selection for binding to carbonic anhydrase, *Nla*III digestion reveals that the templates from the macrocycle library do not contain a noticeable representation of template **1e**, as expected because the library consists predominantly of other templates. Each selection for binding to carbonic anhydrase successively enriches the template pool for the sequence in **1e**, such that after two selections the pool predominantly contains the sequence encoding the phenyl sulfonamide–containing macrocycle (**8e**) (Fig. 4D). We therefore conclude that a single member of the 65-member DNA-templated macrocycle library was efficiently selected for carbonic anhydrase binding activity.

Macrocycles of the general structure **8** are promising compounds for perturbing the activity of biologically important proteases (*18*) because of their partial peptidic and conformationally constrained nature. In addition, the electrophilic fumaramide group can capture proximal nucleophiles (Figs. 2C and 4D) such as those present in protease active sites. On the basis of the above findings, efforts to generate and select DNA-templated synthetic libraries of high complexity and structural diversity are under way in our laboratory.

References and Notes

1. D. S. Wilson, J. W. Szostak, *Annu. Rev. Biochem.* **68**, 611 (1999).
2. H. Lin, V. W. Cornish, *Angew. Chem. Int. Ed. Engl.* **41**, 4402 (2002).
3. G. F. Joyce, *Annu. Rev. Biochem.* **73**, 791 (2004).
4. S. V. Taylor, P. Kast, D. Hilvert, *Angew. Chem. Int. Ed. Engl.* **40**, 3310 (2001).
5. Z. J. Gartner, D. R. Liu, *J. Am. Chem. Soc.* **123**, 6961 (2001).
6. Z. J. Gartner, M. W. Kanan, D. R. Liu, *Angew. Chem. Int. Ed. Engl.* **41**, 1796 (2002).
7. Z. J. Gartner, R. Grubina, C. T. Calderone, D. R. Liu, *Angew. Chem. Int. Ed. Engl.* **42**, 1370 (2003).
8. Z. J. Gartner, M. W. Kanan, D. R. Liu, *J. Am. Chem. Soc.* **124**, 10304 (2002).
9. C. T. Calderone, J. W. Puckett, Z. J. Gartner, D. R. Liu, *Angew. Chem. Int. Ed. Engl.* **41**, 4104 (2002).
10. J. B. Doyon, T. M. Snyder, D. R. Liu, *J. Am. Chem. Soc.* **125**, 12372 (2003).
11. R. B. Woodward *et al.*, *J. Am. Chem. Soc.* **103**, 3210 (1981).
12. C.-J. Li, T.-H. Chan, *Organic Reactions in Aqueous Media* (Wiley, New York, 1997).
13. Synthesis and characterization details are available on *Science* Online.
14. B. E. Maryanoff, A. B. Reitz, *Chem. Rev.* **89**, 863 (1989).
15. A. Jain, G. M. Whitesides, R. S. Alexander, D. W. Christianson, *J. Med. Chem.* **37**, 2100 (1994).
16. D. R. Halpin, P. B. Harbury, *PLoS Biol.* **2**, E174 (2004).
17. B. C. Tripp, K. Smith, J. G. Ferry, *J. Biol. Chem.* **276**, 48615 (2001).
18. D. Lamarre *et al.*, *Nature* **426**, 186 (2003).

19. Supported by NIH (National Institute of General Medical Sciences R01GM065865), the Office of Naval Research (N00014-03-1-0749), the Arnold and Mabel Beckman Foundation, the Searle Scholars Foundation (00-C-101), and the Alfred P. Sloan Foundation (BR-4141). Z.J.G. is a Bristol-Myers Squibb Graduate Research Fellow. B.N.T. and T.M.S. are NSF Graduate Research Fellows. J.B.D. is a National Defense Science and Engineering Graduate Research Fellow. We are grateful to the Bauer Center for Genomics Research for MALDI-TOF mass spectrometric analyses, G. Verdine for LC-MS instrument access, and DNA Software for assistance with codon screening. The rights to commercial development of DNA-templated synthesis have been licensed to Ensemble Discovery, a company for which D.R.L. is a consultant and shareholder.

Supporting Online Material
www.sciencemag.org/cgi/content/full/1102629/DC1
Materials and Methods
Figs. S1 to S5

12 July 2004; accepted 4 August 2004
Published online 19 August 2004;
10.1126/science.1102629
Include this information when citing this paper.

Hydrophobic Collapse in Multidomain Protein Folding

Ruhong Zhou,[1,2]* Xuhui Huang,[2] Claudio J. Margulis,[2] Bruce J. Berne[1,2]*

We performed molecular dynamics simulations of the collapse of a two-domain protein, the BphC enzyme, into a globular structure to examine how water molecules mediate hydrophobic collapse of proteins. In the interdomain region, liquid water persists with a density 10 to 15% lower than in the bulk, even at small domain separations. Water depletion and hydrophobic collapse occur on a nanosecond time scale, which is two orders of magnitude slower than that found in the collapse of idealized paraffin-like plates. When the electrostatic protein-water forces are turned off, a dewetting transition occurs in the interdomain region and the collapse speeds up by more than an order of magnitude. When attractive van der Waals forces are turned off as well, the dewetting in the interdomain region is more profound, and the collapse is even faster.

In the folding of globular proteins, it is often useful to picture the hydrophobic residues as being driven together by the action of water, in much the same way as droplets of oil would be driven together in water (*1–4*), but the presence of both a polar backbone and polar hydrophilic side chains complicates this picture. Most of our current understanding of hydrophobic collapse springs from studies on simple solutes (*1–3*, *5–18*) or of model hydrophobic chains (*19–22*). The role of the hydrophobic interaction in the folding of peptide chains in water is unfortunately a complex problem. We have chosen to study a structurally simpler problem, the collapse of two-domain proteins, where the starting point is the already folded domains.

In a two-domain protein folding, we can probe the hydrophobic collapse and possible dewetting in the interdomain region when the two complementary domain surfaces (largely hydrophobic) approach each other. The relative stability of each individual domain and the comparable surface area of the interfacial region also make two-domain protein folding somewhat comparable to the previously studied collapse of idealized paraffin-like plates (*3*). Furthermore, by turning off various portions of the protein-water interaction, we can better understand the important features of collapse present in the case of proteins, but perhaps not in the collapse of paraffin-like plates or the aggregation of oil droplets.

We simulated, by molecular dynamics (MD), the hydrophobic interaction between the domains of a two-domain protein, the BphC enzyme (1dhy), which functions in degrading toxic polychorinated biphenyls. One focus is on how the water molecules behave in the interdomain region when the multidomain protein folds (or collapses) into its final shape, after each individual domain has been formed, and how this behavior changes in response to changes in the protein-water interaction. The MD simulations were carried out with an all-atom model of both the

[1]Computational Biology Center, IBM Thomas J. Watson Research Center, 1101 Kitchawan Road, Yorktown Heights, NY 10598, USA. [2]Department of Chemistry, Columbia University, New York, NY 10027, USA.

*To whom correspondence should be addressed. E-mail: ruhongz@us.ibm.com (R.Z.); berne@chem.columbia.edu (B.J.B.)

protein and water. We then omitted various components of the protein-water interaction potential in further simulations to better understand the solvent-solute response.

The two-domain protein, BphC enzyme of KKS102 (1dhy.pdb) (Fig. 1), was selected on the basis of a recent study of the spatial hydrophobicity profiling (*23*) on all multidomain proteins in the Protein Data Bank (PDB). The hydrophobicity profiling analysis shows that this two-domain protein has large hydrophobic surface areas on the domain boundary, and it is one of the best such proteins in terms of the first-order hydrophobic moment or hydrophobic dipole reorientation (*23*). The BphC enzyme is an oligomeric enzyme made up of eight identical subunits, each with 292 amino acid residues. Each subunit consists of two domains: domain 1 (residues 1 to 135) and domain 2 (residues 136 to 292). In the current study, only one subunit (1dhy.pdb) is included, and we refer to it as a two-domain protein. The focus is on the interdomain region of the protein during folding; the details of the simulation are given in (*24*–*27*).

For each configuration, three different types of simulations were performed: (i) a "dewetting" simulation started with wet initial conditions (water molecules in the interdomain gap region), and with protein atoms constrained but water and ions free to move; (ii) a "wetting" simulation started with dry initial condition (no water molecules in the interdomain gap), and with protein constrained but water and ions free to move; and (iii) a "folding" simulation, i.e., normal folding simulation with everything flexible. In both the dewetting and wetting simulations, the protein atoms are constrained with a harmonic potential with a force constant of 1000 kJ mol^{-1} $Å^{-2}$.

For the wetting simulation, the water molecules between the two domains are removed after equilibration with a simple criterion, $d_1 + d_2 \leq D + \delta$, where d_1 and d_2 are the distances of a water oxygen atom to each of the two-domain boundary surface atoms, respectively; D is the domain displacement distance defined in (*24*); and δ is set equal to 2.5 Å to account for the average sum of two surface-atom radii. This approach allows us to estimate the gap volume as the number of removed water molecules divided by the bulk water number density. Knowing this volume, we can then estimate the water density in this gap as a function of time by counting the number of molecules inside the gap.

For all of the above simulations, at each gap distance D, 5-ns constant pressure and temperature (NPT) runs are performed for data collection. Simulations are done for the full protein-water interaction and full domain-domain interaction and for a variety of cases where electrostatic and van der Waals attractive parts (r^{-6} term) of the protein-water and domain-domain interactions were turned on or off, as defined below.

Each trajectory from the 5-ns NPT runs for various gap distances D were analyzed in detail. The snapshots from one such dewetting simulation with an initial interdomain gap distance (*28*) of 4 Å are shown in Fig. 2A (top). The number of water molecules inside the interdomain region decreases slowly with time but never approaches zero as in the case of idealized paraffin-like plates (*3*). It instead converges to a roughly constant number after about 500 ps. The water density decreased from 1.00 g cm^{-3} to about 0.86 ± 0.04 g cm^{-3} in about 500 ps for $D = 4$ Å (Fig. 2A, bottom). Even for very small gap distances, such as 2.5 Å, which can barely contain one layer of water molecules inside the interdomain region, no complete dewetting, or strong dewetting transition (SDT), was observed. For larger gap distances, as expected, dewetting was not observed, and the water density inside the gap region approached 1.0 g cm^{-3} for the gap distances $D > 6.0$ Å.

Snapshots from the wetting simulation started from the dry initial condition, again with the interdomain gap distance of $D = 4$ Å (Fig. 2A, middle), show that the number of water molecules inside the interdomain gap increases very quickly in the first few tens of picoseconds and then slowly increases until it converges after about 400 to 500 ps. The final number of the water molecules inside the gap, and thus the water density, agrees very well with the dewetting simulation above, as shown in Fig. 2A (bottom). The converged water density (*29*) is about 14% lower than the bulk density. Thus, no hysteresis is observed: It appears that thermodynamic equilibrium has been achieved in both simulations after about 500 ps. Because there are eight Na^+ ions in the simulation (to neutralize the system), it is interesting to see if they played a role in the water depletion as a result of osmotic effects. We added 20 more Na^+ and 20 Cl^- (~0.15 M) in the simulation and found no meaningful change in the water density in the interdomain gap; thus, it seems that the water depletion is mainly due to the hydrophobic effect, not to an osmotic effect.

To see whether there is local water depletion in the neighborhood of the hydrophobic surfaces of the isolated domains of BphC, as would be expected from recent work on the equivalent of "oil droplets," where this deple-

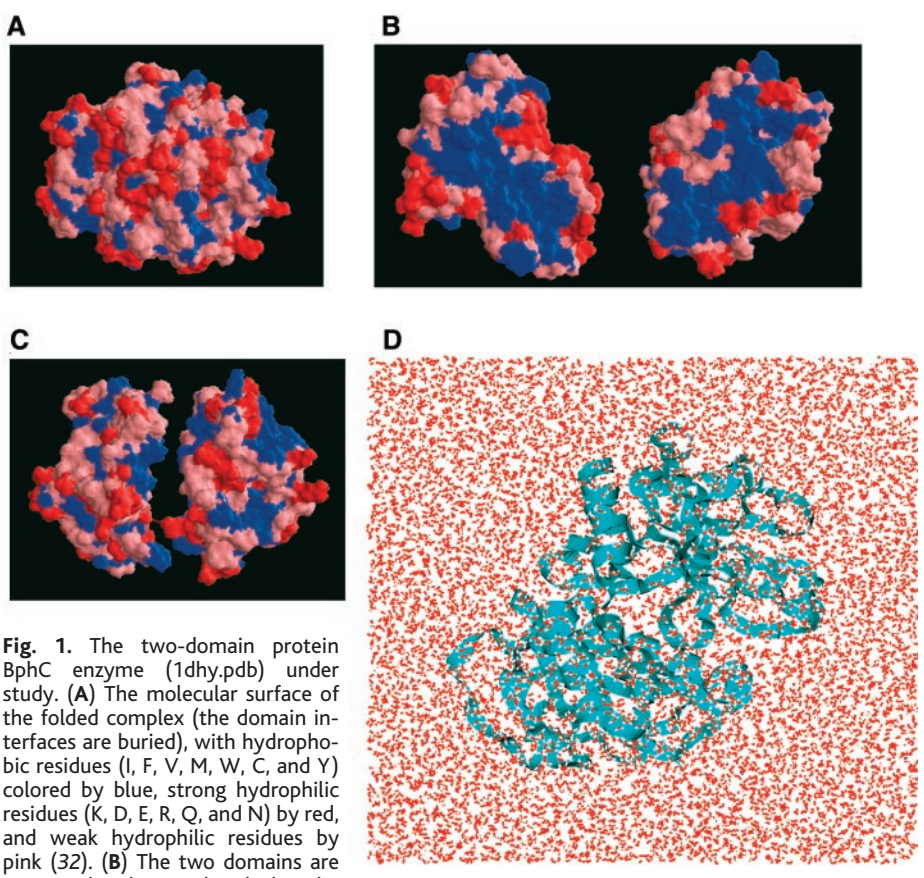

Fig. 1. The two-domain protein BphC enzyme (1dhy.pdb) under study. (**A**) The molecular surface of the folded complex (the domain interfaces are buried), with hydrophobic residues (I, F, V, M, W, C, and Y) colored by blue, strong hydrophilic residues (K, D, E, R, Q, and N) by red, and weak hydrophilic residues by pink (*32*). (**B**) The two domains are separated and rotated such that the interface areas are facing the reader. Large hydrophobic surface areas can be seen on the domain boundary. (**C**) The two domains are separated along the line of the two domain centers so that the interface can be seen. (**D**) Solvated protein system in water, with the interdomain gap distance $D = 6$ Å.

tion gives rise to a vapor layer a few water molecules thick (*1*, *2*), each domain is solvated in water alone and a 2-ns NPT simulation is run after a normal 100-ps equilibration. No meaningful vapor layer was found in either of the two single domains of BphC. This result is not unexpected, because the electrostatic and dispersion attractions in the protein-water interactions should not only "pull" the water interface closer to the surface of the protein but also damp out the capillarity waves, two effects contributing to the disappearance of a vapor layer.

To investigate the time scale and kinetics for dewetting in the hydrophobic collapse of BphC, we initially set the interdomain gap distance $D = 6$ Å. In a 5-ns NPT simulation, D consistently decreases as water molecules leave the intervening region. After about 1.5 ns, the decrease slows because the final residual water molecules are becoming harder to expel. Some of them are deeply buried in the hydrophobic cavities between the two domains, which makes them more difficult to escape because most possible escape pathways are blocked. After about 5 ns, only a few water molecules are still left in the interdomain region. During the entire 5-ns folding simulation, the two individual domains stay folded, with backbone root mean square displacement from the starting native structures less than 2.0 to 2.5 Å and the fluctuations in the radius of gyration less than 0.5 Å for each domain. The dynamics of the interdomain collapse are shown in Fig. 3B. The two domains approach each other faster in the first nanosecond and then slow down considerably when D decreases to about 1.2 Å. Consistent with the dewetting and wetting simulations discussed above, no SDT is observed.

The collapse of BphC is much different from the collapse of idealized paraffin-like plates (*3*). The observed kinetics of hydrophobic collapse of two hydrophobic plates is characterized by two temporal regimes (Fig. 3A). Initially, the distant plates diffuse toward each other, with water filling the region between them, until they reach a critical separation; then a drying transition takes place that is equivalent to a liquid-gas phase transition of the confined liquid. The two plates are then driven quickly together, so there are two kinetic regimes. The equivalent collapse of the two-domain protein BphC enzyme (Fig. 3B) showed no two-speed collapse, and the actual speed is two orders of magnitude slower than that found in the idealized paraffin-like plates.

Why do these two systems behave so differently? To better understand the observed differences in the dewetting and collapse of idealized paraffin-like plates and of the two-domain protein, we turn off different parts of the protein-water and domain-domain interactions. We designate three different ways for turning interactions off. In "Turnoff1," we turn off protein-water electrostatic interactions. In "Turnoff2," we also turn off protein-water van der Waals attractions (r^{-6} term). In "Turnoff3," we additionally turn off domain-domain electrostatic and van der Waals attractive interactions. The snapshots for dewetting and wetting simulations are shown in Fig. 2 for both Turnoff1 (Fig. 2B) and Turnoff2 (Fig. 2C). (Because domains are constrained in space in both dewetting and wetting simulations, the Turnoff3 option does not apply here.) The water density drops (Fig. 2B, bottom) to approximately 0.3 g cm^{-3} in the Turnoff1 case. These remaining water molecules are at the edge of the interdomain gap region, leaving the center area empty. The water density drops further to essentially zero in the Turnoff2 case (Fig. 2C, bottom). Thus, for these last two cases, an SDT is found, even though the protein domain surfaces are rough (*30*). A dewetting critical distance (*3*) of 7 to 9 Å and 18 to 20 Å are found, respectively, for the Turnoff1 and Turnoff2 cases. The critical distance increases greatly when the protein-water van der Waals attraction is turned off. The critical distance for the Turnoff2 case agrees very well with the results for the idealized paraffin-like plates (*3*), which indicates that the extent of dewetting in Turnoff2 resembles that of the hydrophobic plates despite its rough hydrophobic surfaces.

The water depletion around isolated single domains is also very sensitive to turning off parts of the interaction (*31*). With the full potential, no depletion was observed. With protein-water electrostatic interactions turned off (Turnoff1), the water depletion extends to 5 to 6 Å, with an average water density approximately 10% lower than the bulk. With the van der Waals attractions also turned off (Turnoff2), the water depletion extends to about 8 Å, with an average water density approximately 30% lower than the bulk. Interestingly, two recent experiments (*6*, *9*, *10*) have also found about a 10% water density decrease near hydrophobic surfaces. Steitz *et al*. (*9*), studying D_2O in contact with deuterated polystyrene in neutron reflectivity experiments, found a 6 to 12% density decrease in

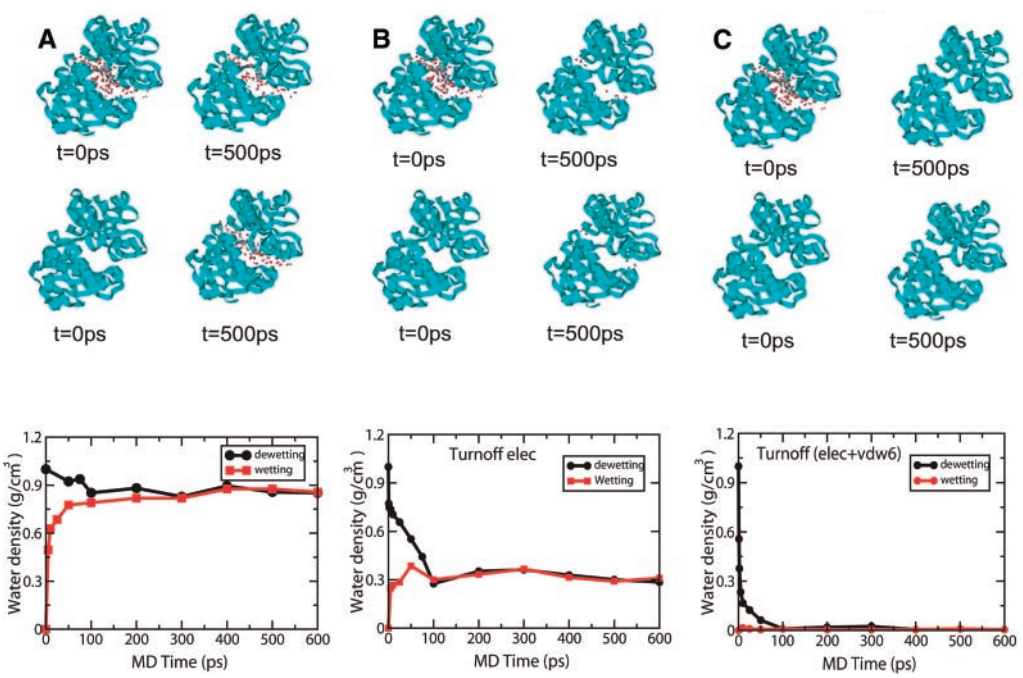

Fig. 2. (**A**) Snapshots of water configurations inside the domain gap region started from both the initial wet condition (top) and the initial dry condition (middle) for $D = 4$ Å. (To provide a better view, only the water molecules inside the gap region are shown.) The corresponding water densities inside the gap region are also shown for both cases versus time (bottom). This is for a simulation with full force-field interactions. (**B**) Same as (A), except that the protein-water electrostatic interactions are turned off. (**C**) Same as (A), except that both the protein-water electrostatic interactions and the van der Waals attractive interactions are turned off.

a depletion layer of roughly 20 Å. Jensen *et al*. (*10*) used x-ray reflectivity to study water in contact with paraffin and found a 10% density decrease in a depletion layer of no more than 15 Å. Thus, the water depletion for Turnoff1 is similar to the results found in these experiments but does not extend as far out from the hydrophobic surface. The reorganization of water around simple but sufficiently large hydrophobic solutes with concomitant depletion was also anticipated theoretically (*1*, *2*, *4*).

The folding kinetics for different turnoff schemes are shown in Fig. 3C. The snapshots of protein-water configurations are shown only for the Turnoff2 case, whereas the time evolution of D is shown for all three cases. The folding (and drying) time decreases by a factor of 10 in Turnoff1, from about 1500 ps to 150 ps. It further decreases to about 25 ps in Turnoff2, which is comparable to the time scale in idealized paraffin-like plate collapse. Interestingly, Turnoff3 increases the drying time slightly compared with Turnoff2 because of the net van der Waals (r^{-12}) repulsion between the two domains (note the slightly larger equilibrated gap distance), but both are comparable to the idealized hydrophobic plates. This much faster speed can also be seen from the time scales required to reach equilibrium in the dewetting and wetting simulations in Fig. 2. These results indicate that turning off protein-water electrostatic interactions can dramatically speed up the drying kinetics, which is further accelerated by turning off the van der Waals attractions. Thus, by removing the protein-water attractive interactions, the dewetting and collapse resemble what was previously seen in idealized paraffin-like plates, with respect to both the extent of dewetting and the speed of hydrophobic collapse, despite the protein's having much rougher hydrophobic surfaces than the idealized plates. We found that the kinetics of collapse is more affected by the electrostatic interactions, whereas the critical distance D_c of dewetting is more affected by the van der Waals attractions.

Finally, as mentioned above, for idealized paraffin-like plates that do not attract each other or water, the plates diffuse toward each other until they reach a critical separation, upon which a large-scale drying transition takes place, followed by a rapid collapse, i.e., a two-speed–like collapse. However, even in the collapse of the two domains in Turnoff3, which supposedly mimics the idealized plates, we do not observe this two-speed–like collapse, partly because the two protein domains have a linker (loop) between them that constrains the speed at which the domains can collapse even in the absence of water and also limits the pathways through which water can flow.

One lesson learned from our simulations is that models found useful for describing the dewetting and collapse of aggregation of oil drop–like particles, although useful for understanding the collapse of simple hydrophobes, cannot, in their present form, account for the behavior observed in the simulation of the collapse of BphC. These simple models would predict that as the two domains approach each other, when they get closer than some critical distance, there would be a sudden drying transition in the interdomain region (much like what would happen in a gas-liquid phase transition), followed by a rapid collapse of the two domains. This behavior is not seen in our two-domain protein, and we believe that it will not be seen in other multidomain proteins either. We find that the degree of dewetting depends critically on the strength of the solute-solvent electrostatic interactions, which apparently are large enough in proteins to make the simple models of hydrophobic dewetting and collapse inapplicable in their present form. It is of considerable interest to devise experiments to test our above predictions for multidomain proteins or protein aggregates.

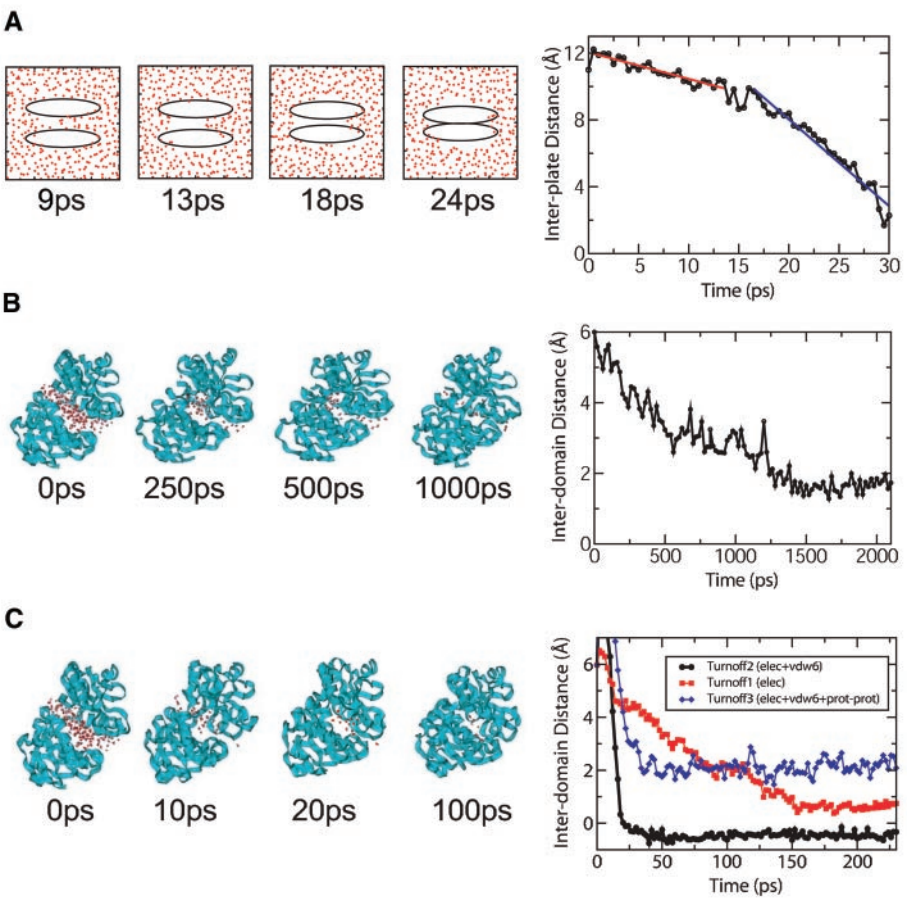

Fig. 3. Comparison of the kinetics of hydrophobic collapse for the idealized plates and the two-domain protein, with or without part of the interactions turned off. (**A**) Snapshots of the hydrophobic collapse of the two plates (left) and the distance between two plate centers versus time (right). (**B**) Snapshots of the folding of the two-domain protein with full interactions (left) and its gap distance versus time (right). (**C**) Same as (B) but with various interactions turned off. The snapshots (left) are for the case in which the protein-water electrostatic and van der Waals attractions are turned off (Turnoff2). The distance curves (right) show three different options: red for Turnoff1 (only protein-water electrostatic interactions are turned off); black for Turnoff2 (Turnoff1 plus turning off the protein-water van der Waals attractive interactions); and blue for Turnoff3 (Turnoff2 plus turning off the domain-domain electrostatic and van der Waals attractive interactions). These figures show a very fast collapse of the hydrophobic plates and a very slow (orders of magnitude slower) two-domain protein folding. However, with part of the attractive interactions turned off, the protein domains collapse on a much faster time scale, just like the idealized plates.

References and Notes

1. K. Lum, D. Chandler, J. D. Weeks, *J. Phys. Chem. B* **103**, 4570 (1999).
2. D. M. Huang, D. Chandler, *J. Phys. Chem. B* **106**, 2047 (2002).
3. X. Huang, C. J. Margulis, B. J. Berne, *Proc. Natl. Acad. Sci. U.S.A.* **100**, 11953 (2003).
4. F. H. Stillinger, *J. Solution Chem.* **2**, 141 (1973).
5. D. Chandler, *Nature* **417**, 491 (2002).
6. P. Ball, *Nature* **423**, 25 (2003).
7. C. Pangali, M. Rao, B. J. Berne, *J. Chem. Phys.* **71**, 2982 (1979).
8. G. Hummer, J. C. Rasaiah, J. P. Noworyta, *Nature* **414**, 188 (2001).

9. R. Steitz *et al.*, *Langmuir* **19**, 2409 (2003).
10. T. R. Jensen *et al.*, *Phys. Rev. Lett.* **90(8)**, 86101 (2003).
11. A. Wallqvist, B. J. Berne, *J. Phys. Chem.* **99**, 2893 (1995).
12. A. Wallqvist, B. J. Berne, *J. Phys. Chem.* **99**, 2885 (1995).
13. K. Leung, A. Luzar, *J. Chem. Phys.* **113**, 5845 (2000).
14. K. Leung, A. Luzar, D. Bratko, *Phys. Rev. Lett.* **90**, 65502 (2003).
15. M. E. Paulaitis, L. R. Pratt, *Adv. Protein Chem.* **62**, 283 (2002).
16. L. R. Pratt, *Annu. Rev. Phys. Chem.* **53**, 409 (2002).
17. G. Hummer, S. Garde, A. E. Garcia, L. R. Pratt, *Chem. Phys.* **258**, 349 (2000).
18. K. Lum, A. Luzar, *Phys. Rev. E.* **56**, R6283 (1997).
19. D. M. Huang, D. Chandler, *Proc. Natl. Acad. Sci. U.S.A.* **97**, 8324 (2000).
20. P. R. ten Wolde, D. Chandler, *Proc. Natl. Acad. Sci. U.S.A.* **99**, 6539 (2002).
21. K. Lum, D. Chandler, *Int. J. Thermophys.* **19**, 845 (1998).
22. R. D. Mountain, D. Thirumalai, *J. Am. Chem. Soc.* **125**, 1950 (2003).
23. R. Zhou, B. D. Silverman, A. Royyuru, P. Athma, *Proteins* **52**, 561 (2003).
24. The starting structure is taken from the crystal structure deposited in PDB (entry 1dhy.pdb). The interdomain distance of the crystal structure is increased by D along the direction of two domain centers of geometry to create "gaps" between the two domains (to make room for water). Various distances ranging from $D = 2.5$ Å to 20.0 Å are studied. The resulting protein configurations are then solvated in a water box, with water layers at least 8 Å from the protein surfaces. Figure 1 shows one such solvated configuration. Eight Na^+ counterions are added to make the system electrically neutral. The solvated protein systems have up to 42,000 atoms (the actual size varies for different interdomain distances). The GROMACS simulation package is used here for this large system because of its fast speed (*25*). Each NPT MD simulation [(*26*), 1 atm and 300 K] is run in parallel with 8 to 16 processors on IBM SP2-Power3-375 MHz clusters. The OPLSAA force field is used for the protein (*27*), and a simple point charge (SPC) water model is used for the explicit solvent. For the long-range electrostatic interactions, the particle-mesh Ewald method is used. For the van der Waals interactions, a typical 10 Å cutoff is used. A time step of 2.0 fs is used with bond lengths constrained. A standard equilibration procedure, which includes a conjugate gradient minimization and a 100-ps MD simulation with position restraints, is followed to equilibrate each solvated system. The final configurations from equilibration are then used for data collection. We have modified GROMACS to allow us to selectively turn off certain terms in the force field, in particular, the protein-water electrostatic potential, the attractive part of the protein-water van der Waals potential, the domain-domain electrostatic potential, and the attractive part of the domain-domain van der Waals potential. This approach allows us to make a sensitivity analysis of hydrophobic collapse and to compare the protein collapse with what is already known about the hydrophobic collapse of the plates.
25. E. Lindahl, B. Hess, D. van der Spoel, *J. Mol. Model.* **7**, 306 (2001).
26. One caveat is that NPT MD introduces fictitious dynamics from both the temperature and pressure control. New fictitious degrees of freedom are introduced, with corresponding kinetic energies, fictitious masses, and fictitious frequencies. These influence the time scales and can affect the rate processes observed. Nevertheless, the thermodynamic equilibrium water densities inside the interplate or interdomain region and the water depletion or dewetting phenomena should stay the same. Our observations about kinetics are borne out in careful studies.
27. W. L. Jorgensen, D. Maxwell, J. Tirado-Rives, *J. Am. Chem. Soc.* **118**, 11225 (1996).
28. The original total interdomain distance is about 18.8 Å, so after the enlargement, the total interdomain distance is about 22.8 Å . For simplicity, we will refer to it as interdomain gap distance $D = 4$ Å in the following.
29. It is tricky to define the water density inside the domain gap region, particularly for cases with very small D values, because the fluctuation in the number of water molecules can be fairly large compared with the total number of water molecules inside the region. In general, it is very difficult to directly measure the volume inside the domain gap region because of the irregularity of the protein domain structures; thus, we used a comparative way to measure the water density.
30. Y. Cheng, P. J. Rossky, *Nature* **392**, 696 (1998).
31. H. S. Ashbaugh, M. E. Paulaitis, *J. Am. Chem. Soc.* **123**, 10721 (2001).
32. Single-letter abbreviations for the amino acid residues are as follows: A, Ala; C, Cys; D, Asp; E, Glu; F, Phe; G, Gly; H, His; I, Ile; K, Lys; L, Leu; M, Met; N, Asn; P, Pro; Q, Gln; R, Arg; S, Ser; T, Thr; V, Val; W, Trp; and Y, Tyr.
33. This work was partially supported by a grant to B.J.B. from NIH (GM4330) and a Shared University Research (SUR) grant from the IBM Corporation to Columbia University.

7 June 2004; accepted 20 August 2004

Climate Impact on Plankton Ecosystems in the Northeast Atlantic

Anthony J. Richardson[1]* and David S. Schoeman[2]

It is now widely accepted that global warming is occurring, yet its effects on the world's largest ecosystem, the marine pelagic realm, are largely unknown. We show that sea surface warming in the Northeast Atlantic is accompanied by increasing phytoplankton abundance in cooler regions and decreasing phytoplankton abundance in warmer regions. This impact propagates up the food web (bottom-up control) through copepod herbivores to zooplankton carnivores because of tight trophic coupling. Future warming is therefore likely to alter the spatial distribution of primary and secondary pelagic production, affecting ecosystem services and placing additional stress on already-depleted fish and mammal populations.

Not only do plankton provide food for marine mammals and commercially important fish, they also play a fundamental role in the functioning of marine ecosystems by providing half the global primary production (*1*) and contributing substantially to biogeochemical cycling (*2*). How global climate change might affect biological communities such as marine plankton is therefore a matter for concern (*3*). There is evidence of climate-mediated biogeographical shifts among some groups of marine plankton such as the calanoid copepods (*4*), but the overall response of phytoplankton and zooplankton communities, which is likely to depend on the form and strength of the linkages between successive trophic levels, is not known. Until we understand these processes, we will not know how resilient such food webs are to global-scale impacts, such as climate change, eutrophication, pollution, or over-fishing, and it will be difficult to manage marine resources sustainably.

To predict the response of the base of the marine food web to climate change, we need a better understanding of the type and degree of coupling between trophic levels in marine systems. Complex biological systems are generally controlled by their top predators through top-down control, by their producers through bottom-up control, or by a number of key species in the middle through wasp-waist control (*5*). For the plankton ecosystem within the marine pelagic realm, there is currently conflicting evidence on when these types of control operate, and on what scales. Some workers suggest tight bottom-up coupling of plankton trophic levels (*2*, *6*, *7*), whereas others conclude that strong top-down control (*8*) or weak coupling (*9*, *10*) is operative.

Complicating the identification of processes underpinning marine food web dynamics is a range of methodological limitations: time series of biotic variables tend to be short; spatial coverage of most studies is restricted to point sampling; and syntheses often attempt to combine results from studies with very different field and analytical approaches. We overcome such problems by using 115,322 samples taken by the Continuous Plankton Recorder (CPR) survey in the Northeast Atlantic between 1958 and 2002. These samples have been collected, processed, and analyzed in a consistent manner, yielding reliable time series for ~400 taxa (*11*) and providing a unique opportunity to investigate planktonic ecology over decadal and ocean basin scales. Using these data, we construct a conceptual pelagic food web

[1]Sir Alister Hardy Foundation for Ocean Science, The Laboratory, Citadel Hill, Plymouth, PL1 2PB, UK. [2]Department of Zoology, University of Port Elizabeth, Port Elizabeth, South Africa.

*To whom correspondence should be addressed. E-mail: anr@sahfos.ac.uk

comprising phytoplankton (diatoms and dinoflagellates), copepod herbivores, and zooplankton carnivores (see supporting online text for taxonomic membership of functional groups). Because we are interested in ecosystem responses, rather than local or taxon-specific responses as in many previous studies (*5*, *8*, *12*, *13*), we calculate the total abundance (*11*) of all species sampled within each of these functional groups (*14*). We use mean annual sea surface temperature (SST; HadISST Version 1.1 from Hadley Centre, UK Met Office) as an environmental proxy because it is an important manifestation of climate change (*4*), it is associated with changes in phytoplankton community structure (*15*), and it is available over the time and space scales necessary for this study (*16*).

Because of the difficulty of testing hypotheses in the global oceans by conducting in situ manipulative experiments at the scale of the present study, conclusive cause-and-effect evidence of underlying mechanisms is not possible. The comparative approach is often useful in such situations, and we use this method to test ideas concerning the impact of climate change on the plankton community and also to investigate the form and strength of trophic linkages (relationships between functional feeding groups that are adjacent to one another in the conceptual food web) within the plankton. This is achieved by partitioning the Northeast Atlantic into regions based on "standard boxes" used in the survey (Fig. 1). Within these regions we calculate annual mean SST and abundance time series for each trophic level (*17*) to minimize temporal autocorrelation associated with strong seasonality. We then correlate time series of annual means from different trophic levels. Strong bottom-up control should result in a positive correlation between predator and prey, strong top-down control should result in a negative correlation between predator and prey, and strong climate control at any level within the food web should result in significant correlations between abundance within a trophic level and some environmental (here SST) variable (*13*). To identify general patterns, we then use a random-effects meta-analysis (*13*) to combine individual correlation coefficients across our study domain. We focus on the 20 regions in the Northeast Atlantic that have sufficient data (20 or more years) (Fig. 1) to estimate the temporal autocorrelation functions that are required for adjusting effective degrees of freedom using the modified Chelton Method (*18*, *19*). To minimize potential effects of spatial autocorrelation, we also perform a meta-analysis on a subset of nine noncontiguous regions (A1, A6, B2, C3, C5, D1, D3, E5, and F4—this is the largest possible number of noncontiguous regions that has the longest overall time series). Examination of patterns of covariation in environmental and trophic relationships in pairwise combinations of these nine noncontiguous regions (supporting online text) confirms that their spatial separation allows them to be regarded as replicates.

Correlations between phytoplankton abundance and SST for each of the 20 regions that have sufficient data for analysis are shown in Fig. 2A. We set α at 0.01 for all analyses to ameliorate the effects of multiple hypothesis tests, so correlations are significant when the 99% confidence intervals do not overlap zero. There is no consistent pattern in the sign of the correlations over the regions, and only two of the individual correlation coefficients are significant. Furthermore, neither the meta-analysis for all regions [$\bar{r}_{All} = 0.12$, $Z = 1.94$, not significant (n.s.)] nor that for the subset of nine noncontiguous regions ($\bar{r}_{Subset} = 0.06$, $Z = 0.60$, n.s.) is significant, suggesting no overall linear relation.

The possibility remains, however, that although the relation between phytoplankton abundance and SST is not consistent throughout the study domain, its strength nevertheless varies in a predictable way (*13*, *20*). To examine this hypothesis, we plot the phytoplankton abundance–SST correlation against mean SST for each region (Fig. 2B) and find a strong negative relation for all areas ($r = -0.61$, $P < 0.01$, $n = 20$) as well as for the subset of noncontiguous areas ($r = -0.81$, $P < 0.01$, $n = 9$). These results imply that the abundance of phytoplankton increases as SST warms in cooler waters of the Northeast Atlantic, but that it decreases as SST increases in warmer waters.

This complex response of phytoplankton abundance to SST probably arises because temperature not only affects biota directly, but also acts as a useful proxy for other physical processes regulating the size structure, taxonomic composition, and abundance of phytoplankton communities (*15*, *21*). For instance, seasonal

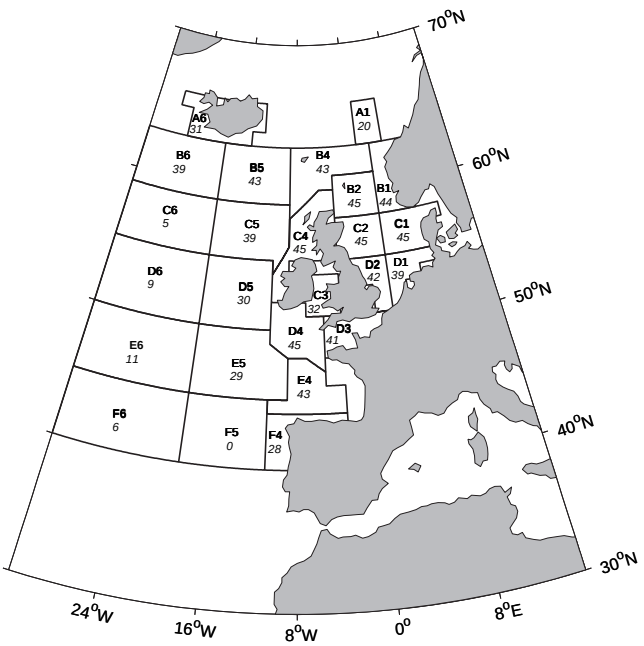

Fig. 1. Map of the Northeast Atlantic Ocean showing standard CPR boxes (bold) and the number of years (from 1958 to 2002) that eight or more months were sampled within each box (italics). Because of the strong seasonality in plankton populations, annual means were only calculated for years when eight or more months were sampled (*17*).

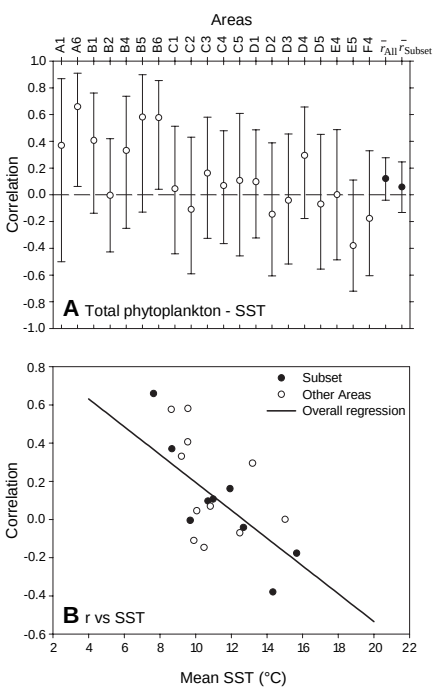

Fig. 2. (**A**) Meta-analysis of the relation between phytoplankton abundance and SST, showing no overall relation. Weighted mean correlations (circles) are shown with 99% confidence limits (bars) calculated using the random-effects model B for the entire study area ($\bar{r}_{All}$) and a subset of nine noncontiguous regions ($\bar{r}_{Subset}$). Bars not overlapping zero are significant. (**B**) The inverse relation between phytoplankton abundance–SST correlations and mean SST (°C) in each region. Points represent individual regions.

and regional changes in vertical stratification and nutrients are often associated with changes in SST (*22*, *23*). In the Northeast Atlantic, there is also a strong relation between winds and SST, particularly westerly winds (*24*) that are important for mixing and stratification, a likely consequence of the large-scale atmospheric forcing by the North Atlantic Oscillation (NAO) (*25*).

The regions in this study generally fall into two turbulence–nutrient regimes associated with temperature (*15*), namely, turbulent–nutrient–rich cool waters (left side of Fig. 2B) and stratified–nutrient-poor warm waters (right side of Fig. 2B). In cooler waters with relatively strong turbulence and plentiful nutrients, it is likely that warming will boost phytoplankton metabolic rates as well as increase stratification, both processes leading to increased phytoplankton abundance (*21*). In warmer, more stratified waters with limited nutrients, it is likely that warming may reduce total phytoplankton abundance (at least of large cells), because increased heating can enhance existing stratification (*2*), reducing the availability of nutrients to phytoplankton and leading to a microbial-dominated community (*26*). This inverse linear relation between the response of phytoplankton abundance to SST and mean regional SST may therefore hold for large areas of the open ocean and continental shelf.

This does not discount the existence of other oceanographic processes in areas where factors such as salinity can play a dominant role in controlling water-column stability (*15*). Examples include areas close inshore where stability is influenced by riverine runoff (stratified–nutrient rich), and polar regions where stability is controlled predominantly by ice melt (turbulent–nutrient poor/high nitrate). However, such areas make up only a tiny fraction of the temperate marine pelagic environment and are not well sampled by the CPR survey, thereby effectively excluding them from our analysis.

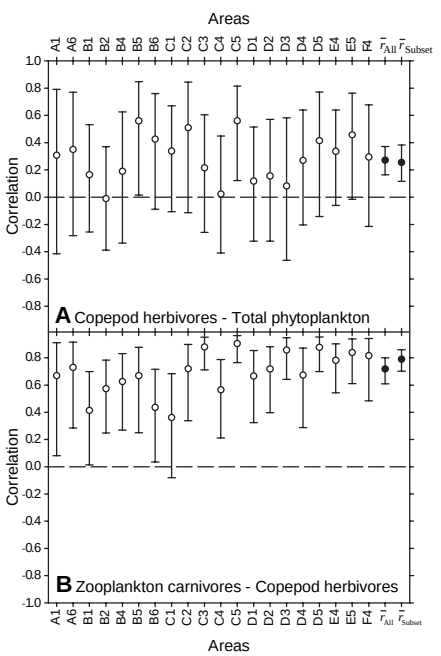

Fig. 3. Meta-analysis of trophic linkages suggesting strong bottom-up control of (**A**) copepod herbivores by phytoplankton and (**B**) zooplankton carnivores by copepod herbivores. Symbols as in Fig. 2A.

To determine whether the climate signal propagates up the plankton food web (bottom-up) or whether grazing by herbivores may impact phytoplankton abundance (top-down), we investigate the link between the abundances of copepod herbivores and their phytoplankton prey. All but one linkage is positive, although most of the correlations are not significant individually (Fig. 3A). The meta-analysis of all regions nevertheless indicates that the overall relation between the abundances of herbivorous copepods and phytoplankton is positive and highly significant ($\bar{r}_{All} = 0.27$, $Z = 6.41$, $P < 0.0001$), with the analysis of the noncontiguous regions verifying this result ($r_{Subset} = 0.25$, $Z = 3.54$, $P < 0.001$). These positive correlations are unlikely to be a consequence of both trophic levels responding directly to SST, because there was no significant relation between copepod herbivore abundance and SST ($r_{All} = -0.04$, $Z = -0.65$, n.s.; $\bar{r}_{Subset} = 0.06$, $Z = 0.60$, n.s.). These relationships are therefore likely to result from consistent bottom-up control of herbivorous copepods by their phytoplankton prey, although the relatively small correlation coefficients suggest that other factors such as disparities in P/B (production/biomass) ratios between predators and their prey might also be important in this link.

To assess whether the signal propagates as far as secondary consumers, we investigated the link between abundances of zooplankton carnivores and their copepod herbivore prey (Fig. 3B). All correlations are strongly positive and all but one are individually significant. The meta-analysis of all regions confirms that there is a very strong and significant positive relation between abundances of secondary consumers and herbivorous copepods ($\bar{r}_{All} = 0.72$, $Z = 11.92$, $P < 0.0001$), with the analysis of noncontiguous regions supporting this conclusion ($\bar{r}_{Subset} = 0.79$, $Z = 10.10$, $P < 0.0001$). These strong positive correlations are unlikely to be a consequence of both trophic levels responding directly to SST, because there was no significant relation between carnivorous zooplankton abundance and SST ($\bar{r}_{All} = 0.11$, $Z = 1.63$, n.s.; $\bar{r}_{Subset} = 0.12$, $Z = 0.88$, n.s.). These results suggest that there is close and consistent bottom-up control of carnivorous zooplankton by their herbivorous copepod prey.

By investigating the linkages in the plankton food web at large time and space scales that subsume local variation, meaningful patterns are revealed (*21*). The magnitude, together with the consistency in form, of the linkages from phytoplankton through copepod herbivores to zooplankton carnivores provides strong support for dominant bottom-up control within the plankton community in the Northeast Atlantic over the time (decades) and space (ten thousands of km^2) scales of the present study. This contrasts with recent meta-analyses (*9*, *10*), which conclude that linkages within the marine plankton community tend to be weak or inconsistent across trophic levels. The strengths of our study, and hence the value of our results, include its wide spatial and temporal scales, the incorporation of a broad taxonomic diversity in each trophic level, and the uniform sampling methodology through time for all plankton in the different regions.

The present findings suggest a possible mechanism underlying some previously observed relationships between fish ecology and climate. For example, recent work has shown that warmer temperatures in northern areas of the Northeast Atlantic support good cod recruitment, whereas warmer temperatures in areas to the south are detrimental to cod recruitment (*27*). Moreover, relationships between the NAO and many fish stocks in the Northeast Atlantic (*28*) may be a consequence of the impact of the NAO on local conditions, such as temperature (*24*), which then may propagate up the plankton food web.

The tight coupling between the plankton trophic levels in marine pelagic ecosystems over the large time and space scales shown in this study should aid prediction of impacts of future climate change on marine food webs. Over the study period (1958 to 2002), we observed a slight cooling of 0.1°C in some northern areas, but a substantial warming of 0.5°C in the southern regions. Ocean temperatures are likely to be further affected by anthropogenic climate change; the Intergovernmental Panel on Climate Change predicts a rise in temperature of between 2° and 4°C in the northeast Atlantic by 2100, with greater increases in the north than in the south (*29*). Our findings suggest that any effects of such climate change will have an impact on phytoplankton, copepod herbivores, and zooplankton carnivores, thereby affecting ecosystem services, such as oxygen production, carbon sequestration, and biogeochemical cycling. Although the direct consequences of these changes for fisheries are not clear, it seems inevitable that fish, seabirds, and marine mammals will need to adapt to a changing spatial distribution of primary and secondary production within pelagic marine ecosystems. Given the scales at which our analyses were conducted and the consistency

of our results, it is reasonable to expect that our findings may generalize to other mid-latitude marine pelagic ecosystems. Under such a scenario, impacts will undoubtedly be felt not only in the oceans, but also in terrestrial ecosystems globally.

References and Notes

1. P. G. Falkowski, R. T. Barber, V. Smetacek, *Science* **281**, 200 (1998).
2. D. Roemmich, J. McGowan, *Science* **267**, 1324 (1995).
3. L. Hughes, *Trends Ecol. Evol.* **15**, 56 (2000).
4. G. Beaugrand, P. C. Reid, F. Ibañez, J. A. Lindley, M. Edwards, *Science* **296**, 1692 (2002).
5. P. Cury *et al.*, *ICES J. Mar. Sci.* **57**, 603 (2000).
6. N. J. Aebischer, J. C. Coulson, J. M. Colebrook, *Nature* **347**, 753 (1990).
7. X. Irigoien, J. Huisman, R. P. Harris, *Nature* **429**, 863 (2004).
8. G. M. Daskalov, *Mar. Ecol. Prog. Ser.* **225**, 53 (2002).
9. F. Micheli, *Science* 285, **1396** (1999).
10. J. B. Shurin *et al.*, *Ecol. Lett.* **5**, 785 (2002).
11. P. C. Reid, J. M. Colebrook, J. B. L. Matthews, J. Aiken, *Prog. Oceanogr.* **58**, 117 (2003).
12. G. Beaugrand, K. M. Brander, J. A. Lindley, S. Souissi, P. C. Reid, *Nature* **426**, 661 (2003).
13. B. Worm, R. A. Myers, *Ecology* **84**, 162 (2003).
14. The spatial, temporal, taxonomic, and ecological scales considered here force some simplifications. For example, all abundance estimates in this study represent indices of near-surface plankton abundance and not absolute values, because the CPR is towed at a depth of ~10 m and many taxa, especially smaller ones, are caught only semiquantitatively. We calculate abundance rather than biomass time series for each trophic level because neither mass nor length measurements are taken from CPR samples, so biomass estimates would require additional assumptions. Within the coarse trophic categories in this study, members (supporting online text) are deemed to be generalist feeders, so each is considered a functional group. Although the phytoplankton compartment does not include nanoflagellates (they are too delicate to be preserved on CPR silks), we are primarily interested in phytoplankton as food for herbivorous copepods, and these feed preferentially on the larger phytoplankton. The zooplankton carnivore compartment includes data on siphonophore abundance, but corresponding data for other cnidarians are not available due to damage during sampling. We do not include meroplankton because their dynamics can be heavily influenced by processes independent of the pelagic ecosystem. We also do not include various other functional groups such as picoplankton, fish, birds, or marine mammals because time series are not available at the appropriate scales for our study. Thus, our conclusions can only be applied to groups sampled quantitatively by the CPR and cannot easily be extended to include the entire pelagic ecosystem.
15. H. A. Bouman *et al.*, *Mar. Ecol. Prog. Ser.* **258**, 19 (2003).
16. We do not use wind or hydrographic (current) data because they have differential effects over the study domain. Reliable time series for clouds are rare over the entire study period (1958 to 2002) and domain. We also do not use an integrative environmental index such as the NAO because it does not allow analysis of the direct responses of plankton communities to their local environment, and because the effects of climate change on the NAO are less clearly understood than are those on SST.
17. J. M. Colebrook, *Bull. Mar. Ecol.* **8**, 143 (1975).
18. B. J. Pyper, R. M. Peterman, *Can. J. Fish. Aquat. Sci.* **55**, 2127 (1998).
19. To apply the modified Chelton Method we estimated autocorrelation functions for each time series. Because many were broken, we used a spline smoother to interpolate data for up to two missing years. These interpolated data were used only to determine the number of degrees of freedom to be removed from analyses; in no way were they used to inflate the time series or to alter correlation coefficients.
20. B. Planque, T. Frédou, *Can. J. Fish. Aquat. Sci.* **56**, 2069 (1999).
21. W. K. W. Li, *Nature* **419**, 154 (2002).
22. K. L. Carder, F. R. Chen, Z. P. Lee, S. K. Hawes, D. Kamykowski, *J. Geophys. Res.* **104**, 5403 (1999).
23. S. Sathyendranath, G. Cota, V. Stuart, H. Maass, T. Platt, *Int. J. Remote Sens.* **22**, 249 (2001).
24. J.-M. Fromentin, B. Planque, *Mar. Ecol. Prog. Ser.* **134**, 111 (1996).
25. J. W. Hurrell, *Science* **269**, 676 (1995).
26. D. H. Cushing, *J. Plankton Res.* **11**, 1 (1989).
27. C. M. O'Brien, C. J. Fox, B. Planque, J. Casey, *Nature* **404**, 142 (2000).
28. L. S. Parsons, W. H. Lear, *Prog. Oceanogr.* **49**, 167 (1999).
29. J. T. Houghton *et al.*, Eds., *Climate Change 2001: The Scientific Basis* (Cambridge Univ. Press, Cambridge, 2001).

30. We thank A. Lindley and M. Gibbons for helping us assign zooplankton to functional groups, as well as the Hadley Centre, UK Met Office, for providing the SST data (HadISST Version 1.1) at no cost. D.S.S. gratefully acknowledges the funding generously provided for this work by the South African National Research Foundation (GUN 2053579), the Ernest Oppenheimer Memorial Trust, and the University of Port Elizabeth, and A.J.R. acknowledges the financial support of Department of Environment Food and Rural Affairs contract MFO430. The CPR survey would not be possible without the cooperation of the agents, owners, masters, and crews of the vessels that tow the recorders. A funding consortium made up of governmental agencies from Canada, France, Iceland, Ireland, the Netherlands, Portugal, the United Kingdom, and the United States financially supports the survey. CPR data are available freely to the international scientific community for research (see www.sahfos.org).

Supporting Online Material

www.sciencemag.org/cgi/content/full/305/5690/1609/DC1
SOM Text
Table S1
References

1 June 2004; accepted 10 August 2004

Methanobactin, a Copper-Acquisition Compound from Methane-Oxidizing Bacteria

Hyung J. Kim,[1]* David W. Graham,[1]† Alan A. DiSpirito,[5] Michail A. Alterman,[2] Nadezhda Galeva,[3] Cynthia K. Larive,[4] Dan Asunskis,[6] Peter M. A. Sherwood[6]

Siderophores are extracellular iron-binding compounds that mediate iron transport into many cells. We present evidence of analogous molecules for copper transport from methane-oxidizing bacteria, represented here by a small fluorescent chromopeptide ($C_{45}N_{12}O_{14}H_{62}Cu$, 1216 daltons) produced by *Methylosinus trichosporium* OB3b. The crystal structure of this compound, methanobactin, was resolved to 1.15 angstroms. It is composed of a tetrapeptide, a tripeptide, and several unusual moieties, including two 4-thionyl-5-hydroxyimidazole chromophores that coordinate the copper, a pyrrolidine that confers a bend in the overall chain, and an amino-terminal isopropylester group. The copper coordination environment includes a dual nitrogen- and sulfur-donating system derived from the thionyl imidazolate moieties. Structural elucidation of this molecule has broad implications in terms of organo-copper chemistry, biological methane oxidation, and global carbon cycling.

The mechanisms involved in microbial copper homeostasis are rapidly being elucidated, although the workings of such systems are only understood in model organisms such as *Escherichia coli*, *Enterococcus hirae*, and *Saccharomyces cerevisiae* (*1–4*). In these organisms, copper homeostatic systems are geared toward active detoxification as opposed to accumulation and storage. However, in many methanotrophic bacteria (aerobes that oxidize CH_4 for carbon and energy and play a major role in the global carbon cycle), copper homeostasis differs because copper requirements can be up to fourfold higher than iron requirements (*5–7*). In such methanotrophs, copper plays a central role in metabolism, regulating expression of two methane monooxygenases: a soluble methane monooxygenase (sMMO) and particulate methane monooxygenase (pMMO) (*5*, *8–10*). Copper also influences the expression of at least two of the four formaldehyde dehydrogenases (*11–13*), the development of internal membranes (*5*, *8*, *14*, *15*), and the expression of other polypeptides related to copper regulation or transport (*5*, *16–19*).

Given the notable role of copper in methanotroph physiology, we postulated that these

[1]Department of Civil, Environmental, and Architectural Engineering, [2]Biochemical Research Service Laboratory, [3]Mass Spectrometry Laboratory, [4]Department of Chemistry, University of Kansas, Lawrence, KS 66045, USA. [5]Department of Biochemistry, Biophysics, and Molecular Biology, Iowa State University, Ames, IA 50011, USA. [6]Department of Chemistry, Kansas State University, Manhattan, KS 66506, USA.

*Present address: Department of Biochemistry, Molecular Biology, and Biophysics, University of Minnesota, St. Paul, MN 55108, USA.
†To whom correspondence should be addressed. E-mail: dwgraham@ku.edu

organisms possess a specialized copper-trafficking mechanism dedicated to transporting higher amounts of copper while protecting cellular components from its toxic effects. Several low–molecular weight copper-containing compounds, previously called copper-binding compounds (CBCs), were implicated in such a mechanism (*5*, *7*, *20–22*); however, sizes among CBCs varied, and no complete structures could be determined. We now suspect that many of the compounds identified earlier were actually breakdown products of a primary molecule described here, which we identify as methanobactin.

Methanobactin appears to fulfill all the presumed roles of such a copper-trafficking molecule. Methanobactin accumulates to high amounts in the growth media of *Methylosinus trichosporium* OB3b and *Methylococcus capsulatus* Bath when grown under copper-limited conditions; however, it is rapidly internalized into the cell when copper is provided. Furthermore, methanobactin stimulates growth in copper-grown *M. trichosporium* OB3b with an optimal 1:1 copper:methanobactin binding stoichiometry (*23*), and copper uptake–deficient mutants accumulate methanobactin in their growth medium in the presence of copper (*20–22*). Lastly, methanobactin co-purifies with pMMO at ratios of 8 to 13 methanobactins per pMMO complex, and the removal of methanobactin results in the loss of pMMO activity in cell-free systems (*5*, *7*). These combined results suggest a previously unknown copper acquisition system in *M. trichosporium* OB3b, mediated by a molecule or molecules that resemble iron siderophores in other bacteria. Furthermore, given the limited understanding of the molecular structure of pMMO and the mechanism of methane oxidation by this enzyme, investigations into the structure and function of methanobactin are of interest.

Here, we report the complete crystal structure of methanobactin excreted into the growth media by *M. trichosporium* OB3b. Typically, 15 to 20 mg of this yellowish-red compound is isolated per liter of spent medium with 3-day-old copper-limited cultures [optical density at 600 nm (OD_{600nm}) ~ 0.7], but the yield is heavily dependent on extracellular copper amounts, copper-to-biomass ratios, and culture ages. Purification of the compound involved solid-phase extraction and reversed-phase high-performance liquid chromatography (RP-HPLC) (*23–25*). Mass spectrometry (MS) of the isolated product showed two predominant ions differing in mass by 62 daltons (Fig. 1). The peak with $[M - H]^-$ at *m/z* 1153 was assigned to the molecular ion for the deprotonated compound, whereas the most intense peak at *m/z* 1215 was assigned to the corresponding copper complex $[M - 2H + {}^{63}Cu^+]^-$. Additionally, this signal shows an isotopic distribution characteristic of copper (69.2% ^{63}Cu, 0% ^{64}Cu, and 30.8% ^{65}Cu).

X-ray photoelectron spectroscopy (XPS) analysis (*25*, *26*) of the methanobactin-copper complex indicates that the majority of the copper is present as Cu^+. Some Cu^{2+} is noted after extended exposure to air, but this is atypical of physiological conditions and the predominant copper oxidation state in methanobactin is Cu^+ (*24*). Figure 2 presents the XPS binding energy spectra for the copper 2p region for freshly bound copper-methanobactin and CuO, which indicate two low-intensity satellite features (peaks 2 and 3) and a shifted position of the main peaks (1 and 4) relative to CuO, characteristic of Cu^+. This observation is consistent with an earlier electron paramagnetic resonance study (*7*) and is similar to other cell systems with mediated copper transport (*27*).

The overall structural features of methanobactin, including amino acid composition and sequence, and N- and C-terminus identification were established by a combination of biochemical and mass spectroscopic analyses (*23–25*). The presence of unusual residues was deduced from a significant mass difference (> 358 daltons) between sequence data and MS investigations. Early results suggested that methanobactin was composed of about 10 to 12 residues arranged in a nonlinear motif with a high affinity for copper. Methanobactin was subsequently crystallized (*23*, *25*), and the structure was resolved by direct methods and refined by full-matrix least-squares methods on F^2 to 1.15 Å (*28*).

Crystallographic data (Table 1) indicate that methanobactin is a small chromopeptide that contains one copper ion per molecule, coordinated by a previously unobserved ligand system with a peptide backbone comprising amino acid and non–amino acid residues. The primary sequence of methanobactin is *N*-2-isopropylester–(4-thionyl-5-hydroxy-imidazole)–Gly^1–Ser^2–Cys^3–Tyr^4–pyrrolidine–(4-hydroxy-5-thionyl-imidazole)–Ser^5–Cys^6–Met^7, with an empirical formula of $C_{45}N_{12}O_{14}H_{62}Cu$ (Fig. 3A). Methanobactin is observed as a crystallographic dimer (fig. S1), although the apparent lack of direct interactions

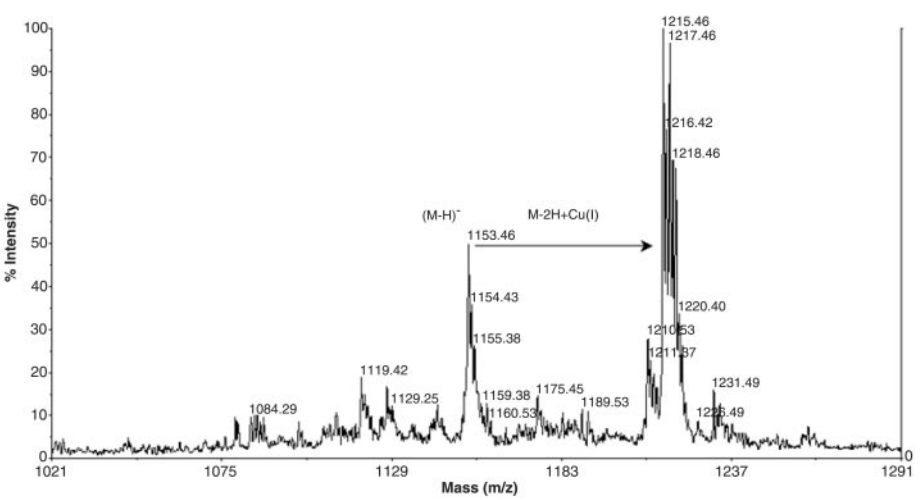

Fig. 1. Negative-ion MALDI-TOF mass spectrum of extracellular copper compound from *M. trichosporium* OB3b showing copper complexation. The isotopic distribution of the most dominant peak is that of copper.

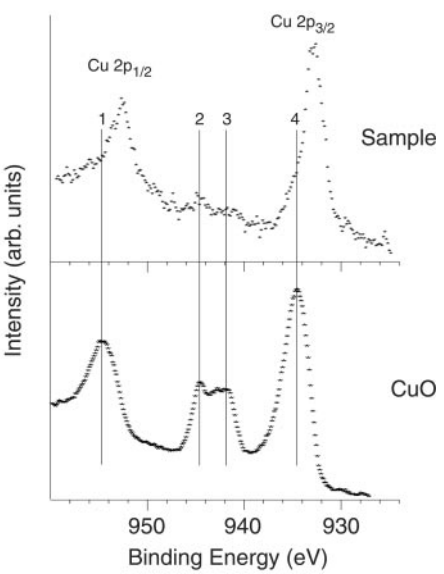

Fig. 2. XPS binding energy spectra for the copper 2p region for methanobactin and for CuO, a reference compound that has copper in the formal oxidation state of Cu^{2+}. The low intensity of the satellite features (2 and 3) and the shifted position of the Cu $2p_{1/2}$ and Cu $2p_{3/2}$ peaks (1 and 4) in methanobactin indicate that copper is primarily in the Cu^+ oxidation state.

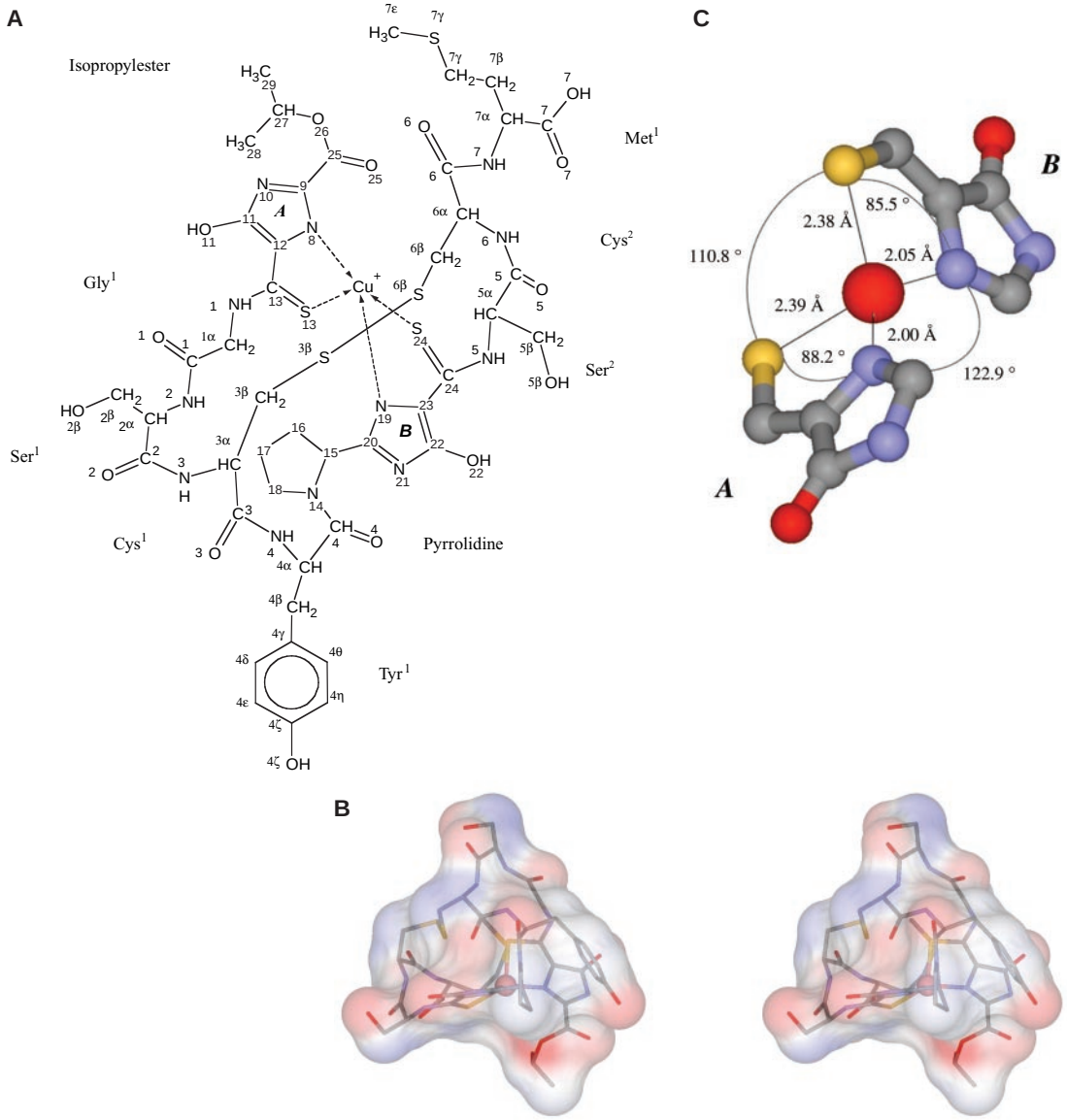

Fig. 3. (**A**) Schematic drawing of methanobactin along with the International Union of Pure and Applied Chemistry atom numbering scheme used in the text. (**B**) The copper coordination sphere derived from 4-hydroxy-5-thionyl imidazoles. Atom colors: carbon, gray; oxygen, red; nitrogen, blue; and sulfur, yellow. Copper ion is represented by central red sphere. (**C**) Stereoview of methanobactin surface modeled with the use of solvent-molecule interaction (probe interaction is 1.4 Å).

between each component suggests that the dimerization in crystals does not persist in solution and is not physiologically relevant.

Overall, methanobactin can be described as having a very compact pyramid-like shape (Fig. 3B) with the metal complexation site being located at the base of the pyramid and not buried. The isopropylester group folds underneath this surface, creating a tail-like projection and a cleft, and appears to obscure the metal site to some extent. The metal coordination environment is composed of dual N- and S-donating systems that are derived from two 4-thionyl-5-hydroxy imidazolate moieties. The bond distances between the donating sulfur atom and its adjacent carbon are 1.68 Å (in thionyl imidazolate A) and 1.67 Å (in thionyl imidazolate B) (Fig. 3C). The sulfur is thus modeled as a thionyl ligand (C=S–Cu) rather than the more commonly found thiolate (C–S–Cu). The C=S distances agree well with previous synthetic N,S-thionyl donor complexes that possess antibacterial properties (*29*). Furthermore, the thioamide bonds that link each imidazole moiety to a Gly^1 and a Ser^2 are found in the thiopeptide antibiotics promoinducin and thiostreptone from the *Streptomyces* species, which is interesting given that methanobactin has also shown to be bacteriocidal for a variety of Gram-positive bacteria (*30*). This unusual thiopeptide bond is also found in the nickel enzyme methyl–coenzyme reductase from methanogenic archaea that catalyzes methane formation from methyl–coenzyme M and coenzyme B (*31*, *32*).

The N^{ε} atom of each imidazole and the S atom of the two thionyl substituents coordinate the copper in a distorted tetrahedron geometry (Fig. 3C). A solvent molecule is not coordinated to the copper in the crystal structure. The $N^{\varepsilon}(8)$-Cu-S(13) and $N^{\varepsilon}(19)$-Cu-S(24) bond angles (ligand bite angles) of 85.5° and 88.2°, respectively, deviate from the ideal tetrahedral bond angle (109.5°). Both heterocycle rings along with the thionyl substituents are essentially co-planar. The copper atom lies in the plane of thionyl imidazole B but deviates by 0.87 Å from the plane of thionyl imidazole A. The two planes defining the N,S-chromophoric moieties bisect at nearly perpendicular angles. The copper-to-ligand distances are 2.39 and 2.38 Å for Cu-S(13) and Cu-S(24), respectively, and 2.01 and 2.05 Å for $N^{\varepsilon}(8)$-Cu and $N^{\varepsilon}(19)$-Cu (numbers in parentheses designate relative atom numbers), respectively, and indicate strong interactions (Fig. 3C).

The structure of methanobactin as well as growth and physiological data argues for its function as a copper-sequestration compound (*20*–*22*). The cells appear to excrete methanobactin continuously, and it accumulates in the culture media under copper-deficient conditions. If copper is provided, methanobactin binds the copper and the methanobactin-copper

Table 1. Crystallographic data and refinement statistics. A total of 1663 parameters were refined against 698 restraints and 8765 data to give wR(F^2) = 0.2464 and S = 1.1 (where S is goodness of fit) for weights of $w = 1/[\sigma^2(F^2) + (0.1600P)^2 + 130.00P]$, where $P = ([F^2_{obs} - F^2_{cal}])/3$. The final R factor, R(F), was 0.0824 for the 7025 observed, [$F > 4\sigma$ (F)], data. The largest shift/standard uncertainty was 0.012 in the final refinement cycle. The final difference map had maxima and minima of 0.624 and −0.393 e/Å^3, respectively. Parentheses denote the highest resolution shell. $R_{sym} = \Sigma[\Sigma|F^2_{obs} - F^2_{cal}|]/\Sigma(\Sigma F^2_{obs})/n]$ and R factor $= \Sigma||F_{obs}| - |F_{cal}||/\Sigma|F_{obs}|$, $F_{obs} > 0$.

$(C_{44}H_{54}CuN_{12}O_{15}S_5) \cdot 10.5(H_2O)$	
Formula weight	1404
Molecular weight $(C_{44}H_{54}CuN_{12}O_{15}S_5)$	1217.2
Data collection	
Wavelength	0.71073 Å
Reflections collected	66,370
Refinement	
Redundancy	7.55
I/σ	18.23 (14.81)
Rsym (%)	8.05 (37.62)
Resolution (Å)	1.15
R factor	0.0832
Completeness	99.8
Goodness of fit on F^2	1.1

complex is internalized to the cell, possibly to be associated with pMMO (*5*, *7*, *24*). Further, its metal-ion shuttling role is suggested by structural similarities to the amino acid–containing pyoverdin class of iron siderophores, which also have antibacterial properties (*33*–*36*). In fact, the similarities between methanobactin and the pyoverdin siderophores (e.g., azotobactin and pseudobactin produced by *Azotobacter* spp. and *Pseudomonas* spp.) led to the renaming of CBC to methanobactin.

If methanobactin is indeed a "copper-siderophore" or a "chalkophore" (after the Greek for copper), a specialized copper-trafficking or defense mechanism probably exists in organisms that produce the compound. However, whether methanobactin acts exclusively as an extracellular copper-sequestering agent or has other in vivo functions related to the delivery and insertion of copper ions to copper-containing proteins like pMMO must still be determined. Regardless, the elucidation of the methanobactin structure has major implications in understanding the molecular mechanism of biological methane oxidation and methane cycling in the environment and may also lead to the identification of other copper-trafficking molecules.

References and Notes

1. D. L. Huffman, T. V. O'Halloran, *Annu. Rev. Biochem.* **70**, 677 (2001).
2. L. A. Finney, T. V. O'Halloran, *Science* **300**, 931 (2003).
3. C. Rensing, G. Grass, *FEMS Microbiol. Rev.* **27**, 197 (2003).
4. A. C. Rosenzweig, *Chem. Biol.* **9**, 673 (2002).
5. D. W. Choi *et al.*, *J. Bacteriol.* **185**, 5755 (2003).
6. H.-N. Nguyen *et al.*, *J. Biol. Chem.* **269**, 14995 (1994).
7. J. A. Zahn, A. A. DiSpirito, *J. Bacteriol.* **178**, 1018 (1996).
8. H. Dalton, S. D. Prior, D. J. Leak, S. H. Stanley, in *Microbial Growth on C_1 Compounds*, R. L. C. Hanson, R. S. Hanson, Eds. (American Society for Microbiology, Washington, DC, 1984), pp. 75–82.
9. S. D. Prior, H. Dalton, *J. Gen. Microbiol.* **131**, 155 (1985).
10. S. Lontoh, J. D. Semrau, *Appl. Environ. Microbiol.* **64**, 1106 (1998).
11. J. A. Zahn, D. J. Bergmann, J. M. Boyd, R. C. Kuitz, A. A. DiSpirito, *J. Bacteriol.* **183**, 6832 (2001).
12. S. Tate, H. Dalton, *Microbiology* **145**, 159 (1999).
13. J. A. Vorholt, L. Chistoserdova, S. M. Stolyar, R. K. Thauer, M. E. Lidstrom, *J. Bacteriol.* **181**, 5750 (1999).
14. C. A. Brantner *et al.*, *Can. J. Microbiol.* **43**, 672 (1997).
15. P. Peltola, P. Priha, S. Laakso, *Arch. Microbiol.* **159**, 521 (1993).
16. O. Berson, M. E. Lidstrom, *Environ. Sci. Technol.* **30**, 802 (1998).
17. H. J. Kim, D. W. Graham, *FEMS Microbiol. Lett.* **201**, 133 (2001).
18. G. P. Stafford, J. Scanlan, I. R. McDonald, J. C. Murrell, *Microbiology* **149**, 1771 (2003).
19. O. A. Karlsen *et al.*, *Appl. Environ. Microbiol.* **69**, 2386 (2003).
20. A. A. DiSpirito *et al.*, *J. Bacteriol.* **180**, 3606 (1998).
21. M. W. Fitch *et al.*, *Appl. Environ. Microbiol.* **59**, 2771 (1993).
22. C. M. Tellez, K. P. Gaus, D. W. Graham, R. G. Arnold, R. Z. Guzman, *Appl. Environ. Microbiol.* **64**, 1115 (1998).
23. H. J. Kim, thesis, University of Kansas (2003).
24. H. J. Kim *et al.*, in preparation.
25. Materials and methods are available as supporting material on *Science* Online.
26. G. D. Claycomb, P. M. A. Sherwood, *J. Vac. Sci. Technol. A* **20**, 1230 (2002).
27. S. Puig, E. M. Rees, D. J. Thiele, *Structure* **10**, 1292 (2002).
28. G. M. Sheldrick, SHELXTL version 5 reference manual (Bruker-AXS, Madison, WI), (1994).
29. C. Brückner, S. J. Rettig, D. Dolphin, *Inorg. Chem.* **39**, 6100 (2000).
30. A. A. DiSpirito *et al.*, U.S. Provisional Patent Application Serial No. 60/434, 873 (2004).
31. C. Brükner *et al.*, *Inorg. Chem.* **39**, 6100 (2000).
32. W. Grabarse *et al.*, *J. Mol. Biol.* **303**, 329 (2000).
33. T. Selmer *et al.*, *J. Biol. Chem.* **275**, 3755 (2000).
34. O. Knosp *et al.*, *J. Bacteriol.* **159**, 341 (1984).
35. P. A. Demange *et al.*, *Biochemistry* **27**, 2745 (1988).
36. P. A. Demange *et al.*, *Biochemistry* **29**, 11041 (1990).

37. We thank J. Aube, B. Blagg, K. Camarda, D.W. Choi, T. Ebihara, A. Hooper, B. Elmore, E. Schönbrunn, and T. Williams for assistance on the project. The work was supported by NSF grant no. BES-9407286 (D.W.G.), Department of Energy grant no. 029ER2037 (A.A.D.), and University of Kansas Research Development Funds (D.W.G., C.K.L., M.A.A.). All crystallography was performed at the University of Kansas Crystallography Facility, with the diffractometer provided by NSF grant no. CHE-0079282. The crystal structure of methanobactin has been deposited at the Cambridge Crystallographic Data Centre and allocated the deposition number CCDC 241254. This work was done in fulfillment of dissertation requirements of H.J.K. at the University of Kansas, Department of Civil, Environmental, and Architectural Engineering.

Supporting Online Material

www.sciencemag.org/cgi/content/full/305/5690/1612/DC1
Materials and Methods
Figs. S1 and S2

25 March 2004; accepted 3 August 2004

Activation of Endogenous Cdc42 Visualized in Living Cells

Perihan Nalbant,* Louis Hodgson,* Vadim Kraynov, Alexei Toutchkine, Klaus M. Hahn†

Signaling proteins are tightly regulated spatially and temporally to perform multiple functions. For Cdc42 and other guanosine triphosphatases, the subcellular location of activation is a critical determinant of cell behavior. However, current approaches are limited in their ability to examine the dynamics of Cdc42 activity in living cells. We report the development of a biosensor capable of visualizing the changing activation of endogenous, unlabeled Cdc42 in living cells. With the use of a dye that reports protein interactions, the biosensor revealed localized activation in the trans-Golgi apparatus, microtubule-dependent Cdc42 activation at the cell periphery, and activation kinetics precisely coordinated with cell extension and retraction.

Cdc42, a member of the Rho family of small guanosine triphosphatase (GTPase) proteins, regulates multiple cell functions, including motility, proliferation, apoptosis, and cell morphology (*1*–*3*). In order to fulfill these diverse roles, the timing and location of Cdc42 activation must be tightly controlled. The Cdc42 biosensor used here to examine the spatiotemporal dynamics of Cdc42 activation represents an in vivo application of a dye (I-SO) designed specifically to report protein conformational changes and protein interactions in living cells (*4*). In this biosensor, a domain from the Cdc42 effector protein WASP that binds only to activated Cdc42 was covalently labeled with the dye. The labeled domain showed a strong increase in fluorescence intensity upon binding to activated, underivatized Cdc42.

On the basis of the nuclear magnetic resonance (NMR) structure of the Cdc42-WASP

Department of Pharmacology, University of North Carolina School of Medicine, Chapel Hill, NC 27599–7365, USA.

*These authors contributed equally to this work.
†To whom correspondence should be addressed. E-mail: khahn@med.unc.edu

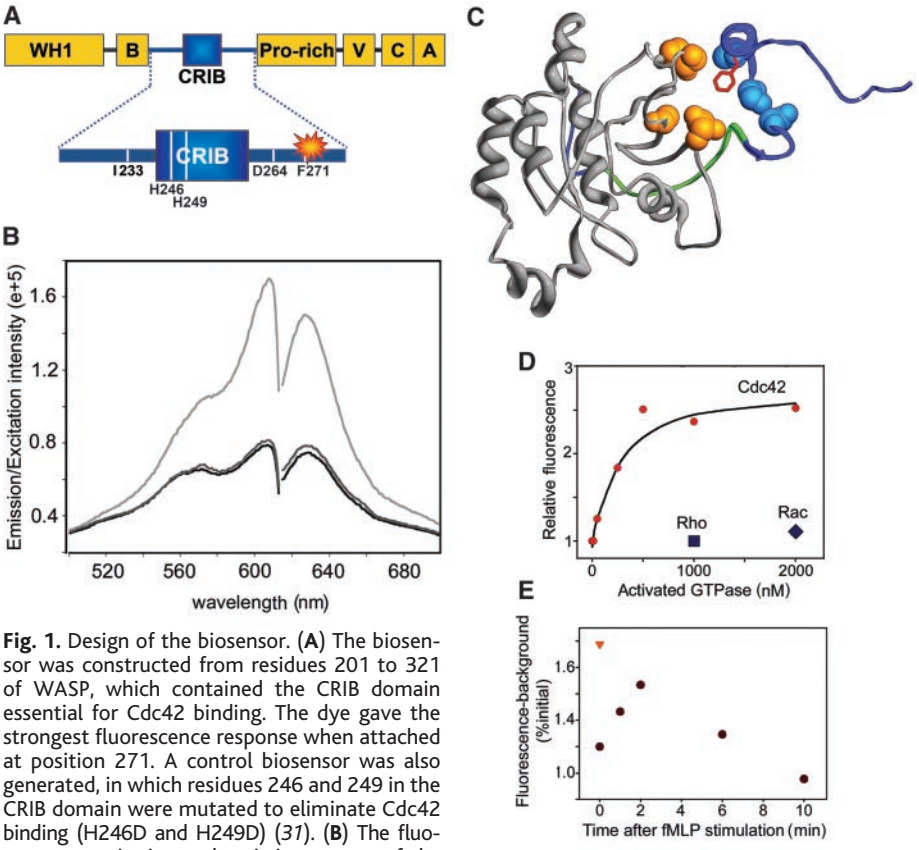

Fig. 1. Design of the biosensor. (**A**) The biosensor was constructed from residues 201 to 321 of WASP, which contained the CRIB domain essential for Cdc42 binding. The dye gave the strongest fluorescence response when attached at position 271. A control biosensor was also generated, in which residues 246 and 249 in the CRIB domain were mutated to eliminate Cdc42 binding (H246D and H249D) (*31*). (**B**) The fluorescence excitation and emission spectra of the biosensor showed a 2.8-fold increase in intensity upon interacting with activated Cdc42 (black line, biosensor alone; dark gray line, biosensor with saturating Cdc42-GDP; light gray line, biosensor with saturating Cdc42-GTPγS). (**C**) Binding of the biosensor to Cdc42 placed the dye attached at position 271 (red) in a hydrophobic pocket formed by amino acids from both WASP (blue) and Cdc42 (orange). The CRIB domain is shown in green. (**D**) The biosensor showed a concentration-dependent fluorescence increase in response to Cdc42-GTPγS, but did not respond to Rho-GTPγS or Rac-GTPγS. (**E**) Human neutrophils were lysed at different times after stimulation with fMLP, and biosensor was added to the lysates. Circles, fluorescence intensity in lysates at each time point; triangle, unstimulated lysate equilibrated with GTPγS.

complex (*5*), the dye was tested at three positions (I233, D264, and F271 of WASP) to optimize fluorescence response and binding (Fig. 1A). Site-specific labeling was accomplished by inserting a single cysteine and reacting the WASP domain with cysteine-selective iodoacetamide dye (*4*). The dye showed the greatest response at position 271, undergoing a 2.8-fold increase in fluorescence intensity upon binding to Cdc42-GTPγS, relative to either biosensor alone or GDP-loaded Cdc42 (Fig. 1B). The NMR structure of the Cdc42-WASP complex indicated that the dye at position 271 is inserted into a hydrophobic pocket formed from amino acids of both Cdc42 and WASP (Fig. 1C). The dissociation constant (K_d) for the Cdc42-biosensor interaction, determined by fitting fluorescence changes to the Michaelis equation, was 150 ± 50 nM (Fig. 1D). This was slightly higher than previously reported for a similar, unlabeled WASP fragment (77 ± 9 nM) (*6*), indicating that the dye minimally perturbed binding of the domain. To determine the specificity of the biosensor, we examined interactions with different activated GTPases. The biosensor distinguished proteins closely related to Cdc42 from other members of the Rho family. It did not interact with RhoA or Rac at concentrations well above physiological levels (Fig. 1D), but responded to both Cdc42 and the closely related protein TC10, which bind WASP with similar affinity (*7*) (fig. S1).

Figure 1E shows that the labeled WASP fragment provides a straightforward means to assay Cdc42 activation in cell lysates. By simply adding the biosensor to the lysate, one can obtain a fluorescence readout of Cdc42 activa-

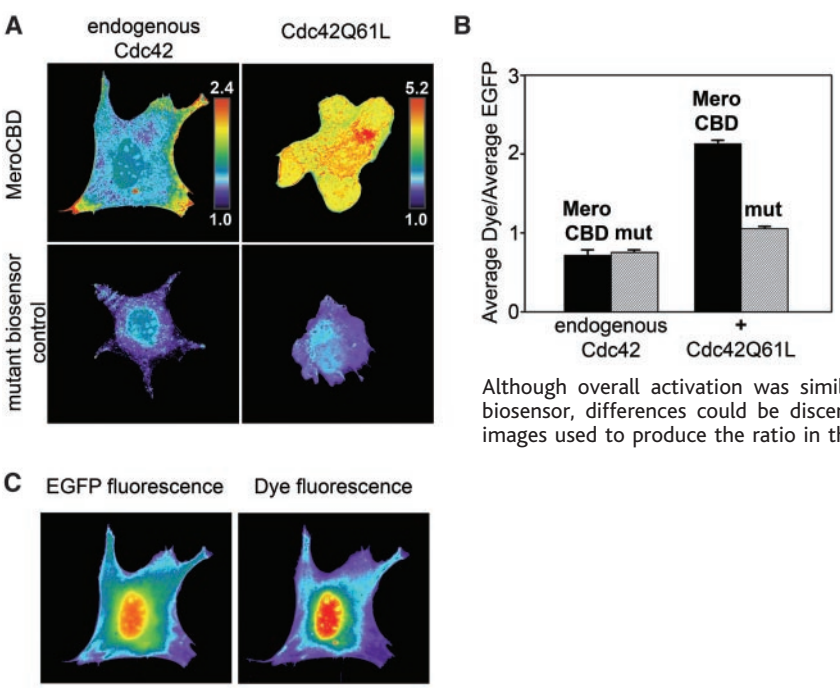

Fig. 2. Activation of endogenous Cdc42 in living cells. (**A**) Distribution of activated Cdc42 in MEF/3T3 cells. Cells were injected with MeroCBD (upper panels) or with mutant control biosensor (lower panels). MeroCBD showed localized activation of endogenous, wild-type Cdc42 in unstimulated cells (left column). Overexpression of constitutively active Cdc42-Q61L (right column) led to increased activation signal throughout the cell. Results were unaffected by biosensor concentrations over the broad range examined (EGFP fluorescence per unit area = 50 to 400, normalized for exposure time). (**B**) Average Cdc42 activity in cells with and without expression of Cdc42-Q61L (with Cdc42-Q61L = mean ± SEM: 12 MeroCBD cells, 7 control cells; without Cdc42-Q61L = mean ± SEM: 7 MeroCBD cells, 11 control cells). Although overall activation was similar in unstimulated cells loaded with real versus control biosensor, differences could be discerned because activation was localized. (**C**) EGFP and dye images used to produce the ratio in the cell shown at upper left in (A).

tion. The method was used to determine the kinetics of Cdc42 activation in neutrophils after stimulation with chemoattractant fMetLeuphe (fMLP) peptide. Results paralleled those previously reported using well-established methods (*8*). Fluorescence of the biosensor was also used to monitor the real-time kinetics of Cdc42 GDP/GTP exchange in vitro (fig. S2D).

Because the labeled WASP fragment responded to activated Cdc42 through fluorescence intensity modulation, a ratiometric imaging approach was used to correct for effects of varying cell thickness, uneven illumination, and other factors that could affect imaging of dye intensity (*9*). The biosensor was fused to enhanced green fluorescent protein (EGFP) to provide a fluorescence signal insensitive to Cdc42 binding, but with the same subcellular distribution as the sensitive dye. The dye image could be divided by the EGFP image to normalize changes in dye intensity not originating from Cdc42 binding. A proline-rich region of WASP (amino acids 315 to 321) was also deleted to preclude possible binding to proteins containing SH3 domains. Fluorescence response and Cdc42 binding of the biosensor remained intact after these modifications (fig. S2A). It was named MeroCBD, for the combination of the Cdc42 binding domain with a merocyanine dye.

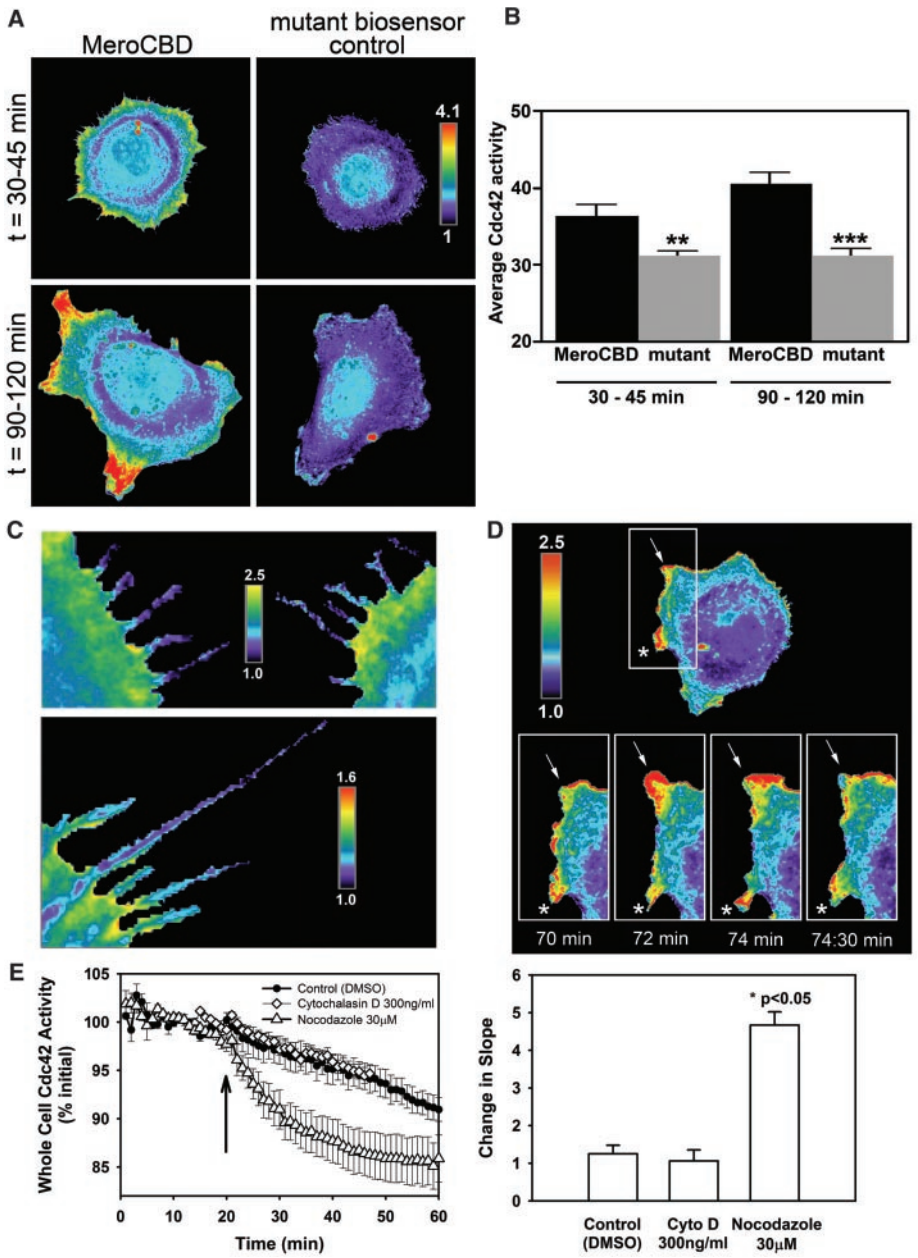

Fig. 3. Cdc42 activation during cell adhesion and spreading. (**A**) Cdc42 activation was examined at different times after MEF/3T3 cell adhesion to fibronectin. Activity was first distributed in a narrow band around the cell, then concentrated in the larger protrusions that formed at later time points (n = 11 cells at 30 to 45 min, n = 22 cells at 90 to 120 min). (**B**) Total integrated Cdc42 activity divided by cell area (average cellular activation) was higher during later stages when cells were polarized and producing large extensions (t = 30 to 45 min: $^{**}P < 0.01$, n = 11 cells; t = 90 to 120 min: $^{***}P < 0.001$, n = 12 cells). Error bars represent the SEM. (**C**) Activation was observed at the cell edges near filopodia, but not in the filopodia themselves (n > 300 filopodia). Areas of low activation sometimes extended into the cell at the base of filopodia (lower panel). (**D**) Active remodeling of the cell perimeter was associated with high levels of Cdc42 activation (movies S1 to S3). (**E**) Cells were treated with nocodazole (30 μM, n = 7 cells), cytochalasin D (300 ng/ml, n = 9 cells), or dimethyl sulfoxide (DMSO) control (n = 6 cells). Average whole-cell Cdc42 activity was monitored before and after drug treatment (at the time indicated by the arrow). Error bars represent the SEM. See movies S4 to S6.

The biosensor was injected into living fibroblasts, where it showed localized Cdc42 activation even in unstimulated cells, which was highest at cell extensions (Fig. 2A). In cells expressing constitutively active Cdc42-Q61L (*10*), the overall levels of activity shown by MeroCBD were much higher (Fig. 2, A and B), and activation was distributed throughout the cell. It was important to show that the dye was not binding nonspecifically to membranes or to other hydrophobic cell components that could produce spurious fluorescence intensity increases. When MeroCBD was compared to a control biosensor with severely reduced Cdc42 binding (Fig. 2B; fig. S2, B and C), the mutant biosensor showed no localized activation for either endogenous or dominant positive Cdc42 (Fig. 2A), and showed only slightly increased total activity in cells expressing Cdc42-Q61L (Fig. 2B). Simple localization of the CBD-EGFP was not sufficient to reveal Cdc42 activation (Fig. 2C).

The ability to detect endogenous protein with the high sensitivity provided by the dye was important in studying Cdc42. High sensitivity enabled detection of protein activation at native concentrations, unlike previous fluorescence resonance energy transfer (FRET) biosensors that required overexpression of Cdc42 (*11*), and showed more uniform activation. MeroCBD did not require modification of the Cdc42 terminus with a GFP mutant for FRET (*12*), thus maintaining normal regulation by guanosine dissociation inhibitors (GDIs) (*13*).

Cdc42 is known to be important for maintaining cell polarity in motility (*14*), but the role of localized Cdc42 activation is poorly understood. Cdc42 promotes leading-edge extension through activation of Rac and of WASP, which causes Arp2/3 to nucleate actin filaments (*15*, *16*). It also induces the fine cell extensions known as filopodia (*17*, *18*). The relative spatiotemporal dynamics of Cdc42 activation, protrusion, and filopodia formation were examined in fibroblasts as they attached and spread on fibronectin (*19*). At 30 to 45 min after plating, Cdc42 was

activated in a thin band at cell edges extending filopodia (Fig. 3A). No activation was observed within the filopodia themselves (Fig. 3C). Regions of lower activation sometimes extended into the cell body at the base of filopodia (Fig. 3C, lower cell), consistent with studies showing that actin bundles in filopodia extend into the cell body (*20*). At 90 to 120 min after attachment, activity became localized within larger dynamic protrusions, and overall activity increased (Fig. 3B); protrusions had more than twice the average activity of any other region (n = 22 cells) (Fig. 3, A and D) (movies S1 to S3; see also motion control fig. S6). Controls showed that biosensor levels did not perturb spreading or motility (figs. S3 to S5).

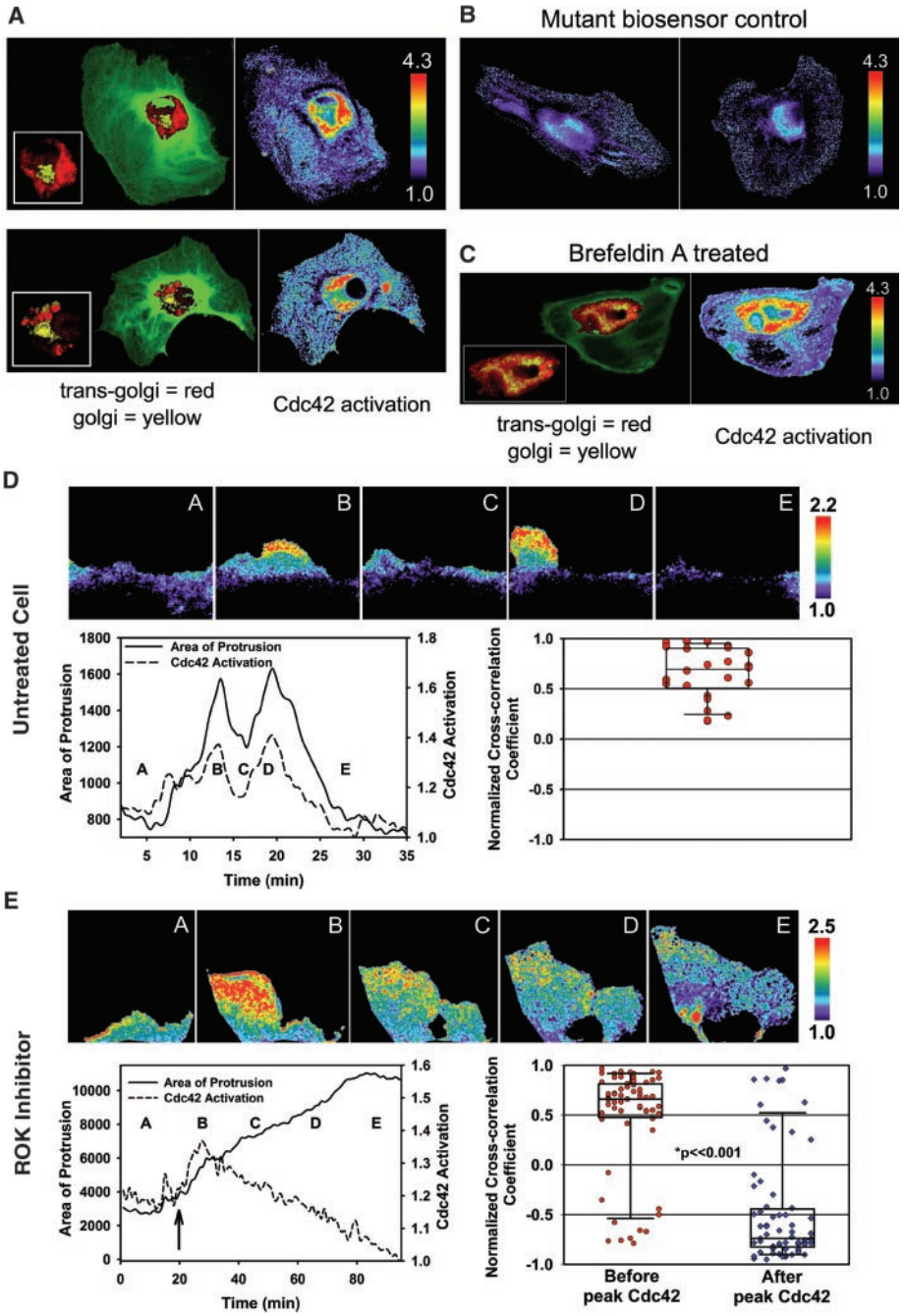

Fig. 4. Cdc42 activation at trans-Golgi. Activation kinetics synchronized with extension and retraction. (**A**) Immunofluorescence colocalization of trans-Golgi markers and Cdc42 activation in human umbilical vein–derived endothelial cells (HUVEC). Trans-Golgi fluorescence is in red, Golgi fluorescence is in yellow. EGFP fluorescence is in green. (**B**) Mutant control biosensor in fixed HUVEC cells. (**C**) Upon collapsing the Golgi using Brefeldin A, the trans-Golgi and Cdc42 activation remained intact. (**D**) For individual protrusions, area and Cdc42 activation per unit area were monitored over time. Of 22 cell regions analyzed, 17 showed high synchrony between protrusions and Cdc42 activity during both extension and retraction, as was apparent through inspection of the graphs and using cross-correlation analysis (*32*). Data from a representative protrusion are shown. Images correspond to the time points indicated in the plots. All other data are shown in fig. S7. (**E**) When cells were treated with Rho kinase inhibitor Y27632 (30 μM, at the time indicated by the arrow), cells continued to extend even after Cdc42 activation receded (see also fig. S8 and movie S7).

Microtubules or actin may direct Cdc42 activation to specific peripheral locations (*21*–*24*). We explored this possibility by treating cells with the microtubule-depolymerizing agents nocodazole and colchicine, or with cytochalasin D, an inhibitor of actin polymerization. Only nocodazole and colchicine markedly affected peripheral Cdc42 activation (Fig. 3E; fig. S9, movies S4 to S6). Microtubules may localize interactions between Cdc42 and guanine nucleotide exchange factors (*25*), by directing vesicle trafficking or regulating events at adhesion complexes (*26*, *27*). Cdc42 has been implicated in intracellular trafficking (*28*–*30*). Our biosensor consistently showed activation in the trans-Golgi apparatus of endothelial cells (Fig. 4, A to C), and sometimes also in fibroblasts. Activation in this major secretory compartment suggests that Cdc42 regulates directional sorting or trafficking of polarity cues, or that microtubules mediate trafficking of activated Cdc42 to specific portions of the periphery (Fig. 3E).

Using the dye's ability to obtain more than a hundred sequential images at low biosensor concentrations, we carried out high-resolution kinetic studies of Cdc42 activation during extension and retraction of individual protrusions (Fig. 4D; fig. S7). Using an algorithm to objectively determine the boundaries of protrusions, we plotted the changing areas of individual protrusions against the protrusions' total activation per unit area. The rise and fall of Cdc42 activity was markedly correlated with both extension and retraction. This close correlation suggested that Cdc42 activation and deactivation could be rate-determining steps for extension and retraction. Alternatively, upstream signals might coordinately inhibit Cdc42 activity while inducing retraction. We distinguished these possibilities by blocking retraction using an inhibitor of Rho kinase (Y27632). This caused protrusions to continue expanding even after Cdc42 activity decreased (Fig. 4E; fig. S8 and movie S7), indicating that upstream signals (possibly regulated by the microtubule cytoskeleton) control Cdc42 activity and retraction in parallel. Cdc42 activity did not remain elevated during protrusion, suggesting that Cdc42 initiates rather than maintains extension.

MeroCBD exemplifies a biosensor approach that combines the ability to sense endogenous molecules with the sensitivity provided by direct excitation of a fluorescent dye. This extends our ability to examine proteins that cannot be derivatized or overex-

pressed for live cell studies, and enabled detailed kinetic analysis of rapid cellular processes. The biosensor revealed Cdc42 activation in the trans-Golgi compartment, microtubule-dependent activation at the cell periphery but not in filopodia, and tightly coordinated kinetics of cell extension, retraction, and Cdc42 activation.

References and Notes

1. J. W. Erickson, R. A. Cerione, *Curr. Opin. Cell Biol.* **13**, 153 (2001).
2. L. Kjoller, A. Hall, *Exp. Cell Res.* **253**, 166 (1999).
3. M. C. Subauste *et al.*, *J. Biol. Chem.* **275**, 9725 (2000).
4. A. Toutchkine, V. Kraynov, K. Hahn, *J. Am. Chem. Soc.* **125**, 4132 (2003).
5. N. Abdul-Manan *et al.*, *Nature* **399**, 379 (1999).
6. M. G. Rudolph *et al.*, *J. Biol. Chem.* **273**, 18067 (1998).
7. E. Vignal *et al.*, *J. Biol. Chem.* **275**, 36457 (2000).
8. V. Benard, B. P. Bohl, G. M. Bokoch, *J. Biol. Chem.* **274**, 13198 (1999).
9. G. R. Bright, G. W. Fisher, J. Rogowska, D. L. Taylor, *Methods Cell Biol.* **30**, 157 (1989).
10. P. J. Miller, D. I. Johnson, *Mol. Cell. Biol.* **14**, 1075 (1994).
11. A. Seth, T. Otomo, H. L. Yin, M. K. Rosen, *Biochemistry* **42**, 3997 (2003).
12. R. E. Itoh *et al.*, *Mol. Cell. Biol.* **22**, 6582 (2002).
13. G. R. Hoffman, N. Nassar, R. A. Cerione, F. Bachmair, *Cell* **100**, 345 (2000).
14. S. Etienne-Manneville, *J. Cell Sci.* **117**, 1291 (2004).
15. A. L. Bishop, A. Hall, *Biochem. J.* **348**, 241 (2000).
16. H. N. Higgs, T. D. Pollard, *J. Cell Biol.* **150**, 1311 (2000).
17. C. D. Nobes, A. Hall, *Biochem. Soc. Trans.* **23**, 456 (1995).
18. R. Kozma, S. Ahmed, A. Best, L. Lim, *Mol. Cell. Biol.* **15**, 1942 (1995).
19. L. S. Price, J. Leng, M. A. Schwartz, G. M. Bokoch, *Mol. Biol. Cell* **9**, 1863 (1998).
20. T. M. Svitkina *et al.*, *J. Cell Biol.* **160**, 409 (2003).
21. S. Etienne-Manneville, A. Hall, *Cell* **106**, 489 (2001).
22. C. M. Waterman-Storer, R. A. Worthylake, B. P. Liu, K. Burridge, E. D. Salmon, *Nat. Cell Biol.* **1**, 45 (1999).
23. C. Higashida *et al.*, *Science* **303**, 2007 (2004).
24. R. Wedlich-Soldner, S. Altschuler, L. Wu, R. Li, *Science* **299**, 1231 (2003).
25. A. Schmidt, A. Hall, *Genes Dev.* **16**, 1587 (2002).
26. I. R. Nabi, *J. Cell Sci.* **112**, 1803 (1999).
27. A. F. Palazzo, G. G. Gundersen, *Sci. STKE* **2002**, pe31 (2002).
28. J. W. Erickson, C. Zhang, R. A. Kahn, T. Evans, R. A. Cerione, *J. Biol. Chem.* **271**, 26850 (1996).
29. W. J. Wu, J. W. Erickson, R. Lin, R. A. Cerione, *Nature* **405**, 800 (2000).
30. R. A. Cerione, *Trends Cell Biol.* **14**, 127 (2004).
31. H. Miki, T. Sasaki, Y. Takai, T. Takenawa, *Nature* **391**, 93 (1998).
32. J. T. Mandeville, R. N. Ghosh, F. R. Maxfield, *Biophys. J.* **68**, 1207 (1995).

33. We are grateful to P. Hordijk, G. Bokoch, and L. Dehmelt for critical reading of the manuscript; to G. Bokoch for help with neutrophil stimulation assays; and to M. Berba for secretarial assistance. This work was funded by grants from the Deutsche Forschungsgemeinschaft (P.N.), the Arthritis Foundation (V.K.), the Leukemia and Lymphoma Society (A.T.), and by the NIH (grants GM57464 and GM64346) (K.M.H.). K.M.H. has a financial interest in and is a consultant for and member of the Scientific Advisory Board for Genospectra Company, which seeks to develop products that precisely characterize molecular events that occur in cells.

Supporting Online Material

www.sciencemag.org/cgi/content/full/305/5690/1615/DC1
Materials and Methods
Figs. S1 to S9
Movies S1 to S7
References

17 May 2004; accepted 30 July 2004

Advanced Cardiac Morphogenesis Does Not Require Heart Tube Fusion

Shanru Li,[1] Deying Zhou,[1] Min Min Lu,[1] Edward E. Morrisey[1,2]*

The bilateral cardiac mesoderm migrates from the lateral region of the embryo to the ventral midline, where it fuses to form the primitive heart tube. It is generally accepted that migration and fusion are essential for subsequent stages of cardiac morphogenesis. We present evidence that, in *Foxp4* mutant embryonic mice, each bilateral heart-forming region is capable of developing into a highly differentiated four-chambered mammalian heart in the absence of midline fusion. These data demonstrate that left-right chamber specification, cardiac looping, septation, cardiac myocyte differentiation, and endocardial cushion formation are preprogrammed in the precardiac mesoderm and do not require midline positional identity or heart tube fusion.

Although the molecular mechanisms underlying cardiac myocyte differentiation have been extensively examined and initial molecular pathways have been identified, much less is understood about how specified myocardial cells form the primitive heart tube and the four-chambered mammalian heart. This complex morphological process has a major impact on human health, because cardiovascular defects account for a substantial percentage of neonatal congenital disease. The bilateral precardiac mesoderm forms at the anterior pole of the vertebrate embryo (*1*, *2*). How this mesoderm migrates to the ventral midline to form the single heart tube in the embryo is not well understood, although contributions from anterior foregut endoderm have been implicated. Moreover, whether this fusion event is required for cardiac differentiation and morphogenesis is not known, although some markers of the cardiac myocyte lineage that become spatially restricted in later development (such as *eHAND*, *MLC2a*, and *MLC2v*) are expressed throughout the early precardiac mesoderm (*1*, *2*). The heart is also the first organ to exhibit left-right asymmetry. Whether this asymmetry is preprogrammed into the precardiac mesoderm or whether it is acquired coincident with midline fusion is unknown. Most genetic models of defective heart tube fusion, also known as cardia bifida, are characterized by bilateral regions of specified cardiac mesoderm that express cardiac-specific genes but fail to progress through later stages of cardiac morphogenesis (*3*–*5*). In addition, most murine models of cardia bifida exhibit additional extracardiac defects in body pattern formation, including severe defects in ventral morphogenesis and embryonic turning (*3*, *6*). These data have led to a working model in which ventral midline fusion of the bilateral cardiac primordia is essential for subsequent cardiac development and morphogenesis, especially later aspects of chamber identity, left-right cardiac asymmetry, and looping morphogenesis (*1*, *7*).

We have previously cloned and characterized *Foxp4*, a member of the Fox gene family that is expressed in multiple tissues, including the lung, gut, and brain, in the developing mouse embryo (*8*, *9*). *Foxp4* is expressed in early foregut endoderm and later in development in lung and hindgut (*8*). To generate a mutant allele of *Foxp4*, we replaced two exons encoding the forkhead DNA binding domain with the neomycin resistance cassette (fig. S1, A and B). Proper gene targeting was confirmed by Southern blotting and polymerase chain reaction (fig. S1, D and E). Immunohistochemistry with a Foxp4-specific polyclonal antibody confirmed that mutant embryos no longer expressed Foxp4 protein, suggesting that we had generated a null allele (fig. S1C). Heterozygous embryos were fertile and exhibited no obvious defects (*10*). The majority of homozygous embryos died around embryonic day 12.5 (E12.5) (table S1).

Histological analysis from E8.5 to E12.5 revealed the development of two complete hearts in *Foxp4* mutant embryos (Fig. 1B). This was apparent as early as E8.5, when midline fusion of the bilateral cardiac primordia has normally occurred (Fig. 1, C and D). The two hearts in *Foxp4* mutants were positioned bilaterally, suggesting a lack of proper migration of the precardiac primordia to the midline (Fig. 1, C to H). *Foxp4* mutants exhibited grossly normal ventral morphogenesis and embryonic turning (Fig. 1, A to H), suggesting that cardia bifida was not due to secondary defects in these processes, as has been observed in other mouse models (*3*–*6*, *11*). Upon sacrifice (E8.5 to E12.5), each of the two bilateral hearts was beating at approximately the same rate as in wild-type embryos, although they were asynchronous (*10*).

[1]Department of Medicine, [2]Department of Cell and Developmental Biology, University of Pennsylvania, Philadelphia, PA 19104, USA.

*To whom correspondence should be addressed. E-mail: emorrise@mail.med.upenn.edu

Hematoxylin and eosin (H+E) staining showed that each heart in *Foxp4* mutants had distinct atria and ventricles (Fig. 1, I and J). Proper chamber septation and left-right chamber specification was evident from the expression of *eHAND* and *dHAND* (Fig. 1, J and K). Endocardial cushions were also present (Fig. 1L). In both wild-type and *Foxp4* mutant hearts, *MLC2a* and *MLC2v* were expressed in the atria and ventricles, respectively (Fig. 2, A to D), while plexin D1 was expressed in the developing endocardium (Fig. 2E) (*12*, *13*). These data support the conclusion that bilateral heart tube fusion is not required for cell or chamber specification in the heart. Furthermore, the position of the atria dorsal and cranial to the ventricles suggests that looping morphogenesis occurs in the bilateral hearts of *Foxp4* mutants despite the absence of midline fusion (Fig. 2, B and D).

A hallmark of ventricular myocyte differentiation and maturation is the generation of compact and trabecular myocardium. Compact myocardium lies in the outer region of the ventricular wall and is more proliferative and less mature than trabecular myocardium (*14*). Development of distinct trabecular and compact myocardium is thought to enhance contractility and compartmentalization of oxygenated and unoxygenated blood before septation (*14*). The formation of trabecular myocardium is essential for cardiac function as demonstrated in *neuregulin* knockout mice that lack trabecular myocardium and die at E10.5 because of heart failure (*15*). Compact myocardium can be distinguished by expression of *N-myc*, whereas trabecular myocardium can be distinguished by expression of atrial naturetic factor (*ANF*) (*16*). To determine whether proper development of compact and trabecular myocardium occurred in *Foxp4* mutant hearts, we performed in situ hybridizations to assess *N-myc* and *ANF* expression. *N-myc* and *ANF* were expressed in *Foxp4* mutant hearts in the same pattern as in wild-type hearts, with expression of *N-myc* observed in compact myocardium and *ANF* expression observed in trabecular myocardium (Fig. 2, F and G) (*15*, *16*). Taken together, these data demonstrate that *Foxp4* mutants develop two hearts with proper chamber formation and normal trabecular and compact myocardial development.

The heart is the first organ to display asymmetry during development (*17*, *18*). Along with other lateral-plate mesoderm derivatives, the heart expresses *Pitx2*, a bicoid-related homeodomain transcription factor, only on its left side; *Pitx2* mutants exhibit multiple embryonic defects, including defective cardiac positioning after looping (*19*). At E10.5, *Foxp4* mutants have two visible hearts that were positioned bilateral to the ventral midline (Fig. 3, A to D). *Pitx2* expression was observed in the left heart of *Foxp4* mutant embryos, whereas expression was not observed in the right heart (Fig. 3E). These data suggest that embryonic left-right asymmetry was retained in *Foxp4* mutants. To determine whether cardiac specific left-right asymmetry was retained in *Foxp4* mutant hearts, we performed in situ hybridization to determine expression of the basic helix-loop-helix (bHLH) transcription factors *eHAND* and *dHAND* and of *FGF10*, a member of the fibroblast growth factor family. *eHAND* is normally expressed primarily in the left side of the developing heart, whereas *dHAND* and *FGF10* are expressed primarily on the right side of the developing heart (*20*, *21*). We observed *eHAND* expression in the

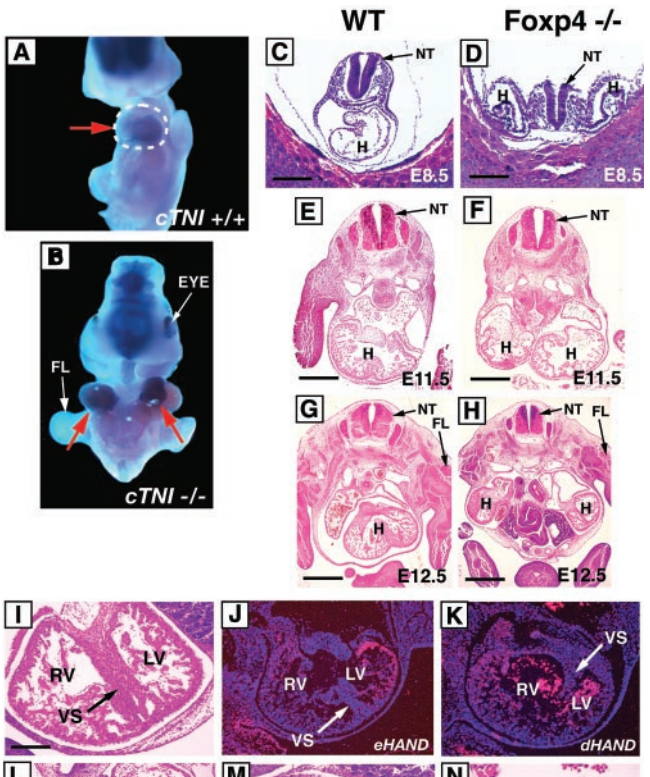

Fig. 1. Loss of *Foxp4* results in the formation of two hearts with extensive differentiation. (**A**) Wild-type and (**B**) *Foxp4* mutant embryos at E11.5 were processed for whole-mount in situ hybridization with a probe for *cTNI* to detect cardiac myocardium (arrows and dotted line). FL, forelimb. (**C** to **H**) H+E–stained sections of wild-type [(C), (E), and (G)] and *Foxp4* mutant [(D), (F), and (H)] embryos at E8.5 [(C) and (D)], E11.5 [(E) and (F)], and E12.5 [(G) and (H)], showing two well-developed hearts in the mutant embryos. H, heart; NT, neural tube. (**I**) *Foxp4* mutant hearts have two ventricles, expressing (**J**) *eHAND* and (**K**) *dHAND* properly, i.e., in the left and right ventricle, respectively. Panels (I), (J), and (K) are adjacent sections of the same heart; bright interluminal fluorescence in (K) is due to autofluorescence from red blood cells. RV, right ventricle; LV, left ventricle; VS, ventricular septum. (**L** to **N**) *Foxp4* mutant hearts exhibit formation of (L) endocardial cushions (arrow), (M) two atria, and (N) the endocardium (arrow). The atria are dorsal and anterior to the ventricles, and the neural tube, forelimbs, and eyes are positioned correctly in *Foxp4* mutants. a, atria; v, ventricle. Scale bars, (C) and (D), 200 μm; (E) to (H), 400 μm; (I) to (M), 100 μm; (N), 50 μm.

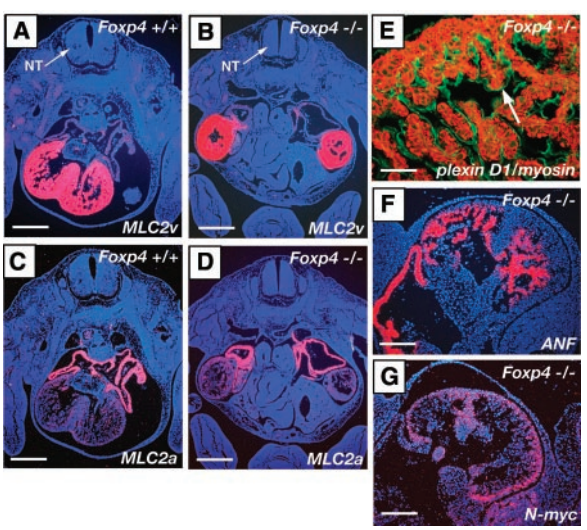

Fig. 2. Marker gene analysis demonstrates proper chamber and cell-type differentiation in *Foxp4* mutant hearts. In situ hybridization to detect (**A** and **B**) *MLC2v*, (**C** and **D**) *MLC2a*, (**F**) *ANF*, and (**G**) *N-myc* expression and (**E**) double immunofluorescent staining to detect plexin D1 (green, arrow) and myosin-MF20 (red) protein expression. Analysis was performed on wild-type [(A) and (C)] and *Foxp4* mutant [(B), (D), and (E) to (G)] embryos at E12.5. Scale bars, (A) to (D), 400 μm; (E), 50 μm, (F) and (G), 100 μm.

left ventricle of both *Foxp4* mutant hearts (Fig. 3, D and E), whereas *dHAND* and *FGF10* were expressed on the right side of *Foxp4* mutant hearts, including the right ventricle (Fig. 3, F and G, and fig. S2). These data demonstrate that development of cardiac left-right asymmetry does not require heart tube fusion and that embryonic and cardiac asymmetry are specified by distinct mechanisms. These data demand a reconsideration of the currently accepted models of cardiac development and morphogenesis to accommodate the observation that precardiac mesoderm is capable of left-right asymmetrical chamber development, looping, myocyte differentiation, and endocardial cushion formation in the absence of midline heart tube fusion.

Our previous studies have shown that Foxp4 mRNA expression in the heart at E10.5 cannot be demonstrated by in situ hybridization, although it can be demonstrated in the adult heart by Northern blot analysis (*8*). However, abundant levels of Foxp4 protein expression in the embryo are observed in the anterior foregut endoderm (fig. S3F). Immunohistochemistry shows that Foxp4 protein expression is not observed in cardiac myocytes at E9.5 to E14.5 (fig. S2, A to C). In contrast, expression is observed in the epicardium and endocardium at these times (fig. S3, A to C).

Histological analysis identified defects in anterior foregut endoderm development in *Foxp4* mutants. As shown in Fig. 1D, at E8.5, the anterior foregut was open in mutant embryos, whereas in wild-type embryos it was a closed tube. At E10.5, the most anterior aspects of the foregut remained open in *Foxp4* mutants, whereas more posterior regions were closed (Fig. 4, A to C). By E11.5, the foregut had closed in *Foxp4* mutants in the anterior region, but failed to separate into the esophagus and trachea; however, it did give rise to endodermally derived tissues, including the lung and liver (Fig. 4, D to I). At E11.5, terminal deoxynucleotidyl transferase–mediated deoxyuridine triphosphate nick end labeling assays revealed that anterior endoderm was highly apoptotic (fig. S4, A and B), and by E12.5, this region of the foregut had degraded, leaving a large open cavity in the embryo (Fig. 4, J to O). However, foregut endoderm was properly specified as demonstrated by expression of *sonic hedgehog* (*SHH*) and *Foxa2* (fig. S4, C to H) (*10*). Together, these data suggest that *Foxp4* mutants exhibit a delay in anterior foregut closure and cell death–mediated loss of anterior foregut endoderm after closure. We hypothesize that the defects in anterior foregut development may be responsible for cardia bifida in *Foxp4* mutants. Although these defects led to a delay in foregut closure in *Foxp4* mutants, the neural tube, limb buds, and head structures formed normally, indicating that the vast majority of ventral morphogenetic processes were unperturbed (Figs. 1 to 3).

Defects in anterior foregut endoderm development have previously been associated with

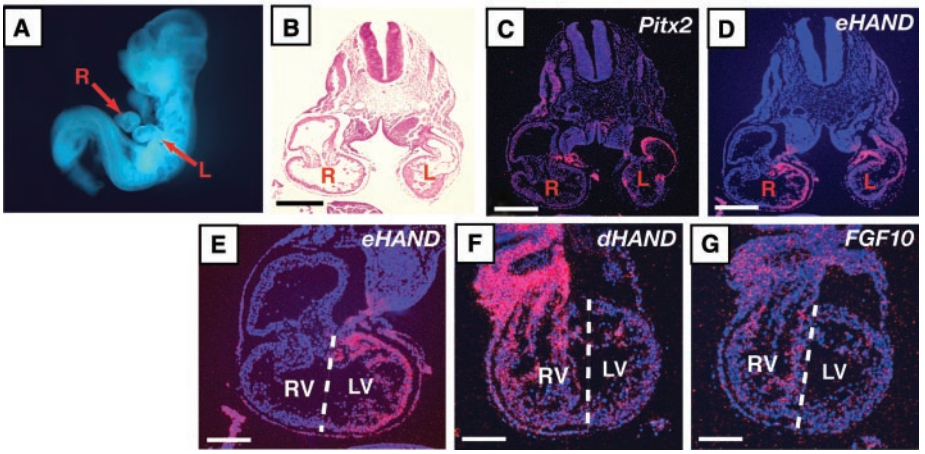

Fig. 3. Left-right asymmetry is retained in *Foxp4* mutant embryos. (**A**) At E10.5, *Foxp4* mutants clearly have two hearts bilateral to the ventral midline. R, right heart; L, left heart. (**B**) H+E–stained section of E10.5 *Foxp4* mutant. (**C**) In situ hybridization for *Pitx2* demonstrates that only the left heart in *Foxp4* mutant embryos is *Pitx2* positive. (**D** to **G**) In situ hybridization using [(D) and (E)] *eHAND*, (F) *dHAND*, and (G) *FGF10* probes to demonstrate that *eHAND* expression is observed in the left side (left ventricle) of *Foxp4* mutant hearts [(E) is a higher magnification of (D)], whereas *dHAND* and *FGF10* is expressed in the right side (right ventricle) of *Foxp4* mutant hearts. Scale bars, (B) to (D), 300 μm; (E) to (G), 200 μm.

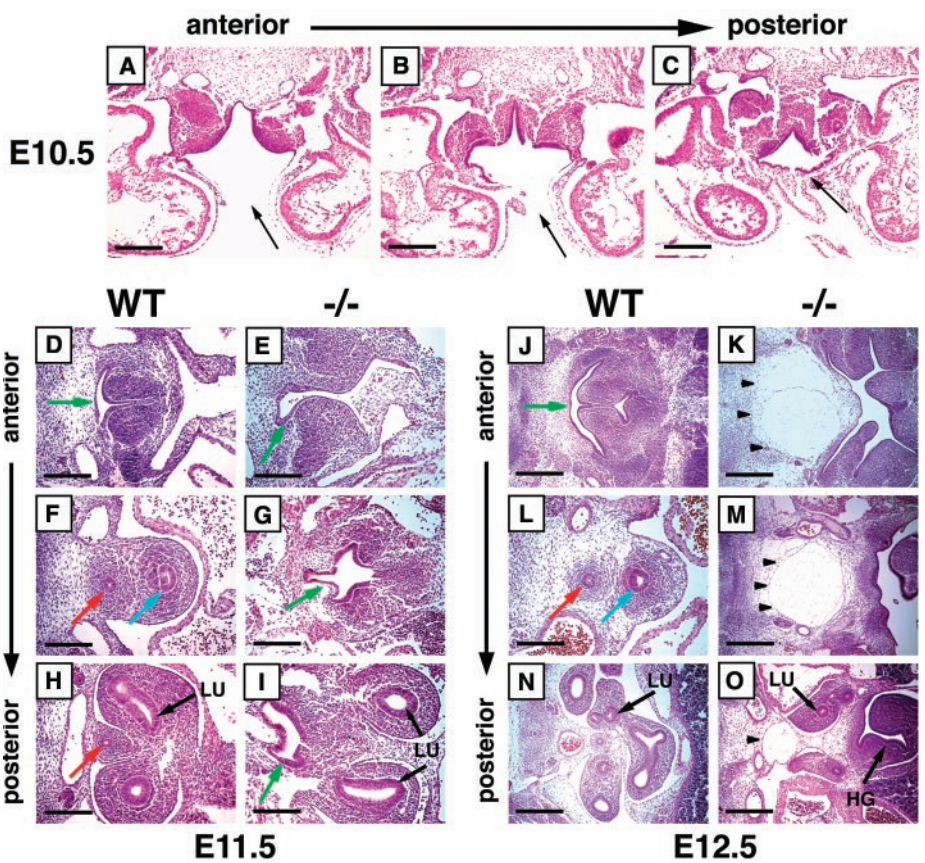

Fig. 4. Anterior foregut development in *Foxp4* mutant embryos. (**A** to **C**) The anterior region of the foregut remains open at E10.5 in *Foxp4* mutants, whereas the posterior region is closed (arrow). (**D** to **I**) In wild-type embryos at E11.5, the (D) anterior foregut is closed (green arrow) and has bifurcated into the [(F) and (H)] esophagus (red arrow) and trachea (blue arrow). In *Foxp4* mutants at E11.5, the (E) anterior region of the foregut has closed but does not bifurcate into the [(G) and (I)] esophagus and trachea (green arrow). LU, lung. (**J** to **O**) At E12.5, wild-type embryos continue to show development of (J) the foregut (green arrow) including (L) the trachea (blue arrow) and esophagus (red arrow). [(K), (M), and (O)] By E12.5, the anterior foregut endoderm in *Foxp4* mutants has degraded, leaving a large cavity in this region of the embryo (black arrowheads). HG, hindgut. Scale bars, (A) to (M), 100 μm; (N) to (O), 200 μm.

cardia bifida. Mutations in several zebrafish genes expressed in the foregut endoderm, including *casanova* (*sox32*) and *faust* (*GATA5*), result in cardia bifida, and these mutants display severe defects or complete lack of foregut endoderm development (*22*, *23*). In mice lacking *GATA4*, anterior foregut endoderm development is defective, and *GATA4*-null embryos display cardia bifida (*3*, *4*). Thus, the correlation between foregut defects and cardia bifida phenotypes is very strong. However, there are distinct differences between these mutants and *Foxp4* mutants. *GATA4* mutants have severe defects in ventral morphogenesis and lack proper cardiac chamber development (*3*, *4*). Moreover, zebrafish cardiac morphogenesis is distinctly different from that in mammals, in that there are only two chambers and the heart does not loop or septate, but instead forms a serial connection between the single atria and ventricle. Although other models of cardia bifida have been reported, including *Mesp1* and *furin* mutant mice, these embryos either die too early to examine the complex morphogenetic processes required for late-stage cardiac development or they exhibit other severe defects in general developmental processes such as embryonic turning (*5*, *6*, *11*). Thus, none of the cardia bifida mutants described previously has permitted the analysis of complex cardiac development in sufficient detail to determine whether the later stages of cardiac morphogenesis require heart tube fusion.

Foxp4 mutant embryos demonstrate that bilateral heart tube migration and fusion are not required for extensive cardiac development, including chamber formation, ventricular myocyte differentiation, looping, endocardial cushion formation, and development of cardiac left-right asymmetry. These data indicate a higher degree of preprogramming in the bilateral precardiac mesoderm than has been appreciated and indicate that a redefinition of the current model of cardiac development is required (*1*).

References and Notes

1. D. Srivastava, E. N. Olson, *Nature* **407**, 221 (2000).
2. D. Yelon, D. Y. Stainier, *Semin. Cell Dev. Biol.* **10**, 93 (1999).
3. C. T. Kuo *et al.*, *Genes Dev.* **11**, 1048 (1997).
4. J. D. Molkentin, Q. Lin, S. A. Duncan, E. N. Olson, *Genes Dev.* **11**, 1061 (1997).
5. Y. Saga *et al.*, *Development* **126**, 3437 (1999).
6. A. J. Roebroek *et al.*, *Development* **125**, 4863 (1998).
7. T. Brand, *Dev. Biol.* **258**, 1 (2003).
8. M. M. Lu, S. Li, H. Yang, E. E. Morrisey, *Mech. Dev.* **119** (suppl. 1), S197 (2002).
9. W. Shu, H. Yang, L. Zhang, M. M. Lu, E. E. Morrisey, *J. Biol. Chem.* **276**, 27488 (2001).
10. S. Li, D. Zhou, M. M. Lu, E. E. Morrisey, unpublished data.
11. Y. Saga, *Mech. Dev.* **75**, 53 (1998).
12. A. D. Gitler, M. M. Lu, J. A. Epstein, *Dev. Cell* **7**, 107 (2004).
13. B. van der Zwaag *et al.*, *Dev. Dyn.* **225**, 336 (2002).
14. D. Sedmera, T. Pexieder, M. Vuillemin, R. P. Thompson, R. H. Anderson, *Anat. Rec.* **258**, 319 (2000).
15. R. Kramer *et al.*, *Proc. Natl. Acad. Sci. U.S.A.* **93**, 4833 (1996).
16. M. Tanaka, Z. Chen, S. Bartunkova, N. Yamasaki, S. Izumo, *Development* **126**, 1269 (1999).
17. B. W. Bisgrove, J. J. Essner, H. J. Yost, *Development* **127**, 3567 (2000).
18. B. W. Bisgrove, H. J. Yost, *Am. J. Med. Genet.* **101**, 315 (2001).
19. C. R. Lin *et al.*, *Nature* **401**, 279 (1999).
20. C. L. Cai *et al.*, *Dev. Cell* **5**, 877 (2003).
21. T. Thomas, H. Yamagishi, P. A. Overbeek, E. N. Olson, D. Srivastava, *Dev. Biol.* **196**, 228 (1998).
22. J. F. Reiter *et al.*, *Genes Dev.* **13**, 2983 (1999).
23. J. Alexander, M. Rothenberg, G. L. Henry, D. Y. Stainier, *Dev. Biol.* **215**, 343 (1999).

24. We thank J. Epstein, M. Kahn, J. Lepore, M. Parmacek, and C. Simon for their critical comments on this work and manuscript, E. Olson for sharing the *eHAND* and *dHAND* in situ probes, J. Epstein and A. Gitler for sharing the plexin D1 antibody, and C. Luce for his expert artwork. Supported by the National Institutes of Health (through grant no. HL71589 to E.E.M.) and the American Heart Association (through a Scientist Development Grant to E.E.M and a Postdoctoral Fellowship Grant to S.L.).

Supporting Online Material

www.sciencemag.org/cgi/content/full/305/5690/1619/DC1
Materials and Methods
SOM Text
Figs. S1 to S4
Table S1
References and Notes

1 April 2004; accepted 2 August 2004

Bacterial Persistence as a Phenotypic Switch

Nathalie Q. Balaban,[1,2]* Jack Merrin,[1] Remy Chait,[1] Lukasz Kowalik,[1] Stanislas Leibler[1]

A fraction of a genetically homogeneous microbial population may survive exposure to stress such as antibiotic treatment. Unlike resistant mutants, cells regrown from such persistent bacteria remain sensitive to the antibiotic. We investigated the persistence of single cells of *Escherichia coli* with the use of microfluidic devices. Persistence was linked to preexisting heterogeneity in bacterial populations because phenotypic switching occurred between normally growing cells and persister cells having reduced growth rates. Quantitative measurements led to a simple mathematical description of the persistence switch. Inherent heterogeneity of bacterial populations may be important in adaptation to fluctuating environments and in the persistence of bacterial infections.

When a population of genetically identical bacterial cells is exposed to a sufficiently strong antibiotic treatment, most of the population is killed. Killing can be measured by monitoring the fraction of viable cells as a function of the exposure to the antibiotic treatment. The resulting killing curve for wild-type *Escherichia coli* is plotted in Fig. 1A. The death of the majority of the population takes place as a fast exponential decay characterized by a single parameter, the killing rate. After a few hours, the initial purely exponential decay of the killing curve changes to a more complex, slowly decreasing function. By the time the antibiotic is removed, a small fraction of the cells still survives. These cells have not genetically acquired antibiotic resistance: They regrow a new population that is as sensitive to the antibiotic. This phenomenon, termed bacterial persistence, was first reported for staphylococcal infections treated with penicillin (*1*) and has since been observed in many bacterial species. Despite being observed almost 60 years ago, the mechanism behind persistence remains a puzzle (*2*). It has been suggested that persistent bacteria are in some protected part of the cell cycle at the time of exposure to antibiotics or are able to adapt rapidly to the antibiotic stress (*3*). It has also been proposed that those cells are in a dormant state or are unable to initiate programmed cell death (*2*, *4*). To clarify the nature of persistence, it is crucial to know whether persistent bacteria differ from others before exposure to antibiotics and, if so, what triggers such phenotypic differentiation.

To answer these questions quantitatively, we investigated the persistence of *E. coli* at the level of single cells by direct observation and measurement with the use of optical microscopy. Such measurements were made possible by the use of previously isolated high persistence (*hip*) mutants of *E. coli* that have an increased proportion of persisters (*5*, *6*) and by the recent development of transparent microfluidic devices (*7*, *8*).

We designed and fabricated microfluidic devices by using the techniques of soft lithography (*9*, *10*) to pattern layers of poly (dimethylsiloxane) (PDMS) (Fig. 1B). With

[1]Laboratory of Living Matter and Center for Studies in Physics and Biology, Rockefeller University, 1230 York Avenue, New York, NY 10021, USA. [2]Racah Institute for Physics, Hebrew University, Jerusalem 91904, Israel.

*To whom correspondence should be addressed. E-mail: nathalieqb@phys.huji.ac.il

these devices, we can record the growth of individual bacteria under normal conditions, expose them to antibiotic treatment, detect the rare survivors, and analyze the survivors' history. Even before the antibiotic treatment, all the observed persisters could be clearly distinguished from the normal cells by their reduced growth rate. These single-cell observations allowed us to describe mathematically the switching behavior between rapidly growing normal cells, *n*, and nongrowing or slowly growing persister cells, *p*, in the framework of a simple two-state model (Fig. 2). Once the mechanism of persistence was demonstrated at the level of single cells, measurements of the parameters of the model could be done in batch cultures. The growth-death rates of the persisters and the normally growing cells were characterized in this model by the constants μ_p and μ_n, respectively. The cells switched from the *n* state to the *p* state with a constant rate *a* or from the *p* state to the *n* state with a constant rate *b*.

We first chose to study *hip* mutants with the *hipA7* allele, isolated in a pioneering work by Moyed and colleagues (*5*). Interestingly, the persistence of the *hipA7* allele after ampicillin exposure was shown to be linked to persistence in many other stresses (*6*, *11*). The killing curve of these mutant cells (Fig. 1A) is well described by double-exponential kinetics: The majority of the population is characterized by a fast killing time (25 min), whereas the subpopulation of persisters dies off over a much longer characteristic time (6 hours) (*12*). A good fit to experimental data is obtained by the two-state model presented in Fig. 2.

For single-cell measurements, the *hipA7* bacteria are first grown in a microfluidic device under the microscope on Luria-Bertani Lennox medium (LBL) (Fig. 1C) (*12*). During growth, the descendants of each bacterium form a separate linear microcolony (Fig. 1, C to E). By using time-lapse microscopy and measuring the length of newly formed linear microcolonies, we derived growth rates of the progeny of individual cells. The average growth rate of *E. coli* in our devices was the same as that for batch cultures. After several cell divisions, ampicillin was added to the medium, and the death of cells, accompanied by lysis, was easily observed (Fig. 1F). After 5 hours of ampicillin, killing slowed, and ampicillin was cleared from the device with fresh LBL (Fig. 1G). After the removal of ampicillin, rare bacteria, which survived, started growing and dividing again (Fig. 1, G and H): These were identified as the persister cells. The persistence phenotype was not due to spatial inhomogeneities inside our devices: The locations of persisters showed no pattern, and these cells were often found in close proximity to nonpersister cells. Following the behavior of those cells back in time (movie S1) (*12*), we observed that they differed in their growth rate from the majority of the population before the exposure to antibiotics. Persister cells, which seemed to be in an arrested growth state, could spontaneously switch to fast growth and generate a population that is sensitive to the antibiotic (*12*) (fig. S1). We thus conclude that persistence in the *hipA7* population is linked to an inherent heterogeneity of growth rates in the bacterial population.

We have established the following properties of *hipA7* persisters, characteristic of what we call type I persisters:

1) Type I persisters constitute a preexisting population of nongrowing ($\mu_p \approx 0$) cells that are generated at stationary phase.

2) Type I persistence is characterized by a negligible spontaneous switching rate from *n* to *p* during exponential growth ($a \approx 0$) (*13*). In batch culture (Fig. 3B), the number of persister cells is directly proportional to the number of stationary phase cells inoculated into the culture, consistent with recent observations (*14*, *15*) .

3) Type I persisters inoculated into fresh medium from stationary phase switch back to growing cells with a characteristic extended time lag. The *hipA7* population consists of two distinct subpopulations, each characterized by a different time constant for the exit from stationary phase (Fig. 3A). The apparent lag time for the persister population is the inverse of *b*, the switching rate from *p* to *n*. We measured *b* by plating an overnight culture of the *hipA7* mutant on LBL agar plates and monitoring the appear-

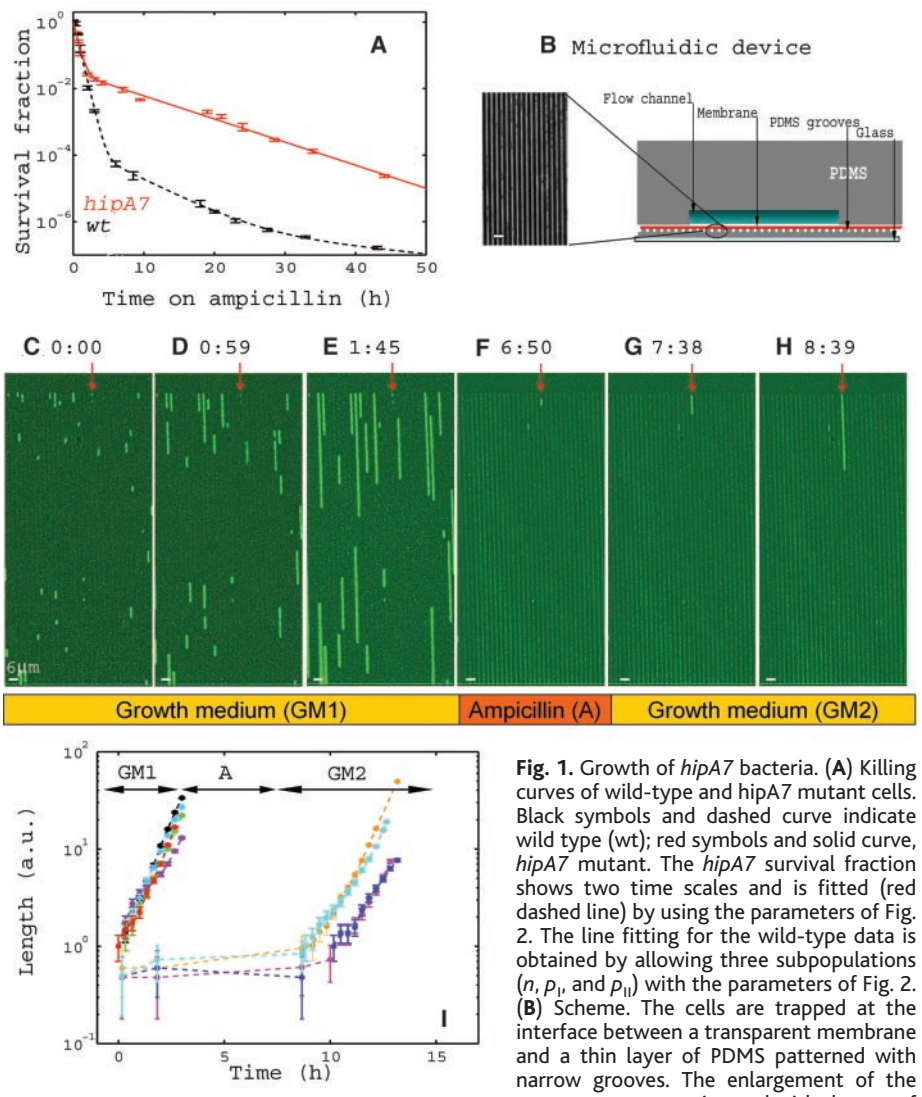

Fig. 1. Growth of *hipA7* bacteria. (**A**) Killing curves of wild-type and hipA7 mutant cells. Black symbols and dashed curve indicate wild type (wt); red symbols and solid curve, *hipA7* mutant. The *hipA7* survival fraction shows two time scales and is fitted (red dashed line) by using the parameters of Fig. 2. The line fitting for the wild-type data is obtained by allowing three subpopulations (n, p_I, and p_{II}) with the parameters of Fig. 2. (**B**) Scheme. The cells are trapped at the interface between a transparent membrane and a thin layer of PDMS patterned with narrow grooves. The enlargement of the groove pattern was imaged with the use of phase-contrast microscopy. (**C** to **H**) Time lapse of *hipA7* cells expressing yellow fluorescent protein. Times from $t = 0$ are indicated in hours:min. (C to E) Bacteria taken from an overnight culture are exposed to growth medium (GM1) and divide on narrow grooves, thus forming strings of cells originating from the same cell. (F) Same field of view after exposing the cells to ampicillin (denoted by A). Only persister cells remain. (G and H) Same field of view after removal of the ampicillin by washing with growth medium (GM2). The red arrow points to the location of a type I persister bacterium. (**I**) The length of the lineages of several *hipA7* cells is monitored during GM1, A, and GM2 time periods. Individual cells are plotted as different colors. Type I persister cells do not grow during the GM1 and A periods. a.u., arbitrary units.

ance of visible colonies (Fig. 3A) (*12*). The majority of the population is characterized by a short lag time (40 min) comparable to the wild-type lag, whereas a subset is characterized by a lag time of about 14 hours (b = 0.07 hours^{-1}). Upon introduction of fresh nutrients, cells with the shorter lag time rapidly begin growth and become susceptible to killing by ampicillin, whereas the rest remain dormant and less sensitive to ampicillin, which is known to target mainly growing cells (*16*, *17*).

The fraction of persisters in the wild-type population is more than three orders of magnitude smaller than in the *hipA7* population, making their detection under the microscope or by a colony appearance assay on plates very difficult. Despite similarities in the initial behavior of the wild-type and the *hipA7* data, the killing curve for the wild type is more complex at longer times and cannot be fitted by using only two time constants (Fig. 1A). In contrast to the *hipA7* persisters, whose number is independent of the total number of growing cells, the number of wild-type persisters increases as the total population increases (Fig. 3B). We conclude that type I persistence does not fully characterize wild-type persisters.

Another mutant, *hipQ*, was previously isolated in a screen for high persistence to norfloxacin treatment and, like *hipA7*, was later found to persist through treatment with several antibiotics, including ampicillin (*6*). However, the *hipQ* locus is found in a different region of the chromosome and has not been fully characterized. Our experiments show that the *hipQ* persisters can be described within the same mathematical model (Fig. 2) but with dynamics that differ in important ways from type I. These persisters, which we call type II persisters, constitute a subpopulation of slowly growing cells ($\mu_p \neq 0$). An inherent heterogeneity in the growth rate was also present in the *hipQ* mutants before the antibiotic treatment (Fig. 4) (*18*). In contrast to *hipA7* persisters, which are found in an arrested growth state, *hipQ* persisters grow and divide continuously but an order of magnitude slower than nonpersisters (Fig. 4G and movie S2). This persistence growth state is inherited for several generations (fig. S2).

Type II persisters do not appear to originate from passage through stationary phase. The number of persisters in a growing culture is determined by the total number of cells and not by the size of the inoculum from stationary phase ($a \neq 0$) (table S1). The dynamics of type II persistence for the *hipQ* population qualitatively follows the equations presented in Fig. 2. Batch culture experiments (Fig. 4H) showing the ability of *hipQ* persister cells to switch back to fast growth allowed us to set a lower limit on b (Fig. 2).

We now turn to the more complex wild-type population dynamics. Persisters in the wild-type population are continuously generated during exponential growth (Fig. 3B) ($a \neq 0$). However, passage through stationary phase also increases the number of persisters (table S1). The wild-type population can be thus described as consisting of three subpopulations: normal cells, n; continuously generated type II persisters, p_{II}; and stationary phase type I persisters, p_I. The dynamical model can then be used to fit the killing curve of the wild-type population (Fig. 1A) and

Type I persisters		Type II persisters	
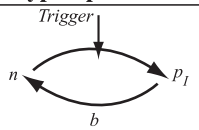		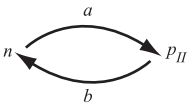	
$\begin{cases} \frac{dp_I}{dt} = -bp_I + \mu_p p_I \\ \frac{dn}{dt} = bp_I + \mu_n n \end{cases}$ Eq.(1)		$\begin{cases} \frac{dn}{dt} = -an + bp_{II} + \mu_n n \\ \frac{dp_{II}}{dt} = an - bp_{II} + \mu_p p_{II} \end{cases}$ Eq. (2)	
Estimated rates (units: hours^{-1})			
hipA7: b=0.07±0.01	*wt* Type I subpopulation: μ_p-b= -0.05±0.01 *(23)*	*wt* Type II subpopulation: a=1.2±0.2 x10^{-6} b=0.1±0.05	*hipQ* a=1.0±0.2x10^{-3} 10^{-7}<b<10^{-4}
For a general solution of Eqs (1&2) see the Supplementary Online Material			

Fig. 2. Mathematical description of persistence. General equations describing the dynamics of two subpopulations, here denoted as normal (n) and persister (p) cells. Type I persisters are generated by trigger events during stationary phase, whereas type II persisters are continuously generated during growth. The parameters for the *hip* populations and for the wild type are determined by fitting the plots of Figs. 1, 3, and 4 to the solutions of the kinetics equations (Eqs. 1 and 2).

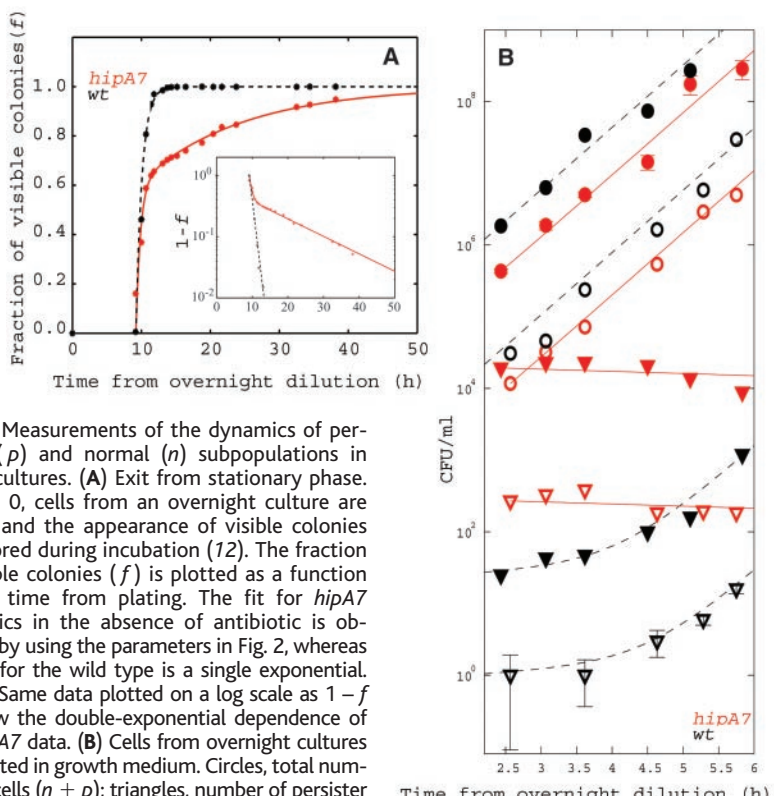

Fig. 3. Measurements of the dynamics of persister (p) and normal (n) subpopulations in batch cultures. (**A**) Exit from stationary phase. At t = 0, cells from an overnight culture are plated and the appearance of visible colonies monitored during incubation (*12*). The fraction of visible colonies (f) is plotted as a function of the time from plating. The fit for *hipA7* dynamics in the absence of antibiotic is obtained by using the parameters in Fig. 2, whereas the fit for the wild type is a single exponential. (Inset) Same data plotted on a log scale as $1 - f$ to show the double-exponential dependence of the *hipA7* data. (**B**) Cells from overnight cultures are diluted in growth medium. Circles, total number of cells ($n + p$); triangles, number of persister cells (p); open and solid symbols, dilutions from overnight cultures of 10^{-6} and 5×10^{-5}, respectively. Fits represent the solutions of Eqs. 1 and 2 with the parameters of Fig. 2. During exponential growth of the total population, the number of persisters decreases slowly for the *hipA7* mutant, whereas it increases for the wild type.

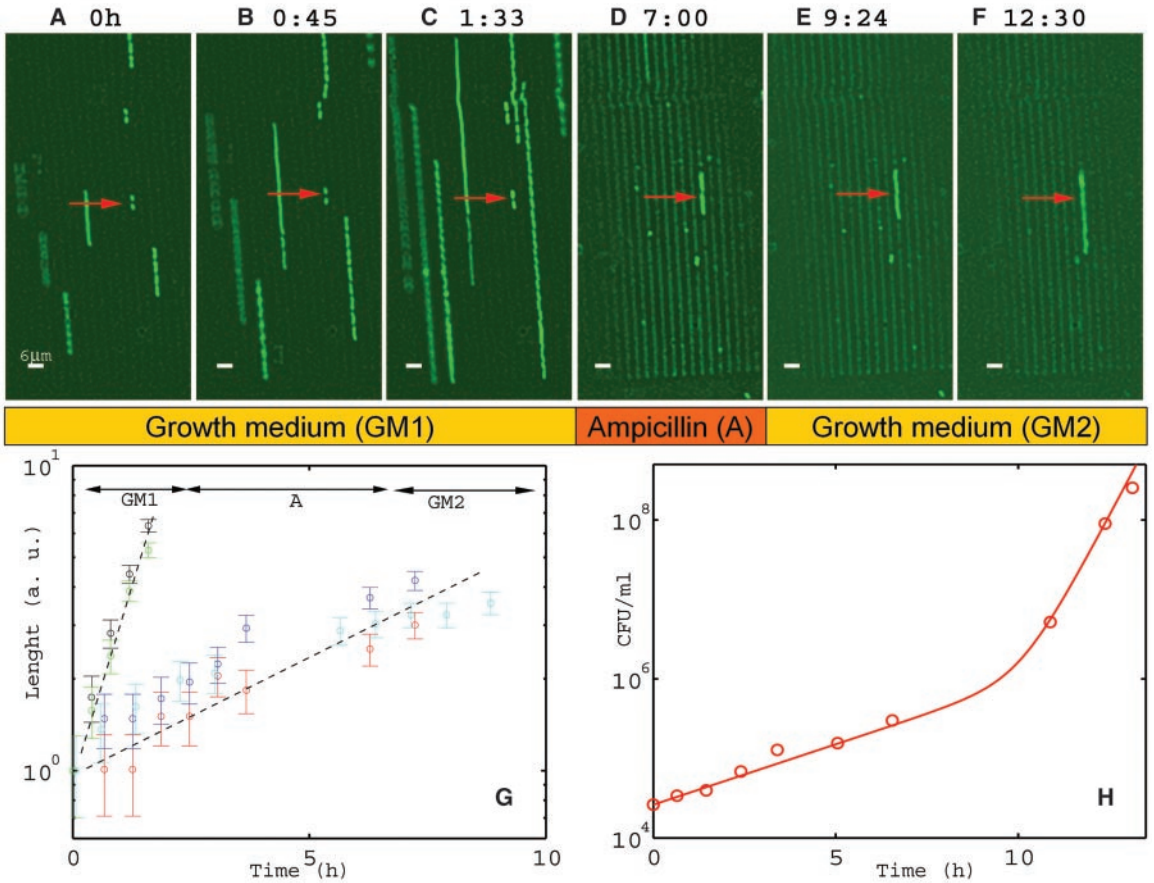

Fig. 4. (**A** to **F**) Growth of *hipQ* bacteria in a microfluidic chamber. Time lapse of *hipQ* cells expressing yellow fluorescent protein. (A to C) Bacteria taken from an exponentially growing culture are exposed to growth medium (GM1) and divide on narrow grooves, thus forming strings of cells originating from the same cell. (D) Same field of view after exposing the cells to 4 hours of ampicillin (denoted by A). Only few cells remain. (E and F) Same field of view after removal of the ampicillin by washing with growth medium (GM2). The red arrow points to the location of a type II persister bacterium. (**G**) Growth of *hipQ* bacteria in a microfluidic chamber. The length of the lineages of several cells are monitored during GM1, A, and GM2. The cells that grow quickly during GM1 die during A. The type II persister cells grow slowly during GM1, A, and GM2. (**H**) Switch of *hipQ* persisters in batch cultures from slow growth to fast growth after an antibiotic treatment of 4.5 hours. The red line was obtained by fitting the solutions of Eqs. 1 and 2 with free parameter b, whereas μ_p and μ_n were determined from the growth rates near $t = 0$ and $t \gg 0$, respectively, and a was determined from the measurement of the persisters ratio (table S1). CFU, colony-forming units.

extract the different time scales characterizing the three subpopulations (Fig. 2). Despite the good agreement between the simple theoretical model and the experimental data, we cannot exclude the possibility of other persister types.

Possibly, persisters have been selected to increase chances of survival of bacterial populations in fluctuating environments (fig. S3). Similar strategies are not uncommon in more complex organisms: Variable maturation rates in insects or germination events in plant seeds have been described as bet-hedging strategy for facing unpredictable environments (*19*). The quantitative characterization of persistence states and the associated phenotypic transitions should find clinical application in treatment of pathogens such as *Mycobacterium tuberculosis* (*20*), *Staphylococcus aureus* (*3*), and *Pseudomonas aeruginosa* in cystic fibrosis patients (*21*). The identification of the switch responsible for persistence suggests different possible drug targets: Stationary phase–induced persistence could be reduced with factors that affect the lag period (*22*), whereas spontaneous persistence could be targeted by factors specifically enhancing the switching rate from persister to normal cells.

References and Notes

1. W. B. Bigger, *Lancet* **ii**, 497 (1944).
2. K. Lewis, *Microbiol. Mol. Biol. Rev.* **64**, 503 (2000).
3. R. C. Massey, A. Buckling, S. J. Peacock, *Curr. Biol.* **11**, 1810 (2001).
4. B. Sat *et al.*, *J. Bacteriol.* **183**, 2041 (2001).
5. H. S. Moyed, K. P. Bertrand, *J. Bacteriol.* **155**, 768 (1983).
6. J. S. Wolfson, D. C. Hooper, G. L. McHugh, M. A. Bozza, M. N. Swartz, *Antimicrob. Agents Chemother.* **34**, 1938 (1990).
7. M. A. Unger, H. P. Chou, T. Thorsen, A. Scherer, S. R. Quake, *Science* **288**, 113 (2000).
8. J. C. McDonald *et al.*, *Electrophoresis* **21**, 27 (2000).
9. G. M. Whitesides, E. Ostuni, S. Takayama, X. Jiang, D. E. Ingber, *Annu. Rev. Biomed. Eng.* **3**, 335 (2001).
10. N. Q. Balaban *et al.*, *Nat. Cell Biol.* **3**, 466 (2001).
11. R. Scherrer, H. S. Moyed, *J. Bacteriol.* **170**, 3321 (1988).
12. Materials and methods are available as supporting material on *Science* Online.
13. The $a = 0$ approximation is valid in experiments where the amount of persistence of *hipA7* cells is high, that is, after passage through stationary phase, thus occluding detection of any substantially smaller subpopulations.
14. I. Keren, N. Kaldalu, A. Spoering, Y. Wang, K. Lewis, *FEMS Microbiol. Lett.* **230**, 13 (2004).
15. S. B. Korch, T. A. Henderson, T. M. Hill, *Mol. Microbiol.* **50**, 1199 (2003).
16. R. M. Cozens *et al.*, *Antimicrob. Agents Chemother.* **29**, 797 (1986).
17. We verified that the *hip* mutants used in this study also show increased persistence to norfloxacin.
18. We showed that the heterogeneity in the *hip* populations is not due to the ampicillin. However, the ability of each subpopulation to persist might be due to a response to the antibiotic itself.
19. M. J. Bradford, D. A. Roff, *Ecology* **74**, 1129 (1993).
20. G. R. Stewart, B. D. Robertson, B. D. Young, *Nat. Rev. Microbiol.* **1**, 97 (2003).
21. E. Drenkard, F. M. Ausubel, *Nature* **416**, 740 (2002).
22. G. V. Mukamolova, S. S. Kormer, D. B. Kell, A. S. Kaprelyants, *Arch. Microbiol.* **172**, 9 (1999).
23. The small fraction of the type I persisters in the wild type does not allow the separation of the two variables.

24. We thank the laboratory of D. C. Hooper for retrieving the *hip* strains; M. B. Elowitz for the MRR strain; R. Kishony for helpful discussions as well as for suggesting the colony appearance assay; J. McKinney, A. Tomasz, P. Model, M. Russel, A. Keynan, T. J. Silhavy, S. Quake, C. Guet, J. Paulsson, E. Kussell, A. Kondrashov, and J. Lederberg for useful discussions; many members of the Rockefeller University community, especially J. McKinney and A. J. Levine, for encouragement; and S. Shaham, J. McKinney, and A. W. Murray for their comments on the manuscript. This work was initiated at the Princeton University and partially supported there by NIH and the Howard Hughes Medical Institute. N.Q.B. acknowledges the support of the Princeton University Dicke Fellowship and of the Rockefeller University Fellowship.

Supporting Online Material

www.sciencemag.org/cgi/content/full/1099390/DC1
Materials and Methods
Figs. S1 to S3
Table S1
Movies S1 and S2

21 April 2004; accepted 16 July 2004
Published online 12 August 2004;
10.1126/science.1099390
Include this information when citing this paper.

Iron-Source Preference of *Staphylococcus aureus* Infections

Eric P. Skaar,[1,2] Munir Humayun,[3]*
Taeok Bae,[1,2] Kristin L. DeBord,[1,2] Olaf Schneewind[1,2]†

Although bacteria use different iron compounds in vitro, the possibility that microbes distinguish between these iron sources during infection has hitherto not been examined. We applied stable isotope labeling to detect source-specific iron by mass spectrometry and show that *Staphylococcus aureus* preferentially imports heme iron over transferrin iron. By combining this approach with computational genome analysis, we identified *hts* (heme transport system), a gene cluster that promotes preferred heme iron import by *S. aureus*. Heme iron scavenging by means of *hts* is required for staphylococcal pathogenesis in animal hosts, indicating that heme iron is the preferred iron source during the initiation of infection.

Bacterial nutrient-uptake assays traditionally provide a sole nutrient source and rely on measurements of microbial growth as indicators of usage (*1*). This experimental strategy imposes pressure on bacterial populations to acquire nutrients for survival and does not provide information regarding the preferred nutrient sources of microbes. We developed an assay that provides multiple stable isotope–labeled nutrient compounds and allows independent tracking of each compound by its isotope label. The assay provides a growth medium containing elemental nutrients in which each compound is prepared from a different separated stable isotope tracer, which is then tracked through metabolic pathways by isotopic analysis of cultured cells or cellular fractionations by inductively coupled plasma mass spectrometry (ICP-MS). We applied this technique to iron (Fe) acquisition in *S. aureus*.

The ability to sequester iron is a primary defense mechanism against bacterial infection. In response, during human infections, bacterial uptake systems specific for host iron sources such as heme Fe and transferrin Fe combine to obtain this nutrient (*2*, *3*). These systems can take the form of receptors specific for heme Fe or transferrin Fe, or secreted siderophores that are capable of removing iron from human transferrin (*2*, *3*). Transferrin Fe accounts for less than 1% of the body's total iron, whereas heme Fe can represent greater than 80% (*4*), leading us to speculate that the abundance of heme Fe in humans may select for bacterial pathogens that preferentially acquire iron from this source. We used isotope-labeled nutrients to track simultaneous uptake of heme Fe and transferrin Fe and to determine whether *S. aureus* has a preferred iron source. Natural terrestrial iron is composed of four stable isotopes present in fixed relative proportions, 5.85% [^{54}Fe], 91.75% [^{56}Fe], 2.12% [^{57}Fe], and 0.28% [^{58}Fe], and mass-dependent fractionations of iron by microbial biochemical and inorganic redox processes have been studied and are much less than 1% (*5*–*7*). Thus, tracer compounds made up exclusively of the minor isotopes of iron can be followed in biological systems by monitoring changes in cellular iron isotope ratios by ICP-MS. For analysis, we obtained hemin and transferrin samples consisting almost exclusively of ^{54}Fe and ^{57}Fe, respectively (*8*). Isotopic labeling did not affect the ability of *S. aureus* to use these compounds as iron sources for growth (*9*).

To determine whether *S. aureus* exhibits source-dependent iron preference, we first serially passaged bacteria in low-iron medium until a decrease in growth rate indicative of iron starvation was observed (*10*). Iron-starved bacteria were subcultured into chemically defined medium and supplemented with equimolar amounts of [^{54}Fe] hemin and [^{57}Fe] transferrin, the exact ratio of which was confirmed by ICP-MS (*11*) (Fig. 1A). Natural Fe was present as a ubiquitous contaminant in all experiments, therefore all measured ratios reflect a combination of natural Fe (dominated by ^{56}Fe, 91.75%) and isotopically labeled Fe. Analysis of bacteria removed throughout the growth of the culture revealed as much as fourfold to fivefold enrichment in the ratio of heme Fe to transferrin Fe as compared

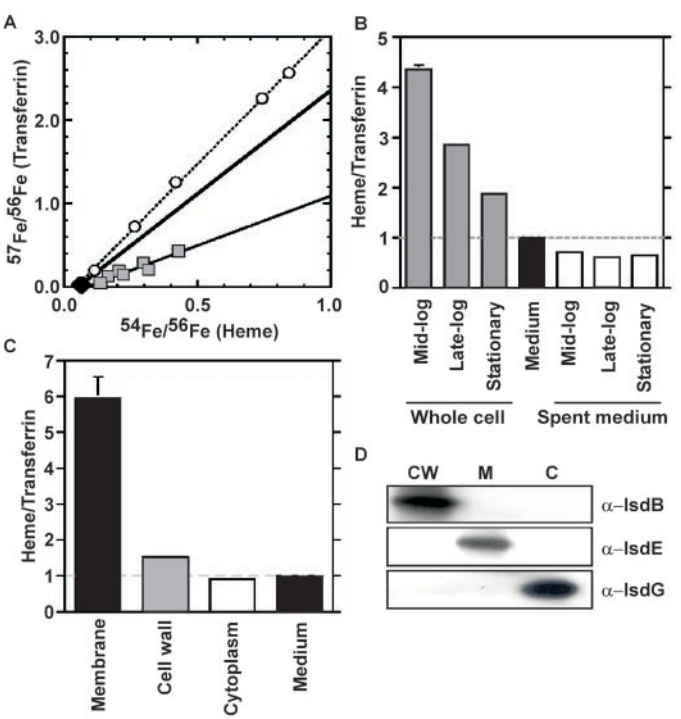

Fig. 1. Growth phase–dependent preference for heme Fe uptake in *S. aureus*. (**A**) ICP-MS measurement of iron isotope ratios in *S. aureus* cultures. The *x* and *y* axes indicate the measured ^{54}Fe/^{56}Fe (heme preference) and ^{57}Fe/^{56}Fe (transferrin preference) ratios, respectively. The natural isotopic composition of iron is shown by the black diamond. The heavy line indicates the ratio of iron isotopes present in the growth medium supplemented with [^{54}Fe] hemin and [^{57}Fe] transferrin. The squares represent bacterial samples and the circles represent spent medium samples. Each point represents an individual sample taken at different time points during three separate experiments. (**B**) Time course of iron uptake by *S. aureus*. Isotopic composition presented as ratios of heme Fe:transferrin Fe calculated from the ^{54}Fe/^{56}Fe and ^{57}Fe/^{56}Fe ratios measured by ICP-MS by correcting for the contributions to both ^{54}Fe and ^{57}Fe from natural iron, and accounting for the presence of ^{56}Fe in both tracers. Bacterial samples were taken at mid-log (9 hours), late-log (12 hours), and stationary (24 hours) phase. (**C**) Measurement of Fe isotope ratios in subcellular fractions (cytoplasm, cell wall, and membranes) from late-log cultures (12 hours) presented as the ratio of heme Fe to transferrin Fe. (**D**) Immunoblots of IsdB, IsdE, and IsdG as a fractionation control (*19*). CW, cell wall; M, membrane; C, cytoplasm. Error bars show mean + SE for all measurements but are usually too small to be seen.

[1]Committee on Microbiology, [2]Department of Molecular Genetics and Cell Biology, 920 East 58th Street, University of Chicago, Chicago, IL 60637, USA. [3]Department of Geophysical Sciences, 5734 South Ellis Avenue, University of Chicago, Chicago, IL 60637, USA.

*Present address: National High Magnetic Field Laboratory, 1800 East Paul Dirac Drive, Florida State University, Tallahassee, FL 32310, USA.

†To whom correspondence should be addressed. E-mail: oschnee@bsd.uchicago.edu

with that from the nutrient medium (Fig. 1, A and B). The heme Fe preference was further reflected in measurable heme Fe depletion from the spent media in the growth culture (Fig. 1, A and B). The intracellular ratio of heme Fe to transferrin Fe decreased as bacterial cells progressed through the growth of the culture (Fig. 1B), suggesting growth phase–dependent changes in heme Fe usage. Although bacterial removal of [^{54}Fe] hemin from the medium is clearly evident, there is little difference between the isotopic composition of the spent media from mid-log, late-log, and stationary phases. Thus, bacterial removal of [^{54}Fe] hemin from the medium is not responsible for the observed growth phase–dependent decrease in heme Fe preference. Together, these results not only demonstrate that *S. aureus* preferentially uses [^{54}Fe] hemin over [^{57}Fe] transferrin but are consistent with a growth phase–dependent up-regulation of transferrin Fe or siderophore Fe acquisition systems.

To determine the subcellular localization pattern of heme Fe and transferrin Fe, we removed late-log–phase bacterial cells from isotopically labeled medium. The bacterial cells were fractionated into three subcellular compartments (membrane, cell wall, and cytoplasm), and the abundance and isotopic ratio of iron in each compartment was determined by ICP-MS. The data presented in Fig. 1C show that the iron isotope ratios varied across subcellular fractions, suggesting that iron partitions differentially inside the bacterial cell. The magnitude of the observed variations in the Fe isotope ratio of the subcellular fractions is considerably greater than natural fractionations (*5*–*7*), requiring an explanation entirely in terms of the source of iron used. The ratio of heme Fe to transferrin Fe in the staphylococcal cytoplasm was less than that of the growth medium. This suggests that when heme is present, transferrin is primarily sorted to the cytoplasm, presumably for iron storage or use in cytoplasmic metalloproteins. The ratio of heme Fe to transferrin Fe in the cytoplasmic membrane was fivefold enriched relative to the culture medium, suggesting that iron obtained from heme may be preferentially sorted to this compartment. This degree of fractionation on the basis of isotope mass alone may be due to either the sorting of intact tetrapyrrol to the membrane or the selective membrane segregation of iron that has been removed from exogenously acquired heme. On the basis of the observation that the gram-positive cytoplasmic membrane is the primary site of heme-binding proteins such as cytochromes (*12*), it seems plausible that iron-containing tetrapyrrol may be sorted intact to the membrane and assembled as a cofactor for redox active proteins.

The assay provides a useful method to identify genes responsible for nutrient preferences by measuring changes in the intracellular isotopic ratio that occur upon gene inactivation. Analysis of the complete *S. aureus* genome identifies seven putative membrane transport systems possessing homology to known adenosine triphosphate–binding cassette (ABC)–type iron transporters, four of which have been previously studied (Fig. 2A). Staphylococcal siderophore transporter (SstABCD) (*13*), staphylococcal iron regulated (SirABC) (*14*), and ferric hydroxamate uptake (FhuCBG) (*15*) are thought to be involved in siderophore Fe transport, whereas iron-regulated surface determinants (IsdDEF) is involved in heme Fe transport from scavenged hemoglobin (*16*). Genetic inactivation of *isdDEF* does not inhibit growth on heme Fe as a sole iron source (*16*), implying that the primary heme Fe membrane transporter has yet to be identified. To address the role of these transport systems in heme Fe and transferrin Fe usage, each predicted iron transport system was inactivated through insertional mutagenesis. The mutagenesis strategy was designed so as to abrogate the expression of at least one gene in each transport system. Inactivation of *isdDEF*, *sirABC*, *fhuCBG*, *sav0609-10*, or *sav1554-1557* did not alter the heme preference of *S. aureus*. Inactivation of *sstABCD* resulted in a strain exhibiting a similar iron preference to that of the wild type at 9 hours (Fig. 2B). However, samples taken at 12 hours revealed an increase in heme preference (Fig. 2C). This observation is consistent with the role of SstABCD in siderophore Fe acquisition and supports the results presented in Fig. 1, suggesting temporal regulation of iron acquisition systems.

An alternate set of mutations in a previously uncharacterized transport system, which we have named *htsABC* (heme transport system), exhibited a unique isotopic profile. Inactivation of either *htsB* or *htsC* resulted in an increased ratio of transferrin Fe to heme Fe as compared with that of the wild type at various time points throughout the growth curve (Fig. 2, B and C), demonstrating that inactivation of HtsABC significantly reduces staphylococcal heme Fe acquisition. Sequence analysis showed that HtsB and HtsC are ABC transporter permeases representing the closest homologs in the *S. aureus* genome to HemU (*17*) and HmuU (*18*), the heme transport system permeases of *Yersinia enterocolitica* and *Corynebacterium diphtheriae*, respectively. A nucleotide sequence closely resembling the canonical staphylococcal Fur box (*19*), the site to which the iron-dependent repressor Fur binds (*20*), is located eight nucleotides upstream of the predicted start codon for HtsA (*9*), implying that the Hts system is activated under low-iron conditions. These observations suggest that the application of stable isotope tracking to strains mutant in predicted nutrient transporters successfully identified a previously unrecognized iron-regulated heme-transport system responsible for the heme Fe preference of *S. aureus*.

The strong preference for heme Fe exhibited by *S. aureus* implies a role for heme

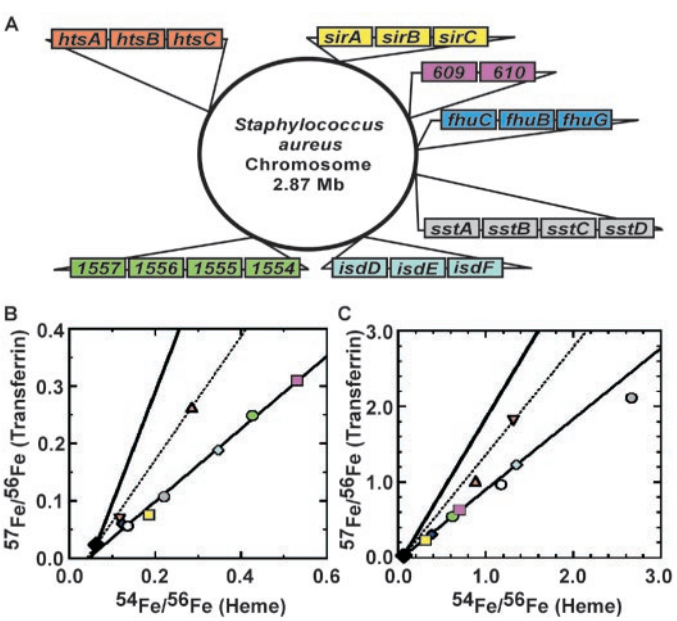

Fig. 2. (**A**) Genomic arrangement of *S. aureus* iron transport systems. Uncharacterized genes are denoted by the assigned locus tag number from the complete genome annotation (*S. aureus* strain MU50) (*30*). Mb, megabase. Measurement of iron isotope ratios in iron-transporter mutants at 9 hours (**B**) and 12 hours (**C**) of staphylococcal growth are displayed in the same format as in Fig. 1A. Measurements of whole-cell samples of strains mutant in *sirABC* (yellow square), *sav609-10* (purple square), *fhuCBG* (dark blue diamond), *sstABCD* (gray circle), *isdDEF* (light blue diamond), *sav1554-7* (green circle), and *htsABC* (orange triangles). The thin black line is a best-fit curve through the data points representing strains mutant in *isdDEF*, *fhuCBG*, *sirABC*, *sav1554-7*, and *sav609-10*. The dotted black line is a best-fit curve through the natural isotopic composition of iron, and the data points representing mutations in *htsB* and *htsC*.

Fe scavenging during infection. *S. aureus* infection of *Caenorhabditis elegans*, a nematode that uses heme proteins for oxygen transport (*21*), leads to intestinal multiplication of invading microbes, distension of the worm digestive tract, and staphylococcal killing of animals within 2 to 4 days (*22*, *23*) (Fig. 3A). Infection of *C. elegans* with *S. aureus* variants lacking either the *htsB* or the *htsC* gene caused a significant reduction in the ability of staphylococci to kill infected worms (Fig. 3A).

S. aureus abscess formation in various organ tissues of intravenously infected mice more closely resembles human infections (*24*, *25*). Twenty-four hours after intravenous infection, mice inoculated with *S. aureus* strains inactivated for *htsB* or *htsC* did not exhibit any of the overt signs of disease associated with wild-type infection (*9*). Examination of the organs of mice 96 hours postinfection demonstrated abscess formation in virtually all kidneys from mice infected with wild-type *S. aureus* (Fig. 3B), whereas abscesses were not detected in mice infected with *htsB* and *htsC* mutant mice (Fig. 3C). Additionally, there was a large reduction in the number of *htsB* and *htsC* mutant staphylococci in the kidneys and livers of infected mice as compared with that of the wild type (Fig. 3, D and E). The liver is the primary iron storage organ of mammals and the site of heme recycling through circulating hemopexin and hemoglobin-haptoglobin complexes (*26*). The severe defects in liver abscess formation of *S. aureus* Δ(*htsB*) or Δ(*htsC*) strains identify the acquisition of heme Fe at the site of heme recycling as a previously unknown pathogenic strategy of staphylococci. During infection, the *S. aureus* Hts system likely acquires additional heme Fe through hemolysin-mediated erythrocyte destruction and the subsequent release of hemoglobin (*27*). Previous work has revealed that *S. aureus* strains mutant in a siderophore synthesis operon display normal infection kinetics until 6 days after infection, at which time a substantial decrease in animal-associated bacterial counts is observed (*28*). Thus, early during infection staphylococci appear to satisfy their iron requirements through the most abundant iron source, hemoproteins. Upon depletion of hemoproteins, or once bacteria have occupied niches in the host environment that are devoid of hemoproteins, siderophores assume a vital function for the acquisition of iron from nonheme sources.

The inhibition of bacterial iron uptake has long been considered a promising area of research toward the creation of novel therapeutic options (*29*). Identifying the nutrient sources preferentially utilized during infection allows us to refine drug design strategies against the primary acquisition systems of bacteria.

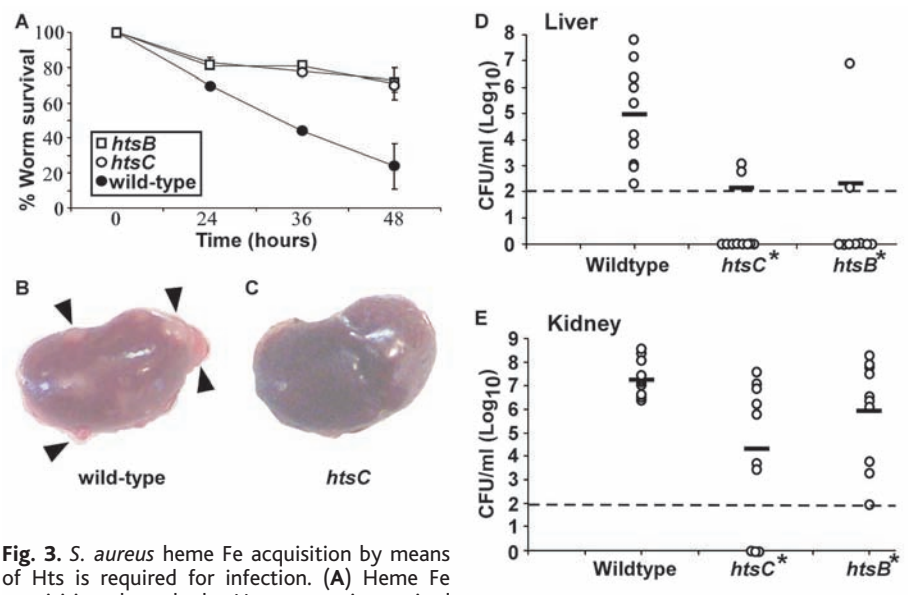

Fig. 3. *S. aureus* heme Fe acquisition by means of Hts is required for infection. (**A**) Heme Fe acquisition through the Hts system is required for *C. elegans* intestinal infection and *S. aureus* Newman (wild-type)–mediated host killing within 48 hours. Error bars show mean ± SD. Photographs of kidneys from Balb/c mice infected with wild-type (**B**) or isogenic *htsC* mutant *S. aureus* (**C**). Arrowheads mark staphylococcal abscesses. *S. aureus* multiplication in infected organs, liver (**D**), or kidney (**E**), was measured by tissue homogenization, dilution, and colony formation on agar medium. Each symbol represents data from one infected animal. The limit of detection is indicated as a dashed line, and the horizontal line denotes the mean of the log of the colony forming units. Asterisks denote statistically significant differences from the wild type as determined by a Student's *t* test ($P \leq .05$). CFU, colony forming units.

References and Notes

1. J. E. Posey, F. C. Gherardini, *Science* **288**, 1651 (2000).
2. J. J. Bullen, E. Griffiths, *Iron and Infection: Molecular, Physiological and Clinical Aspects* (Wiley, New York, 1999).
3. V. Braun, *Int. J. Med. Microbiol.* **291**, 67 (2001).
4. R. Crichton, *Inorganic Biochemistry of Iron Metabolism: From Molecular Mechanisms to Clinical Consequences* (Wiley, West Sussex, UK, 2001), vol. 2.
5. B. L. Beard *et al.*, *Science* **285**, 1889 (1999).
6. A. D. Anbar, *Frontiers (Boulder)* **217**, 223 (2004).
7. T. Walczyk, F. von Blanckenburg, *Science* **295**, 2065 (2002).
8. The isotopic composition of [^{54}Fe] hemin (±SE) was 90.7 ± 0.6% [^{54}Fe], 8.99% [^{56}Fe], 0.184% [^{57}Fe], and <0.13% [^{58}Fe]. The isotopic composition of [^{57}Fe] transferrin was 0.051% [^{54}Fe], 5.035% [^{56}Fe], 94.4 ± 0.4% [^{57}Fe], and 0.497% [^{58}Fe].
9. E. P. Skaar, M. Humayun, T. Bae, K. L. DeBord, O. Schneewind, data not shown.
10. Natural iron is a ubiquitous source of iron in bacterial culturing experiments and is traced by the ^{56}Fe (91.75%) isotope. The availability of this iron can be limited during culture experiments by the addition of an aqueous phase iron chelator, but this was found to selectively remove iron from transferrin, and therefore no chelator was used in the present experiments. The potential sources of natural iron in our experiments include the natural iron stores of the bacteria, rust introduced by handling procedures and as a laboratory contaminant, and iron leached from the walls of containers used to handle the analytical solutions.
11. Materials and methods are available as supporting material on *Science* Online.
12. C. von Wachenfeldt, L. Hederstedt, *J. Biol. Chem.* **265**, 13939 (1990).
13. J. A. Morrissey, A. Cockayne, P. J. Hill, P. Williams, *Infect. Immun.* **68**, 6281 (2000).
14. J. H. Heinrichs, L. E. Gatlin, C. Kunsch, G. H. Choi, M. S. Hanson, *J. Bacteriol.* **181**, 1436 (1999).
15. M. T. Sebulsky, D. Hohnstein, M. D. Hunter, D. E. Heinrichs, *J. Bacteriol.* **182**, 4394 (2000).
16. S. K. Mazmanian *et al.*, *Science* **299**, 906 (2003).
17. I. Stojiljkovic, K. Hantke, *Mol. Microbiol.* **13**, 719 (1994).
18. E. S. Drazek, C. A. Hammack, M. P. Schmitt, *Mol. Microbiol.* **36**, 68 (2000).
19. E. P. Skaar, A. H. Gaspar, O. Schneewind, *J. Biol. Chem.* **279**, 436 (2004).
20. L. Escolar, J. Perez-Martin, V. de Lorenzo, *J. Bacteriol.* **181**, 6223 (1999).
21. A. P. Kloek, J. P. McCarter, R. A. Setterquist, T. Schedl, D. E. Goldberg, *J. Mol. Evol.* **43**, 101 (1996).
22. D. A. Garsin *et al.*, *Proc. Natl. Acad. Sci. U.S.A.* **98**, 10892 (2001).
23. C. D. Sifri, J. Begun, F. M. Ausubel, S. B. Calderwood, *Infect. Immun.* **71**, 2208 (2003).
24. A. Albus, R. D. Arbeit, J. C. Lee, *Infect. Immun.* **59**, 1008 (1991).
25. D. McKenney *et al.*, *Science* **284**, 1523 (1999).
26. A. Smith, W. T. Morgan, *Biochem. J.* **182**, 47 (1979).
27. A. W. Bernheimer, L. S. Avigad, P. Grushoff, *J. Bacteriol.* **96**, 487 (1968).
28. S. E. Dale, A. Doherty-Kirby, G. Lajoie, D. E. Heinrichs, *Infect. Immun.* **72**, 29 (2004).
29. V. Braun, M. Braun, *Curr. Opin. Microbiol.* **5**, 194 (2002).
30. M. Kuroda *et al.*, *Lancet* **357**, 1225 (2001).

31. We thank D. Missiakas for the gift of mutant *S. aureus* strains, W. Williams and H. S. Seifert for critical reading of this manuscript, and A. J. Campbell for assistance with ICP-MS operations. Supported by U.S. Public Health Service grant AI52474. E.P.S. was supported by a Greater Midwest Affiliate Postdoctoral Fellowship of the American Heart Association.

Supporting Online Material

www.sciencemag.org/cgi/content/full/305/5690/1626/DC1

Materials and Methods

References

4 May 2004; accepted 15 July 2004

SOS Response Induction by β-Lactams and Bacterial Defense Against Antibiotic Lethality

Christine Miller,[1] Line Elnif Thomsen,[2] Carina Gaggero,[1]* Ronen Mosseri,[1]† Hanne Ingmer,[1,2]‡ Stanley N. Cohen[1]§

The SOS response aids bacterial propagation by inhibiting cell division during repair of DNA damage. We report that inactivation of the *ftsI* gene product, penicillin binding protein 3, by either β-lactam antibiotics or genetic mutation induces SOS in *Escherichia coli* through the DpiBA two-component signal transduction system. This event, which requires the SOS-promoting *recA* and *lexA* genes as well as *dpiA*, transiently halts bacterial cell division, enabling survival to otherwise lethal antibiotic exposure. Our findings reveal defective cell wall synthesis as an unexpected initiator of the bacterial SOS response, indicate that β-lactam antibiotics are extracellular stimuli of this response, and demonstrate a novel mechanism for mitigation of antimicrobial lethality.

The ability of bacteria to reduce their susceptibility to antimicrobial drugs importantly affects both bacterial ecology and the treatment of infectious diseases. Previously known mechanisms of bacterial defense against antibiotics include mutation of the drug target, inactivation or destruction of the antimicrobial, and inhibition of antibiotic entry (*1*). We report a mechanistically novel type of defense mechanism that uses a bacterial two-component signal transduction system to induce the SOS response and temporarily inhibit cell division during exposure to β-lactam antibiotics, consequently limiting the bactericidal effects of these drugs.

Two-component signal transduction systems have a key role in mediating the response of bacteria to environmental stimuli. Normally, receptor-mediated detection of a stimulus at the cell surface leads to autophosphorylation of a sensor kinase component, which then phosphorylates the effector protein component (i.e., the response regulator), enabling the effector to bind to operator/promoter sequences of target genes and either increase or repress transcription (*2*). DpiA, the effector for the DpiBA two-component system, not only regulates transcription (*3*) but also regulates DNA replication and segregation by virtue of its uncommon ability to bind to A+T-rich sequences in the replication origins of the *E. coli* chromosome and certain plasmids (*4*). Interaction of DpiA with replication origins competes with binding of the replication proteins DnaA and DnaB: When overexpressed, DpiA can interrupt DNA replication and induce the SOS response (*4*), thereby inhibiting cell division (*4*, *5*).

Previous sequence analysis has suggested that the adjacent *E. coli dpiB* and *dpiA* genes (*3*), like their *Klebsiella pneumoniae* orthologs *citA* and *citB* (*6*), comprise a polycistronic operon (Fig. 1A). Polymerase chain reaction (PCR) analysis using combinations of primers corresponding to sequences within each of these genes confirmed that *dpiB* and *dpiA* are encoded by a common transcript (Fig. 1B). We wished to identify stimuli that activate the *dpiBA* operon; to monitor such activation, we fused a Hind III–Sma I DNA segment containing the region 5′ to *dpiB* to a *lacZ* reporter gene fragment (pHI1508 in Fig. 1A) (*3*, *7*). β-Galactosidase synthesis from this construct was investigated under a variety of growth-limiting conditions known to activate two-component systems and/or the SOS response (including growth in media containing different carbon sources; starvation for O_2, PO_4, or carbon; heat or cold shock; high salt; exposure to ultraviolet light; culture in stationary phase or in conditioned media; and concentration to a high cell density). Whereas none of the above conditions increased β-galactosidase synthesis, we observed during our experiments that expression of the reporter gene was stimulated by exposure of bacteria to ampicillin and other β-lactam antibiotics (penicillin, cefuroxan, cephalexin, pipericillin) (Fig. 2A) (*7*, *8*). In contrast, none of the non–β-lactam categories of antibiotics we tested activated the *dpiBA* promoter (Fig. 2A).

Increased expression of the *dpiB* and *dpiA* operon by β-lactam treatment was confirmed by quantitative PCR (*9*) analysis (Fig. 1C), which showed a β-lactam–dependent fourfold increase in *dpiBA* transcripts encoded by the *E. coli* chromosome. Consistent with these observations was a concurrent threefold increase in expression of the *E. coli citC* gene (Fig. 1C), which is divergently transcribed from *dpiBA* (Fig. 1A) and previously was shown to be upregulated by overexpression of the DpiA protein (*3*). Similarly, *lacZ* fusions to promoters found in earlier studies to be activated by DpiA (*7*) showed DpiA-dependent elevation of expression during treatment

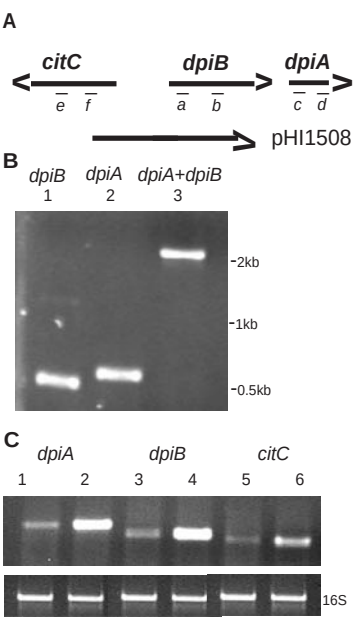

Fig. 1. Structure and transcripts of the *dpiBA* operon. (**A**) The *dpiB* and *dpiA* genes are aligned in the 5′ → 3′ direction; *citC* is 5′ of the *dpiBA* promoter/operator region and is transcribed divergently from it (*3*). The segment of the *dpiBA* operon included in plasmid pHI1508 (*7*) is indicated. (**B**) Agarose gel electrophoresis showing bands generated by reverse transcription PCR amplification of *E. coli* SC1088 (*26*) RNA using pairs of oligonucleotide primers corresponding to sequences within *dpiB* (lane 1, primers a + b), *dpiA* (lane 2, primers c + d), or both genes (lane 3, primers a + d). Locations of primer sequences are indicated in (A). (**C**) Induction of *dpi* transcripts (*7*) by ampicillin from SC1088 grown at 30°C in the absence (lanes 1, 3, and 5) or presence (lanes 2, 4, and 6) of ampicillin (4 μg/ml for 4 hours), shown with loading controls.

[1]Department of Genetics, Stanford University, Stanford, CA 94305, USA. [2]Department of Veterinary Pathobiology, Royal Veterinary and Agricultural University, Stigboejlen 4, Fredericksberg C, DK-1870, Denmark.

*Present address: Departamento de Biologia Molecular, Instituto de Investigaciones Biológicas Clemente Estable, Av. Italia 3318, 11600 Montevideo, Uruguay.
†Present address: Department of Pediatrics B, Schneider Children's Medical Center of Israel, Petah Tiqva 49202, Israel.
‡Present address: Department of Veterinary Pathobiology, Royal Veterinary and Agricultural University, Stigboejlen 4, Frederiksberg C, DK-1870, Denmark.
§To whom correspondence should be addressed. E-mail: sncohen@stanford.edu

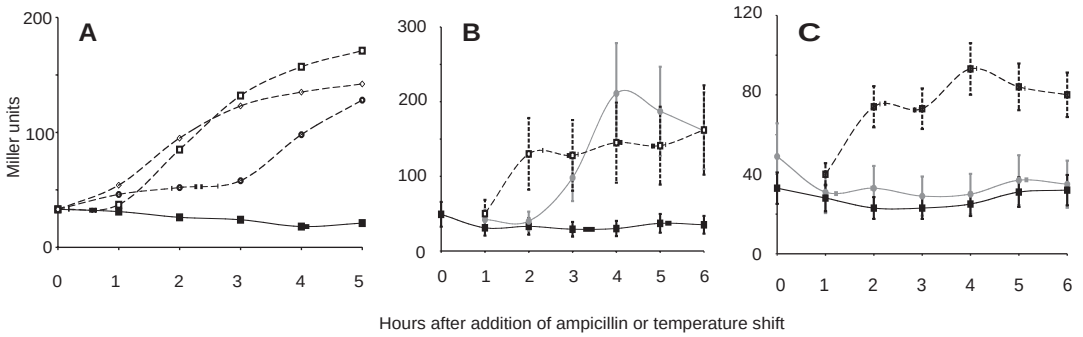

Fig. 2. Induction of the *dpi* operon by β-lactam antibiotics. (**A**) Expression of the *dpi* operon as measured in *lacZ*⁻ *E. coli* strain UT481 by a *lacZ* reporter fusion to the *dpiB* promoter on pHI1508 [in Miller units (*27*)]. Bacteria were grown at 30°C with or without (black squares) antibiotics. Values similar to the control without antibiotics were observed after addition at time zero of kanamycin, streptomycin, spectinomycin, mitomycin C, chloramphenicol, tetracycline, nalidixic acid, rifampicin, vancomycin, or phosphomycin: Open symbols indicate *lacZ* expression after addition at time zero of ampicillin (squares), cephalexin (diamonds), or pipericillin (circles). [See (*7*) for concentrations.] All points represent the average of at least three separate experiments. (**B**) Induction of *dpiB/lacZ* (as measured by β-galactosidase expression calculated in Miller units) in *E. coli* JOE339, a *lacZ*⁻ mutant strain that carries an *ftsI*^{ts} mutation. Cells were grown at 30°C with (dashed line and open squares) or without (black squares) ampicillin (4 μg/ml), or at 42°C in the absence of ampicillin (gray circles). (**C**) Same as (B) but in MC4100, the parent of JOE339. For (B) and (C), bars indicate SD.

with ampicillin (Table 1), further establishing the ability of ampicillin to induce the *dpiBA* operon. Up-regulation of the *dpiB/lacZ* fusion by ampicillin was also observed in the *dpiA* null mutant strain (Table 1), indicating that induction of *dpiBA* expression by ampicillin does not require the DpiA protein.

The lethality of β-lactam antibiotics stems from their interaction with transmembrane penicillin binding proteins (PBPs) and the consequent disruption of cell wall integrity (*10*). Whereas ampicillin binds to all 12 *E. coli* PBPs (*11*), pipericillin and cephalexin, which were among the β-lactam drugs we found to increase expression of the *dpiBA* operon (Fig. 2A), bind only to PBP3 (*12*, *13*), which suggests that PBP3 specifically mediates the β-lactam effect. PBP3 is encoded by *ftsI*, one of a group of filamentation temperature–sensitive genes implicated in cell division (*14*), and is a membrane transpeptidase required for peptidoglycan synthesis at the septum generated by cell division (*15*). Binding of β-lactam antibiotics to PBP3 molecules at the septum inactivates transpeptidase function, leading to lysis of dividing cells in bacterial populations (*10*).

Inactivation of PBP3 also occurs when cultures of the *ftsI*^{ts} strain, JOE339 *ftsI*23 (*16*), are shifted to 42°C (*14*). We found that shift of JOE339 *ftsI*23 to 42°C increased expression of the *dpi/lacZ* reporter gene fusion to a level similar to that observed after addition of ampicillin (4 μg/ml) to the culture medium (Fig. 2B). In contrast, expression from the *dpi/lacZ* fusion was unchanged at 42°C in the parental strain (Fig. 2C); in a mutant of the *rodA* gene, which encodes PBP2 (a transpeptidase required for cell wall elongation) [strain S1 (*10*)]; or in a *ts* mutant of *ftsZ* [*ftsZ84* in JOE337 (*16*)], a filamentation temperature–sensitive gene involved in septum ring formation (*8*). Collectively, these results strongly suggest that inactivation of PBP3 is a stimulus for increased expression of the *dpiBA* operon.

Table 1. Induction of *lacZ* fusions by DpiA or ampicillin in wild-type (WT) and mutant strains. Ampicillin was added at 10 μg/ml and time points were taken after 2 hours of growth at 37°C. DpiA was overproduced at twice the normal amount from a multicopy plasmid pHI1429 (*3*). pHI1627 carries a *lacZ* fusion to *pabA*, which has been identified as a gene up-regulated by DpiA (*7*). pHI1508 carries a *lacZ* fusion to the promoter/operator region of *dpiB* (*7*). The *lacZ*⁻ *E. coli* strain 1088 (*26*) and null mutations of *dpiA* (*3*), *recA*, and *lexA* (*7*) were used. Values are averages of at least three experiments. β-Galactosidase production is indicated in Miller units (*27*).

lacZ⁻ strain and plasmids	Miller units	Induction ratio
WT + pHI1627	29 ± 4	
+ DpiA overproduction	118 ± 20	4
+ ampicillin	185 ± 20	6.4
dpiA null mutant + pHI1627	16 ± 5	
+ ampicillin	18 ± 1	1
WT + pHI1508	52 ± 3	
+ DpiA overproduction	138 ± 25	2.8
+ ampicillin	345 ± 50	6.6
dpiA null mutant + pHI1508	27 ± 3	
+ ampicillin	113 ± 15	4.1
recA null mutant + pHI1508	24 ± 3	
+ ampicillin	80 ± 8	3.3
lexA null mutant + pHI1508	22 ± 6	
+ ampicillin	110 ± 10	5

A biological consequence of DpiA overexpression is induction of the SOS response (*4*); the extent of such induction can be determined by β-galactosidase synthesis from a *lacZ* fusion with the SOS-regulated promoter of the *sfiA* gene [e.g., (*17*, *18*)], which prevents FtsZ polymerization and inhibits cell division when SOS is activated (*5*). Addition of ampicillin (4 μg/ml) to cell cultures increased *lacZ* expression from the fusion construct to a level comparable to that observed when DpiA was overproduced from a multicopy plasmid (Fig. 3A) (*4*). However, we observed no change in *sfiA/lacZ* expression in bacteria containing a *dpiA* null mutation (Fig. 3A); this result implies that the increase in *sfiA* expression by ampicillin requires *dpiA* function. β-Galactosidase synthesis by the *sfiA/lacZ* fusion construct was also increased by shifting of the *ftsI*^{ts} strain to 42°C, further establishing the ability of FtsI/PBP3 inactivation to induce SOS (Fig. 3B). This result, which identifies SOS as a response to impaired cell septum synthesis, was also dependent on an intact *dpiA* gene (Fig. 3B).

Mutations in *recA* or *lexA* that preclude induction of the SOS response (*19*) prevented the effects of either ampicillin treatment or temperature shift of the *ftsI* mutant strain on expression of the *sfiA/lacZ* fusion protein (Fig. 3A) (*8*), confirming that *sfiA* induction by the β-lactam–PBP3–DpiA pathway is SOS dependent. Still further confirmation that the observed activation of *sfiA* expression by this pathway is due to induction of the SOS response was provided by Western blot data showing that the RecA protein also was elevated by DpiA overproduction and by inactivation of PBP3 through *ftsI* temperature inactivation

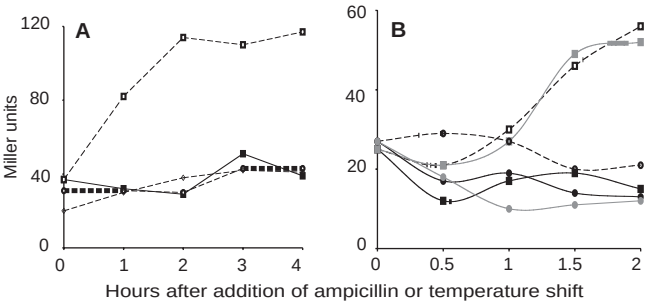

Fig. 3. SOS response induced by PBP3 inactivation. (**A**) *E. coli* BR3151, a *lacZ*$^-$ mutant strain containing a *sfiA/lacZ* fusion used to measure the SOS response (*5*), was grown in the absence (black squares) or presence (open squares) of ampicillin (4 μg/ml). Analogous experiments in the presence of ampicillin (4 μg/ml) used a *dpiA* (open circles) or *recA* derivative (open diamonds), which appear as overlapping lines. (**B**) Expression of the *sfiA/lacZ* fusion from *ftsI*^{ts} JOE339 (squares) or *dpiA* JOE339 (diamonds) was followed by measuring β-galactosidase production (in Miller units) in bacteria grown at 30°C in the absence (black solid lines, closed symbols) or in the presence (black dashed lines, open symbols) of ampicillin (4 μg/ml), or at 42°C in the absence of ampicillin (gray lines, closed symbols). Both (A) and (B) are averages of three separate experiments (*7*).

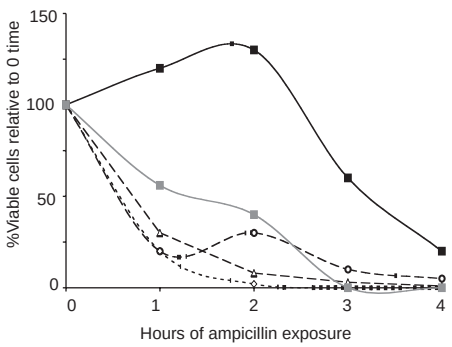

Fig. 4. Effect of SOS response induction on survival of bacterial cells expressing DpiA during β-lactam exposure. SC1088 wild-type (squares) cultures were exposed to ampicillin at time zero, and percent survival was determined. Survival data are also shown for strains containing null mutations in *recA* (open diamonds), *dpiA* (*3*) (open circles), or *sfiA* (open triangles). Ampicillin was added at 3 μg/ml (black lines) or 9 μg/ml (gray lines) (*7*).

or by ampicillin, and that the effect of PBP3 inactivation was dependent on an intact *dpiA* gene (*7*). The dependence of β-lactam/PBP3–mediated SOS induction on *dpiA* contrasted with the lack of effect of the *dpiA* mutation on RecA expression induced by the DNA damaging agent mitomycin C (*7*), indicating the distinctive nature of the cell wall–mediated and DNA damage–mediated paths to SOS induction.

Because β-lactam antibiotics kill only bacteria that are dividing (*20*), we hypothesized that the ability of these drugs to induce the SOS response, and consequently delay cell division by increasing the expression of *sfiA* (*5*), may provide temporary protection from β-lactam lethality. We therefore tested wild-type *E. coli* cells, *dpiA* null mutant bacteria, bacteria known to be unable to generate an SOS response [i.e., *recA* mutant cells (*19*)], and *sfiA* mutant bacteria (*21*) for their relative ability to withstand exposure to ampicillin, as measured by survival in cultures containing different concentrations of this antibiotic. Mutation of *dpiA*, *recA*, or *sfiA* increased bacterial susceptibility to killing by ampicillin (Fig. 4): 90% of cells mutated in these genes were unable to form colonies after 1 hour of exposure to ampicillin (3 μg/ml), whereas the same extent of killing of wild-type cells required 1 hour of exposure to ampicillin at 9 μg/ml or 4 hours of exposure at 3 μg/ml. During overnight exposure to pipericillin (2 μg/ml), a PBP3-specific β-lactam, 10 times as many wild-type bacteria as *dpiA* mutant bacteria survived (0.01% versus 0.001% of cells relative to the number before addition of antibiotic). However, the minimum inhibitory concentration of ampicillin required to permanently inhibit cell growth (1.5 μg/ml) was unchanged by mutation of *dpiB*, *dpiA*, or both. Thus, although *dpiBA*-mediated induction of the SOS response delayed β-lactam antibiotic lethality, it did not reverse the effects of extended exposure to these drugs.

Our results indicate a hitherto unsuspected role for the SOS response in temporarily halting cell division when the transpeptidase encoded by the *ftsI* gene at the cell septum is functionally impaired, and additionally demonstrate a novel role for both the DpiBA two-component system and the *sfiA* gene in this process. The consequence of *dpiBA* operon-dependent induction of SOS by β-lactam antibiotics is to mitigate the lethal effects of these drugs on bacteria. Recent evidence indicates that even subinhibitory concentrations of a variety of antibiotics can modulate transcription in bacteria (*22*), and microarray data suggest that altered expression of SOS and other stress response genes are among the many global changes that can result from exposure to antibiotics (*23*, *24*). Additionally, induction of the SOS response also can affect the interbacterial transfer of genetic material, increasing dissemination of antibiotic resistance among microbial populations (*25*). The further ability of the SOS response to enhance the survival of bacteria exposed to β-lactams identifies the SOS response as a potential target for drugs aimed at enhancing the efficacy of β-lactam antimicrobials.

References and Notes

1. D. J. Chadwick, J. Goode, Eds., *Antibiotic Resistance: Origin, Evolution, Selection and Spread* (Wiley, Chichester, UK, 1997).
2. J. A. Hoch, T. J. Silhavy, *Two-Component Signal Transduction* (American Society for Microbiology, Washington, DC, 1995).
3. H. Ingmer, C. A. Miller, S. N. Cohen, *Mol. Microbiol.* **29**, 49 (1998).
4. C. A. Miller, H. Ingmer, L. E. Thomsen, K. Skarstad, S. N. Cohen, *J. Bacteriol.* **185**, 6025 (2003).
5. O. Huisman, R. D'Ari, S. Gottesman, *Proc. Natl. Acad. Sci. U.S.A.* **81**, 4490 (1984).
6. M. Bott, M. Meyer, P. Dimroth, *Mol. Microbiol.* **18**, 533 (1995).
7. See supporting data on *Science* Online.
8. C. Miller *et al.*, data not shown.
9. R. D. Sleator, C. G. M. Gahan, B. O'Driscoll, C. Hill, *Int. J. Food Microbiol.* **60**, 261 (2000).
10. B. G. Spratt, *Proc. Natl. Acad. Sci. U.S.A.* **72**, 2999 (1975).
11. S. A. Denome, P. K. Elf, T. A. Henderson, D. E. Nelson, K. D. Young, *J. Bacteriol.* **181**, 3981 (1999).
12. G. A. Botta, J. T. Park, *J. Bacteriol.* **145**, 333 (1981).
13. J. Pogliano, K. Pogliano, D. S. Weiss, R. Losick, J. Beckwith, *Proc. Natl. Acad. Sci. U.S.A.* **94**, 559 (1997).
14. B. G. Spratt, *J. Bacteriol.* **131**, 293 (1977).
15. M. Nguyen-Disteche, C. Fraipont, N. Buddelmeijer, N. Nanninga, *Cell. Mol. Life Sci.* **54**, 309 (1998).
16. J. Chen, J. Beckwith, personal communication.
17. E. C. Hendricks, H. Szerlong, T. Hill, P. Kuempel, *Mol. Microbiol.* **36**, 973 (2000).
18. A. Bacolla, A. Jaworski, T. D. Connors, R. D. Wells, *J. Biol. Chem.* **276**, 18579 (2001).
19. G. C. Walker, *Microbiol. Rev.* **48**, 60 (1984).
20. A. Tomasz, in *Mode of Action of Antibiotics on Microbial Walls and Membranes*, M. R. J. Salton, A. Tomasz, Eds. (New York Academy of Sciences, New York, 1974), pp. 439–447.
21. H. Ohmori *et al.*, *J. Bacteriol.* **177**, 156 (1995).
22. E.-B. Goh *et al.*, *Proc. Natl. Acad. Sci. U.S.A.* **99**, 17025 (2002).
23. K. J. Shaw *et al.*, *J. Mol. Microbiol. Biotechnol.* **5**, 105 (2003).
24. S. Utaida *et al.*, *Microbiology* **149**, 2719 (2003).
25. J. W. Beaber, B. Hochhut, M. K. Waldor, *Nature* **427**, 72 (2004).
26. D. P. Biek, S. N. Cohen, *J. Bacteriol.* **171**, 2066 (1989).
27. J. Sambrook, E. F. Fritsch, T. Maniatis, *Molecular Cloning: A Laboratory Manual* (Cold Spring Harbor Laboratory, Cold Spring Harbor, NY, ed. 2, 1989).
28. We thank J. Davies for comments on the manuscript. Supported by NIH grant R01 AI08619 (S.N.C.), a grant from the Danish Agricultural and Veterinary Research Council (L.E.T.), and a Pew Latin American Fellows Program award (C.G.).

Supporting Online Material
www.sciencemag.org/cgi/content/full/1101630/DC1
Materials and Methods
References

18 June 2004; accepted 15 July 2004
Published online 12 August 2004;
10.1126/science.1101630
Include this information when citing this paper.

Species Coextinctions and the Biodiversity Crisis

Lian Pin Koh,[1]*† Robert R. Dunn,[2]*‡ Navjot S. Sodhi,[1]§
Robert K. Colwell,[3] Heather C. Proctor,[4] Vincent S. Smith[5]‖

To assess the coextinction of species (the loss of a species upon the loss of another), we present a probabilistic model, scaled with empirical data. The model examines the relationship between coextinction levels (proportion of species extinct) of affiliates and their hosts across a wide range of coevolved interspecific systems: pollinating *Ficus* wasps and *Ficus*, parasites and their hosts, butterflies and their larval host plants, and ant butterflies and their host ants. Applying a nomographic method based on mean host specificity (number of host species per affiliate species), we estimate that 6300 affiliate species are "coendangered" with host species currently listed as endangered. Current extinction estimates need to be recalibrated by taking species coextinctions into account.

Rapid population declines and extinctions of species following the widespread destruction of natural habitats have been reported across the natural world (*1*). Up to 50% of species are predicted to be lost in the next 50 years (*2*, *3*). This seemingly inevitable biodiversity crisis has galvanized the study of population and species extinctions (*4*). However, while investigations have focused on the pathology of independent taxon-based extinctions, the possible cascading effects of species loss, while acknowledged (*5*–*7*), have not been estimated quantitatively for extinct or endangered taxa. Such a view underestimates the intricate processes of species extinctions, especially in complex ecosystems such as tropical rainforests, where many species obligately depend on one another.

The term "coextinction" was first used to describe the process of the loss of parasitic insects with the loss of their hosts (*5*). The concept has been expanded to describe the demise of a broader array of interacting species, including predators with their prey (*6*) and specialist herbivores with their host plants (*7*). Here, we define coextinction as the loss of a species (the affiliate) upon the loss of another (the host). The most often cited example is that of the extinct passenger pigeon (*Ectopistes migratorius*) and its parasitic louse (*Columbicola extinctus*) (*5*), although the latter has been shown to be alive and well on other hosts (*8*, *9*). More recently, the loss of tropical butterfly species from Singapore was attributed to the loss of their specific larval host plants (*7*).

Here, we apply a simple probabilistic model to empirical "affiliation matrices" (host by affiliate presence/absence matrices) to examine the relationship between affiliate and host extinctions across a range of coevolved interspecific systems: pollinating *Ficus* wasps and *Ficus*, primate parasites (*Pneumocystis* fungi, nematodes, and lice) and their hosts, parasitic mites and lice and their avian hosts, butterflies and their larval host plants, and ant butterflies and their host ants. The model estimates the number of affiliate extinctions as a function of the number of host extinctions, assuming a random order of host extinction (*10*). Figure 1 shows the predicted coextinction curves for eight relatively well studied affiliate-host systems. The coextinction curve is linear for affiliate-host systems in which each affiliate species was associated with only one host, such as *Pneumocystis* fungi and their primate hosts, and curvilinear for systems in which at least some affiliate species have multiple hosts, such as butterflies and their larval host plants.

This probabilistic model relies on fully specified affiliation matrices and thus is not useful for estimating expected numbers of affiliate extinctions in affiliate-host systems for which host specificity distributions are unavailable. To estimate coextinction levels for these affiliate-host systems, we have developed a nomographic model of affiliate extinctions that expresses affiliate extinction

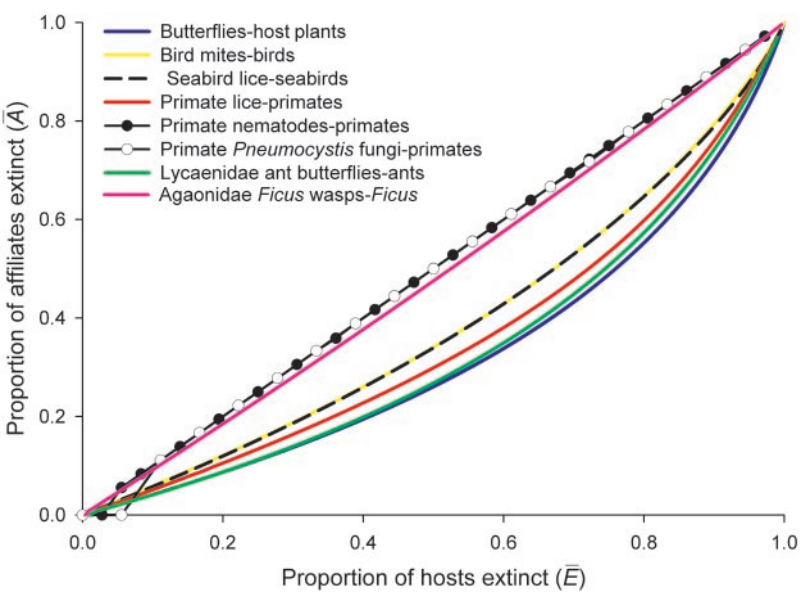

Fig. 1. Proportion of affiliate species expected to go extinct through coextinction for a given proportion of host extinction in eight affiliate-host systems: pollinating Agaonidae *Ficus* wasps–*Ficus*, primate *Pneumocystis* fungi–primates, primate nematodes–primates, primate lice–primates, seabird lice–seabirds, bird mites–birds, butterflies–host plants, and Lycaenidae ant butterflies–ants. Coextinction curves were estimated with a rigorous probabilistic model. Briefly, we used an explicit combinatorial model (*20*) as implemented in EstimateS 7 (*21*) to estimate, for each data set, the number of affiliate species expected to survive, given a decreasing number of surviving host species. The estimated number of affiliate extinctions for a given number of host extinctions was then computed by subtracting the number of surviving species from the respective total number of species. See (*10*) for details.

[1]Department of Biological Sciences, National University of Singapore, 14 Science Drive 4, Singapore 117543. [2]Department of Environmental Biology, Curtin University of Technology, GPO Box U1987 Perth, Western Australia 6845. [3]Department of Ecology and Evolutionary Biology, University of Connecticut, Storrs, CT 06269–3043, USA. [4]Department of Biological Sciences, University of Alberta, Edmonton, Alberta T6G 2E9, Canada. [5]Institute of Biomedical and Life Sciences, University of Glasgow, Glasgow, G12 8QQ, United Kingdom.

*These authors contributed equally to this work.
†Present address: Department of Ecology and Evolutionary Biology, Princeton University, Princeton, NJ 08544–1003, USA.
‡Present address: Department of Ecology and Evolutionary Biology, University of Tennessee, 1416 Circle Drive, 569 Dabney Hall, Knoxville, TN 37996–1610, USA.
§To whom correspondence should be addressed. E-mail: dbsns@nus.edu.sg
‖Present address: Illinois Natural History Survey, 607 East Peabody Drive, Champaign, IL 61820–6970, USA.

probability as a function of host extinction probability and mean host specificity (Fig. 2) (*10*). This alternative approach is useful for estimating coextinction levels because mean host specificity is easier to approximate than complete host specificity distributions for many affiliate-host systems. The nomographic model reveals that affiliate extinction levels can be expected to decrease approximately log-linearly as the mean number of hosts increases, for any given level of host extinction (Fig. 2). The estimated affiliate extinction probability, $\overline{A}$, is described by the equation

$$\overline{A} = (0.35\overline{E} - 0.43)\overline{E}\ln(\overline{s}) + \overline{E} \quad (1)$$

where $\overline{E}$ is the host extinction probability and $\overline{s}$ is the mean host specificity of the affiliate species. Affiliate extinction levels estimated by this equation are highly concordant (concordance correlation $R_c > 0.99$) with those predicted by the probabilistic model for all 20 affiliate-host systems we analyzed (*10*).

For selected affiliate-host groups, we estimate the magnitude of historical affiliate extinctions due to the documented loss of their hosts, as well as future affiliate extinctions if all their currently endangered hosts [International Union for Conservation of Nature and Natural Resources (IUCN) categories of "critically endangered," "endangered," and "vulnerable" (*11*)] were to go extinct. We estimate that at least 200 affiliate species have become extinct historically from the extinction of their hosts in these groups (Fig. 3A), and another 6300 affiliate species are currently "coendangered"—likely to go extinct if their currently endangered hosts in these groups become extinct (Fig. 3B).

For all but the most host-specific affiliate groups (e.g., primate *Pneumocystis* fungi and primates), affiliate extinction levels may be modest at low levels of host extinction but can be expected to rise quickly as host extinctions increase to levels predicted in the near future (*2*, *3*). This curvilinear relationship between host and affiliate extinction levels may also explain, in part, why so few coextinction events have been documented to date (*10*). We modeled extinction risk as a probability. The actual numbers of affiliate extinctions depend on the species richness of affiliate groups at risk and can be expected to be substantial for species-rich affiliate taxa (e.g., beetles, Fig. 3B). Affiliate extinctions may already have resulted from historical extinctions of their hosts (Fig. 3A). However, only a small proportion of the number of affiliate extinctions that we predict on probabilistic grounds have been documented (*10*). The study of the skins or other remains of extinct potential host organisms (e.g., birds and mammals) would likely yield many more coextinct parasites or mutualists.

Organisms with complex life histories would be expected to have higher risks of coextinction over evolutionary time than those with simpler life histories. For example, hummingbird flower mites face extinction if either the hummingbirds they use for transport or the flowers on which the mites depend for nectar and pollen go extinct (*12*). Conversely, in interactions where hosts are associated with many obligately dependent affiliate species, the loss of the host will result in the coextinctions of all its affiliated organisms. For example, the army ant, *Eciton burchelli*, hosts no fewer than 100 affiliate species, including springtails, beetles, mites, and ant birds (*13*). Many of these affiliate organisms would hence be lost were *E. burchelli* to go extinct (*14*). Because a disproportionate number of affiliate species obligately depend upon them for their continued existence, species like *E. burchelli* may be considered a "keystone mutualist," a keystone species in an evolutionary sense (*15*). The ecological importance and conservation implications of keystone mutualists deserve further investigation because their loss will likely result in multiple extinction cascades.

It might be argued that there is no need to focus on the endangerment of affiliate species, because their protection follows automatically from the protection of their endangered hosts. Although this may be the case for some categories of affiliates (e.g., obligate endoparasites with simple life cycles), affiliates that depend on complex ecological interactions between multiple hosts, or affiliates that have demographic thresholds more sensitive than those of their hosts (*7*, *12*) may be at greater risk of extinction than their hosts. Further, some affiliates may be lost when their hosts are intentionally fumigated (*16*). On the other hand, in some cases declines in host populations threatened by human activities may be exacerbated by the negative effects of affiliates. For example, forest habitat fragmentation in North America has favored the parasitic brown-headed cowbird (*Molothrus ater*) at the expense of some of its declining hosts (*17*). In such cases, if other threats to hosts cannot be remedied, control of affiliates, even at the risk of their possible extinction, must be contemplated. There is no point in attempting to save an affiliate if its host(s) become extinct in the process. Although this study is about species coextinctions, we expect the loss of host populations to result in the loss of affiliate populations. For example, Koh *et al.* (*7*) recently reported that local extinc-

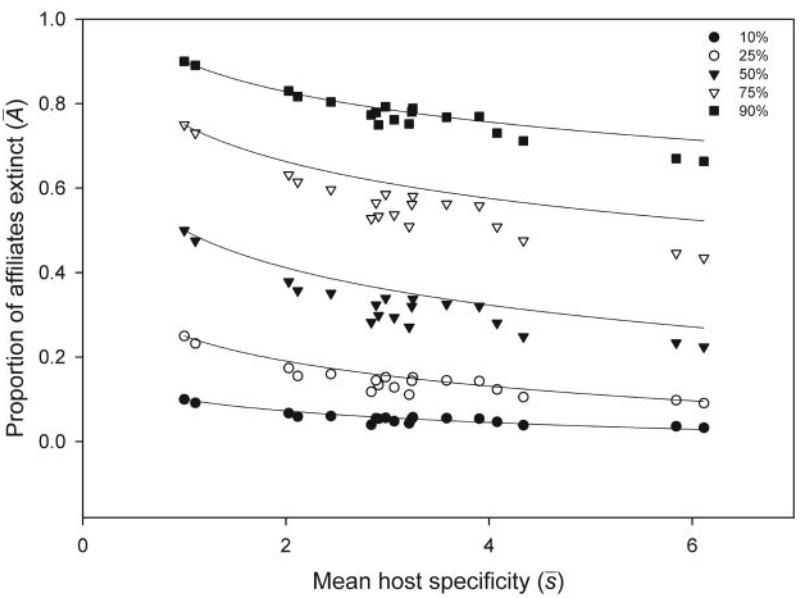

Fig. 2. Nomographic model expressing affiliate extinction probability as a function of host extinction probability and mean host specificity for 20 affiliate-host systems of varying mean host specificities: pollinating Agaonidae *Ficus* wasps–*Ficus*, primate *Pneumocystis* fungi–primates, primate nematodes–primates, primate lice–primates, seabird lice–seabirds, bird mites (including Avenzoariidae, Alloptidae, Analgidae, Proctophyllodidae, Pterolichidae, Pteronyssidae, Ptiloxenidae, Syringobiidae, and Xolalgidae)–birds, butterflies (including Papilionidae, Nymphalidae, Pieridae, Lycaenidae, and Hesperiidae)–host plants, and Lycaenidae ant butterflies–ants. See (*10*) for method. The affiliate extinction levels predicted by the nomographic model were highly concordant (concordant correlations $R_c > 0.99$) with those predicted from the probabilistic model (*10*). Symbols and lines represent predicted affiliate extinction levels from the probabilistic and nomographic models, respectively.

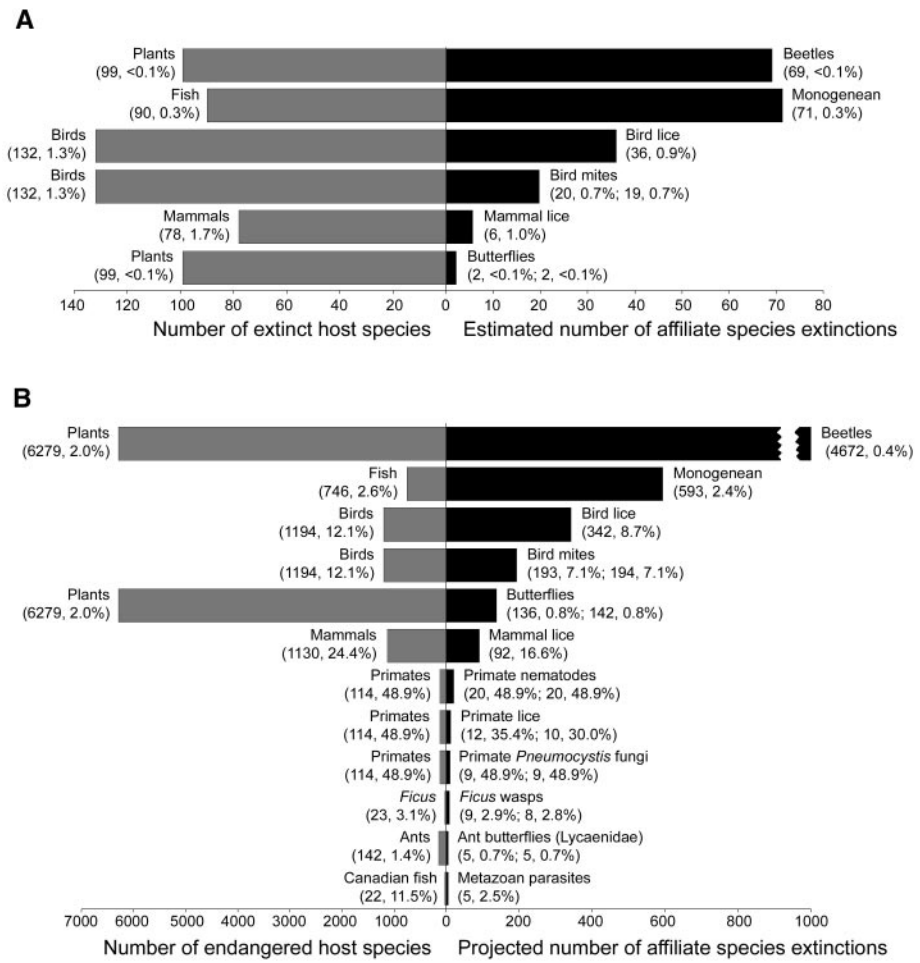

Fig. 3. Predictions of affiliate extinctions from the nomographic and combinatorial models. (**A**) Estimated numbers of historically extinct affiliate species based on the number of host species recorded as extinct. (**B**) Projected numbers of affiliate species extinctions, were all currently endangered hosts to go extinct. The first value in parentheses represents the absolute number and the second value the percentage of species extinct or endangered as predicted by the nomographic model; the second set of values in parentheses represents predictions from the combinatorial model for selected affiliate-host groups for which affiliation matrices are available. See (*10*) for details.

tions of butterfly species were significantly correlated with local extinctions of specific larval host plants (*7*). The issue of species or population coextinction has immediate implications for local conservation and management decisions.

Species coextinction is a manifestation of the interconnectedness of organisms in complex ecosystems. The loss of species through coextinction represents the loss of irreplaceable evolutionary and coevolutionary history (*18*, *19*). In view of the global extinction crisis (*3*), it is imperative that coextinction be the focus of future research to understand the intricate processes of species extinctions. While coextinction may not be the most important cause of species extinctions, it is certainly an insidious one.

References and Notes

1. B. W. Brook, N. S. Sodhi, P. K. L. Ng, *Nature* **424**, 420 (2003).
2. S. L. Pimm, P. Raven, *Nature* **403**, 843 (2000).
3. J. A. Thomas *et al.*, *Science* **303**, 1879 (2004).
4. M. Castelletta, N. S. Sodhi, R. Subaraj, *Conserv. Biol.* **14**, 1870 (2000).
5. N. E. Stork, C. H. C. Lyal, *Nature* **366**, 307 (1993).
6. L. A. N. Amaral, M. Meyer, *Phys. Rev. Lett.* **82**, 652 (1999).
7. L. P. Koh, N. S. Sodhi, B. W. Brook, *Biotropica* **36**, 272 (2004).
8. D. H. Clayton, R. D. Price, *Ann. Entomol. Soc. Am.* **92**, 675 (1999).
9. R. D. Price, D. H. Clayton, R. J. Adams, *J. Parasitol.* **86**, 948 (2000).
10. Materials and methods are available as supporting material on *Science* Online.
11. C. Hilton-Taylor, *2000 International Union for Conservation of Nature and Natural Resources (IUCN) Red List of Threatened Species* (IUCN, Gland, Switzerland, 2000; www.redlist.org).
12. R. K. Colwell, S. Naeem, in *Mites: Ecology and Evolutionary Analyses of Life-History Patterns*, M. A. Houck, Ed. (Chapman, New York, 1994), pp. 23–44.
13. W. H. Gotwald, Jr., *The Cornell Series in Arthropod Biology. Army Ants: The Biology of Social Predation* (Cornell Univ. Press, Ithaca, 1995).
14. G. P. Boswell, N. F. Britton, N. R. Franks, *Proc. R. Soc. Lond. B. Biol. Sci.* **265**, 1921 (1998).
15. L. E. Gilber, in *Conservation Biology*, M. E. Soule, B. A. Wilcox, Eds. (Sinauer Associates, Sunderland, MA, 1980), pp. 11–33.
16. D. A. Windsor, *Conserv. Biol.* **9**, 1 (1995).
17. T. M. Donovan *et al.*, *Ecology* **78**, 2064 (1997).
18. S. Nee, R. M. May, *Science* **278**, 692 (1997).
19. A. Purvis, P. M. Agapow, J. L. Gittleman, G. M. Mace, *Science* **288**, 328 (2000).
20. R. K. Colwell, C. X. Mao, J. Chang, *Ecology*, in press.
21. R. K. Colwell, *EstimateS: Statistical Estimation of Species Richness and Shared Species from Samples. Version 7* (http://viceroy.eeb.uconn.edu/estimates; permanent URL www.purl.oclc.org/estimates).

22. We thank K. Brennan, C. L. Nunn, S. V. Mironov, D. H. Clayton, J.-P. Hugot, J. M. Morales, J. Dabert, V. Novotny, and C. Mao for useful discussions. We also thank three anonymous reviewers for their comments. R.R.D. was funded by a Fulbright Fellowship, N.S.S and L.P.K were supported by the National University of Singapore (R-154-000-210-112), R.K.C. was supported by US-NSF grant DEB-0072702, H.C.P.'s databasing work was funded by a Natural Sciences and Engineering Research Council Canada Discovery Grant, and V.S.S. was supported by a Wellcome Trust Biodiversity Fellowship.

Supporting Online Material

www.sciencemag.org/cgi/content/full/305/5690/1632/DC1
Materials and Methods
Figs. S1 and S2
Tables S1 and S2

4 June 2004; accepted 29 July 2004

New Products

Qiagen
For more information
800-426-8157
www.qiagen.com
www.scienceproductlink.org

Automated DNA and RNA Preparations

The BioRobot M48 workstation, with MagAttract purification technology, provides fully automated purification of DNA, RNA, or viral nucleic acids from a range of clinically relevant samples, including blood and tissues. The systems can process six to 48 samples per run through easy-to-use software protocols. Flexible sample and elution volumes allow purification of nucleic acids at the yield and concentration required to ensure streamlined workflow and reliable performance in sensitive downstream applications, such as quantitative reverse transcription–polymerase chain reaction, microarray analysis, or amplification of a single-copy gene. In addition, an integral ultraviolet light allows convenient decontamination of the workstation interior betweens runs and disposable filter tips prevent carryover. The MagAttract Virus Mini M48 Kit provides a fully automated procedure for simultaneous purification of viral DNA and RNA from 400 µl serum and plasma for sensitive detection in downstream assays. The kit can be used with a broad range of DNA and RNA viruses for life science applications.

Bruker Daltronics
For more information
978-663-3660
www.bruker-biosciences.com
www.scienceproductlink.org

ClinProt 3D Platform

The ClinProt 3D research platform for metabolic or peptide/protein biomarker discovery makes use of high-resolution, high-performance liquid chromatography followed by high-mass accuracy mass spectrometry, typically using electrospray ionization–time-of-flight for the measurement of potentially thousands of molecules in human body fluids and tissues. With the intuitive and simple-to-use software, researchers can visualize a virtual gel, in three-dimensional stacking or contour-plot mode, or view the data in an average spectra view. The software features multiple algorithms for mining information that is not obvious on initial visual inspection.

UVP
For more information
800-452-6788
www.uvp.com
www.scienceproductlink.org

Ultraviolet Illuminator

The FirstLight UV Illuminator for fluorescent samples delivers even and uniform ultraviolet (UV) illumination. The instrument allows accurate and reproducible analysis quantitation of one-dimensional and two-dimensional electrophoretically separated DNA, RNA, or protein gels. The sensitivity and dynamic range are consistent across the full illumination surface for superior results. The edge-to-edge illumination and the large 25-by-26-cm imaging area, accommodating multiple gel sizes, ensure consistent uniformity for all gels. The patented design combines a high-density UV lighting system with a tuned-phosphor coating and filter assembly to achieve the uniform UV illumination that is critical for accurate quantitative analysis.

BD Biosciences
For more information
650-424-8222
www.bdbiosciences.com/clontech
www.scienceproductlink.org

NucleoSpin Tissue Kits

The NucleoSpin 96 and NucleoSpin 8 Tissue Kits are for purification of genomic DNA from a variety of tissue sources. These tissue kits are designed for rapid processing of a variable number of samples without the inconvenience of phenol-chloroform extractions. These kits allow the user to choose between processing multiples of 8 samples or to use 96-column plates for high-throughput. The NucleoSpin columns contain special silica membranes designed to ensure a high DNA binding capacity. The resulting DNA preparation is suitable for polymerase chain reaction, southern blotting, or any enzymatic reaction.

Immunetics
For more information
617-896-9100
www.immunetics.com
www.scienceproductlink.org

Miniblotters

Two new Miniblotters are for protein immunoblot screening on membranes blotted from popular precast gels. The Miniblotters enable users to incubate different antibodies with antigens run in separate gel lanes and transferred to a membrane. The MN18 and MN26 have 18 and 26 channels, respectively, which match the lanes in BioRad's Criterion precast gels. In practice, an intact blotted membrane is mounted directly in the unit. The patented design creates discrete parallel channels on the membrane, which act as independent incubation chambers. Each chamber holds sample volumes from 100 to 300 µl. A patented sealing system ensures that there is no cross-channel contamination. Miniblotters increase productivity by eliminating the need to cut, process, and mount individual strips. Applications include protein immunoblotting, DNA hybridization, and other membrane-based assays.

Ambion
For more information
800-888-8804
www.ambion.com
www.scienceproductlink.org

Cell Lysates

The patent-pending Cells-to-Signal Kit makes use of a chemical lysis method to create cell lysates in less than five minutes at room temperature. The cell lysate can be used directly for reverse transcription-polymerase chain reaction, bypassing RNA isolation altogether. The kit is suitable for monitoring small interfering-RNA–induced knockdown. The procedure is highly reproducible, is compatible with a wide variety of cell types, and offers a single-step procedure that is optimized for high-throughput analysis, both in manual processing and on robotic platforms.

USB Corp
For more information
216-765-5000
www.usbweb.com
www.scienceproductlink.org

RT-PCR Master Mixes

RT-PCR Master Mix and FideliTaq RT-PCR Master Mix provide convenience and performance for sensitive and specific, one-step reverse transcription-polymerase chain reaction (RT-PCR) reactions in a single tube. These ready-to-use mixes are available with Taq DNA Polymerase, optimized for routine detection, or FideliTaq DNA Polymerase, optimized for high-fidelity applications. Targets can be detected down to 10 pg of total RNA and 100 ng of polyA RNA.

Newly offered instrumentation, apparatus, and laboratory materials of interest to researchers in all disciplines in academic, industrial, and government organizations are featured in this space. Emphasis is given to purpose, chief characteristics, and availability of products and materials. Endorsement by *Science* or AAAS of any products or materials mentioned is not implied. Additional information may be obtained from the manufacturer or supplier by visiting www.scienceproductlink.org on the Web, where you can request that the information be sent to you by e-mail, fax, mail, or telephone.

Published by AAAS